THE UNIVERSITY *of* EDINBURGH

Examining mechanisms underlying the selective vulnerability of motor units in a mouse model of Spinal Muscular Atrophy

Sophie Rose Thomson

A thesis submitted for the degree of PhD at the University of Edinburgh

2013

Declaration

I declare that the work described in this thesis and its composition are entirely my own.

…….

Sophie Rose Thomson

Acknowledgements

There are many people which I would like to thank for supporting me over the last three years.

First, I would like to thank my supervisor Prof Tom Gillingwater for his unending encouragement and support. I really appreciate all of the opportunities that he has given me throughout this project, along with all of his ideas for this project. Without his support and advice over the last three years, my PhD project would simply not have been possible.

I would like to thank my second supervisor Prof Siddharthan Chandran, for first offering me the opportunity to undertake this PhD, and for his support and advice.

I would also like to thank Dr Paul Skehel and Dr Paul Heath for their invaluable input and advice into the experiments carried out in this thesis. Additionally, I would like to thank Masters students, Joya Nahon and Wen-Yo Tu for their contribution to this thesis.

I would like to thank everyone in the Gillingwater lab and others in the Hugh Robson Building for making the last three years so enjoyable, and for all their ideas and technical expertise. Particularly, I would like to thank Dr Gillian Hunter, Dr Tom Wishart, Prof Simon Parson and Derek Thomson for their support and for answering my endless questions.

I would also like to thank Maurice, Sarah, Eilidh, Gillian, Ines, Arwin, Yvonne and Scott for their support and for helping me proof read this thesis. I would also like to

thank Lewis for his support and for helping me produce some of the diagrams in this thesis.

Lastly, I would like to thank MND Scotland and the Euan MacDonald Centre for Motor Neuron Disease for my studentship, and the Anatomical Society for funding which enabled me to travel to Sheffield University to undertake the microarray studies.

Abstract

Spinal Muscular Atrophy (SMA) is a childhood form of motor neuron disease that causes a progressive paralysis that, in its most severe form, results in death before two years of age. There is currently no cure or treatment for SMA. SMA is caused by a reduction in levels of Survival Motor Neuron (SMN) protein, which results in the degeneration of lower motor neurons. This degeneration is first observed at the neuromuscular junction (NMJ), where pre-synaptic nerve terminals belonging to the motor neuron become dysfunctional and degenerate during the early stages of disease. Several previous studies have shown that the some populations of motor neurons appear to have a resistance to SMA pathology, while other neighbouring populations are vulnerable. In this study, we attempted to elucidate the cause of this vulnerability spectrum. Initially, we characterised the relative vulnerability of ten different motor unit pools in an established mouse model of severe SMA and attempted to correlate these vulnerabilities with quantified aspects of motor unit morphology. From this study, no significant correlation could be found with any aspect of motor unit morphology examined, suggesting that morphological parameters of motor neurons do no influence their relative susceptibility. We then attempted to identify changes in basal gene expression between protected and vulnerable pools of motor units using microarray analysis. Motor unit pools were labelled using a retrograde tracer injected into muscles that had previously been identified as having highly vulnerable or resistant motor units. Labelled motor neuron cell bodies were then isolated from the spinal cord using laser capture micro-dissection and RNA was extracted for microarray analysis. From this study, we identified several molecular pathways and individual genes whose expression levels

compared the gene expression profiles of vulnerable and resistant motor units. Thus, molecular differences between motor neuron pools likely underlie their relative vulnerability to degeneration in SMA. Lastly, we attempted to identify a novel peptide that could be used to label synapses, including neuromuscular junctions, *in vivo*. This would allow us to non-invasively visualise degenerating NMJs and other synapses in human patients without the need for a biopsy. Such a tool would be extremely valuable in assessing the effectiveness of drug trials, both in human patients and animal models, and may also contribute to earlier diagnosis of motor neuron disorders. To identify a potentially suitable peptide, we used a phage display library and panned for peptides that specifically bound to the outer surface of synapses using synaptosome preparations. From this panning we successfully enriched two peptides, the sequences of which were used to manufacture fluorescently tagged peptides.

Table of Contents

Chapter 1: Introduction

1.1 – The Neuromuscular System

1.1.1 - Motor Neurons

Motor neurons can be split into two main classes: upper and lower motor neurons. Upper motor neurons originate in the motor cortex in the brain and project their axons into the spinal cord. Lower motor neuron cell bodies lie in the ventral horn of the spinal cord, and are synapsed by upper motor neurons. The axons of lower motor neurons project into the periphery where they form synapses. There are two main classes of lower motor neurons: α-motor neurons and γ-motor neurons. α-motor neurons have large cell bodies and synapse extrafusal skeletal muscle, which is responsible for generating tension by contracting (Kanning et al., 2010). The synapse formed between α-motor neurons and extrafusal skeletal muscle is known as the neuromuscular junction (NMJ) (Figure 1). γ-motor neuron cell bodies are smaller than those of α-motor neurons, and they innervate intrafusal skeletal muscle. Intrafusal skeletal muscle comprises the muscle spindle – a sensory organ involved in proprioception and monitoring muscle tension. γ-motor neurons are not responsible for eliciting muscle contraction (Kanning et al., 2010).

1.1.2 - The Neuromuscular Junction Structure and Function

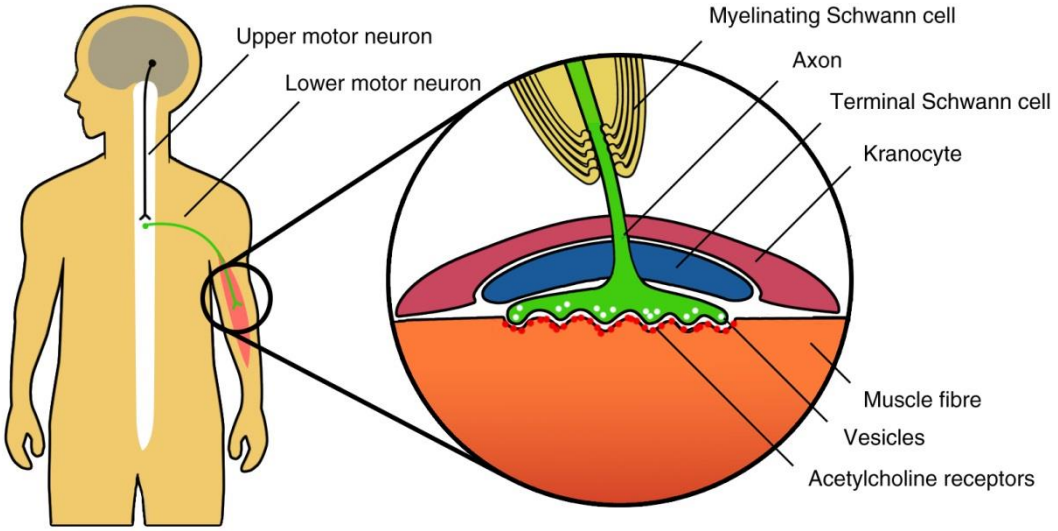

Figure 1 – Structure and location of the neuromuscular junction. Neuromuscular junctions form at the interface between lower motor neurons, which extend from the spinal cord into the periphery, and skeletal muscle fibres. The pre-synaptic terminal contains vesicles of acetylcholine which is released into the synaptic cleft when stimulated by an action potential. Acetylcholine receptors on the skeletal muscle fibre perfectly mirror the shape of the pre-synaptic terminal, and facilitate transduction of the action potential from the motor neuron to the muscle fibre. The neuromuscular junction is capped by non-myelinating glia, termed terminal Schwann cells, and the extra-laminar capping cell known as the kranocyte.

The neuromuscular junction is a peripheral cholinergic synapse that forms between lower α-motor neurons and skeletal muscle fibres (Figure 1). The NMJ is made up of three cell types: the lower motor neuron; the skeletal muscle fibre; and terminal Schwann cells (Figure 1). Recently, a fourth cell type associated with the NMJ was

identified by Court et al., 2008. This extra-laminar capping cell was termed the "kranocyte" and is found surrounding the terminal Schwann cell that caps the NMJ (Court et al., 2008). The function of the kranocyte has not yet been elucidated, but it may be involved in synaptic maintenance (Court et al., 2008).

Axons of lower motor neurons project from the ventral horn of the spinal cord, to the periphery. Upon entry into a muscle, the motor neuron axons arborise and extend their processes to many individual muscle fibres. One motor neuron and the many muscle fibres that it synapses onto make up a motor unit; the higher the number of synapses that an individual motor neuron makes, the larger the motor unit. The pre-synaptic nerve terminal is formed at the distal end of the motor neuron. The distal axon arborises to form the terminal branches of the pre-synaptic nerve terminal. The pre-synaptic nerve terminal contains synaptic vesicles containing acetylcholine (the neurotransmitter released at the neuromuscular junction), synaptic vesicle associated apparatus, and mitochondria (Sanes & Lichtman, 1999). The post-synaptic component of the NMJ consists of a large cluster of acetylcholine receptors on the muscle fibre surface, which makeup the motor endplate. The plaque of receptors perfectly mirrors the shape of the pre-synaptic terminal for optimal transmission of acetylcholine across the synaptic cleft. The motor endplate contains many post-synaptic folds, or invaginations, which increase the surface area of the motor endplate. Acetylcholine receptors are found clustered at the crests of the post-synaptic folds of the motor endplate (Sanes & Lichtman, 1999). Enveloping the synapse is a non-myelinating glial cell, known as a terminal Schwann cell. The terminal Schwann cell functions to provide trophic support to the neuromuscular

junction, and appears to be involved in NMJ re-modelling during development (Griffin & Thompson, 2008).

The axon of the motor neuron is myelinated by a myelinating Schwann cell (Figure 1). The membranes of Schwann cells associate with segments of axons and wrap around axons to form a myelin sheath (Figure 1). The points between individual Schwann cells' myelin along an axon are called the Nodes of Ranvier, and sodium channels and other proteins involved in action potential conduction are concentrated there. The myelination of axons facilitates salutatory conduction of action potentials - a form of impulse propagation that speeds up action potential conduction along large fibres (Quarles et al., 2006).

1.1.3 - Organisation of the Neuromuscular System

Motor neurons that control skeletal muscle contraction are organised into motor units. When a motor neuron axon enters a muscle, it arborises and synapses skeletal muscle fibres. A motor unit consists of an α-motor neuron, its axon, and all of the skeletal fibres that are innervated by that axon (Buchthal & Schmalbruch, 1980). Motor units vary in size, with the size of the motor unit being determined by the number of synapses that the motor neuron makes onto skeletal muscle fibres. Small motor units innervated a small number of skeletal muscle fibres, and large motor units innervate a large number of muscle fibres. Estimates of motor unit size in humans vary from 13 to over 2000, depending on the size of the muscle (Bradley, 1987). Motor units are recruited, or activated, in order of size. This is referred to as "the size principle": small motor units are recruited initially, followed by

progressively larger motor units. All the motor neurons that innervate a single muscle make up a motor pool (Buchthal & Schmalbruch, 1980).

1.1.4 – Motor Neuron Diseases

Motor neuron diseases are a group of untreatable neurological disorders that cause the degeneration of motor neurons. Motor neuron diseases result in a progressive paralysis due to the denervation of skeletal muscle. The most common form of motor neuron disease is the adult onset amyotrophic lateral sclerosis (ALS), which causes the degeneration of upper and lower motor neurons and results in death 3-5 years after diagnosis (Al-Chalabi et al., 2012). Mutations in a number of different genes, such as *SOD1*, *TDP-43* and *FUS* lead to ALS, however it is not known how these mutations result in the selective degeneration of motor neurons (Al-Chalabi et al., 2012).

Spinal muscular atrophy (SMA) is a childhood form of motor neuron disease, and is the most common genetic cause of infant death (Lunn & Wang, 2008). SMA causes the specific degeneration of lower motor neurons and, in its most severe form, results in death before two years of age (Lunn & Wang, 2008). SMA differs from ALS, in that it is caused by a mutation in a single gene, *SMN1*, resulting in a reduction in the levels of SMN protein (Lefebvre et al., 1995; Lorson et al., 1999). However, it is not known why low levels of SMN protein lead to the selective degeneration of lower motor neurons (Burghes & Beattie, 2009).

The degeneration of motor neurons in motor neuron diseases such as ALS and SMA are well-characterised, having been reported in both human patients and animal

models of the diseases for decades. More recently, evidence from research has shown that not all motor units are equally affected by the pathological processes of motor neuron diseases. Understanding the underlying causes of differences in motor unit vulnerability would shed new light onto motor neuron diseases, and may even lead to new therapeutic targets, preventing or delaying the degeneration of motor neurons.

In ALS, it is widely recognised that large diameter motor neurons that form large motor units are preferentially affected (Bradley et al., 1983; Fischer et al., 2004; Hegedus et al., 2007; Valdez et al., 2012). This evidence has been presented both in animal models of ALS, such as the $SOD1^{G93A}$ mouse model, and human tissue.

There are many similarities between ALS and SMA, the most obvious being that they cause the degeneration of motor neurons. Both ALS and SMA cause a degeneration of the peripheral synapse, the neuromuscular junction, which causes a progressive paralysis eventually resulting in death. Additionally, ALS has been described in the literature as a dying-back neuropathy (Reviewed by Dadon-Nachum et al., 2011), meaning that pathologies begin at the most distal segment of the motor neuron, the neuromuscular junction, and progress proximally towards the motor neuron cell body (Dadon-Nachum et al., 2011). Evidence has also been presented showing that neuron degeneration occurs in the same fashion in SMA, with pathologies occurring first at the neuromuscular junction before symptom onset, and progressing proximally towards the cell body in the spinal cord (Cifuentes-Diaz et al., 2002; Kariya et al., 2008; Ito et al., 2011). Based on this evidence, we can use the extent of neuromuscular junction pathologies to inform on the health of the entire

motor unit. Neuromuscular junctions that are undergoing degeneration are evidence of motor neurons in the first stages of degeneration.

In this study, motor unit vulnerability in SMA has been characterised in a large cohort of muscles by quantifying the extent of neuromuscular junction pathologies present in anatomically distinct muscles of the severe mouse model of SMA, *Smn*$^{-/-}$*;SMN2*$^{+/+}$. This data was then used in correlational studies to determine if motor unit morphology influenced motor unit vulnerability in SMA, as it does in ALS. Next, a molecular correlate was sought using microarray analysis to determine the gene expression profiles of vulnerable and resistant motor units in healthy mice. This provides insight into the underlying molecular mechanisms that may be perturbed in SMA, resulting in higher levels of vulnerability, and conversely, insight into protective factors present in some motor units.

From the study carried out here and the evidence that synapses in general are severely affected in SMA and other forms of neurodegenerative diseases such as ALS, it became evident that *in vivo* tools to study synapses in detail in humans are necessary. Currently, human synapses can only be accessed in rare post-mortem brain, spinal cord or muscle tissue, or muscle biopsies. Both post-mortem tissue and, to a lesser extent, muscle biopsy tissue offer an insight to human synapses only at late stages of disease and provide little insight into synapse pathologies as neurodegenerative diseases progress. Based on this need, we also sought to develop an *in vivo* labelling system that could safely be used to transiently label synapses in living patients and animal models. This was carried out using a phage display system to screen millions of random peptides for binding affinities to synapses.

In this chapter, the literature will be reviewed, detailing: the clinical and genetic background of SMA; the structure and function of the neuromuscular junction; neuromuscular junction involvement in SMA pathology; evidence for differential motor unit vulnerability in SMA; and the pathologies of central synapses in SMA.

1.2 - Spinal Muscular Atrophy

1.2.1 - Incidence and Aetiology

Spinal muscular atrophy (SMA) is a fatal childhood form of motor neuron disease for which there is currently no treatment or cure. SMA is caused by mutations in the Survival Motor Neuron 1 (*SMN1*) gene and affects between 1:6000 and 1:10000 live births (Pearn, 1978). This makes SMA the leading genetic cause of infant mortality (Lunn & Wang, 2008). Approximately 1:50 people are carriers of SMA (Ogino et al., 2002).

SMA causes the selective degeneration of lower motor neurons, causing a progressive flaccid paralysis and skeletal muscle atrophy (Lunn & Wang, 2008). Clinical features of SMA include a symmetrical weakness in legs and arms, with postural muscles in the trunk of the body also being severely affected (Lunn & Wang, 2008; D'Amico et al., 2011). Patients typically appear to have a bell-shaped upper torso due to atrophy of the respiratory muscles with death often resulting from breathing difficulties due to denervation of these muscles (Lunn & Wang, 2008). Interestingly, the diaphragm appears to be spared denervation in SMA patients and as a result many patients exhibit abnormal "abdominal breathing", or paradoxical

breathing, where the diaphragm alone is used to draw breath (Lunn & Wang, 2008; D'Amico et al., 2011).

There are four clinically defined types of SMA which are classified according to age of symptom onset and any major motor milestones reached (Table 1; Russman, 2007; Wang et al., 2007). Type I SMA (also known as Werdnig-Hoffmann disease), is defined as symptom onset beginning before 6 months of age with patients being unable to sit unaided, and death occurring before two years of age (Lunn & Wang, 2008). Type I SMA is also the most common, with approximately 50% of SMA cases being classed as type I (Markowitz et al., 2004). Type II is defined as symptom onset beginning between 6 and 18 months of age (Lunn & Wang, 2008). Patients with Type II SMA are able to sit unaided and possibly stand with assistance, but will never walk. Death occurs after two years of age but patients generally do not reach adolescence or adulthood (Lunn & Wang, 2008). Many Type I and II patients' lives are prolonged by artificial ventilation after the patients become too weak to breathe independently (Bach et al., 2002). Type III SMA (also known as Kugelberg-Welander disease) patients show symptom onset after 18 months of age. These patients gain the ability to stand and walk independently, but some may be confined to a wheelchair later in childhood. Type III SMA patients generally live until adulthood (Lunn & Wang, 2008). Type IV is considered adult onset and is rare, with patients typically developing mild muscle weakness symptoms in their 20s or 30s (Lunn & Wang, 2008). Type IV patients do not develop respiratory problems and continue to be able to walk during adulthood (Lunn & Wang, 2008).

Type	Age of Symptom Onset	Motor Milestone Reached	Age of Death
I	< 6 months	Unable to sit	< 2 years
II	6 – 18 months	Able to sit, standing with assistance	>2 years
III	>18 months	Able to walk with assistance, may need wheelchair	Adult
IV	Adult	Able to walk unaided	Adult

Table 1 – SMA types as determined by their symptom onset, motor milestones and age of death.

Some muscle groups are spared from paralysis in SMA patients, with the diaphragm, ocular muscles, and facial muscles showing little evidence of weakness (D'Amico et al., 2011). Also, proximal muscles such as the muscles of the trunk are generally more affected than the distal limb muscles (D'Amico et al., 2011).

1.2.2 - Genetics of SMA

SMA is caused by a mutation or deletion of the *SMN1* gene that leads to a reduction in SMN protein. *SMN1* was identified as the genetic determinant of SMA by Lefebvre et al. (1995) who found an inverted duplication of a gene at chromosome location 5q11.2-13.3, an area that had previously been associated with several different clinical manifestations of SMA (Brzustowicz et al., 1990; Melki et al., 1990). The two genes found at this location were named *SMN1* and *SMN2* (Lefebvre et al., 1995). Linkage analysis revealed that *SMN1* and *SMN2* were almost identical, with only five nucleotides differing between the genes (Lefebvre et al., 1995). However, *SMN1* and *SMN2* produce different mRNA transcripts (Lefebvre et al.,

1995). *SMN2* is differently spliced to *SMN1* due to a C to T transition at codon 280 of exon 7, resulting in the excision of exon 7 from the *SMN2* mRNA (Lorson et al., 1999). The mRNA transcripts of *SMN2* were detectable in all SMA patients and controls (Lefebvre et al., 1995). However, the full length mRNA transcripts of the *SMN1* gene were missing in SMA patients (Lefebvre et al., 1995). A study by Hahnen et al. (1995) found that 96% of SMA patients had a homologous deletion of exon 7 in *SMN1*.

Approximately 90-95% of *SMN2* mRNA transcripts undergo alterative splicing, meaning they lack exon 7 (Lorson et al., 1999). Translation of the *SMNΔ7* mRNA results in a truncated and non-functional SMN protein which is rapidly degraded (Lorson et al., 1998). The remaining 5-10% of *SMN2* mRNA transcripts retains exon 7 and produce full length functional SMN protein (Lorson et al., 1999). It is this reduction in SMN protein that leads to SMA, rather than a complete absence of the protein; while a complete loss of SMN protein results in embryonic lethality.

Disease severity in SMA correlates with the copy number of the *SMN2* gene (Coovert et al., 1997). Patients with low copy numbers of *SMN2* produce very little SMN protein and so have more severe clinical manifestations of SMA (Coovert et al., 1997; McAndrew et al., 1997). Patients with high copy numbers of *SMN2* have higher levels of SMN protein and so have less severe clinical manifestations of SMA (Coovert et al., 1997; McAndrew et al., 1997).

1.2.3 - SMN Protein Function

SMN is a 38kDa protein whichis ubiquitously expressed and found in the nucleus (Liu & Dreyfuss, 1996; Coovert et al., 1997), cytoplasm (Battaglia et al., 1997; Coovert et al., 1997) and synapses of cells (Fan & Simard, 2002). SMN protein contains one Tudor domain, the crystal structure of which was recently characterised (Lui et al., 2012).

SMN protein is expressed in all tissues, but is strongly expressed in the brain, spinal cord, skeletal and cardiac muscle, kidneys and liver (Battaglia et al., 1997; Coovert et al., 1997), with particularly strong expression being noted in the motor neurons (Battaglia et al., 1997). In the nucleus, SMN protein is found localised in sub-nuclear structures termed gems, or "Geminis of coiled bodies" (Liu & Dreyfuss, 1996; Coovert et al., 1997). Gems are believed to be involved in RNA processing and metabolism, due to their association with Cajal bodies (Liu & Dreyfuss, 1996). SMN protein's most characterised function is its role in the production of small nucleic ribonuclear protein complexes (snRNPs) known as the splicosome (Reviewed by Workman et al., 2012). snRNPs are involved in the splicing of pre-mRNA and catalyse the splicing of introns to produce mature mRNA (Workman et al., 2012). The SMN protein complex is required for the formation of splicosomal snRNPs in cells by directly binding to snRNAs and Sm proteins and assembling the Sm protein core onto the snRNA (Liu & Dreyfuss, 1996; Pellizzoni et al., 2002b; Workman et al., 2012). The SMN complex interacts with Sm proteins via SMN protein's Tudor domain (Liu et al., 2012). The SMN complex was once believed to have pre-mRNA splicing functions but recently it has been shown that the SMN

complex only acts to synthesise snRNPs and is not directly involved with pre-mRNA splicing (Coady & Lorson, 2011; Workman et al., 2012).

SMN protein has also been shown to interact with proteins involved in apoptosis signalling, such as Bcl-2 (Sato et al., 2000) and P53 (Young et al, 2002). SMN protein binds to Bcl-2 via a region near exon 6, preventing pro-apoptotic signalling (Sato et al., 2012). SMN protein has also been shown to directly bind to P53 protein and translocate to the Cajal bodies (Young et al., 2002). It is thought that by binding P53 protein, SMN prevents excess pro-apoptotic signalling (Young et al, 2002).

As SMN protein is ubiquitously expressed (Lunn & Wang, 2008), it is currently unclear why low levels of SMN protein specifically cause the degeneration of lower motor neurons (Burghes & Beattie, 2009).

1.3 - Motor Unit Vulnerability in SMA

1.3.1 - NMJ Pathology in SMA

Neuromuscular junction pathology in SMA is well-characterised in several different mouse models, as well as zebrafish and drosophila models. NMJ abnormalities were first reported in a severe mouse model of SMA by Cifuentes-Diaz et al. (2002). Here, they reported that the pre-synaptic terminal of the lower motor neuron pulled away from the motor endplate, leaving vacant or partially occupied motor endplates on the muscle fibre (Cifuentes-Diaz et al., 2002). This observation was further characterised in a severe mouse model of SMA, the *Smn*$^{-/-}$;*SMN2*$^{+/+}$ mouse by Murray et al. (2008). This denervation was observed in several different muscles in

late stage symptomatic mice, and evidence of pre-symptomatic NMJ abnormalities was also noted in the postural transversus abdominis muscle (Murray et al., 2008). Also in 2008, Kariya et al. reported similar defects of neuromuscular junctions in a different mouse model of SMA, the *Smn*$^{-/-}$*;SMN2;Δ7* mouse. Kariya et al. (2008) reported abnormal pre-synaptic nerve terminals which became more frequent in appearance as the mice aged. Similarly, Kariya et al. (2008) noted that there was evidence for pre-synaptic nerve terminal abnormalities, such as neurofilament accumulation, in pre-symptomatic mice in the diaphragm and intercostal muscles. Kariya et al. (2008) also described abnormalities at the post-synaptic motor endplate, where they noted a delay in maturation of the endplate. Motor endplates of *Smn*$^{-/-}$*;SMN2;Δ7* mice had fewer folds and perforations compared to wild type littermates, and continued expression of the embryonic γ subunit of acetylcholine receptors (Kariya et al., 2008).

Since these initial observations by Murray et al. (2008) and Kariya et al. (2008), neuromuscular junction abnormalities have been reported extensively in many mouse models. In the *Smn*$^{-/-}$*;SMN2;Δ7* mouse, studies have shown that the pre-synaptic terminals have abnormal ultra-structures, with a decrease in the density of synaptic vesicles and mitochondria (Kong et al., 2009). At the post-synaptic motor endplate, several studies have confirmed the results of Kariya et al. (2008) by providing further evidence of a delay in the maturation of the motor endplate, both in terms of an immature morphology (Kong et al., 2009; Lee et al., 2011) and embryonic acetylcholine receptor subunit expression (Kong et al., 2009). A study by Ling et al. in 2012 further described the widespread denervation of NMJs in the *Smn*$^{-/-}$*;SMN2;Δ7* mouse model in muscles clinically relevant to human patients.

Other mouse models of SMA which have shown defects in their neuromuscular junctions include the *Smn*$^{2B/-}$ mouse, where NMJs have been shown to be denervated, have abnormal neurofilament accumulation, and a delay in motor endplate maturation (Bowerman et al., 2012; Murray et al., 2013). Also, a mouse modelling an intermediate form of SMA, the *Smn1*$^{C/C}$ mouse, has shown synaptic defects with ectopic acetylcholine receptor clusters appearing and aberrant nerve sprouting from neuromuscular junctions (Osbourne et al., 2012).

Morphological neuromuscular junction abnormalities have also been observed in human muscle, both from biopsies of skeletal muscle (Kariya et al., 2008) and post-mortem tissue (Martinez-Hernández et al., 2013). In 2008 Kariya et al. described about 70% of the neuromuscular junctions from the biopsy of a type I SMA patient as showing pre-synaptic abnormalities, such as neurofilament accumulation and poor terminal arborisation. A further study showed an abnormal ultrastructure of the nerve terminal and distribution of synaptic vesicles in post-mortem foetal tissue of type I SMA (Martinez-Hernández et al., 2013).

1.3.2 - The Neuromuscular Junction Pathologies as a Read-Out of Motor Neuron Health

The pathological features of neuromuscular junctions in SMA are so well characterised in mouse models that they are frequently used as a read-out for the effectiveness of experimental therapeutics. Neuromuscular junction abnormalities have been used as a read-out of the therapeutic effects of treatments such as histone deacetylase inhibitors (HDAC inhibitors), which have been shown to increase *Smn*

gene expression in mouse models of SMA (Tsai et al., 2008; Riessland et al., 2010; Kwon et al., 2011). HDAC inhibitors, such as SAHA (Riessland et al., 2010), valproic acid (Tsai et al., 2008) and trichostatin A (Kwon et al., 2011), have been shown to significantly increase the percentage of fully occupied endplates found in SMA mouse models (Tsai et al., 2008; Riessland et al., 2010), and also increase the motor endplate area (Riessland et al., 2010; Kwon et al., 2011). Other studies of drugs such as RG3039 (Meerbeke et al., 2013), fasudil (Bowerman et al., 2012) and quercetin (Wishart et al., In Press) have also used neuromuscular junction pathologies as a readout for the drugs' therapeutic effectiveness.

1.3.3 - In Vitro Models of The Neuromuscular Junction

Understanding the early pathological events that take place at the human neuromuscular junction is an important aspect of motor neuron disease research. Based on this, and the lack of insight into early pathologies in human neuromuscular junctions, many labs have attempted to model neuromuscular junctions *in vitro* using human induced pluripotent stem cells (hiPSCs) (Takahashi et al., 2007). hiPSCs are pluripotent cells produced from fully differentiated adult somatic cells; usually skin fibroblasts (Takahashi et al., 2007). These fully differentiated cells are transformed into pluripotent cells usually by transfection of the transcription factors *OCT3/4*, *SOX2*, *C-MYC* and *KLF4* (Takahashi et al., 2007). The resulting cells are embryonic-like and have the capacity to both self-renew and differentiate into any cell type (Takahashi et al., 2007). As the adult cells used to produce hiPSCs can be taken from patients with genetic disorders, cell lines can be produced that retain the

genetic mutations responsible for the disease, which can then be differentiated into disease-specific cell types (Dimos et al., 2008; Ebert et al., 2009).

hiPSCs can be differentiated into motor neurons by first neuralising the cells and then assigning the cells a caudal positional identity, usually by exposing the cells to retinoic acid (Jessel, 2000; Wichterle et al., 2002). The caudalised neural precursors are then exposed to sonic hedgehog agonists which results in a ventral positional identity (Wichterle et al., 2002; Li et al., 2005). Neurotrophic factors are then added to the culture media and the cells mature over several weeks into motor neuron-like cells (Li et al., 2005). This has been carried out with hiPSCs derived from both ALS and SMA patients, resulting in cells with disease-specific phenotypes (Dimos et al., 2008; Ebert et al., 2009).

Attempts by several labs to produce neuromuscular junctions *in vitro* using healthy hiPSCs or human embryonic stem cells have proved unsuccessful (Li et al., 2005; Singh Roy et al., 2005; Guo et al., 2010; Patani et al., 2011, Marteyn et al., 2011). Motor neurons produced from stem cells have been cultured with the murine myoblast cell line C2C12 (Li et al., 2005; Patani et al., 2011); human muscle cell lines (Marteyn et al., 2011); and primary cultures of rodent muscle (Sing Roy et al., 2005; Guo et al., 2010) but have failed to produce synapses onto these myotubes. Most studies have reported small synaptic contacts forming between the motor neurons and myotubes, with small clusters of acetylcholine receptors forming on the myotube where a neurite outgrowth is visible (Li et al., 2005; Singh Roy et al., 2005; Guo et al., 2010; Patani et al., 2011, Marteyn et al., 2011). However, these clusters of receptors do not recapitulate either the size or complexity of an *in vivo* neuromuscular junction. The lack of synapse formation in these *in vitro* models is

likely due to the limited time period that the cells can be cultured together; a lack of supportive cell types such as myelinating and terminal Schwann cells; and the immaturity of both the motor neuron-like cells and myotubes.

1.4 - Selective Vulnerability of Motor Units in SMA

1.4.1 - Differences in NMJ Vulnerability in SMA

Degeneration of the neuromuscular junction is well characterised in SMA, but recent studies have revealed that not all neuromuscular junctions are equally affected by SMA. This was first observed by Murray et al. (2008) who reported a selective vulnerability of motor units innervating the cranial muscle, the levator auris longus (LAL). The LAL consists of two bands of fast twitch muscle fibres: the thin caudal band and the thick rostral band. When quantifying NMJ denervation in this muscle, it was noted that NMJs in the caudal band appeared to be severely affected, with a large percentage of the NMJs showing signs of denervation (Murray et al., 2008). However, in the rostral band, there was little evidence of any neuromuscular junction denervation (Murray et al., 2008). This phenomenon was noted in two different severe SMA mouse models; *Smn*$^{-/-}$*;SMN2*$^{+/+}$ and *Smn*$^{-/-}$*;SMN2;Δ7* (Murray et al., 2008).

Differences in neuromuscular junction vulnerability in SMA have also been reported by other groups (Bowerman et al., 2012; Ling et al., 2012). In 2012, Ling et al. carried out a study into a large cohort of clinically relevant muscles in the *Smn*$^{-/-}$*;SMN2;Δ7* mouse model in order to assess the extent of NMJ denervation. They found that there was extensive NMJ denervation in a subset of these muscles, notably

in axial muscles (Ling et al., 2012). However, a number of the muscles examined did not show any observable signs of NMJ denervation (Ling et al., 2012).

Selective vulnerability of neuromuscular junctions has also been noted in the intermediate mouse model of SMA, *Smn*$^{2B/-}$ (Bowerman et al., 2012). Bowerman et al. (2012) characterised the extent of NMJ denervation in *Smn*$^{2B/-}$ mice and noted that the postural muscle, the transversus abdominis, was particularly affected in late stage mice. The LAL was also analysed in the study by Bowerman et al. (2012), and interestingly, it was found that the caudal band of the LAL in the *Smn*$^{2B/-}$ mouse was resistant to disease and the rostral band was vulnerable, the opposite of what has been reported in the *Smn*$^{-/-}$*;SMN2*$^{+/+}$ and *Smn*$^{-/-}$*;SMN2;Δ7* mouse models (Bowerman et al., 2012). A delay in endplate maturation and decrease in endplate area were found in all muscles examined, regardless of NMJ vulnerability, consistent with the findings of Murray et al. (2008) in the *Smn*$^{-/-}$*;SMN2*$^{+/+}$ mouse model of SMA (Bowerman et al., 2012).

1.4.2 - What Underlies Differences in NMJ Vulnerability in SMA?

There is a clear spectrum of NMJ vulnerability in SMA, but the underlying cause has not yet been elucidated. Ling et al. (2012) suggested that muscle fibre type could play a role, as it does in ALS where fast twitch muscles are predominantly affected (Frey et al., 2000; Atkin et al., 2005; Pun et al., 2006). However, many of the vulnerable muscles examined in the study were composed of a mix of fast and slow muscle fibres and not all fast twitch muscles were found to contain vulnerable neuromuscular junctions (Ling et al., 2012). Additionally, both bands of the LAL are

also composed of pre-dominantly fast twitch muscle fibres, but caudal and rostral bands show different vulnerabilities (Murray et al., 2008). Ling et al. (2012) go on to suggest that the synapsing phenotype of neuromuscular junctions may play a role in vulnerability however no correlation between fast synapsing neuromuscular junctions and vulnerability was detected.

In the study by Murray et al. (2008), the authors characterised the LAL muscle in detail and noted that there was a distinct reproducible pattern of innervation in the LAL, with two clusters of NMJS present on the thin caudal band and five clusters of NMJs present on the thick rostral band. By tracing the motor units innervating the LAL from the point of entry into the muscle to their terminal synapses, Murray et al. (2008) found that motor units entering the LAL innervated either the rostral or caudal band, but never both. The authors also noted that motor endplate shrinkage was observable in both the rostral and the caudal bands of the LAL (Murray et al., 2008). Taken together, these results imply that it is a difference in the intrinsic properties of the motor units themselves that underlie this difference in vulnerability to SMA pathology.

1.5 – Pathologies of Central Synapses in SMA

While the neuromuscular junction is the most well-characterised and analysed synapse in SMA, there is recent evidence that suggests that central synapses are also affected. Ling et al. first described a reduction in the number of synaptic boutons onto lower motor neuron cell bodies in the spinal cord in 2010. In *Smn$^{-/-}$;SMN2;Δ7* mice, Ling et al. (2010) examined synapses onto lower motor neurons in the spinal

cord and found a reduction in the number of pre-synaptic boutons on the lower motor neuron cell bodies. In order to determine if this reduction in central synaptic boutons was due to a loss of synaptic connectivity or a lack of synapse formation, Ling et al. (2010) examined the number of synapses present in pre-symptomatic mice and found no significant difference in the number of synapses. This confirmed what was already known about synapse degeneration in the peripheral nervous system in SMA, which was that synapses have the ability to form normally, but subsequently degenerate (Ling et al., 2010). It was determined that the reduction in central synapses is pre-dominantly due to the loss of vGlut1-positive synapses, which are known to come from excitatory sensory proprioceptive neurons (Oliveira et al., 2003).

In 2011, Mentis et al. confirmed the results of Ling et al. (2010). Mentis et al. (2011) used the retrograde tracer dextran to specifically label either sensory neurons from the dorsal root, or motor neurons from the ventral roots of isolated spinal cords. In doing so, they confirmed that there was a reduction in the number of proprioceptive synapses in the ventral horns of *Smn*$^{-/-}$*;SMN2;Δ7* mouse spinal cords, and that this reduction was specifically due to the loss of vGlut1-positive synapses onto the soma and dendrites of α-motor neurons (Mentis et al., 2011). Importantly, Mentis et al. (2011) carried out a temporal analysis of vGlut1-positive synaptic loss in *Smn*$^{-/-}$*;SMN2;Δ7* mice. In doing so, they found that a significant reduction of central synapses was evident at post-natal day 4, demonstrating that loss of central synapses, as well as peripheral synapses, is an early event in SMA pathology.

Further studies have also demonstrated the loss of central synapses. A study by Park et al. (2010) showed that by selectively reducing SMN protein expression in motor

neurons they could phenocopy the symptoms and pathologies of SMA, including a loss of vGlut1 positive synapses onto motor neurons in the spinal cord. Conversely, two studies by Gogliotti et al. (2012) and Martinez et al. (2012) demonstrated that by selectively increasing SMN protein expression in motor neurons of a mouse model of SMA they could significantly increase the number of vGlut1-positive synapses onto motor neurons in the spinal cord.

1.6 - Aims.

Based on the evidence that NMJ vulnerability varies considerably across motor units in SMA, the main aim of this study is to determine the underlying cause of motor unit vulnerability in SMA.

Aim 1: Characterise the extent of motor unit vulnerability in a large cohort of muscles in a mouse model of SMA.

In order to determine a pattern of correlation between motor units and vulnerability in SMA, a large cohort of motor units must first be characterised in a mouse model of SMA to establish their relative vulnerabilities. This will be addressed using the established and well-characterised mouse model: $Smn^{-/-};SMN2^{+/+}$. Having established the relative vulnerabilities of these motor units based on the extent of NMJ degeneration present in late stage symptomatic mice, attempts will be made to correlate different parameters with motor unit vulnerability.

Aim 2: Investigate the morphological parameters underlying motor unit vulnerability in SMA.

Based on evidence in ALS, where larger motor units are consistently more vulnerable than small motor units, the morphology of motor units innervating with different vulnerabilities will be quantified. This quantification will be carried out in healthy mice, as to determine the "baseline" morphology of motor units and avoid quantifying aspects of SMA pathology. Healthy YFP-H mice, which express yellow fluorescent protein in a random subset of motor units, will be used to trace motor units. From these traces, morphological parameters such as motor unit size, intra-muscular arbour length, and branching pattern can be quantified and correlated with motor unit vulnerability in the $Smn^{-/-};SMN2^{+/+}$ mouse.

Aim 3: Investigate the molecular parameters underlying motor unit vulnerability in SMA.

Again, based on evidence in ALS, differences in gene expression could drive the motor unit vulnerability pattern seen in SMA. A microarray study comparing vulnerable and resistant motor units in healthy mice will be used to compare gene expression profiles. The results of this microarray will then be analysed to determine if there are differences in pathway activation or gene expression in vulnerable and resistant motor units that could underlie motor unit vulnerability in SMA.

Aim 4: Develop an in vivo transient synaptic marker.

Synapses are an early pathological target of SMA and many other neurodegenerative conditions. The ways in which we can visualise synapses in humans is extremely limited, often restricted to post-mortem tissue which only gives insights to end-stage disease pathology, or rare biopsy tissue. This necessitates the need for a synaptic marker that could transiently label synapses *in vivo* which could then be visualised, either through the skin using a specialised camera, or using *in vivo* imaging techniques. Using a phage display library, an attempt was made to identify a peptide that has a weak binding affinity to synapses that could be developed into an *in vivo* pan-synaptic marker for use in human patients and animal models.

Chapter 2: Motor neuron vulnerability does not correlate with motor unit morphology in spinal muscular atrophy.

2.1 - Introduction

The breakdown of the neuromuscular junction is a well characterised event in SMA pathology. Nerve-muscle and NMJ abnormalities have been described in both patients and animal models of the disease. Swoboda et al. (2005) assessed SMA patients using two electrophysiological techniques and found that both motor unit numbers and maximum compound action potential amplitudes declined as the disease progressed. Furthermore, structural analysis of human pre- and post-natal tissue has also shown abnormalities of NMJs, such as abnormal acetylcholine receptor clustering, synaptic vesicle defects, and aberrant ultrastructure of nerve terminals (Martinez-Hernandez et al., 2013). Animal models of SMA have also provided insights into NMJ degeneration in SMA, for example: a reduction of SMN protein in Drosophila melanogaster larvae resulted in motor behaviour abnormalities and disorganised synaptic boutons (Chan et al., 2003). Several different mouse models of SMA also proved invaluable in demonstrating NMJ abnormalities, such as the *Smn*$^{-/-}$*;SMN2*$^{+/+}$ (Murray et al. 2008); *Smn*$^{-/-}$*;SMN2;Δ7* (Murray et al., 2008; Karyia et al., 2008; Ling et al., 2010; Ling et al., 2012); and *Smn*$^{2B/-}$ (Bowerman et al., 2011; Murray et al., 2013).

However, the rate of NMJ degeneration varies extensively between muscles. For example, the levator auris longus (LAL) is a cranial muscle that is split into two bands: the caudal band (LALc) and the rostral band (LALr) (Murray et al., 2010). In 2008, Murray et al. reported that NMJ degeneration was significantly different

between the LALc and LALr at a post-symptomatic time point of the *Smn*$^{-/-}$;*SMN2*$^{+/+}$ mouse. The LALc was severely denervated whereas the LALr showed almost no observable NMJ abnormalities. This disparity across muscles has also been found in other mouse models of SMA, such as the *Smn*$^{-/-}$;*SMN2;Δ7* mouse model (Ling et al., 2012). These studies have undoubtedly shown that NMJ degeneration is a hallmark of SMA and that the rate of degeneration varies considerably. However, why some motor units appear to have a resistance to SMA pathology whereas others are particularly susceptible has not yet been elucidated.

In the most common form of motor neuron disease, adult onset amyotrophic lateral sclerosis (ALS), there is a well-characterised correlation between susceptibility to disease and motor unit size. In ALS, large motor units are preferentially affected and this has been demonstrated both in human post-mortem tissue and animal models of ALS (Bradley et al., 1983; Fischer et al., 2004; Hegedus et al., 2007; Valdez et al., 2012). In 1983, Bradley et al. demonstrated in post-mortem human tissue that ALS patients had 33% fewer large myelinated fibres in the phrenic nerve than that of controls. This trend was also true for the sural nerve, which had 30% fewer large myelinated fibres than that of controls (Bradley et al., 1983). This correlation has been confirmed in animal models of ALS, specifically the SOD1^{G93A} mouse model (Fischer et al., 2004; Hegedus et al., 2007; Valdez et al., 2012). In a systematic time course study, Fischer et al. (2004) found that there was a significant decrease in large diameter axons in the ventral roots of SOD1^{G93A} mice from age P80 until death. Also observed was an increase in small calibre axons which may have been compensatory sprouting or regeneration (Fischer et al., 2004). The correlation between motor unit susceptibility and motor unit size in the SOD1^{G93A} mouse has

been demonstrated through electromyographical analysis (Hedegus et al., 2007). Hedegus et al. (2007) found that there was a parallel decline in tetanic force of muscles and motor unit number over time in SOD1^{G93A} mice, which implies that the large motor units responsible for forceful muscle contractions were degenerating. Also, Valdez et al. (2012) found that motor units that are vulnerable in ALS are also vulnerable to age-related changes at the NMJ. They went on to show that small motor units were resistant to these age-related changes, whereas large motor units were more susceptible (Valdez et al., 2012).

There is considerable evidence that ALS and SMA are linked at the molecular level (Zou et al., 2007; Turner et al., 2009; Kariya et al., 2012; Yamazaki et al., 2012). In 2007, Zou et al. showed that SMN protein was able to protect NSC34 cells from the toxic effects of mutant SOD1 protein. This relationship between SOD1 and SMN has also been demonstrated in animal models (Turner et al., 2009; Kariya et al., 2012). Turner et al. (2009) found that reducing SMN protein levels in SOD1^{G93A} mice exacerbated the ALS phenotype. Similarly, Kariya et al. (2012) found that over-expressing SMN protein in two different mouse models of mutant SOD1 delayed symptom onset but did not increase the lifespan of mice. SMA and ALS have also been linked through FUS (fused in sarcoma) in a study that showed FUS and SMN interact directly. FUS expression is necessary for gem formation, where the majority of SMN protein is found, and a reduction in gems has been found in fibroblasts of ALS patients with both FUS and TDP-43 mutations (Yamazaki et al., 2012). Based on this evidence that ALS and SMA are molecularly linked, it seems likely that similar mechanisms would underlie motor unit vulnerability in ALS and SMA.

We hypothesised that the pattern of motor unit vulnerability in SMA might be similar to the well-characterised selective vulnerability in ALS, and so we decided to investigate whether there was a correlation between motor unit morphology and vulnerability in SMA. Motor unit morphology can be mapped using the transgenic mouse model Thy.1-YFP-H (Feng et al., 2001). The Thy.1-YFP-H mouse expresses yellow fluorescent protein (YFP) in a random subset of neuronal cells under the control of the Thy.1 promoter (Feng et al., 2001). This means that only a small fraction of motor neurons are visible in skeletal muscle and so entire axonal arbours of motor units can be visualised and traced throughout a muscle, from the point of entry to the terminal branches. From these traces, many morphological characteristics can be assessed and quantified, such as motor unit size, branching pattern and intramuscular arbour length. Motor unit tracing has previously been used for quantification of motor unit size (Valdez et al., 2012).

Here, a cohort of skeletal muscles were selected for analysis to create a heat map of motor unit vulnerability in the *Smn*$^{-/-}$;*SMN2*$^{+/+}$ mouse model of SMA, using NMJ pathology as a readout of motor unit vulnerability. The extent of NMJ degeneration was quantified in each of these muscles using immunohistochemical staining and confocal microscopy. Next, a number of the same muscles were dissected from young adult Thy.1-YFP-H mice and entire motor unit arbours were reconstructed using fluorescent microscopy. Various morphological aspects of the motor units were quantified and Spearman correlation analysis was used to test for correlations between motor unit morphology and vulnerability. In all tests carried out, no significant correlation was found between motor unit vulnerability in SMA and motor unit morphology. Other morphological and developmental parameters that

might affect motor unit vulnerability were also measured, such as terminal Schwann cell number and synapse elimination rate. Again, no correlation was found with motor unit vulnerability in SMA. Other parameters were also examined, such as body axis position, muscle fibre type, motor endplate area, motor endplate morphology and synapsing phenotype however, no significant correlation with motor unit vulnerability could be detected.

2.2 – Method

2.2.1 - Ethics Statement

All animal experiments were approved by a University of Edinburgh internal ethics committee and were performed under license by the UK Home Office (Project License number 60/3891).

2.2.2 - Animal Husbandry

Smn$^{+/-}$*;SMN2*$^{+/+}$ mice (Jackson Labs strain no. 005024) on a congenic FVB background were maintained as heterozygous breeding pairs under standard SPF conditions in animal care facilities in Edinburgh. All animal procedures and breeding were performed in accordance with Home Office and institutional guidelines. Retrospective genotyping was carried out using standard PCR protocols detailed below.

Thy.1-YFP-H (Feng et al., 2001) on a congenic C57Bl/6 background were originally obtained from Jackson Labs and maintained under standard SPF conditions in animal care facilities in Edinburgh.

Neonatal (P5) *Smn*$^{-/-}$;*SMN2*$^{+/+}$ and unaffected littermates were killed by overdose of anaesthetic via intraperitoneal injection of sodium pentobarbital (Euthenal). Young adult Thy.1-YFP-H mice were killed by overdose of anaesthetic via inhalation of iso-fluorane.

2.2.3 - Genotyping of Smn$^{-/-}$;*SMN2*$^{+/+}$ *Mice*

After death, 5mm tail tips were taken from mice for retrospective genotyping. The tail tip was digested overnight in Tail Tip Lysis Buffer + 5µl/ml proteinase K at 55ºC. The next day, the tail tips were vortexed to make sure they were fully dispersed and centrifuged at 14000rpm for 5 minutes. The supernatant was aspirated and added to a new 1.5ml eppendorf containing 500µl iso-propanol. This was mixed by gently inverting the tube several times, until strands of DNA could be seen. This mixture was centrifuged at 14000rpm for 5 minutes to pellet the DNA. The DNA pellet was washed twice in 70% ethanol and then dried for approximately 20 minutes at 37ºC to ensure all traces of ethanol had evaporated. The DNA was then re-suspended in 200µl autoclaved deionised water.

Genotyping was performed by carrying out two separate PCR reactions: one testing for the presence of the endogenous *Smn* mouse gene; the other testing for the presence of the neomycin cassette used to insert the human *SMN2* gene into the mouse genome. Presence of only the endogenous *Smn* mouse gene in a sample

would indicate a wild type pup, whereas presence of only the neomycin cassette would indicate a knockout pup. If both genes were present in a sample, the pup was a heterozygote and considered an unaffected littermate as these mice are indistinguishable from wild type mice.

PCR	Forward Primer	Reverse Primer	Product Length
Neo-mycin	CTTGGGTGGAGAGGCTATTC	AGGTGAGATGACAGGAGATC	280bp
Smn	TTTTCTCCCTCTTCAGAGTGAT	CTGTTTCAAGGGAGTTGTGGC	420bp

Table 1: PCR primer and product size information.

PCRs were carried out using GoTaq Green Master Mix (Promega Express, M7112) according to the manufacturer's instructions. 1µl of extracted DNA was added per reaction. Positive and negative controls were run with each PCR; previously identified heterozygote tissue was used as a positive control, and a reaction with 1µl water replacing DNA was used as a negative control. Samples were run on a PCR machine using the following programme:

Step	Temperature (ºC)	Time (s)
1	94	120
2	94	30
3	61	30
4	72	45
	Go to step 2, repeat 27 times.	
5	72	120
6	4	Hold

Table 2: PCR programme setup for $Smn^{-/-};SMN2^{+/+}$ genotyping.

Samples were then resolved on a 1.5% agarose gel at 100v for approximately 30 minutes with a 100bp DNA ladder (Promega Express, g2101) and visualised.

2.2.4 - Dissections

2.2.4.1 - Cranial Muscles

The cranial muscles were removed intact from the mouse by removing the muscle mass on top of the skull, along with the overlying skin and ear pinnae. The dissection was pinned into a Sylgard dish using insect pins, with the deep muscles facing up. Excess muscle tissue was cut away until the midline and thin cranial muscles could be visualised. The dissection was then fixed in 4% PFA for 10 minutes on a rocking platform. After fixation, the dissection was washed in 0.1M PBS. Any remaining large muscles were removed along with excess fat, connective tissue and skin. The cranial muscles were then dissected individually starting with the most superficial – the intersuctularis (IS) followed by the adductor auris longus (AAL), auricularis superior (AS) and finally the levator auris longus (LAL). All

muscles were cut flush at the point of attachment at the pinnae of the ear, carefully reflected in a lateral to medial manner until they could be cut flush at the midline. The muscles were then cleaned by removing fat and connective tissue by blunt dissection before staining.

2.2.4.2 - Triangularis Sterni

The mouse was decapitated and skinned from the abdomen. When removing the skin, the pectoralis muscles were also cut away so that the fore limbs were removed along with the skin. The abdominal wall was cut all the way around and the spinal cord was also cut at the thoracic region. The hind limbs and pelvis of the mouse were removed, along with the abdominal organs. The remaining spinal cord was removed by cutting along its length, in a caudal to rostral direction. The chest wall could now be opened, and pinned out inside out in a Sylgard dish using insect pins. The diaphragm and the internal organs were removed and the dissection was fixed in 4% PFA for 10 minutes on a rocking platform before being washed in 0.1M PBS. The ribcage was then cut between the sternum and mammary vessels. The edge of the triangularis sterni (TS) could then be identified and gripped with a pair of forceps. By gently lifting and blunt dissecting away fat and connective tissue, the triangularis sterni could be removed from the ribcage. The join between bone and cartilage along the ribs was used as a guide as to the shape of the TS muscle. After removal from the ribcage, the TS was cleaned by removing fat and connective tissue by blunt dissection.

2.2.4.3 - Transversus Abdominis

The mouse was skinned from the abdomen and an incision was made in the abdominal wall. This incision was extended across the abdomen, up both sides of the spinal column and across the sternum, cutting away the diaphragm along the way. The dissection was removed and pinned out in a Sylgard dish using insect pins. The superficial abdominal muscles were removed by cutting down the midline and reflecting the muscle to reveal the transversus abdominis (TVA) underneath. Blood vessels that run down each side of the midline, superficial to the TVA, were then removed and the dissection was fixed in 4% PFA for 10 minutes on a rocking platform before being washed in 0.1M PBS.

After fixation, ribs were removed to expose a larger area of the TVA. The majority of the TVA was then removed by cutting down the midline, through the sternum and as close to the ribs as possible. The TVA was then removed by cutting following the direction of the muscle fibres near the oblique muscles. Once removed from the abdominal wall, the cartilaginous segment of sternum that was attached to the TVA was removed by blunt dissection. The TVA was then cleaned of excess connective tissue by blunt dissection.

2.2.4.4 - Hind Limb Muscles

Hind limb muscles were dissected by removing the limb from the body at the femur using bone scissors. The skin was then reflected over the limb, what was then pinned out in a Sylgard dish using insect pins and fixed with 4% PFA on a rocking platform for 15 minutes, before being washed with 0.1M PBS. After fixation, the muscles of

interest, the tibialis anterior (TA), extensor digitorum longus (EDL), and gastrocnemius (GS) were identified and removed by cutting the tendon at the ankle, then blunt dissecting out the muscles until they had to be cut at the knee.

2.2.4.5 - Sectioning of Hind Limb Muscles

Hind limb muscles were sectioned before staining. Muscles were cyro-protected in approximately 5ml 30% sucrose in 0.1M PBS overnight at 4^{o}C, until the muscle had sunk to the bottom of the bijou. The muscles were then briefly washed in cold 0.1M PBS and embedded in OCT on the freezing platform of a freezing microtome. The muscle was cooled to -40^{o}C for 10 minutes, warmed to -20^{o}C and 100µm longitudinal sections were taken from the muscle. These sections were stored in cold 0.1M PBS so that sucrose and OCT could dissolve before staining.

2.2.5 – Immunohistochemistry

Antibody	Raised in	Concentration	Secondary	Concentration
Neurofilament (2H3, Developmental Studies Hybridoma Bank)	Mouse	1:200	AffiniPure Dylight 488 Donkey Anti-Mouse (H+L)	1:100
SV2 (Developmental Studies Hybridoma Bank)	Mouse	1:100	AffiniPure Dylight 488 Donkey Anti-Mouse (H+L)	1:100
S100 (Dako)	Rabbit	1:400	Dako Swine Anti-Rabbit FITC	1:60

Table 3: Primary and secondary antibody information. Neurofilament and SV2 antibodies were used to stain muscles for occupancy counts and synapse elimination rate quantification. S100 was used to quantify terminal Schwann cell number.

For muscles from P5 *Smn*$^{-/-}$;*SMN2*$^{+/+}$ mice and littermates and P7 and P14 littermates, muscles were stained by permeabilising the tissue in 2% Triton X-100 in 0.1M PBS for 30 minutes. The muscles were then blocked in 4% BSA + 1% Triton X-100 in 0.1M PBS for at least 30 minutes. Primary antibodies were dissolved in blocking solution according to Table 3 and the muscles were incubated in primary antibody solution at 4^{o}C overnight on a rocking platform. The following day, muscles were washed in four changes of cold 0.1M PBS for 30 minutes each. The

muscles were then stained with 5µg/ml TRITC-conjugated α-bungarotoxin in 0.1M PBS for 10 minutes in the dark on a rocking platform. All subsequent incubations and washes were carried out in the dark. Bungarotoxin was washed off in three changes of cold 0.1M PBS for 5 minutes each. Secondary antibody was then made up in 0.1M PBS according to Table 3, and muscles were washed in this for 2-4 hours at room temperature on a rocking platform. The muscles were washed again in three changes of 0.1M cold PBS for 10 minutes each. At this stage, muscles that were to be used for terminal Schwann cell counts were also stained with TO-PRO-3 for 10 minutes before being washed in three changes of cold 0.1M PBS for 5 minutes each. Muscles were then mounted onto glass with glass coverslips using Mowiol containing DABCO as an anti-fade agent. Slides were left to set at room temperature overnight in the dark before being viewed on the fluorescent microscope to check for adequate staining.

For Thy.1-YFP-H mice, muscles were dissected as above, but prior to fixation they were washed in 5µg/ml TRITC-conjugated α-bungarotoxin in 0.1M PBS in the dark for 10 minutes. They were then washed in several quick changes of cold 0.1M PBS and fixed in 4% PFA in 0.1M PBS for 10 minutes. The post-fix dissection was then carried out as above and the muscles were cleaned of connective tissue and fat. The muscles were then mounted on glass slides with glass coverslips using Mowiol containing DABCO as an anti-fade agent. Slides were left to set at room temperature overnight in the dark before being viewed on the fluorescent microscope.

2.2.6 - Imaging

NMJs, terminal Schwann cells and YFP-labelled axons were visualised using a Zeiss LSM 710 laser scanning confocal microscope (20x objective/0.4NA; 40x objective/1.3NA oil objective; 63x objective/1.4NA oil objective). 488nm, 543nm and 633nm laser lines were used for excitation and confocal Z-series were merged using Zen software. Laser intensity and gain was set individually, so that there was no saturation of signal. Z-stack slices were 1µm in thickness and each line was averaged twice to improve image quality.

Micrographs for the reconstruction of motor units were taken using a standard epi-fluorescent microscope equipped with a chilled CCD camera using a 10x objective; 0.3NA. (Nikon IX71 microscope; Hammamatsu C4742-95; OpenLab software). YFP-labelled axons were imaged using 488nm excitation and 520nm emission optics; TRITC-labelled motor endplates were imaged using 543nm excitation and 590nm emission optics.

2.2.7 - Quantification and Analysis

For motor unit vulnerability studies, a minimum of 80 NMJs per muscle per mouse were quantified from confocal images taken with x20 and x40 objectives. For occupancy counts, individual NMJs were categorised as either: fully occupied endplates, defined as the nerve terminal (identified by neurofilament and SV2 staining) covering more than 50% of the motor endplate; partially occupied endplates, defined as the nerve terminal covering less than 50% of the endplate but still being in contact with the motor endplate; or vacant, defined as no longer being

contacted by a nerve terminal. These data were then converted into percentages and plotted as bar charts using Graph Pad Prism v5. Mann-Whitney U tests were used to analyse statistical significance.

Motor unit reconstructions from Thy.1-YFP-H mice were used to quantify morphological characteristics of single motor neurons. Motor unit reconstructions were produced by Masters student Joya Nahon, under my supervision. Motor unit size was determined by counting the number of motor endplates per axon from reconstructed motor units. Total intramuscular arbour length was measured by tracing the axons in reconstructed images by hand from the point at which the axon entered the muscle to all the nerve terminals. This was achieved using ImageJ software using the "measure" function and line tool. The sum of the primary axon trunk and all the distal branches made up the total intramuscular arbour length. The number of branch points was measured by marking branch points by hand on the motor unit reconstructions. These data could then be used to create schematic branching diagrams based on entire motor unit reconstructions. From these schematics, the branch order for each terminal branch could be determined by counting the number of branch points between the nerve terminus and the axon's point of entry into the muscle. Endplate area was determined by measuring the area of the motor endplate from Maximum Intensity Z-stock images taken on a confocal microscope. The outline of the endplate was manually traced on ImageJ and the software calculated the total area of the endplate.

For synapse elimination studies, P7 and P14 unaffected littermates from *Smn*$^{+/-}$*;SMN2*$^{+/+}$ litters were used. The number of axonal inputs in neonatal muscles was

measured by counting the number of axons converging on a single motor endplate. A minimum of 80 endplates per muscle per mouse was counted.

For terminal Schwann cell counts, P5 unaffected littermates from *Smn*$^{+/-}$;*SMN2*$^{+/+}$ litters were used. Maximum intensity Z-stack projections of endplates were taken on a confocal microscope and analysed in Adobe Photoshop. To be counted as a terminal Schwann cell, the cell had to be positive for S100 with a TO-PRO-3 labelled nucleus and be overlying a motor endplate.

Spearman correlation analysis was carried out in Graph Pad Prism v5 to determine if any correlations had statistical significance. Spearman correlation analysis determines whether there is a significant correlation where data contains ordinal variables, as is the case for the vulnerability spectrum data.

2.3 - Results

2.3.1 - Selection, Preparation and Staining of Muscles

In order to determine the extent of the variation in motor unit susceptibility to SMA, anatomically distinct skeletal muscles innervated by distinct motor unit pools in late stage (P5) *Smn*$^{-/-}$;*SMN2*$^{+/+}$ mice were chosen for analysis (Figure 1).

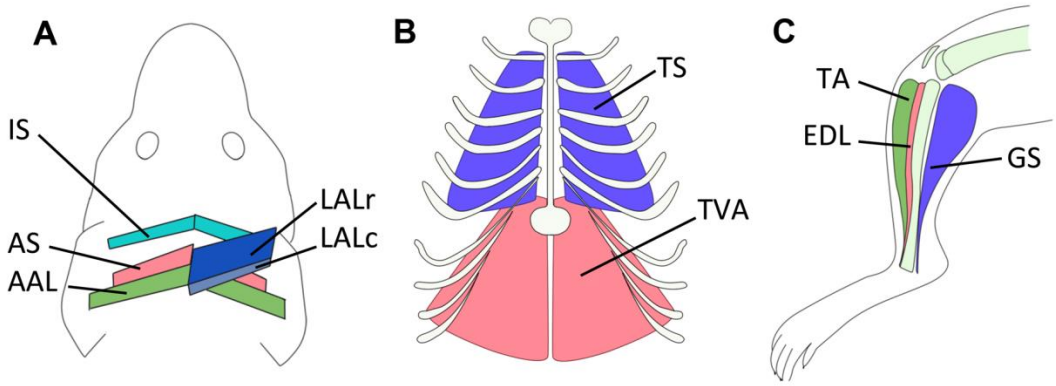

Figure 1 – Schematic of muscles dissection from P5 Smn$^{-/-}$;SMN2$^{+/+}$ mice and unaffected littermates. (A) The location of the four cranial muscles: the levator auris longus rostral and caudal bands, the adductor auris longus, the auricularis superior, and the interscutularis. (B) The location of the trunk muscles: the triangularis sterni, and the transversus abdominis. (C) The location of the three hind limb muscles: the tibialis anterior, extensor digitorum longus and the gastrocnemius.

Muscles were dissected from various body regions, specifically the cranial region (Figure 1A; Figure 2), torso (Figure 1B; Figure 3 and Figure 4) and hind limbs (Figure 1C; Figure 5), in order to determine if body position had an effect on motor unit vulnerability in SMA. Muscles were chosen that could be dissected out prior to fixation, which removes the need to perfuse the whole mouse and improves staining quality of skeletal muscle. Thin flat muscles were also preferentially selected for analysis as they do not require to be sectioned in order to visualise NMJs. The use of whole mount muscle preparations and confocal microscopy allow the entire depth of the muscle to be visualised and ensures that all NMJs are intact for quantification.

D
F
C
G
B
E
A
H

Figure 2 – Cranial muscle dissections. The cranial muscles of interest are the most superficial of the cranial muscle groups and are used for independent ear movement. They were dissected by removing the muscle mass on top of the skull intact with the skin and ears. (A) An incision was made between the eyes and extended around the top of the head, underneath each ear, until the original incision was met. The skin, ears and underlying muscle mass were then removed by cutting along the skull and reflecting the skin. Care was taken to angle the blades towards the skull to minimise the risk of cutting a superficial cranial muscle. (B) Once completely detached, the muscle mass was pinned out (deep muscles facing up) in a Sylgard dish using insect pins. The muscles of interest are now the deepest layer. (C) The large mass of thick muscles was then carefully removed until the thin intact cranial muscles and midline (white arrow) could be seen. At this point, the muscles were fixed using 4% PFA in 0.1M PBS for 10 minutes on a rocking platform. (D) After fixation, the remaining thick muscles were removed and excess skin underneath the muscle layer was removed. The layers of thin cranial muscles were now fully visible and could be removed starting with the most superficial muscle. The IS was removed by cutting it at the midline, then reflecting the muscle in a medial to lateral manner. The muscle was then cut flush at the point of attachment on the skin. (E) The AAL was removed by cutting the attachment at the skin by the ear canal. The muscle was then reflected in a lateral to medial manner before being cut flush at the midline. (F) The AS was removed by cutting the attachment by the ear canal. The AS was then removed by reflecting the muscle in a lateral to medial manner, being careful not to remove the LALc as the two muscles are closely connected by a layer of connective tissue. The

AS was then cut flush at the midline. (G) The LAL was then removed as a single muscle, by cutting the point of attachment along the ear and then cutting the muscle flush along the midline. (H) The muscles are then cleaned of fat and connective tissue. The different sizes and shapes of the muscles are clear when they are removed and separated. Here the muscles are shown in the order (from left to right); IS, AAL, AS and LAL (LALr and LALc).

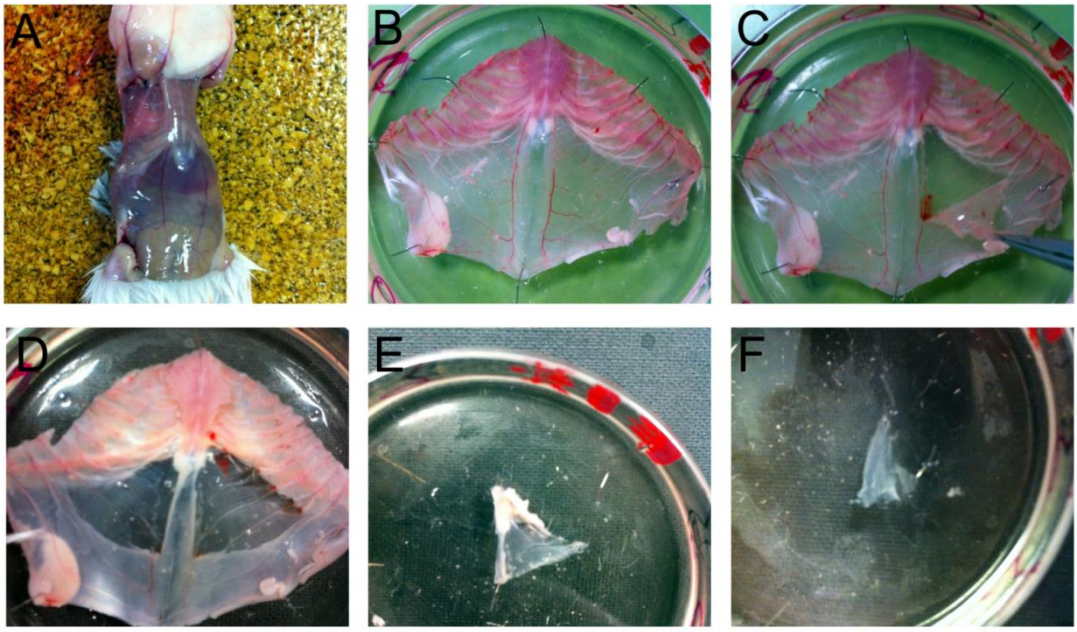

Figure 3 – Transversus abdominis dissection. (A) The mouse was skinned to expose the abdominal and chest wall. (B) The abdominal wall was removed from the mouse and pinned out in a Sylgard dish using insect pins. (C) The overlying superficial abdominal muscles were reflected to reveal the TVA underneath. A superficial blood vessel was also removed. The TVA was then fixed in 4% PFA for 10 minutes on a rocking platform. (D) Portions of the ribs were removed to expose a larger area of the TVA. (E) The TVA was cut from the abdominal wall, with the cartilaginous sternum attached. (F) The sternum was carefully removed by blunt dissection and the TVA was cleaned of fat and connective tissue for staining.

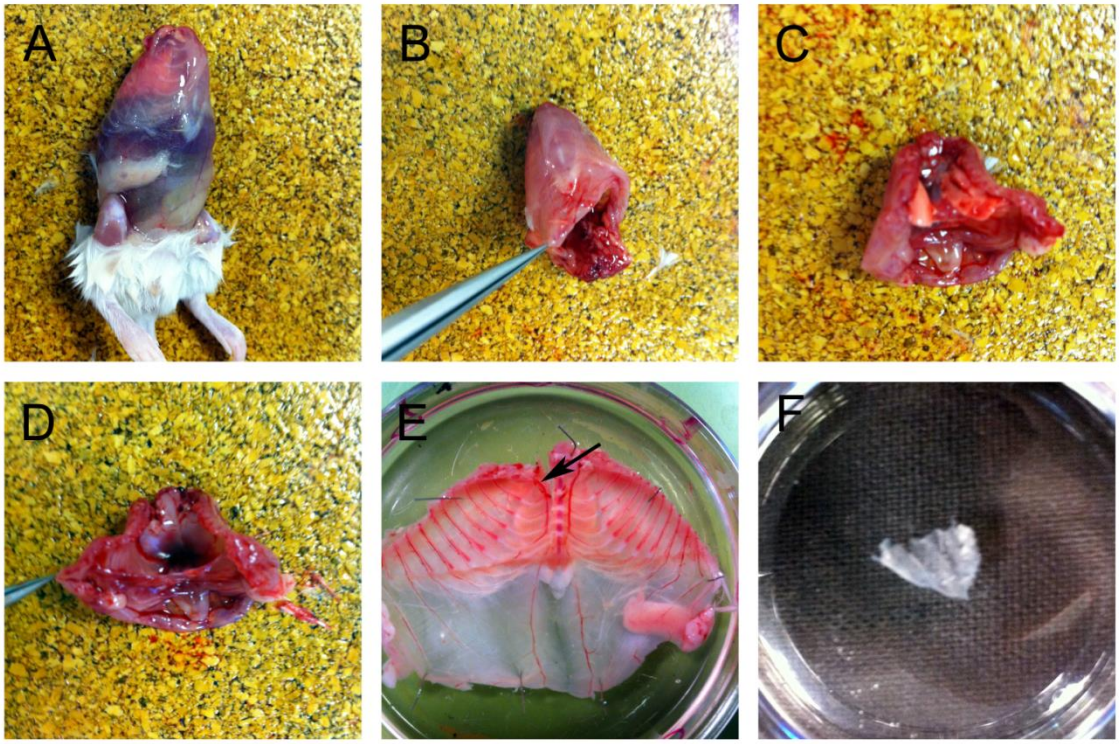

Figure 4 - Triangularis sterni dissection. (A) The mouse was decapitated, skinned and arms removed. (B) The hind limbs, tail, pelvis and lower abdominal organs were removed. (C) The spinal cord was removed. (D) The chest organs and diaphragm were removed. (E) The chest wall was pinned out, deep muscles facing up, in a Sylgard dish using insect pins and fixed for 10 minutes in 4% PFA on a rocking platform. An incision was then made in the chest wall between the sternum and the mammary vessel (black arrow). The TS was now the most superficial muscle, and its cut edge could be identified from this incision. The TS could be lifted using forceps and reflected by cutting the underlying connective tissue. (F) Once the TS had been removed from the chest wall, it was cleaned of fat and connective tissue before staining.

Figure 5 – Hind limb dissections. (A) The hind limb was removed as proximally as possible using bone scissors. (B) The skin was reflected over the foot and removed. (C) The leg was pinned out straight in a Sylgard dish using insect pins and fixed using 4% PFA in 0.1M PBS for 15 minutes on a rocking platform. (D) The muscles of interest were dissected out by cutting the appropriate tendon at the ankle and reflecting the muscle in a distal to proximal manner until the muscle could be cut flush at its origin. The three muscles dissected from the hind limb are shown after they have been removed from the leg. From left to right: tibialis anterior, extensor digitorum longus, and gastrocnemius.

Where the need for sectioning muscle was necessary, as for the large-bellied hind limb muscles, a new sectioning protocol was developed. Muscles were longitudinally sectioned on a freezing microtome at 100µm and then stained using the same protocol as whole mount muscles. Sectioning the hind limb muscles at 100µm allowed for intact NMJs to be visualised through the depth of the muscle section on a confocal microscope.

Name of muscle	Processing	Staining Quality
LALc	Dissected fresh, 4% PFA	Excellent
LALr	Dissected fresh, 4% PFA	Excellent
AAL	Dissected fresh, 4% PFA	Excellent
AS	Dissected fresh, 4% PFA	Good
IS	Dissected fresh, 4% PFA	Excellent
TVA	Dissected fresh, 4% PFA	Good
TS	Dissected fresh, 4% PFA	Excellent
TA	Dissected fresh, 4% PFA, 30% sucrose, sectioned	Excellent
EDL	Dissected fresh, 4% PFA, 30% sucrose, sectioned	Excellent
GS	Dissected fresh, 4% PFA, 30% sucrose, sectioned	Excellent

Table 4: Details of how the muscles were processed and the quality of staining achieved from each muscle. Quality of staining was based on a qualative assessment of intensity of 2H3/SV2 fluorescent signal and intensity of background staining.

In total ten muscles were chosen for analysis: LALc, LALr, AAL, AS, IS, TVA, TS, TA, GS, and EDL (Figures 1, 2, 3, 4 and 5; Table 4).

NMJs were visualised by staining with antibodies against neurofilament (2H3, Developmental Studies Hybridoma Bank) and the synaptic vesicle-associated protein SV2 (Developmental Studies Hybridoma Bank) to visualise the axon and nerve terminal (Figure 6A). The motor endplate was visualised using TRITC-conjugated α-bungarotoxin, which selectively binds to acetylcholine receptors (Figure 6B). After staining, Z-stack images were taken using a confocal microscope. The confocal microscope was used as it produces images higher quality images than those taken from a standard fluorescent microscope. Z-stack images were taken so that larger numbers of NMJs would be in focus in a single micrograph.

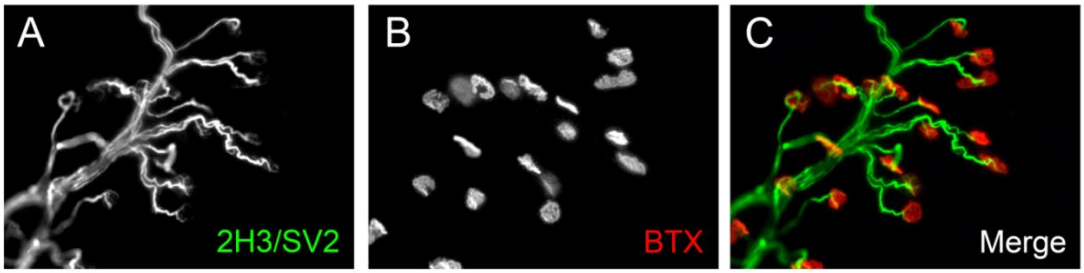

Figure 6 – Neuromuscular junction staining. Neuromuscular junctions were stained using immunohistochemistry to label axons and nerve terminals, and bungarotoxin staining to label motor endplates. (A) Axons and nerve terminals were visualised using antibodies against neurofilament (2H3, Developmental Studies Hybridoma Bank) and SV2 (SV2, Developmental Studies Hybridoma Bank), respectively. Both of these antibodies are raised in mouse, and so they can be labelled with the same

anti-mouse secondary antibody resulting in an apparently continuous staining of axon and nerve terminal. (B) Motor endplates on the muscle fibre are visualised using TRITC-conjugated α-bungarotoxin. α-bungarotoxin is a naturally occurring toxin that is isolated from the venom of the Banded Krate, and specifically binds to the α subunit of the nicotinic acetylcholine receptor. (C) A merged image of the 2H3/SV2 staining (A) and TRITC-conjugated α-bungarotoxin (B).

2.3.2 - Quantification of NMJs

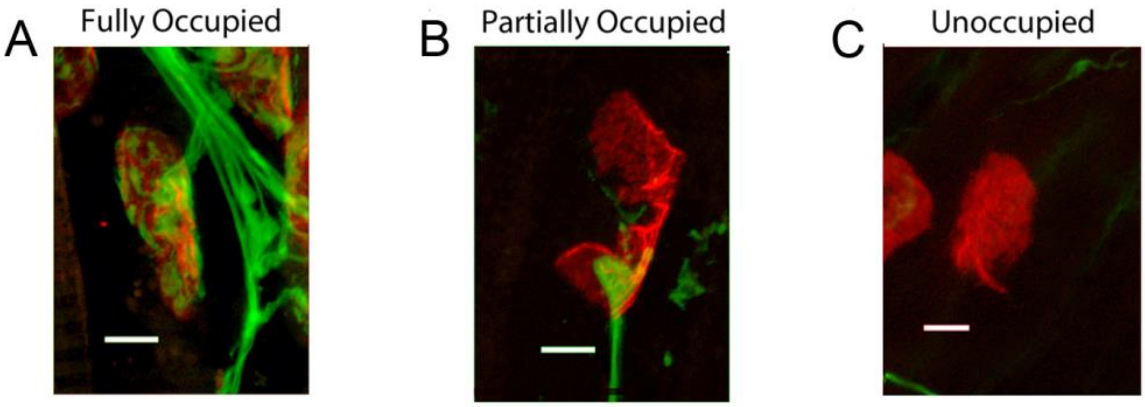

Figure 7 – NMJ categories. Neuromuscular junctions from P5 $Smn^{-/-}$;$SMN2^{+/+}$ mice and healthy littermates were quantified by assignment to one of three categories: fully occupied (A), partially occupied (B) and vacant (C). (A) Endplates were designated "fully occupied" when SV2 and neurofilament staining (green) could be seen overlying more than 50% of the motor endplate (red). (B) Endplates were designed "partially occupied" if the SV2 and neurofilament staining (green) was seen to be overlying less than 50% of the motor endplate (red), but the axon was still in contact with the motor endplate. (C) Endplates were considered "vacant" when

no neurofilament or SV2 staining (green) could be seen overlying or in contact with the motor endplate (red). Scale bars = 5µm.

NMJs were quantified by being assigned to one of three groups: fully occupied (Figure 7A); partially occupied (Figure 7B); or vacant (Figure 7C). NMJs were classed as being fully occupied if the nerve terminal staining overlay the motor endplate by more than 50%. NMJs were classed as being partially innervated if the nerve terminal occupied less than 50% of the endplate, but there was still innervation. NMJs were classed as vacant if there was no evidence of a nerve terminal overlying the motor endplate.

Consistent with results from Murray et al. (2008) a significant reduction in the percentage of fully occupied endplates was observed in the LALc of P5 *Smn*$^{-/-}$;*SMN2*$^{+/+}$ mice compared to unaffected littermates (Figure 8).

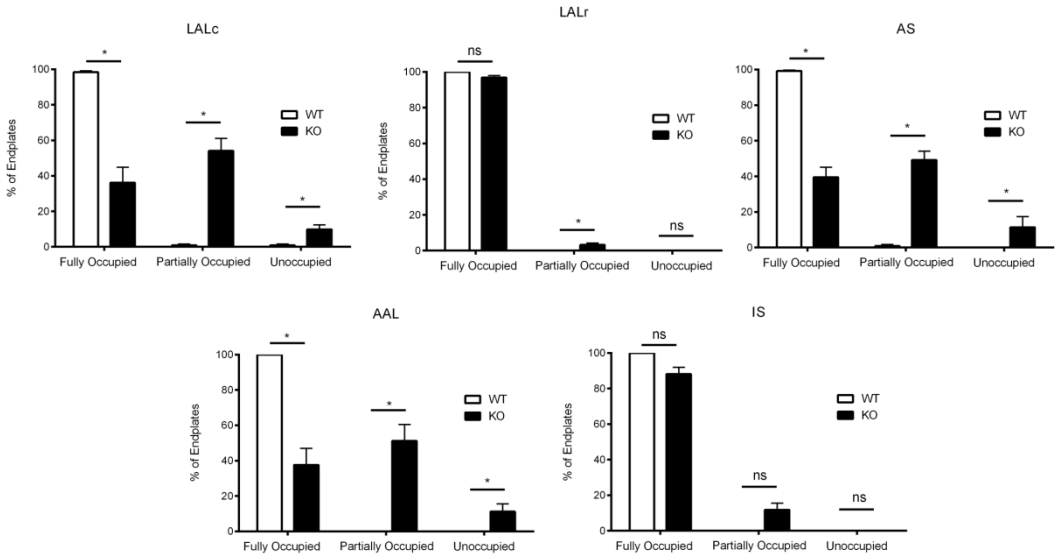

*Figure 8 – Cranial muscles endplate occupation quantification. Bar charts (mean ± S.E.M) showing the percentage of fully occupied, partially occupied, and vacant endplates in the cranial muscles of the Smn$^{-/-}$;SMN2$^{+/+}$ mouse (black bars) and unaffected littermates (white bars). Mann Whitney U test, ns = not significant, * = p ≤ 0.05; n ≥ 3 mice per muscle per genotype.*

Also consistent with Murray et al. (2008) was the apparent resistance of the motor units of the LALr to SMA pathology at the NMJ, with no significant difference in the percentage of fully occupied endplates observed between P5 *Smn$^{-/-}$;SMN2$^{+/+}$* mice and unaffected littermates (Figure 8). The AS and AAL were also found to have a significantly reduced percentage of fully occupied endplates in P5 *Smn$^{-/-}$;SMN2$^{+/+}$* mice (Figure 8). A cranial muscle that was not examined by Murray et al. (2008) was the IS. This muscle was found to have no significant difference in the

percentage of fully occupied endplates between P5 *Smn*$^{-/-}$;*SMN2*$^{+/+}$ mice and unaffected littermates (Figure 8), similar to the LALr.

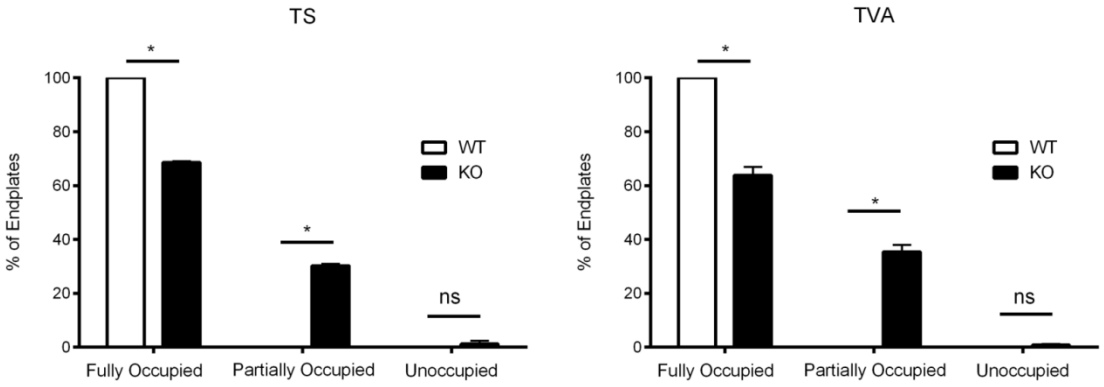

Figure 9 – Abdominal muscles endplate occupation quantification. Bar charts (mean ± S.E.M) showing the percentage of fully occupied, partially occupied, and vacant endplates in the abdominal muscles of the Smn$^{-/-}$*;SMN2*$^{+/+}$ *mouse (black bars) and unaffected littermates (white bars). Mann Whitney U test, ns = not significant, * = $p \leq 0.05$; $n \geq 3$ mice per muscle per genotype.*

The endplate occupation of two abdominal muscles was quantified. The TVA has previously been characterised in late symptomatic *Smn*$^{-/-}$;*SMN2*$^{+/+}$ mice by Murray et al. (2008), and the results here were similar, with the TVA showing a significantly reduced percentage of fully occupied endplates (Figure 9). The endplate occupation status of the motor units of the TS had not previously been quantified in *Smn*$^{-/-}$;*SMN2*$^{+/+}$ mice, and was found to also be vulnerable, with both the percentage of fully occupied and partially occupied endplates significantly reduced (Figure 9).

Hind limb motor units, such as those of the TA, EDL and GS had not previously been quantified in *Smn*$^{-/-}$;*SMN2*$^{+/+}$ mice. The results showed that both the TA and GS showed significantly reduced percentages of fully occupied endplates and significantly increased percentages of partially innervated endplates compared to unaffected littermates (Figure 10). The EDL motor units, however, seemed to show a resistance to SMA with no significant difference found in the number of fully occupied, partially occupied or vacant endplates between *Smn*$^{-/-}$;*SMN2*$^{+/+}$ mice and unaffected littermates (Figure 10).

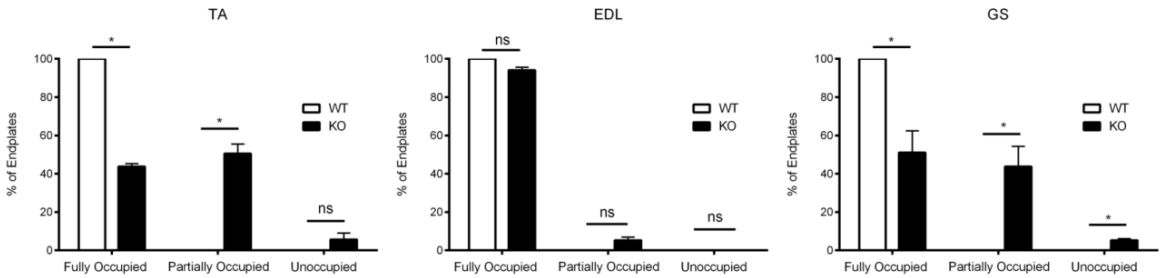

Figure 10 – Hind limb muscle endplate occupation quantification. Bar charts (mean ± S.E.M) showing the percentage of fully occupied, partially occupied, and vacant endplates in the hind limb muscles of the Smn$^{-/-}$*;SMN2*$^{+/+}$ *mouse (black bars) and unaffected littermates (white bars). Mann Whitney U test, ns = not significant, * = p ≤ 0.05; n ≥ 3 mice per muscle per genotype.*

Using the percentage of fully occupied endplates, the muscles were ranked in order of motor unit vulnerability. The bars representing the fully occupied endplate percentages of the *Smn*$^{-/-}$;*SMN2*$^{+/+}$ mice were colour-coded using a graduated yellow

to red colour scheme, to reflect the spectrum of vulnerability observed. In Figure 11, the yellow bars indicate a relative resistance to SMA pathology whereas the red bars indicate that the motor units were vulnerable (Figure 11).

This ranking was then used in all subsequent correlation studies, in order to determine if any morphological aspect of motor units influenced vulnerability. The colour code in Figure 11 is also maintained in all subsequent diagrams in order to convey each muscles' relative motor unit vulnerability.

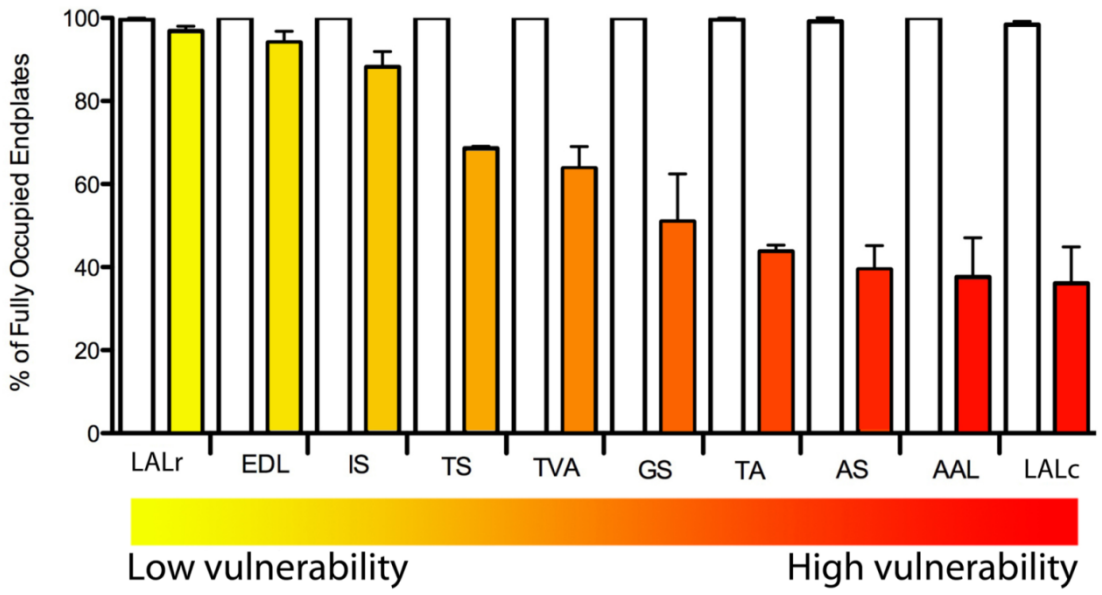

Figure 11 – Bar chart (mean ± SEM) with colour-coded ranking of motor unit vulnerability in $Smn^{-/-};SMN2^{+/+}$ mice. The relative motor unit vulnerability of a muscle was determined by its percentage of fully occupied endplates in P5 $Smn^{-/-};SMN2^{+/+}$ mice ($n \geq 3$ mice per muscle). These values were used to rank the motor units in order of motor unit vulnerability, from the least vulnerable to the most vulnerable. The bars representing $Smn^{-/-};SMN2^{+/+}$ mouse data were then colour-

coded using a graduated colour scheme from yellow to red, with yellow designating low vulnerability motor unit pools and red designating high vulnerability motor unit pools. This colour-code system is used in subsequent figures to identify the relative vulnerability of motor units in each muscle. The percentage of fully occupied endplates in muscles of unaffected littermates are represented by white bars (n ≥ 3 mice per muscle).

2.3.3 - Correlation of Vulnerability with Muscle and Motor Unit Characteristics

2.3.3.1 - Muscle Fibre Type and Body Axis Position

Vulnerability	Muscle	Fibre Twitch Type	Body Position
Low	LALr	Fast	Cranial
	EDL	Fast	Hind limb
	IS	-	Cranial
	TS	Slow	Torso
	TVA	Slow	Torso
	GS	Mixed	Hind limb
	TA	Fast	Hind limb
	AS	Slow	Cranial
	AAL	Fast	Cranial
High	LALc	Fast	Cranial

Table 6: Details of the fibre twitch type and body position of each muscle in the cohort (Lionikas et al., 2005; Murray et al., 2008; Murray et al., 2010).

To assess if the muscle fibre type correlated with motor unit vulnerability, a manual literature search was performed to determine the twitch type of the muscles.

Information on the composition of muscle fibres was found for all muscles, except the IS (Lionikas et al., 2005; Murray et al., 2008; Murray et al., 2010). Using this information, it was determined that muscle fibre type did not correlate with disease susceptibility. Both the LALr and LALc are composed mainly of fast twitch fibres, but were on opposite ends of the vulnerability spectrum (Table 6; Figure 11). Similarly, the EDL and TA are both fast twitch muscles, but are differently affected in late stage *Smn*$^{-/-}$;*SMN2*$^{+/+}$ mice (Table 6; Figure 11)

Body position relating to motor unit vulnerability was assessed qualitatively (Table 6). It was determined that there was no correlation between body position and vulnerability.

2.3.3.2 - Motor Unit Size, Intramuscular Arbour Length and Branching Pattern

After determining that muscle fibre type and body position did not affect motor unit vulnerability to SMA, we next sought to determine whether intrinsic morphological characteristics of the motor units innervating the different muscles correlated with motor unit vulnerability. To do this, we reconstructed entire single motor units innervating several of the muscles that were analysed in the motor unit vulnerability study. Entire motor units were reconstructed for the LALc, LALr, AAL, AS, IS and TS using muscles taken from young adult Thy.1-YFP-H mice (Feng et al., 2001). This transgenic mouse model was initially made by Feng et al. (2001) who generated transgenic mice that expressed different spectral variants of GFP in neuronal cells. Feng et al. (2001) produced 25 different transgenic lines, each of which expressed a fluorescent protein in a random subset of neuronal cells. The Thy.1-YFP-H mouse

expresses yellow fluorescent protein in a small random subset of neurons, meaning that only a small percentage of motor neurons innervating a muscle will be visible (Feng et al., 2001). This allows us to confidently trace individual motor neurons from their point of entry into the muscle to their terminal branches. These experiments were performed in healthy mice in order to ensure that we were comparing intrinsic morphological characteristics of motor neurons rather than their responses to disease stimuli.

Motor units were reconstructed from young adult Thy.1-YFP-H mice by dissecting out the required muscles using the same dissection techniques as for the P5 SMA mice (Figures 1, 2, 3, 4 and 5). With the Thy.1-YFP-H mice, the muscles were stained with TRITC-conjugated α-bungarotoxin only, as a random subset of the motor units were already labelled in the muscles and so only the motor endplates needed to be visualised. Bungarotoxin staining was performed before the muscle was fixed, in order to reduce high background levels. The muscles were then fixed in 4% PFA in 0.1M PBS, dissected out and cleaned of connective tissue and fat before being mounted onto glass slides. Once the mounting media had set, fluorescent micrographs were taken of the labelled axons. These micrographs were taken along the length of the axon, overlapping slightly and following all branches of the motor unit, from where the axon entered the muscle to all of the terminal branches. These images were then overlaid with one another on Adobe Photoshop until the entire motor unit had been reconstructed (Figure 12). From these reconstructed images, of which over 100 were made, motor unit arbour length, motor unit size, and motor unit branching pattern could be quantified.

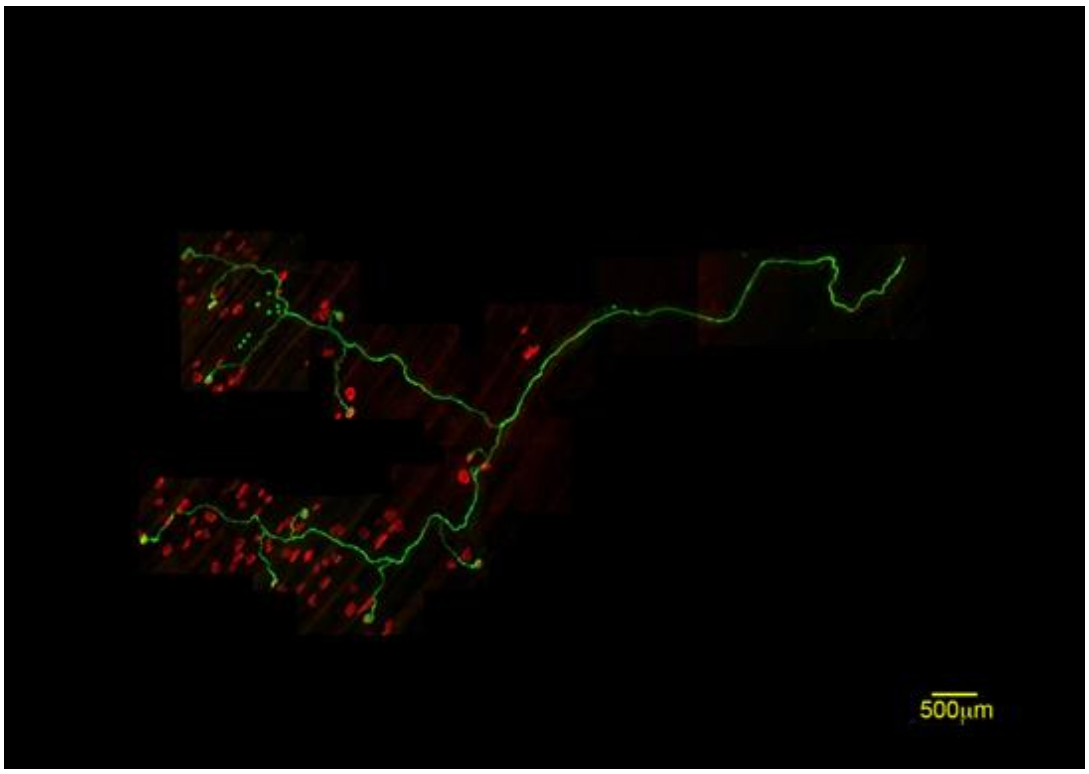

Figure 12 – Composite fluorescent micrograph of a YFP-labelled motor unit. Overlapping fluorescent micrographs were taken, following a YFP-labelled motor neuron from the point at which it entered the muscle, to all the terminal branches. Using Adobe Photoshop, the fluorescent micrographs were overlaid until a single large image of the motor unit was produced. The YFP-labelled motor neuron can be seen in green, and the motor endplates on muscle fibres are visible in red. Motor endplates that are being contacted by the YFP-labelled motor neuron appear yellow.

As motor unit size correlates with motor unit vulnerability in ALS (Bradley et al., 1983; Fischer et al., 2004; Hegedus et al., 2007; Valdez et al., 2012) we first sought to determine whether motor unit size also correlated with motor unit vulnerability in SMA. To measure motor unit size, the total number of motor endplates that were

contacted by the terminal branches of a motor neuron were counted. There was a large range in motor unit size between the muscles, but no significant correlation was found between motor unit size and vulnerability to SMA (Spearman correlation, r = 0.3143, p = 0.5639) (Figure 13B). For example, the motor units innervating the AAL and AS are both vulnerable in SMA, based on the ranking system (Figure 11). However, the AAL has relatively large motor units whereas the AS has relatively small motor units (Figure 13A). This was also true for motor units that were more resistant to synaptic degeneration – the TS has relatively large motor units, and the IS has relatively small motor units (Figure 13A), however, they both show similar levels motor unit resistance (Figure 11).

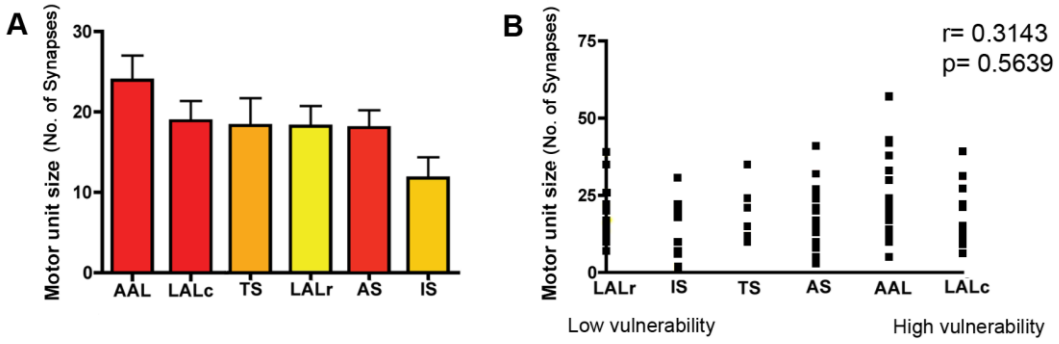

Figure 13 – Motor unit size correlation. The average size of a motor unit innervating the LALc, LALr, AAL, AS, IS and TS muscles was quantified by counting the number of synapses made by a single motor unit. (A) Bar chart (mean ± SEM) of resistant motor units colour-coded yellow and vulnerable motor units colour-coded red (n ≥ 3 per muscle). Bars are ordered according to the size of the motor unit, from largest to smallest. (B) Scatter plot of motor unit size. Spearman correlation

analysis was carried out and no significant correlation was found between motor unit size and vulnerability (Spearman correlation, $p \geq 0.05$; $n \geq 3$ per muscle).

We next examined whether there was a correlation between motor unit vulnerability and total intramuscular axon arbour length. To determine a motor neuron's total intramuscular arbour length, axons were manually traced over the reconstructed motor unit images in Adobe Photoshop (Figure 14). The motor neuron was traced from the point at which it entered the muscle, to the tip of all the terminal branches at neuromuscular junctions. The length of these traces was then measured on ImageJ and the sum of all the branches was used in correlational studies.

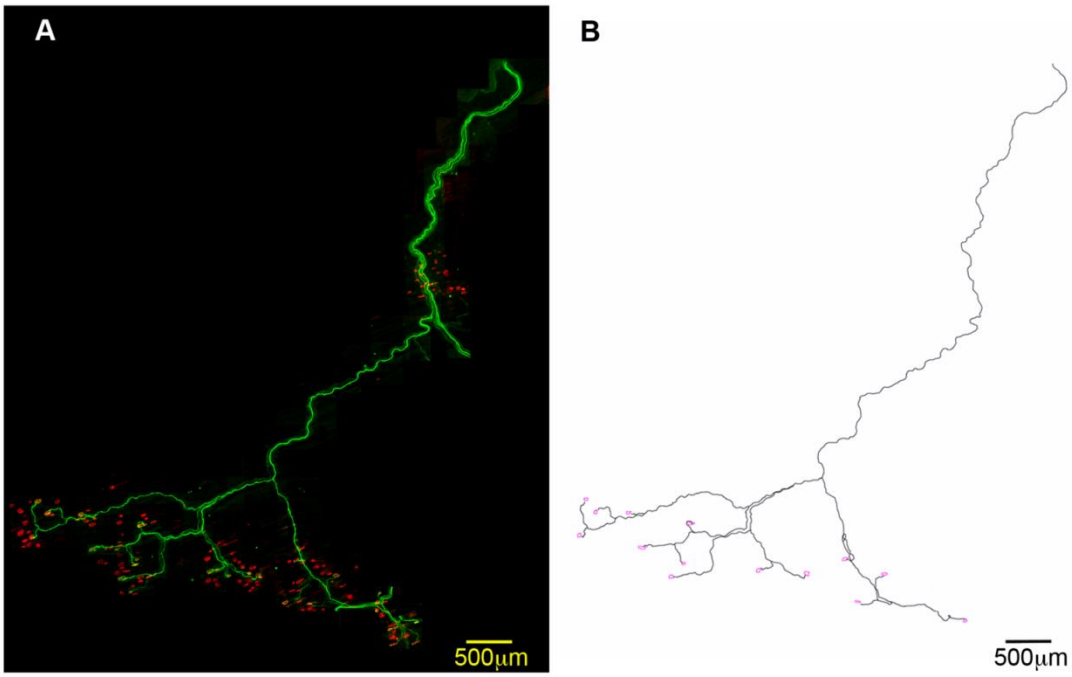

Figure 14 – Example of a reconstructed motor unit and its tracing. (A) Reconstructed motor unit from the LALr. (B) An example of a tracing taken from the

motor unit depicted in A. From this tracing, intramuscular arbour length and branching patterns could be quantified using ImageJ soft

ware..

The AAL was found to contain motor units with the largest intramuscular arbour length, at approximately 2.5cm (Figure 15A), while the motor units innervating the IS were the smallest, at approximately 1cm (Figure 15A). The motor units of the caudal and rostral bands of the LAL had similar intramuscular arbour lengths (Figure 15A), however they appear at opposite ends of the vulnerability spectrum (Figure 11). No significant correlation was found between intramuscular arbour length and motor unit vulnerability (Spearman correlation, r = 0.6571, p = 0.1750) (Figure 15B).

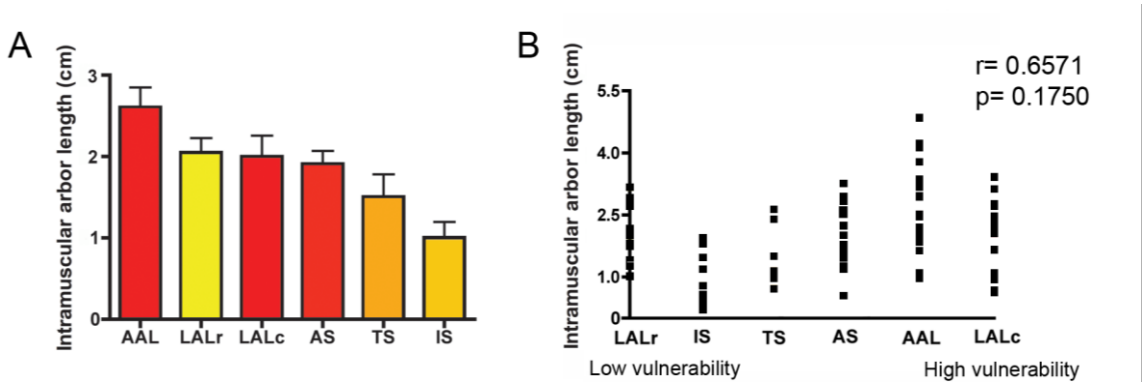

Figure 15 – Intramuscular arbour length quantification and correlation. The average intramuscular arbour length of a motor unit was quantified by measuring the total length of all axonal arbours from the point of entry to the terminal branches. (A) A bar chart (mean ± SEM) showing intramuscular arbour lengths. The bars are ordered from largest intramuscular arbour length to smallest, with muscles innervated by resistant motor units colour-coded in yellow and muscles

innervated by vulnerable motor units colour-coded in red (n ≥ 3 per muscle). (B) A scatter plot of intramuscular arbour length. Spearman correlation analysis was carried out and no significant correlation was found between intramuscular arbour length and relative vulnerability of motor units (Spearman correlation, p ≥ 0.05; n ≥ 3 per muscle).

Branching patterns were examined next, to determine if the number of branches a motor unit made would correlate with vulnerability in SMA. Initially, the number of branch points per motor unit was measured. Branch point number was measured using the reconstructed motor units from Thy.1-YFP-H mice.

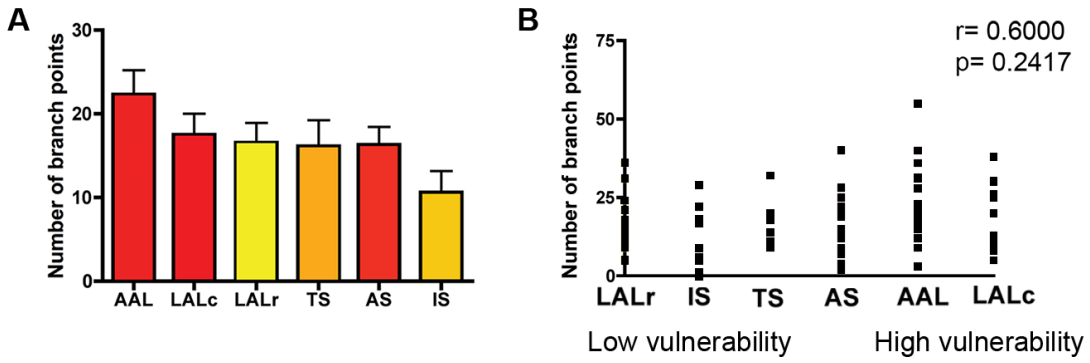

Figure 16 – Number of branch points per motor unit correlation. Branch points were quantified by counting the number of branch points per motor unit. (A) A bar chart (mean ± SEM) of branch points per motor unit. The bars are ordered from largest to smallest number of branch points, with muscles innervated by resistant motor units colour-coded yellow and muscles innervated by vulnerable motor units colour-coded red (n ≥ 3 per muscle). (B) A scatter plot of number of branch points per motor unit. Spearman correlation analysis was carried out and no significant correlation was found between the number of branch points per motor unit and relative vulnerability (Spearman correlation, p ≥ 0.05; n ≥ 3 per muscle).

A branch point was defined as the point at which an axon split into two. The AAL was found to be innervated by motor units with the highest number of branch points per motor unit, at just over 20 (Figure 16A), while the IS was innervated by motor units with the smallest number of branch points per motor unit at around 10 (Figure 16A). Again, the values for the motor units of the caudal and the rostral bands of the LAL were similar (Figure 16A) while their motor unit vulnerabilities are strikingly different (Figure 11). When a Spearman correlation was carried out, no significant correlation was found between vulnerability and the number of branch points per motor unit (Spearman correlation, $r = 0.6000$, $p = 0.2417$) (Figure 16B).

We next decided to investigate whether the pattern of motor unit branching influenced vulnerability, rather than simply the number of branches in a motor unit. Motor unit branching pattern was quantified using a system developed by Valdez et al. (2012) in which the number of times an axon branches before it forms a synapse is quantified. Schematic diagrams of motor neurons were produced where each new branch of a motor unit was assigned a new branch order (Figure 17).

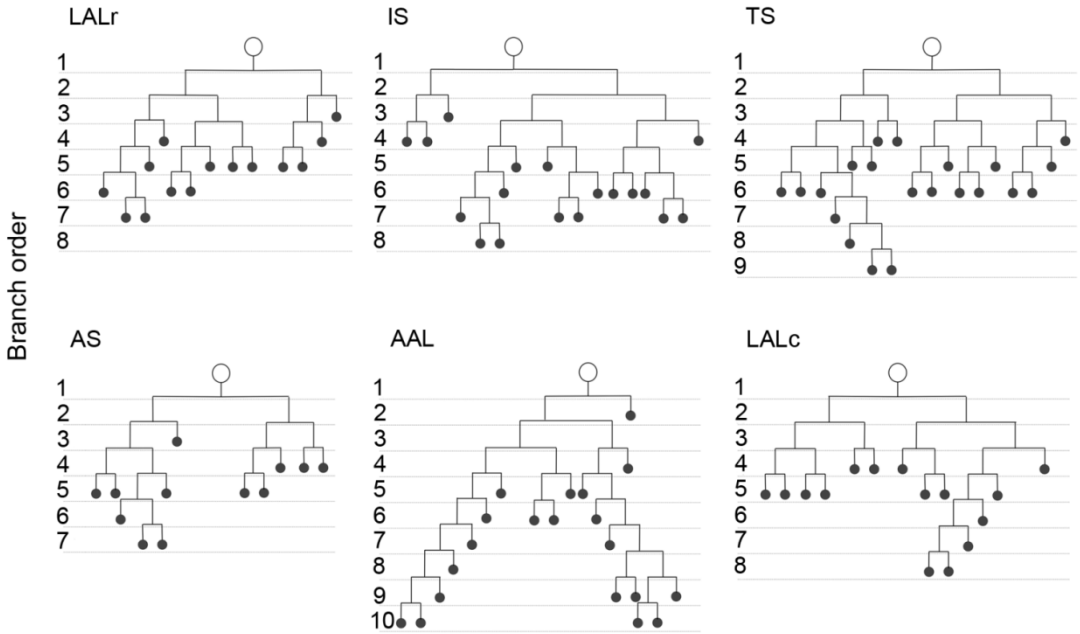

Figure 17 – Example Branch order diagrams. Schematic representations of motor units were produced in order to quantify branching patterns. Branch orders were created and each synapse was assigned to a branch order relating to how many times its axon had branched before forming the synapse. The first branch after the motor unit's entry into the muscle (white circle) was designated branch order 1. The second branch was designated branch order 2, and so on. In the diagrams, synapses are depicted as black circles. The number of synapses in each branch order was then used to quantify the branching pattern (Figure 19).

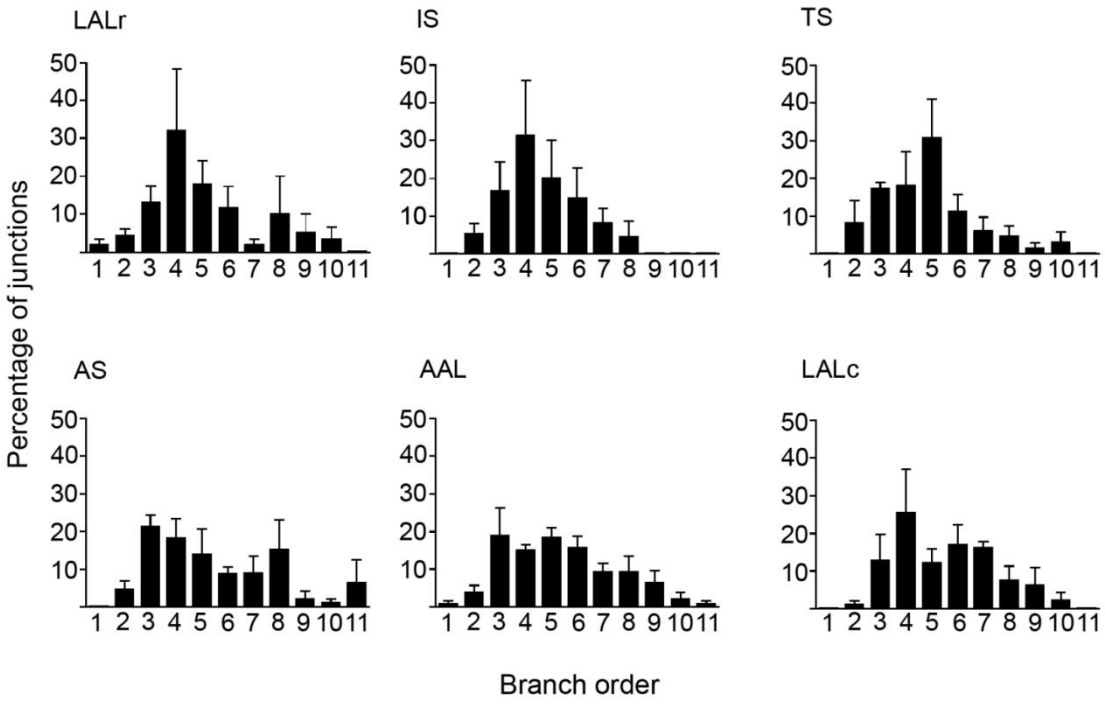

Figure 18 – Branch order quantification. Frequency plots (mean ± SEM) were produced from branching diagrams in Figure 17. The number of synapses in each branch order was quantified and is represented here as frequency plots. The frequency plots looked similar between all the motor unit groups examined and did not show any signs of skewing. Both the motor units of LALc and LALr have the largest number of synapses in branch order 4, however they appear at opposite ends of the vulnerability spectrum in Figure 11. From this we concluded that the branching pattern of motor units does not influence motor unit vulnerability in SMA.

The number of synapses per branch order was then quantified and is represented as frequency charts (Figure 18). No skewing of synapse branch order frequency was noted in any of the muscles examined (Figure 18) and so no qualitative correlation

could be reported between synapse branch order frequency and motor unit vulnerability.

2.3.3.3 - Endplate Size and Morphology

To determine if there were any correlations between motor unit vulnerability and average size of synapses or endplate morphology, high magnification maximum intensity Z-stack projections of motor endplates from Thy.1-YFP-H mice were taken on a confocal microscope. First, motor endplate area was measured by tracing around the outline of the motor endplate in ImageJ, from which the total area (μm^2) could be measured. No correlation was observed between motor endplate area and motor unit vulnerability (Spearman correlation, $p = 0.1361$, $r = 0.7143$) (Figure 19).

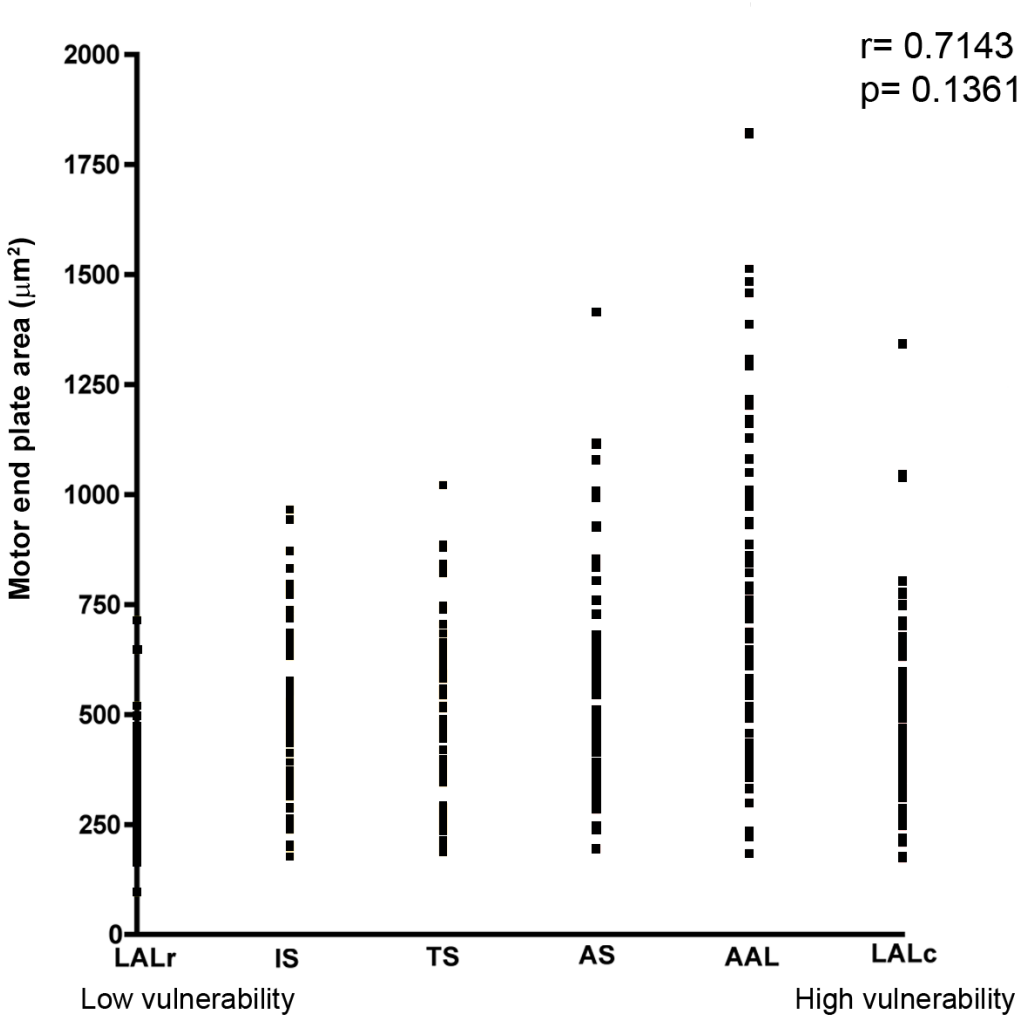

Figure 19 – Endplate area correlation study. The area of motor endplates in young adult Thy.1-YFP-H mice was quantified by tracing around the area of TRITC-conjugated α-bungarotoxin staining on ImageJ. The area was measured as μm^2. No correlation was found between motor endplate area and motor unit vulnerability in SMA (Spearman correlation, $p \geq 0.05$; $n \geq 3$ per muscle).

Next, the morphology of motor endplates in each muscle was examined. Immature endplates are smooth and plaque-like, and as they mature they become perforated

and fold until they resemble the classic adult "pretzel" morphology. Endplate morphology was measured qualitatively and it was determined that all motor endplate displayed similar adult "pretzel"-like morphology. We concluded that there was no correlation between endplate morphology and motor vulnerability (Figure 20).

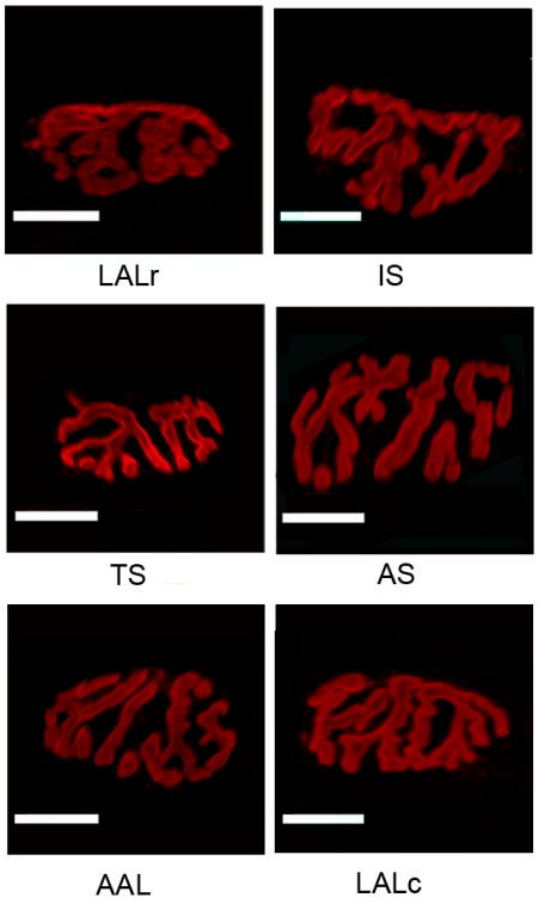

Figure 20 – Endplate morphology. Endplate morphology was examined using high magnification (x40) Z-stack confocal micrographs. Qualitative analysis of motor endplates showed a mature pretzel-like morphology in all motor endplates examined. Based on this, we concluded that there was no difference in NMJ morphology between vulnerable and resistant motor unit pools. Scale bars = 30µm.

2.3.3.4 - Synapse Elimination Rate

After no correlation with motor unit vulnerability could be detected in any of the morphological parameters examined, we decided to investigate synapse elimination as a potential developmental correlate. At birth, the majority of NMJs receive pre-synaptic inputs from more than one axon (Figure 21A). Over the three weeks following birth, these excess inputs withdraw from the motor endplate in a process known as synapse elimination. After synapse elimination, each motor endplate is innervated by only one axonal input (Figure 21B) (Gillingwater & Ribchester, 2003).

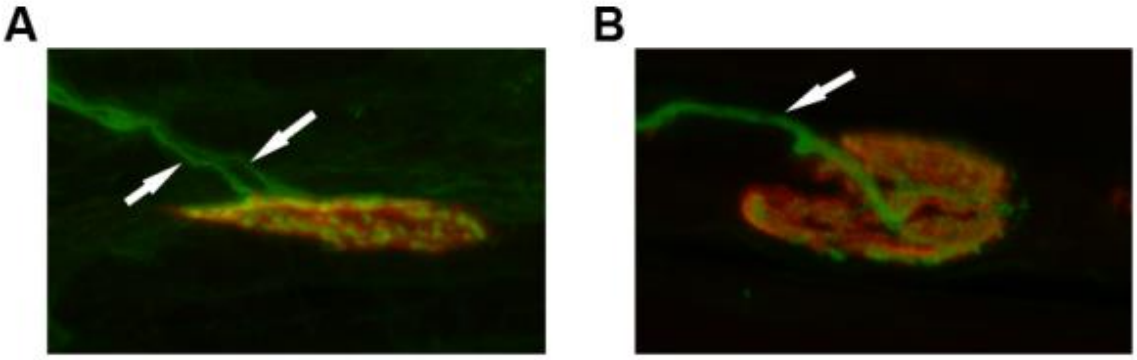

Figure 21 – Synapse elimination example figures. (A/B) High magnification (x40) confocal z-stack micrographs of NMJ stained with 2H3/SV2 (green) and TRITC-conjugated α-bungarotoxin (red). (A) A poly-innervated endplate from a P7 mouse. Two individual axons can be seen converging on one motor endplate (white arrows). (B) A mono-innervated endplate from a P14 mouse. Only one axon can be seen innervating the motor endplate (white arrow). Synapse elimination was quantified by counting the number of axonal inputs per endplate in a range of muscles (LALr, LALc, AAL, AS, IS and TS) in healthy mice at P7 and P14. Endplates were classed as poly-innervated if they had two or more axonal inputs converging on a single endplate.

There are many similarities between the process of synapse elimination and synaptic degeneration, in terms of compartmental degeneration and actin dynamics (Gillingwater & Ribchester, 2003). In *Smn*$^{-/-}$;*SMN2*$^{+/+}$ mice, pathological changes in motor units are taking place as synapse elimination is occurring (Gillingwater & Ribchester, 2003). We hypothesised that the rate of synapse elimination could vary between motor unit pools, and that this could act as a read out of different motor units' intrinsic abilities to remodel axons. Any differences in motor units' ability to remodel axons may reveal an underlying mechanism in differential motor unit vulnerability. Based on this we carried out correlation studies between synapse elimination rate and motor unit vulnerability.

Synapse elimination rates were quantified in P7 and P14 unaffected littermates of *Smn*$^{+/-}$;*SMN2*$^{+/+}$ litters. A range of muscles with vulnerable and resistant motor unit pools were used for quantification; LALr, LALc, AAL, AS, IS and TS. The total number of axonal inputs innervating a single motor endplate was quantified and the data was analysed in two ways: initially, the percentage of poly-innervated endplates per muscle was determined. Secondly, the average number of inputs per motor endplate was quantified from the same data set.

We found that at P7, approximately 50% of endplates remain poly-innervated in all muscles examined (Figure 22A). Using Spearman correlation analysis, it was determined that there was no correlation between poly-innervation and motor unit vulnerability at P7 (Spearman correlation, $r = 0.3143$, $p = 0.5639$) (Figure 22A). At P14, all muscles examined showed either very low levels of poly-innervation or no

poly-innervation (Figure 22B). From this we concluded that synapse elimination occurs at a similar rate in all the motor units examined. A correlation analysis was carried out but no significant correlation was observed between the percentage of poly-innervation and motor unit vulnerability at P14 (Spearman correlation, r = 0.2000, p = 0.7139) (Figure 22B).

The synapse elimination data was also analysed using the average number of inputs per motor endplate. We found that at P7 the average number of axonal inputs per motor endplate was comparable across all muscles examined (Figure 22C). Correlational analysis revealed no significant correlation between average axonal input number at P7 and motor unit vulnerability (Spearman correlation, r = 0.3134, p = 0.5639) (Figure 22C). By P14, the average number of axonal inputs per motor endplate was consistently close to 1 and no significant correlation was observed with motor unit vulnerability (Spearman correlation, r = 0.2000, p = 0.7139) (Figure 22D).

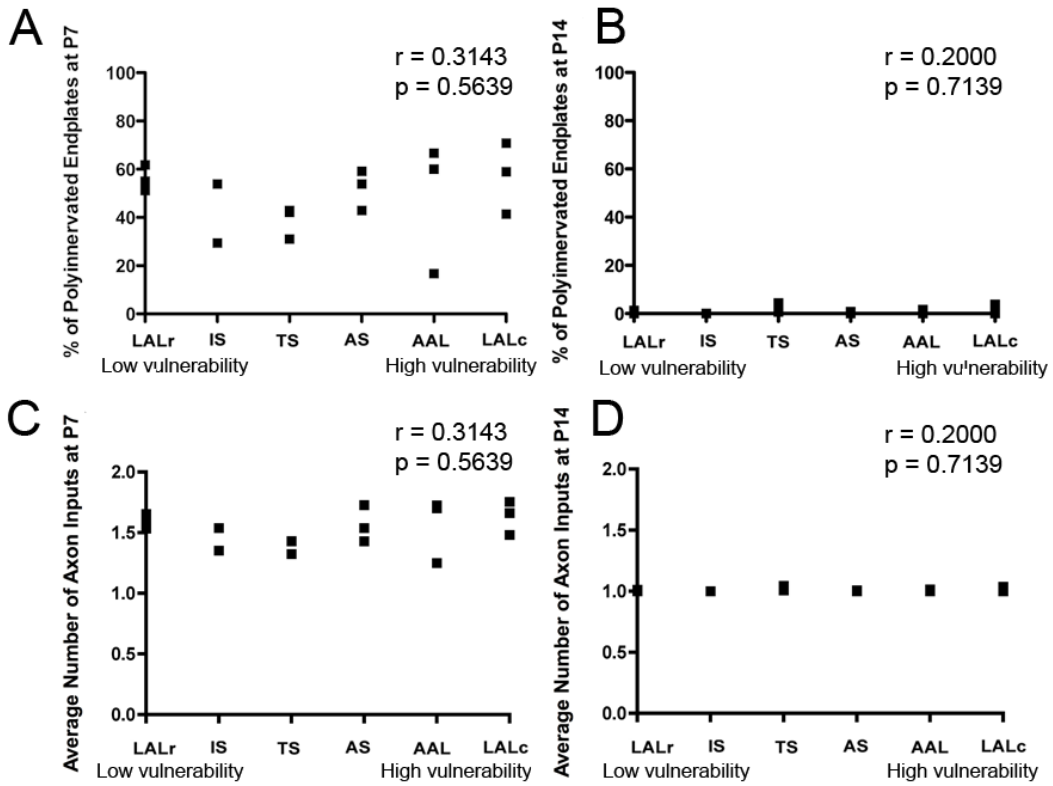

Figure 22 – Synapse elimination rate correlation. (A) Scatter plot of percentage poly-innervated endplates at P7 ordered from low to high vulnerability motor units (n = 3 per muscle). Spearman correlation analysis showed no significant correlation between percentage of poly-innervated endplates and motor unit vulnerability (Spearman correlation, p ≥ 0.05; n= 3 per muscle). (B) Scatter plot of percentage of poly-innervated endplates at P14, ordered from low to high vulnerability motor unit pools (n = 3 per muscle). Spearman correlation analysis showed no significant correlation between percentage of poly-innervated endplates and motor unit vulnerability (Spearman correlation, p ≥ 0.05; n = 3 per muscle). (C) Scatter plot of the average number of axonal inputs per endplate at P7, ordered from low to high vulnerability motor unit pools (n = 3 per muscle). Spearman correlation analysis showed no significant correlation between average axonal input per endplate and motor unit vulnerability (Spearman correlation, p ≥ 0.05; n = 3 per

muscle). (D) Scatter plot of average number of axonal inputs per endplate at P14, ordered from low to high vulnerability motor unit pools (n = 3 per muscle). Spearman correlation analysis showed no significant correlation between average number of axonal inputs per endplate and motor unit vulnerability (Spearman correlation, $p \geq 0.05$; n = 3 per muscle).

2.3.3.5 - Terminal Schwann Cell Number

Terminal Schwann cells represent another morphological characteristic of neuromuscular junctions that may influence motor unit vulnerability in disease (De Winter et al., 2006; Murray et al., 2013; Voigt et al., 2013). Terminal Schwann cells are a specialised form of glial cell that overlie the nerve terminal of the neuromuscular junction. Previous work in SMA mouse models has shown that terminal Schwann cells numbers are reduced (Murray et al., 2013) and that their ultrastructure is abnormal (Voigt et al., 2013). Similarly, terminal Schwann cells have been linked to ALS pathology (De Winter et al., 2006). Terminal Schwann cells are also known to be involved in NMJ development and maintenance (Sugiura & Lin, 2011). We hypothesised that terminal Schwann cells may have an influence on synaptic degeneration at the neuromuscular junction, and so we quantified terminal Schwann cell number for use in correlational analysis.

Terminal Schwann cells were quantified from P5 unaffected littermates of $Smn^{+/-};SMN2^{+/+}$ litters. A range of muscles with vulnerable and resistant motor units were used, as for the synapse elimination studies. Immunohistochemistry using antibodies

against S100 protein was used to detect terminal Schwann cells (Figure 23). During quantification, cells were counted as terminal Schwann cells if the S100-positive cytoplasm was directly overlying a motor endplate (Figure 23). The number of Schwann cells over a motor endplate was determined by staining nuclei with the nuclear marker TO-PRO-3 (Figure 23).

All neuromuscular junctions examined had at least one terminal Schwann cell and the maximum number of terminal Schwann cells found was five. The mean number of terminal Schwann cells was comparable between muscles, with the majority of neuromuscular junctions having two overlying Schwann cells (Figure 24A). No correlation was found between the number of terminal Schwann cells per NMJ and motor unit vulnerability in SMA (Spearman correlation, $r = -0.3769$, $p = 0.4972$) (Figure 24B).

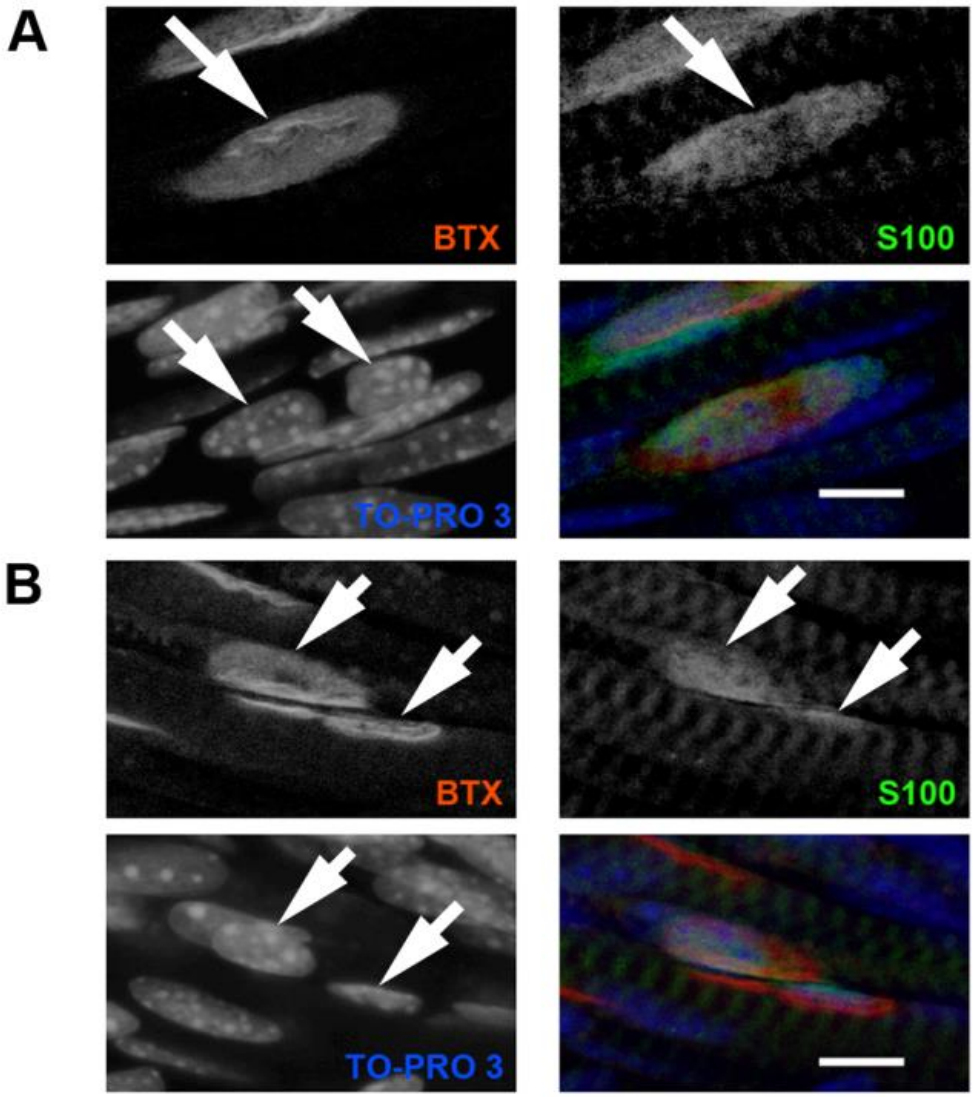

Figure 23 – Example images of terminal Schwann cell counts. (A/B)High magnification (x40) Z-stack confocal micrographs of motor endplates in P5 healthy mice. TRITC-conjugated α-bungarotoxin (BTX) (red) staining was used to identify the motor endplates. S100 staining (green) was used to visualise the cytoplasm of Schwann cells. TO-PRO 3 staining (blue) was used to identify nuclei of terminal Schwann cells. A cell was defined as a terminal Schwann cell if the S100 positive cytoplasm was overlying and within the boundaries of the motor endplate and contained a TO-PRO-3-positive nucleus. The number of nuclei overlying the motor

endplate that were surrounded by S100 positive cytoplasm were used to count the number of terminal Schwann cells per endplate. (A) A motor endplate with two overlying terminal Schwann cells. The white arrows in the BTX and S100 channels show a single endplate and S100 positive cytoplasm. The white arrows in the TO-PRO-3 channel show two nuclei present. (B) Two motor endplates each with a single overlying terminal Schwann cell. The white arrows in the BTX and S100 channels show two separate motor endplates and two separate S100 positive areas of cytoplasm. The white arrows in the TO-PRO 3 channel show one nucleus each overlying the motor endplate. (A/B) Scale bars in merge images = 5µm.

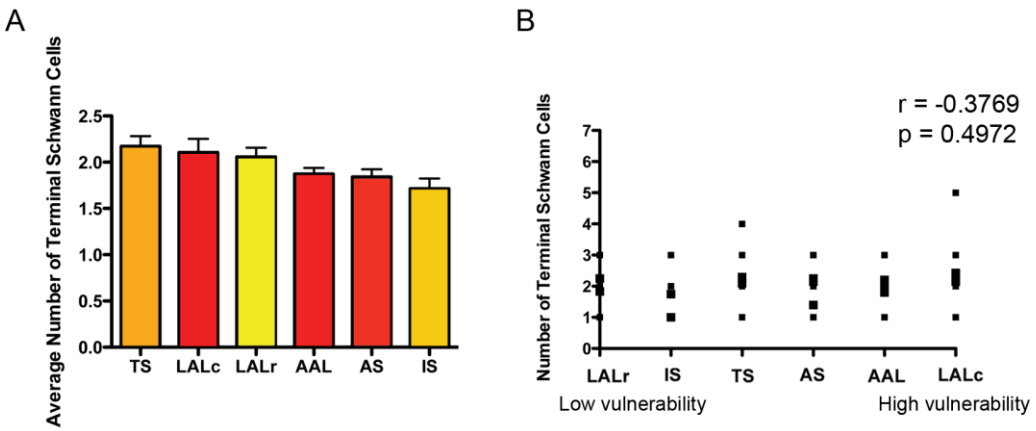

Figure 24 – Terminal Schwann cell counts correlation. (A) Bar chart (mean ± SEM) showing terminal Schwann cell number per endplate in healthy P5 mice (n = 3 per muscle). Muscles innervated by resistant motor units are colour-coded yellow and muscles innervated by vulnerable motor units are colour-coded red. Bars are organised according to the number of terminal Schwann cells per endplate, from highest to lowest. (B) A scatter plot of terminal Schwann cell number per endplate. Spearman correlation analysis showed no significant correlation between terminal

Schwann cell number per endplate and motor unit vulnerability (Spearman correlation, $p \geq 0.05$; $n = 3$ per muscle).

2.4 – Discussion

The findings of this chapter show that motor unit vulnerability in SMA is not influenced by the gross morphology of motor units, or other morphological parameters. Initially, the results of this chapter demonstrated that motor unit vulnerability to SMA varies across muscles. At a late-symptomatic time point (P5) in the *Smn*$^{-/-}$;*SMN2*$^{+/+}$ mouse, some muscles, such as the LALc, AAL and TA, showed widespread denervation of motor endplates with only 40% of endplates remaining fully occupied. However, other muscles, such as the LALr, IS and EDL, showed relatively little denervation of motor endplates. This difference in motor unit vulnerability was striking and particularly interesting as many of the differentially affected motor units were closely linked anatomically. The LALc and LALr, for example, are considered to be one anatomically distinct muscle. The TA and EDL are also differentially affected in the *Smn*$^{-/-}$;*SMN2*$^{+/+}$ mouse model, but are both found on the anterior compartment of the lower hind limb.

Secondly, the results showed that this variation in vulnerability does not correlate with any aspect of gross motor unit morphology, as it does for ALS (Bradley et al., 1983; Fischer et al., 2004; Hegedus et al., 2007; Valdez et al., 2012). Large motor units are known to be preferentially affected in ALS and there is a growing body of evidence suggesting that ALS and SMA are linked molecularly (Zou et al., 2005;

Turner et al., 2009; Kariya et al., 2012; Yamazaki et al., 2012). Based on this, we hypothesised that larger motor units would also be preferentially affected in SMA. However, we could find no correlation between motor unit size and vulnerability. We also investigated other aspects of motor unit morphology, such as intramuscular arbour length, number of branch points and branching patterns. No significant correlation was found for any morphological aspect of motor units that we examined.

Thirdly, the results also showed that other morphological factors such as body position, muscle fibre type, endplate morphology, and synaptic size did not correlate with motor unit vulnerability in SMA.

Fourth, this chapter demonstrates that motor unit dynamics, quantified by synapse elimination rates, also do not correlate with motor unit vulnerability in SMA. Motor unit vulnerability may have been related to synapse elimination as there are several similarities between synapse elimination and degeneration, in terms of actin dynamics and remodelling (Gillingwater & Ribchester, 2003). We hypothesised that motor units dynamics might be more or less vulnerable to pathological changes in SMA. However, we did not see any obvious difference in synapse elimination rates between muscles. Also, neither the percentage of poly-innervated endplates nor the average number of axonal inputs per motor endplate at P7 or P14 showed a significant correlation with motor unit vulnerability in SMA.

Lastly, this chapter showed that terminal Schwann cell number did not correlate with motor unit vulnerability in SMA. Terminal Schwann cells are known to influence NMJ development and maintenance and are involved in NMJ repair and regeneration (Sugiura & Lin, 2011), and are linked to altered neuromuscular junction pathology in

both ALS and SMA (De Winter et al., 2006; Murray et al., 2013; Voigt et al., 2013). Based on this, we hypothesised that terminal Schwann cell numbers might correlate with motor unit vulnerability in SMA. However, no obvious variation in terminal Schwann cell number was found across the range of muscles that were quantified and no significant correlation was found between terminal Schwann cell number and motor unit vulnerability in SMA.

2.4.1 - Molecular links between SMA and ALS.

Despite compelling evidence that ALS and SMA are molecularly linked (Zou et al., 2005; Turner et al., 2009; Kariya et al., 2012; Yamazaki et al., 2012), we did not find the same pattern of motor unit vulnerability in SMA that has been demonstrated in ALS (Bradley et al., 1983; Fischer et al., 2004; Hegedus et al., 2007; Valdez et al., 2012).

It is possible that age plays an important role in motor neuron degeneration. SMA affects motor neurons in the early stages of life, whereas ALS does not affect motor neurons until much later. As the pattern of neuro-degeneration in ALS has been proven to correlate with age-related abnormalities (Valdez et al., 2012), it is possible that larger motor neurons are simply more vulnerable in an aged nervous system. This could potentially explain why no correlation between large motor units and SMA pathology was seen in this experiment.

There are also conflicting reports regarding the contribution of *SMN2* copy number to ALS in patients (Veldink et al., 2001; Gamez et al., 2002; Corcia et al., 2006). Veldink et al. (2001) showed that patients with ALS were more likely to have a

homozygous deletion of *SMN2* than unaffected controls. However, similar studies in 2002 and 2006 failed to find a significant difference in the likelihood of *SMN2* deletion between ALS patients and controls (Gamez et al., 2002; Corcia et al., 2006).

While more recent studies in animal models (Turner et al., 2009; Kariya et al., 2012; Yamazaki et al., 2012) have shown compelling evidence for a molecular link between SMN protein and genes associated with ALS, the reality of their relationship may be much more complicated.

2.4.2 - SMN protein variation across motor unit pools.

The results undoubtedly show that motor unit morphology and vulnerability in SMA are not linked. The most likely explanation for this finding is that motor unit vulnerability in SMA is driven by distinct molecular properties of motor units, rather than morphological properties, as is the case in ALS. The most likely molecular candidate for influencing synapse vulnerability in SMA would, of course, be SMN protein. There is a large body of evidence suggesting that there is a critical threshold of SMN protein that must be expressed in order for motor neurons to remain healthy (Bowerman et al., 2012). There is also a well-documented correlation between *SMN2* copy number and disease severity (Feldkötter et al., 2002; Mailman et al., 2002; Wirth et al., 2006). It is possible that in SMA, SMN protein reduction is not equal between pools of motor units, or indeed between different tissues (Ruggui et al., 2012). This could potentially explain why some motor units seem to have a resistance to SMA.

2.4.3 - Intrinsic protective factors in some motor unit pools.

An alternative explanation for the selective vulnerability of some motor units in SMA is the possibility of the presence of an intrinsic protective factor in these motor units. There is a large body of literature describing neuro-protective factors that have been identified in other neuro-degenerative diseases and traumatic brain or spinal cord injuries. It is possible that an up-regulation of one or more of these "protective" factors in some pools of motor units could allow the motor units to better cope with the cellular stresses brought on by a reduction in SMN protein, thereby delaying or avoiding synapse degeneration. Alternatively, the opposite could also be true, in that some pools of motor units may have an up-regulation of a gene that is detrimental, or enhances the effects of a reduction in SMN protein.

2.4.4 – Study Weaknesses

Although every attempt was made to ensure that this study was as robust as possible, there are several areas of weakness that should be noted. First, is the use of young adult mice to reconstruct motor units. Ideally, the mice used to reconstruct motor units would have been of the same age (P5) as the $Smn^{-/-};SMN2^{+/+}$ mice to control for any changes to motor unit morphology during development. However, Thy.1 expression in neurons increases during development and is expressed at low levels in neonates (Feng et al., 2001). Based on this, the decision was made to reconstruct motor units in adult mice, so that a strong YFP signal would be detected and accurate motor unit reconstructions could be produced.

Also regarding the use of Thy.1-YFP-H mice – it has previously been shown that YFP expression induces abnormalities in motor neurons (Comley et al., 2011). We chose to reconstruct motor units in healthy mice in order to determine characteristics of motor units that were not under the influence of any pathological process; to assess their "default" morphologies. However, as YFP expression is known to induce certain abnormalities at the NMJ (Comley et al., 2011), there is a small risk that the motor unit reconstructions produced here are not representative of completely healthy motor units.

Another weakness in this study is the lack of clinically relevant muscles selected for analysis, such as the diaphragm and extra-ocular muscles. In SMA patients, the diaphragm is spared from denervation and as a result patients often exhibit behaviour known as "abdominal breathing", where the intercostal muscles are paralysed and so the patient uses only the diaphragm to draw breath (Lunn & Wang, 2008). Extra-ocular muscles are also spared denervation in ALS (Nimchinsky, et al. 2000). Initially, attempts were made to quantify NMJ pathology in the diaphragm of *Smn*$^{-/-}$*;SMN2*$^{+/+}$ mice, however, the relative thickness of the diaphragm and the presence of thick connective tissue made good quality staining impossible. High levels of background fluorescence and weak signal meant quantifying NMJ abnormalities in the diaphragm was likely to be inaccurate. Similarly, diaphragms dissected from Thy.1-YFP-H mice showed extremely high background fluorescence that made accurately tracing individual motor units impossible. Attempts were also made to dissect the extra-ocular muscles from the eyeball. This was initially attempted in adult mice, before progressing to neonates. However, it proved impossible to dissect these muscles away from the eyeball intact. Also, to perform these dissections, the

eyeball was removed from the skull, and the muscle dissected away from the eyeball in 0.1M PBS. Due to its roundness, it was impossible to prevent the eyeball from spinning and therefore impossible to accurately distinguish different extra-ocular muscles. Based on these preliminary dissections in adult mice, the decision was made not to attempt extra-ocular muscle dissections in neonates or *Smn*$^{-/-}$;*SMN2*$^{+/+}$ mice.

2.4.5 – Conclusion

From these results, we can conclude that there is a spectrum of vulnerability in motor units throughout the *Smn*$^{-/-}$;*SMN2*$^{+/+}$ mouse model of SMA. This vulnerability spectrum does not correlate with any aspect of motor unit morphology that we quantified. This is strikingly different to the well-characterised correlation between motor unit size and vulnerability which is observed in ALS. Additionally, motor unit vulnerability did not correlate with aspects of muscle morphology that have previously been suggested may underlie motor unit vulnerability in SMA.

Chapter 3: Microarray analysis of vulnerable and resistant motor unit gene expression.

3.1 – Introduction

In Chapter 2, the results demonstrated that there is a spectrum of vulnerability to SMA pathology in motor units in SMA mice. However, no morphological correlate for motor unit vulnerability in SMA could be identified. Motor unit size, intra-muscular arbour length, and branching pattern were quantified, along with synapse elimination rates, terminal Schwann cell numbers, and motor endplate size but no aspect of morphology was found to correlate with motor unit vulnerability. Based on this, we hypothesized that the underlying cause of the vulnerability spectrum was distinct molecular properties of the vulnerable motor units.

There are several lines of evidence that suggest molecular properties drive selective vulnerability in adult onset motor neuron diseases, such as ALS (Saxena et al., 2009; Ringer et al., 2012; Brockington et al., 2013). In 2009, Saxena et al. isolated differentially effected populations of motor neurons in $SOD1^{G93A}$ mice at various time points and used microarray analysis to compare their gene expression profiles. They found that motor units that were known to be vulnerable to ALS expressed endoplasmic reticulum (ER) stress markers from birth, whereas motor units known to be resistant to ALS did not (Saxena et al., 2009). They also showed that ubiquitin signals increased in both vulnerable and resistant motor units before denervation was detectable, but the unfolded protein response and microglial activation were only detected in the vulnerable subset of motor units (Saxena et al., 2009). Also, in 2013, Brockington et al. performed microarray analysis on differentially affected

populations of motor neurons from post-mortem tissue of healthy human patients. Motor neuron cell bodies were extracted from the oculomotor nucleus, the motor neurons of which are known to be resistant to ALS pathology (Nimchinsky et al., 2000); and the lumbar spinal cord, the motor neurons of which are known to be vulnerable to ALS pathology. When the gene expression profiles of the different motor neuron cell bodies were compared, several GABA receptor subunits were identified as being differentially expressed (Brockington et al., 2013). This may relate to the cells' abilities to cope with excitotoxicity, a pathophysiological phenomenon known to occur in ALS (Reviewed by Bogaert et al., 2010). Differences in GABA and AMPA receptors between vulnerable and resistant groups of motor neurons in ALS, has been previously reported (Lorenzo et al., 2006). Brockington et al. (2013) also found that several molecular pathways were altered between the two types of motor neurons, including pathways involved in synaptic transmission, ubiquitin-dependent proteolysis, and the extracellular matrix. A separate study correlated the expression of a specific gene, α-calcitonin gene-related peptide (αCGRP), with the relative vulnerability of motor neurons in different areas of the spinal cord (Ringer et al., 2012). They found that in end-stage $SOD1^{G93A}$ mice, numbers of motor neurons with high levels of αCGRP were reduced by 80%, whereas those with low levels of αCGRP were reduced by 50%, and motor neurons with no αCGRP expression were not significantly reduced (Ringer et al., 2012).

Based on these studies in ALS, we decided to analyse the gene expression profiles of differentially affected motor units in SMA. In order to examine gene expression profiles, it is first necessary to isolate motor units that are known to be differentially affected in SMA. We chose to perform these studies in healthy mice, in order to

avoid including pathological alterations to gene expression in our analysis. From Chapter 2, two muscles were chosen which had been shown to contain differentially affected motor units: the tibialis anterior and the extensor digitorum longus. In order to label the motor neuron cell bodies in the spinal cord, a retrograde tracer was injected; HRP-conjugated wheat germ agglutinin (HRP-WGA). Wheat germ agglutinin (WGA) is a plant lectin that is taken up into neurons by binding to surface membrane oligosaccharides and internalised during endocytosis (Broadwell & Balin, 1985). WGA is then transported along axons towards the cell body. WGA-HRP tracer injection is a well-established method for tracing motor neurons. Studies where WGA-HRP has been injected into muscles to label motor neuron cell bodies or axons have been carried out in cats (Chen & May, 2007), guinea pigs (Sagade, 1990), and mice (Baba et al., 1997; Koyanagi et al., 2006). As in the ALS selective vulnerability studies (Saxena et al., 2009; Brockington et al., 2013), we then performed microarray analysis on the isolated motor neuron cell bodies. By analysing the microarray data, we could detect alterations in both functional networks and individual genes that may have neuro-protective or neuro-detrimental effects.

From these results, it is possible that new therapeutic targets for SMA may be identified. By targeting functional networks that are known to be perturbed in SMA, and are also altered between resistant and vulnerable motor units, we may be able to convey a "protected" status on all motor units, rather than only a select few. Additionally, another possible outcome is the therapeutic targeting of individual genes that are altered between vulnerable and resistant motor units. It is possible that some motor pools intrinsically express higher levels of either neuro-protective genes,

or neuro-detrimental genes. By increasing or decreasing their expression via drug targeting, it may also be possible to convey a "protected" status on all motor units.

In this chapter, motor neuron cell bodies of motor units that were previously identified as being differentially affected in SMA mice were labelled via a retrograde tracer system. The labelled motor neuron cell bodies were isolated from spinal cord sections using laser capture micro-dissection and RNA was extracted and amplified for microarray analysis. From the microarray results, 1029 genes were identified as being significantly differentially expressed between the two motor pools. Of these significantly ($p \leq 0.05$) differentially expressed genes, the gene expression of 196 genes was more than 20% up- or down-regulated between the two motor pools. The list of identified genes that were significantly ($p \leq 0.05$) and more than 20% altered between the two motor pools was used in pathway analysis. Several pathways of interest were identified, such as pathways involved in cellular development, skeletal and muscular system development, and cell death and survival, amongst others. Several individual genes of particular interest were identified from the list as they had previously been implicated in neuro-protection or neuro-degeneration.

3.2 – Methods

3.2.1 - Ethics Statement

All animal experiments were approved by a University of Edinburgh internal ethics committee and were performed under license by the UK Home Office (Project License number 60/3891).

3.2.2 - Animal Husbandry

Phenotypically normal heterozygotic *Smn*$^{+/-}$;*SMN2*$^{tg/0}$ mice on an FVB background were maintained under standard SPF conditions in animal care facilities in Edinburgh. All animal procedures and breeding were performed in accordance with Home Office and institutional guidelines.

3.2.3 - Ink Trial Injections

4-week-old male FVB mice were sacrificed by overdose of anaesthetic via inhalation until no breath had been taken for more than 1 minute and there was no plantar reflex when the foot was stimulated. Approximately 3µl of black ink was injected into the tibialis anterior (TA) via a small incision in the skin. Separately, approximately 1µl of black ink was injected into the extensor digitorum longus (EDL) via a small incision in the skin. The muscles were then dissected out, and the ink staining was compared to the appropriate un-injected muscle.

3.2.4 - WGA Tracer Injections

P14 mice were anaesthetised with 3-5% iso-fluorane in air. Fur was clipped from the anterior surface of the hind limbs and a small incision was made above the TA. For TA motor neuron labelling, 3µl of HRP-conjugated wheat germ agglutinin (HRP-WGA) (PL-1026, Vector Laboratories) was injected into each TA using a Hamilton syringe and a 26G needle. After injecting, the needle was held in the muscle for a further 10 seconds to prevent leakage of the HRP-WGA. For EDL motor neuron

labelling, the fascia surrounding the TA was cut and the EDL identified underneath the TA by its distinctive tendon. 1µl of WGA was injected into each EDL and the needle was held in the muscle for 10 seconds after injection to prevent WGA leakage. The incision was sutured and an injection of Veteragesic was given subcutaneously. After anaesthesia recovery, analgesia was provided to the mice via edible jelly.

3.2.5 - Removal of Spinal Cord

72 hours after tracer injections, the mice were sacrificed by overdose of iso-fluorane via inhalation until no breath had been taken for approximately 1 minute and there was no plantar reflex when the foot was stimulated. The tissues were then cryo-protected by trans-cardial perfusion of approximately 3ml 0.1M PBS followed by approximately 3ml 30% sucrose solution in 0.1M PBS. A laminectomy was performed and the thoracic region of the spinal cord was removed and embedded in OCT contained in a foil boat. The spinal cord and OCT were then frozen in dry ice/ethanol slurry. Once frozen, the spinal cords were stored at -80^{o}C.

3.2.6 - Sectioning and Staining

Sectioning of spinal cords was carried out at Sheffield University. Frozen thoracic regions of spinal cord were cut in half vertically and mounted cut side up on a cryostat chuck. 10µm sections were cut on a cryostat and mounted onto untreated glass slides.

Sections were allowed to warm up to room temperature for 1-2 minutes, then fixed in ice cold acetone for 5 minutes. Excess acetone was wiped from slides and the sections were stained with DAB Peroxidase Substrate Kit (SK-4100, Vector Laboratories) following the manufacturer's instructions. DAB solution was added to the slides for approximately 3 minutes, until a reaction could be seen occurring under a microscope. The slides were then washed with sterile water to remove DAB. Sections were then dehydrated in an alcohol series, from 70% to 100% ethanol followed by xylene. After dehydrating in xylene, the slides were air-dried for at least 45 minutes.

3.2.7 – Laser Capture Micro-dissection

Laser capture micro-dissection was carried out by Masters student Mark Wen-Yo Tu and myself. WGA-labelled motor neuron cell bodies were extracted from sectioned spinal cords using Arcturus PixCell II laser capture micro-dissection machine. A CapSure Macro LCM Cap (Life Technologies, LCM0211) was loaded onto the arm of the PixCell II and placed over the tissue. When a labelled cell was identified the laser was fired using the settings indicated in Table 1.

Laser	Setting
Power	20-39 mW
Duration	25.0 ms
Target	0.25 V
Current	4.4-4.6 mA
Spot Size	7.5 µm

Table 1 – Arcturus PixCell II laser settings.

After all of the labelled cells had been captured from a spinal cord, the cap was removed from the laser capture micro-dissection machine and immediately used for RNA extraction.

3.2.8 - Extraction and Amplification of RNA

RNA extraction and amplification was carried out by Masters student Mark Wen-Yo Tu, Dr Paul Heath, and myself at Sheffield University.

3.2.8.1 - RNA Extraction

RNA was extracted from the LCM captured cells using the PicoPure RNA Isolation Kit (Arcturus, KIT0202). The transfer film with adhered motor neuron cell bodies from the laser capture micro-dissection was removed from the cap with forceps and placed in a sterile 0.5ml tube with Extraction Buffer. The samples were then

centrifuged briefly to ensure the film was fully submerged and incubated at 42°C for 30 minutes to dissolve the transfer film. Meanwhile, RNA Purification Columns were conditioned using Conditioning Buffer for 5 minutes at room temperature then centrifuged at 16000 x g for one minute. 70% ethanol was added to the cell extract and mixed by pipetting before being added to the purification columns. The columns were then centrifuged at 100 x g for 2 minutes, then 16000 x g for 30 seconds. Wash Buffer 1 was added and the columns were centrifuged for one minute at 8000 x g, followed by Wash Buffer 2 that was added to the column and centrifuged for 2 minutes at 16000 x g. The purification column was then transferred to a new 0.5ml tube and Elution Buffer was added. The samples were incubated for 1 minute at room temperature before being centrifuged at 1000 x g for one minute, followed by another 16000 x g centrifugation for one minute. The concentration of extracted RNA was then measured on a Nanodrop.

3.2.8.2 - RNA Amplification

3.2.8.2.1 - First Round of RNA Amplification

RNA was then amplified using the IVT Express Kit to synthesise a strand of cDNA which was then used to amplify the RNA signal via *in vitro* transcription (IVT) using GeneChip 3'IVT Express Kit (Affymetrix, 901228) according to the manufacturer's instructions. Briefly, the First-Strand Master Mix was made up and mixed with the extracted RNA. This was incubated at 42°C for 2 hours. Immediately after incubation, Second-Strand Master Mix was added to the samples and incubated at 16°C for 1 hour, followed by 65°C for 10 minutes. Immediately after incubation,

IVT Master Mix was added to the samples and incubated at 40°C for 16 hours. After incubation, the aRNA was purified using RNA Binding Beads. 60µl of RNA Binding Mix was added to each sample and transferred to a U-Bottom Plate well. 100% ethanol was added to each sample and mixed by pipetting. The samples were mixed thoroughly on a shaking platform for 2 minutes before the plate was moved to a magnetic stand for 5 minutes to capture the RNA Binding Beads. The supernatant was aspirated and discarded and the plate was removed from the magnetic stand. RNA Wash Solution was added to each sample and the samples were mixed thoroughly on a shaking platform for 1 minute. The plate was then moved to the magnetic stand again for 5 minutes and the supernatant aspirated and discarded, before the RNA wash step was repeated. The RNA was eluted from the RNA Binding Beads by adding aRNA Elution Solution pre-heated to 60°C. The plate was shaken vigorously for 3 minutes on a shaking platform before being moved to the magnetic stand. The supernatant was removed and stored at -20°C.

3.2.8.2.2 - Second Round of RNA Amplification

A second round of RNA amplification was then carried out using the MessageAmp II aRNA Amplification Kit (Ambion, AM1751). aRNA amplification was carried out using the optional Second Round Amplification step of the MessageAmp II aRNA Amplification Kit. Briefly, RNA from the first round of RNA amplification was added to a micro-centrifuge tube and Second Round Primers were added. The samples were then incubated at 70°C for 10 minutes. Reverse Transcription Master Mix was added to each sample and pipetted up and down to mix. The samples were

then incubated at 42ºC for 2 hours. RNase H was added to each reaction and incubated at 37ºC for 30 minutes to degrade aRNA, leaving only single stranded cDNA. Immediately after this incubation, second strand synthesis was carried out. T7 Oligo(dT) Primer was added to each sample and then incubated at 70ºC for 10 minutes. Second Strand Master Mix was then added to each reaction and pipetted up and down to mix before being incubated at 16ºC for 2 hours. T4 DNA polymerase from GeneChip Hybridization, Wash and Stain Kit (Affymetrix, 900720) was added to the double-stranded cDNA and incubated at 16ºC for 10 minutes, followed by 4ºC for 2 minutes. cDNA was then purified using the cDNA Filter Cartridges that were supplied with the MessageAmp II aRNA Kit. 250µl cDNA Binding Buffer was added to each sample and pipetted up and down to mix thoroughly. The mixture was then pipetted onto the centre of the cDNA Filter Cartridge and centrifuged at 10000 x g for 1 minute. The flow-through was discarded and Wash Buffer was added to each cDNA Filter Cartridge and centrifuged again at 10000 x g for 1 minute. The flow-through was discarded and the filter cartridges were centrifuged at 10000 x g for 1 minute again to remove all traces of Wash Buffer. The cDNA Filter Cartridges were then moved to cDNA Elution Tubes and nuclease-free water at 55ºC was added to the filter for 2 minutes before being centrifuged at 10000 x g for 1 minute.

Using this eluted cDNA, overnight IVT was carried out again using the GeneChip 3' IVT Express Kit (Affymetrix, 901228) to produce a second round of amplified biotin-labelled RNA. At each stage of RNA extraction and amplification, the concentration of RNA was measured using a Nanodrop.

3.2.9 - Biotin-Labelled cRNA Fragmentation

Biotin-labelled cRNA was fragmented using the 5x Array Fragmentation Buffer supplied in the GeneChip 3'IVT Express Kit (Affymetrix, 901228). 15µg of biotin-labeled cRNA was added to a microcentrifuge tube, along with 8µl of 5x Array Fragmentation Buffer and made up to 40µl with Nuclease-free water. These samples were then incubated at 94ºC for 35 minutes before being placed on ice immediately after the reaction.

3.2.10 - RNA Quality Checks

aRNA samples were quality checked after the first round of RNA amplification; after the second round of RNA amplification; and after fragmentation.

RNA 6000 Pico Kit (Agilent Technologies, 5067-1513) was used to measure RNA quality. Briefly, 1µl of RNA 6000 Pico dye concentrate was added to 65µl filtered RNA 6000 Pico gel matrix and vortexed thoroughly before being centrifuged at 13000 x g for 10 minutes. 9µl of the gel-dye mix was then pipetted into the G marked wells of the RNA Pico 6000 chip and pressurised through the capillaries. 9µl of RNA 6000 Pico conditioning solution was added to the white well marked CS and 5µl of RNA 6000 Pico marker was added to the well marked with the ladder symbol and each of the 11 sample wells. 1µl of RNA 6000 Pico ladder was added to the well marked with the ladder symbol. 1µl of each aRNA sample was then added to each well. The chip was then placed in a horizontal vortex mixer and vortexed at 2000rpm for 1 minute. The chip was then inserted into an Agilent 2100 Bioanalyzer machine and analysed using 2100 Expert Software.

3.2.11 – Microarray

Microarrays were carried out by Dr Paul Heath in Sheffield University. The GeneChip Hybridization, Wash and Stain Kit (Affymetrix, 900720) was used to perform the microarrays. GeneChip Mouse Genome 430 2.0 Arrays (Affymetrix, 9000496) were used to perform the microarrays.

3.2.11.1 – Hybridisation

Hybridization Cocktail was made up for each array, according to Table 2 to a total volume of 300µl and containing 15µg of fragmented RNA. The Hybridization Cocktail was then heated to 99^{o}C for 5 minutes on a heat block, followed by 45^{o}C for 5 minutes. The Hybridization Cocktail was then centrifuged at 14000rpm for 5 minutes.

Component	**Volume (µl)**
Fragmented and Labelled cRNA	Variable
Control Oligonucleotide B2 (3nM)	5
20X Eukaryotic Hybridization Controls (bioB, bioC, bioD and cre)	15
2X Hybridization Mix	150
DMSO	30
Nuclease-free water	Variable

Table 2 – Components and volumes of Hybridization Cocktail required for one reaction.

Meanwhile, 200µl Pre-Hybridization Mix was added to the array probe by filling the array through one of the septa and incubated at 45^{o}C for 10 minutes with rotation in the Hybridization oven. The array probe was then removed from the oven and the array was vented with a clean pipette and the Pre-Hybridization Mix was removed from the array. The array was then refilled with 200µl of the Hybridization Cocktail. The probes were then placed into the Hybridization oven set at 45^{o}C and rotated at 60rpm for 16 hours.

3.2.11.2 - Washing, Staining and Scanning the Array Probes

After hybridisation, the probe was vented by inserting a pipette tip into one of the septa and the Hybridization Cocktail was removed through the remaining septum. 250µl Wash Buffer A was then inserted into the probe array. The probe array was then inserted into a Fluidics Station 420/250 for washing and staining. The Fluidics Station 420/250 was controlled by Affymetrix GeneChip Command Console software. The probe arrays were washed and stained according to the programme listed in Table 3. All reagents used were supplied by Affymetrix.

Step	Reagent	Number of Cycles	Temperature (ºC)
Post-hybridization Wash #1	Wash Buffer A	10	25
Post-hybridization Wash #2	Wash Buffer B	4	50
1st Stain	SAPE Solution	1	25
Post Stain Wash	Wash Buffer A	10	25
2nd Stain	Antibody Solution	1	25
3rd Stain	SAPE Solution	1	25
Final Wash	Wash Buffer A	15	25
Final Wash	Wash Buffer A	15	25

Table 3 - Fluidics Protocol for washing and staining probe arrays. All stains were incubated for 10 minutes.

After staining and washing, the probe arrays were scanned in an Affymetrix GeneChip Scanner 3000 controlled by Affymetrix GeneChip Command Console software.

3.2.12 - Data Analysis

Microarray quality control was carried out using Expression Console software from Affymetrix. .CEL files produced by the Affymetrix GeneChip Command software were uploaded to Expression Console and normalised using the MAS5 algorithm in

order to generate quality control graphs. Expression Console's report metrics was used to generate the quality control line graphs.

Microarray data was analysed using QIUcore software. .CEL files produced by Affymetrix GeneChip Command Console software were uploaded to the QIUcore software and separated into two groups (TA, n = 3; EDL, n = 3) for analysis and the data was normalised using PLIER normalisation. From the QIUcore software, PCA plots and heat maps of gene expression were generated. Lists of genes up- and down-regulated across the two groups were generated using the QIUcore software. Filter variance was set at 0 and the p value was set at 0.05. The q value was set automatically by the software. The gene lists were exported from the QUIcore software as Excel spread sheets for further analysis.

3.2.13- Pathway Analysis

Pathway analysis was performed using IPA software from Ingenuity Systems. This list of genes was filtered to include only genes that had a significance value of 0.05 or less and were more than 20% up- or down-regulated. The genes symbols and their respective ratios (EDL/TA; in that a ratio of 1.2 or more signified an up-regulation of the gene in the EDL-labelled motor neurons, and a ratio of less than 0.8 signified an up-regulation of the gene in the TA-labelled motor neurons) were submitted for pathway analysis. Analysis parameters were set to include both direct and indirect protein/gene interactions that had been confirmed by experimental observation only. All protein and gene databases were searched and interactions observed in all species and cell types were included in analysis.

3.2.14 - Literature Search

The list of up- and down-regulated genes was subjected to a manual literature search. Genes that were more than 20% altered between motor neuron groups were subjected to the literature search. Systematically, gene symbols, names and aliases were searched on PubMed for any implication in neuro-degeneration, neuro-protection, cell death pathways, or involvement at the synapse.

3.3 - Results

3.3.1 - Ink Trial Injections

Muscles were chosen for labelling based on their motor unit vulnerability, as identified in Chapter 2, and whether the muscles could be injected with the WGA tracer. A large number of muscles analysed in Chapter 2 were eliminated due to their thinness. While this was an extremely valuable attribute for NMJ analysis, the thinness of the muscles meant that it would be impossible to accurately and confidently inject specific muscles with WGA tracer. However, the hind limb muscles analysed in Chapter 2 are large-bellied muscles, which could be easily identified and confidently injected. Two hind limb muscles were chosen for tracer injections which were on opposite ends of the vulnerability spectrum and could easily be identified and injected: the tibialis anterior (TA), innervated by vulnerable motor units; and the extensor digitorum longus (EDL), innervated by resistant motor units.

In order to test whether tracer injections would be successful in muscle, the TA and EDL were injected with artists' ink in dead mice. The ink injections were also used to trial various depths and angles that the needle should be inserted into the muscles to ensure an accurate injection, and also the optimal position of the mouse leg and incision for identifying the TA and EDL (Figure 1A). Black ink was injected into the TA (3µl) or EDL (1µl) of dead mice and the hind limbs were removed, skinned, and the TA and EDL muscles were dissected and examined (Figure 1B).

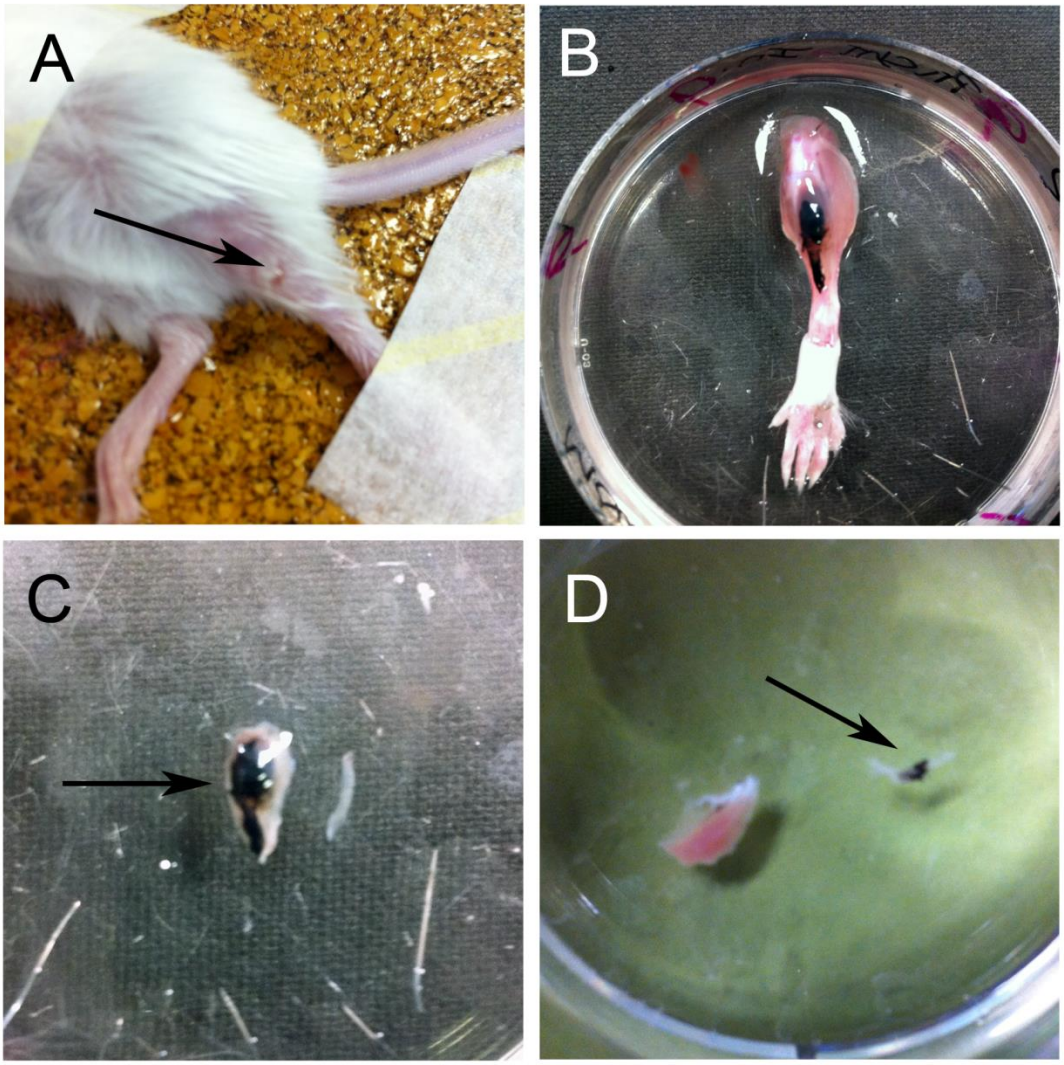

Figure 1 – TA and EDL muscles injected with black ink. Black artist's ink was injected into the TA or EDL of dead mice to test whether small volumes could accurately be injected into these muscles. (A) The foot of the dead mouse was taped into place to prevent movement. The best angle for the foot to be taped relative to the mouse's body for access to the different muscles was also tested. The black arrow shows where the incision was made in the skin in order to access the TA muscle for injection. (B) After injection, the hind limb was removed from the dead mouse and the skin was reflected in order to assess the ink's penetration into the muscle and surrounding tissues. In this image, we can clearly see that the TA muscle has been stained with black ink, but the surrounding muscles have not. (C) Dissection of the TA and EDL muscles where the TA was injected with black ink. The TA (black arrow) is clearly marked with black ink, but there is no evidence of black ink in the EDL. (D) Dissection of the TA and EDL muscles where the EDL was injected with black ink. The EDL (black arrow) is clearly marked with black ink, but there is no evidence of black ink in the TA.

It was found that the ink did not spread from one muscle to another when injected into either the TA or the EDL (Figure 1C and 1D). Also, the ink injections confirmed that, although the EDL is a considerably smaller and thinner than the TA, it could be successfully injected by identifying the muscle tendon and following this tendon with the needle (Figure ID). A problem that was identified during the ink trials was leakage of the ink out of the muscle after the injection. This was overcome by holding the needle in place for approximately 10 seconds after the injection.

3.3.2 - WGA-HRP Injections and Laser Capture Micro-Dissection

P14 mice were injected with 3µl WGA in both TAs (n = 3) or 1µl WGA in both EDLs (n = 3) under anaesthesia (Table 4).

Mouse ID	Muscle Injected	Volume of WGA Injected (µl)
1	TA	3
3	TA	3
6	TA	3
11	EDL	1
31	EDL	1
33	EDL	1

Table 4 – Volumes of locations of injections of HRP-WGA in P14 mice.

72 hours later, the mice were sacrificed by overdose of anaesthetic via inhalation before being trans-cardially perfused with 30% sucrose to cryo-protect the spinal cord. The spinal cord was then removed and embedded in OCT before being frozen on a dry ice and ethanol slurry, and stored at -80^{o}C. The tissue was then transported to Sheffield University on dry ice where it was sectioned at 10µm on a cryostat. The sections were fixed with ice-cold acetone and stained with DAB in order to identify motor neurons that had been labelled with HRP-tagged WGA (Figure 2). The sections were then dehydrated in an alcohol series and xylene before being air-dried. Once dried, the labelled cells could be removed from the tissue by laser capture-micro dissection.

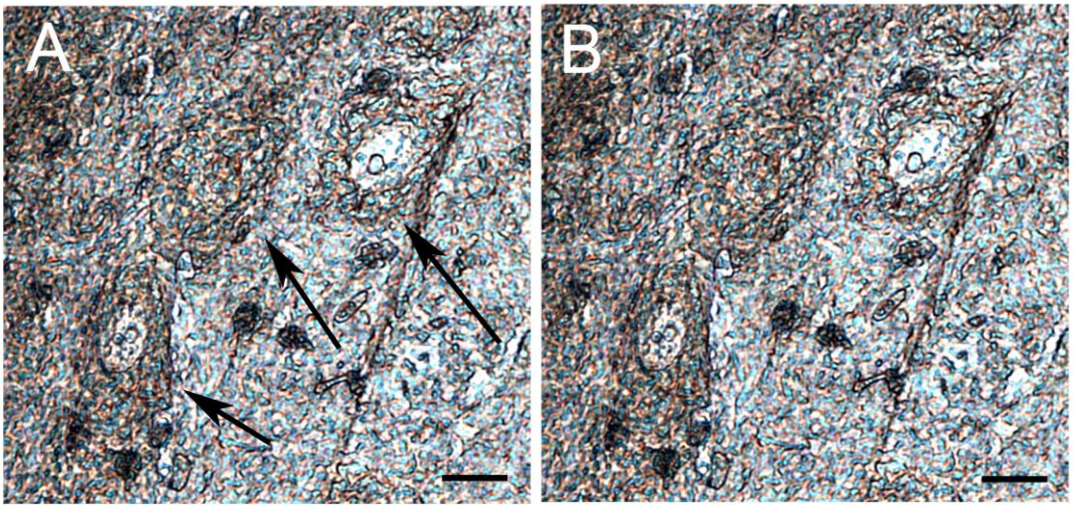

Figure 2 – WGA-HRP labelled motor neurons in the spinal cord. This image was taken from tissue that had been processed through a xylene and alcohol series to remove water, stained with DAB, and air-dried on a glass slide for use on the Arcturus PixCell II. No glass coverslip or mounting media was used for this picture, which is why the tissue has a very granular appearance. (A) Three positively labelled motor neuron cell bodies (black arrows) in the spinal cord of mice injected in the EDL with WGA-HRP. This pattern of three motor neuron cell bodies clustered together was always observed in the EDL-labelled spinal cords. (B) An identical image to Figure 2A, with the outlines of the motor neuron cell bodies highlighted in red. Scale bar = 10µm.

An Arcturus PixCell II laser capture micro-dissection machine was used to do isolate the labelled motor neuron cell bodies. Caps with a transfer film bonded to the lower surface are inserted into the arm of the machine, which is then swung over the tissue and lowered so that it is in direct contact with the tissue (Figure 3). When a labelled motor neuron was identified the laser was aimed and fired through the cap, which

melts the transfer film on the cap. The melted transfer film bonds to the tissue and when the arm of the laser capture machine is lifted, the tissue that has bonded to the transfer film is also lifted from the slide.

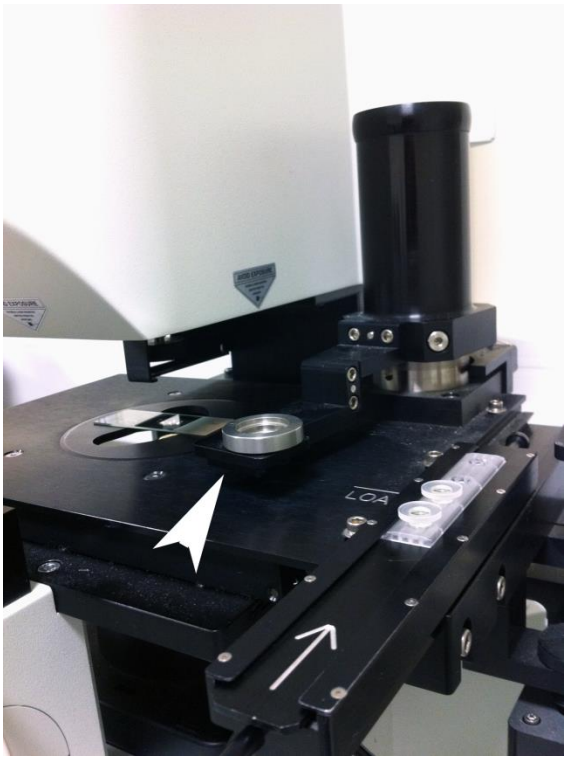

Figure 3 – Arcturus PixCell II laser capture micro-dissection machine. The white arrowhead shows the arm of the machine where the cap is placed. This arm can be swung over the tissue on the slide and the laser is fired down through the cap to melt the transfer film and bond it to the tissue.

3.3.3 - RNA Extraction

To extract RNA, the transfer film with adhered motor neuron cell bodies was removed from the cap by peeling it off with forceps. The film was dissolved in extraction buffer from the Arcturus Pico Pure RNA Isolation Kit and RNA was extracted following the manufacturer's instructions. After extraction, RNA concentrations were measured on a Nanodrop (Table 5).

Sample	Concentration (ng/µl)	260/280
1	5.55	1.51
3	14.73	1.73
6	8.26	1.52
11	8.92	1.33
31	3.76	2.46
33	8.36	1.68

Table 5 – Concentrations and qualities of RNA extracted from motor neuron cell bodies isolated from the spinal cord of P14 mice by laser capture micro-dissection.

3.3.4 - RNA Amplification

While the extraction of RNA from the laser capture micro-dissection tissue was successful, the yield of RNA was far too low to carry out a microarray, which required 15µg of RNA. Based on this, extracted RNA was amplified using a modified *in vitro* transcription (IVT) protocol (Figure 4). IVT was carried out using

the GeneChip 3'IVT Express Kit (Figure 4), and a second round of RNA amplification was carried out using the optional second round RNA amplification step of the Ambion MessageAmp II aRNA Amplification Kit to synthesise cDNA from the already amplified RNA (Figure 5). A second round of IVT was then carried out using the GeneChip 3'IVT Express Kit (Figure 5).

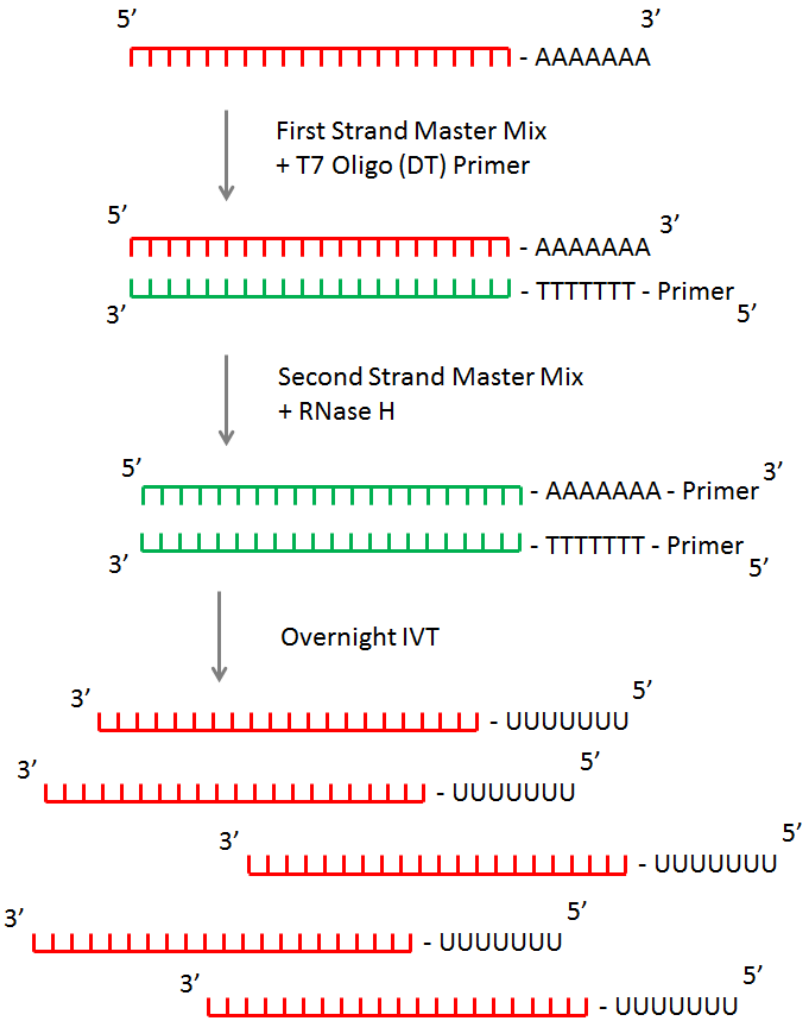

Figure 4 – Schematic of the first round of RNA amplification using the GeneChip 3'IVT Express Kit. Extracted RNA (red) is primed with T7 Oligo (dT) primers, which bind to the poly-A tail of mRNA. A first strand of anti-sense cDNA (green) is then synthesised from the RNA strand. Next, RNA is removed from the cDNA strand

using RNase H enzyme and in the same step, a second strand of cDNA is synthesised using random primers to bind along the length of the anti-sense cDNA strand. From this double-stranded cDNA, in vitro transcription (IVT) is carried out to produce multiple copies of anti-sense RNA.

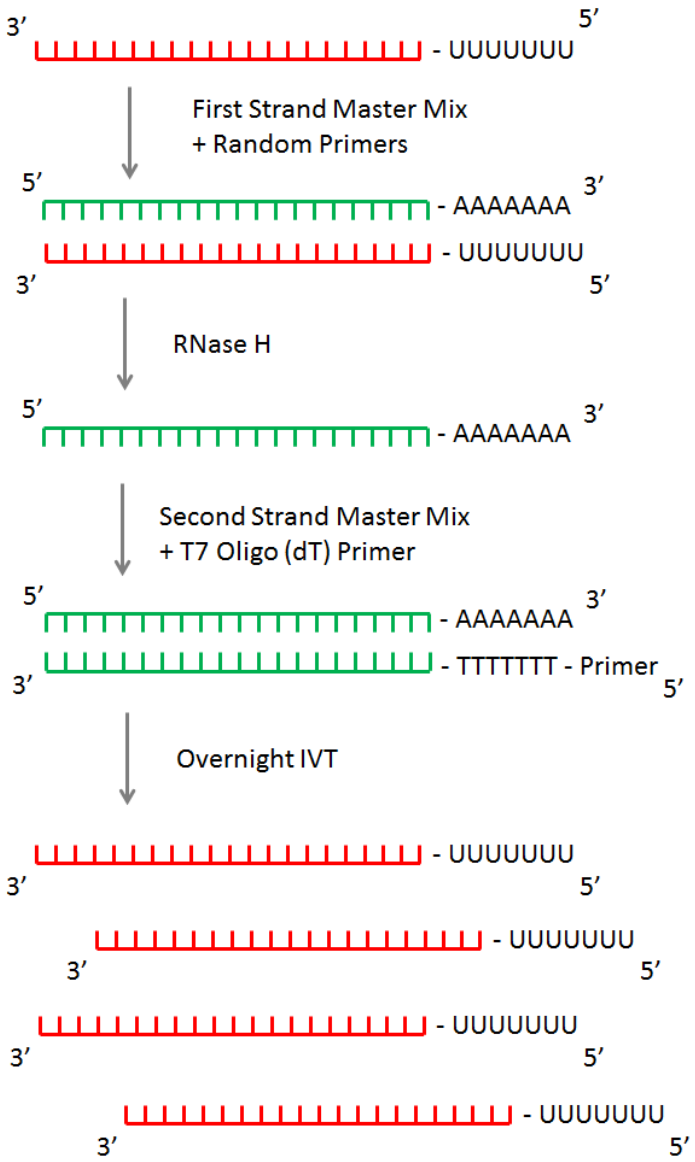

Figure 5 – Schematic of the second round of RNA amplification using Ambion MessageAmp II RNA Amplification Kit and GeneChip 3'IVT Express Kit. The anti-sense amplified RNA (red) from the first round of IVT was used to synthesise a first

strand of cDNA (green) using random primers to bind along the length of the RNA strand. RNase H was then added to remove RNA and leave a single strand of sense cDNA. A T7 Oligo (dT) primer was then used to bind to the poly-A tail of the sense cDNA, from which a second strand of cDNA was synthesised. From this double-stranded cDNA, IVT took place once again, resulting in multiple copies of anti-sense RNA. During IVT, the RNA strands were labelled with biotin.

3.3.4.1 - First Round of RNA Amplification

Using GeneChip 3' IVT Express Kit, a strand of cDNA was synthesised from the extracted RNA. An Oligo (dT) primer binds to the polyA tail of mRNA strands, from which First-Strand Master Mix synthesises an anti-sense strand of cDNA. Second-Strand Master Mix then simultaneously removed RNA and synthesises a second strand of cDNA. *In vitro* transcription was then carried out overnight using this cDNA. Following overnight IVT, the amplified RNA (aRNA) was purified using magnetic beads that specifically bind to RNA and the concentration of aRNA was measured using a Nanodrop (Table 6).

Sample	Concentration (ng/µl)	260/280
1	149.31	1.99
3	125.25	1.99
6	158.14	1.96
11	97.36	1.99
31	136.61	2.00
33	111.86	1.98

Table 6 – Concentrations and qualities of RNA amplified using the GeneChip 3'IVT Express Kit.

Amplified RNA quality was checked using a Bioanalyzer and PicoChip 6000 to detect various lengths of RNA fragments (Figure 6).

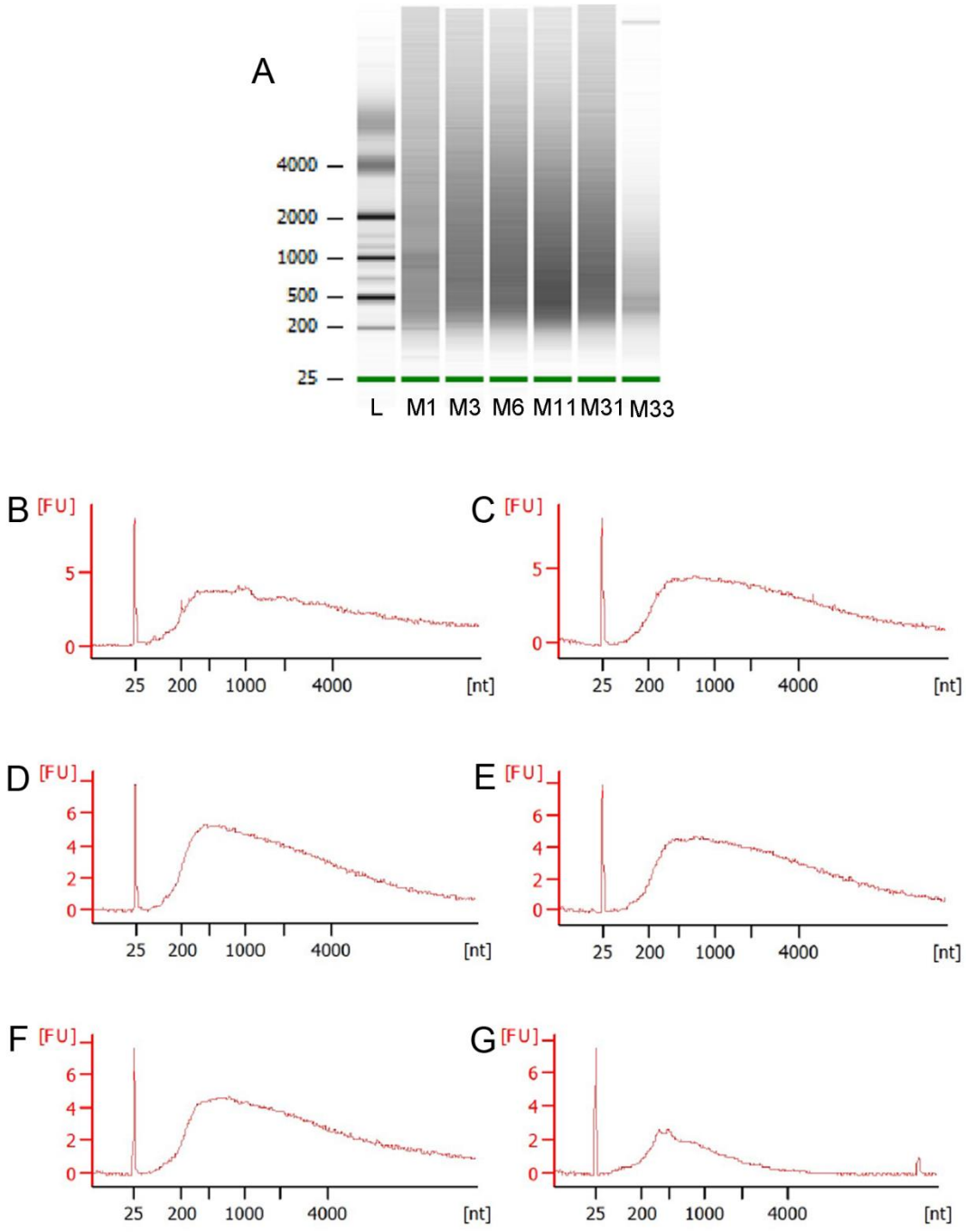

Figure 6 – Amplified RNA qualities as determined by Agilent 2100 Bioanalyzer. (A) The fragments of amplified RNA as it appeared through the capillaries of the PicoChip. (B-G) Quantification of the fluorescence intensity (arbitrary units) of different lengths of RNA fragments (number of nucleotides). In high quality RNA, we

would expect to see two peaks of fluorescence intensity, corresponding to 18S and 28S ribosomal RNA. Due to the nature of the tissue processing and RNA amplification, these peaks were not observed in the sample RNA, which was expected. The fragments sizes of RNA that were present in the samples were comparable. The peak present at 25nt is a marker that was added to all RNA samples.

3.3.4.2 - Second Round of RNA Amplification

While the concentrations of RNA were increased by the IVT, the concentrations of RNA were still too low to carry out a microarray, which requires 15µg of RNA. In order to further increase the yield of RNA, a second round of RNA amplification was carried out using the optional Second Round Amplification step of the MessageAmp II aRNA Amplification Kit. RNA from the first round of IVT was used to synthesise the first strand of cDNA using Second Round Primers that bind randomly along the length of the aRNA, and are elongated by Reverse Transcription Master Mix. RNase H was added to degrade RNA present in the reaction, leaving only a single strand of sense cDNA. A second strand of cDNA was then synthesized by adding T7 oligo (dT) primers, which bind to the poly-A tail of the sense cDNA. A second strand of cDNA is then synthesised from the T7 oligo d(T) primer. After cDNA second strand synthesis, a T4 DNA polymerase from GeneChip Hybridization, Wash and Stain Kit was added in order to fill any gaps in the cDNA produced during cDNA synthesis. The cDNA was then filtered through a cDNA cartridge to purify it. Labelling IVT was then carried out using the GeneChip 3' IVT Express Kit once again, to produce

biotin-labelled amplified RNA for fragmentation. The concentrations of aRNA from the second round of amplification are listed in Table 7.

Sample	Concentration (ng/µl)	260/280
1	3837.48	1.72
3	3564.06	1.75
6	2890.17	1.91
11	3530.84	1.78
31	3583.41	1.76
33	2013.32	2.04

Table 7 – Concentrations and qualities of RNA produced from the second round of RNA amplification.

RNA quality was again analysed using Bioanalyzer 6000 (Figure 7). Similar peaks in RNA fragment size were detected in all samples. This spread of RNA fragment lengths is expected from RNA that has been processed, extracted, and amplified using this method.

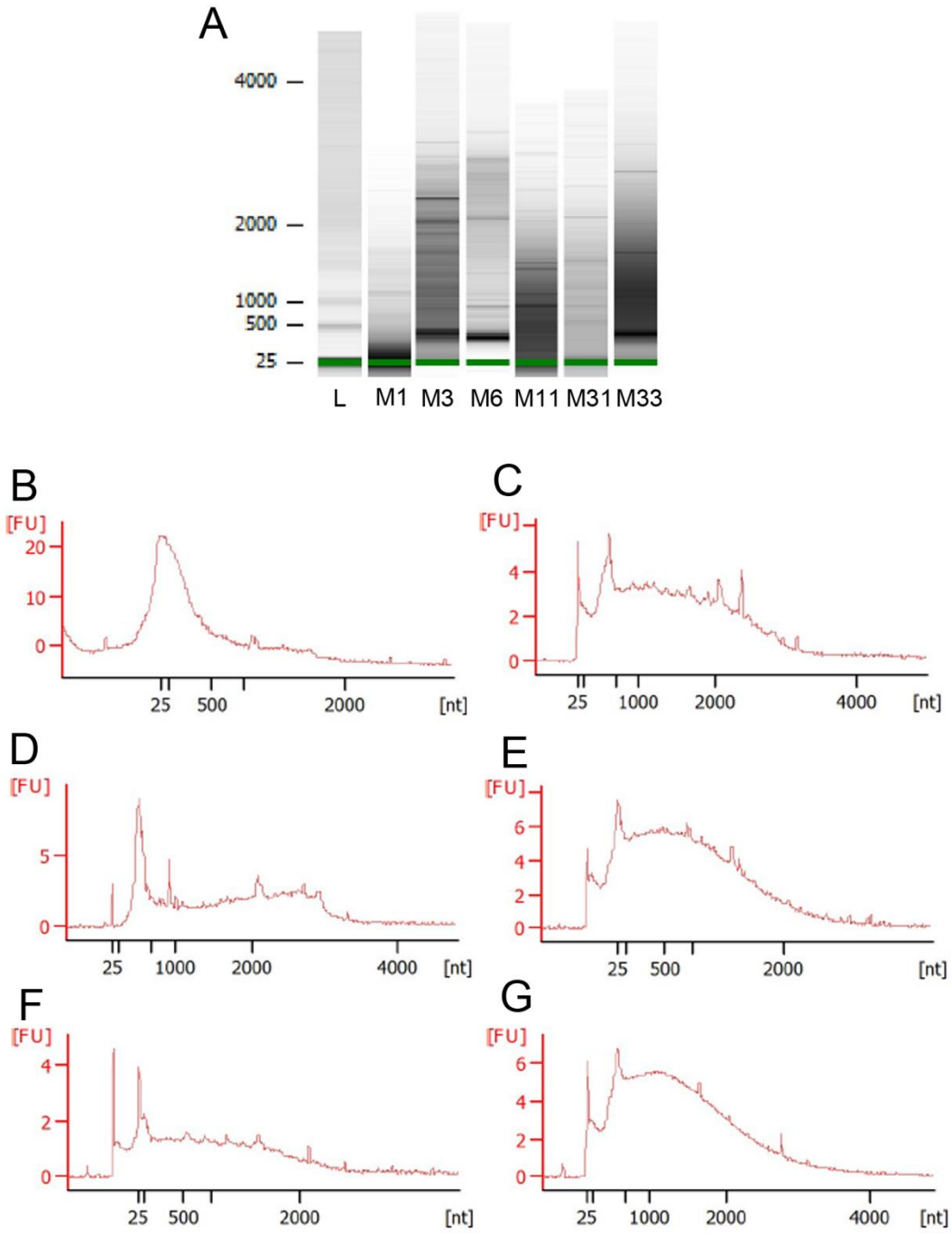

Figure 7 – Bioanalyzer information after second round of RNA amplification. (A) The fragments of amplified RNA as it appeared through the capillaries of the PicoChip. (B-G) Quantification of the fluorescence intensity (arbitrary units) of different lengths of RNA fragments (number of nucleotides). The samples showed a

similar spread and intensity of aRNA fragments after the second round of amplification. This spread of RNA fragment sizes was expected due to the processing of RNA.

3.3.5 - Microarray

Once the cRNA was labelled with biotin, it was then fragmented by heating the biotin-labelled cRNA at 94^{o}C for 35 minutes with Fragmentation Buffer, which fragments the RNA strands into fragments 35-200 nucleotides in length. Bioanalyzer analysis showed that biotin-labelled aRNA was successfully fragmented and produced RNA fragments of the expected sizes (Figure 8).

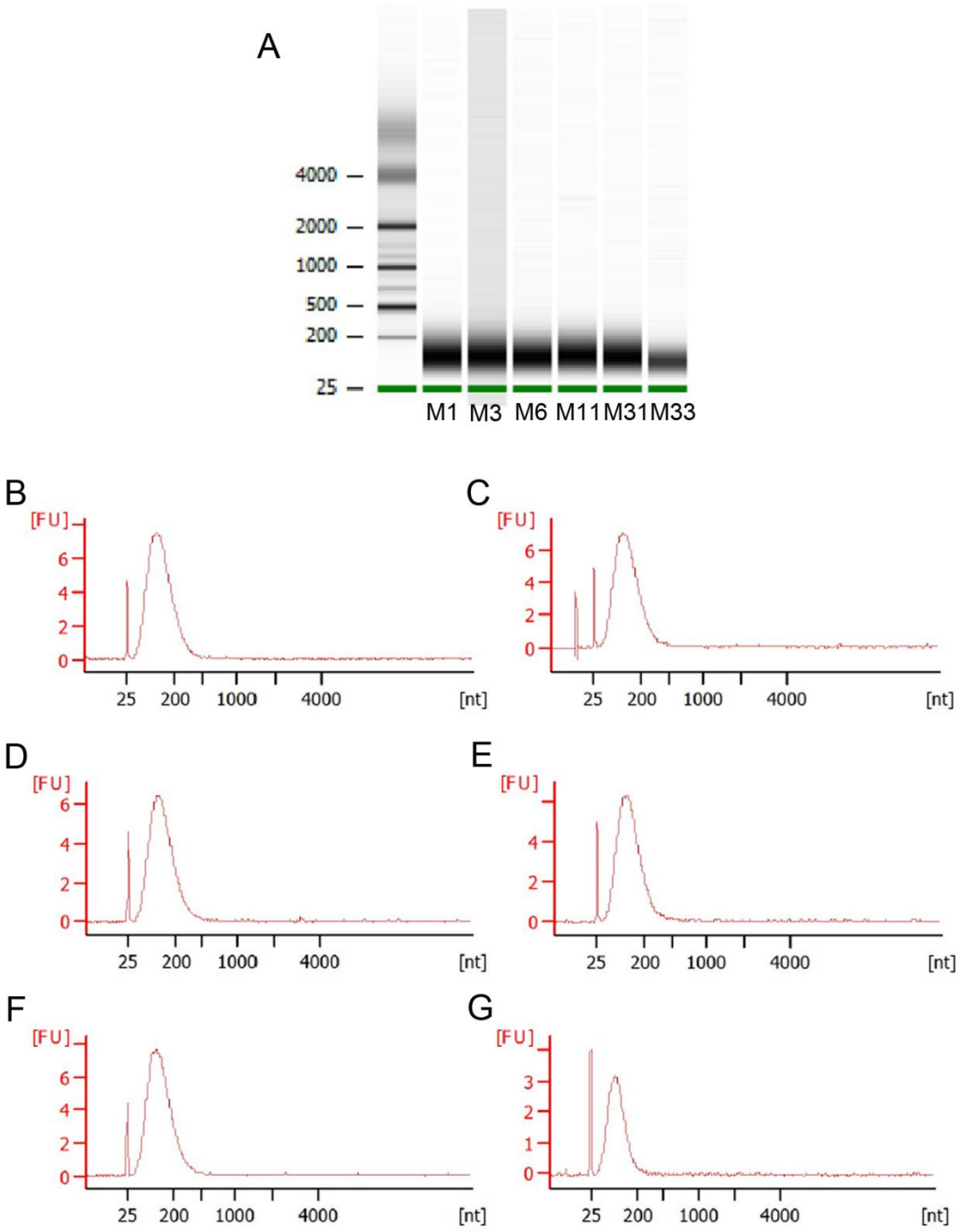

Figure 8 – Amplified and biotin-labelled RNA qualities after fragmentation. Fragmentation of biotin-labelled aRNA should produce fragments of RNA between 35-200 nucleotides long, according to the GeneChip 3'IVT Express Kit User Manual. (A) The fragments of amplified RNA as it appeared through the capillaries

of the PicoChip. (B-G) Quantification of the fluorescent intensity (arbitrary units) of different lengths of RNA fragments (number of nucleotides). The samples show a similar spread of RNA fragment sizes, between approximately 35-200 nucleotides in length. The samples also show a similar fluorescent intensity of RNA after fragmentation.

After fragmentation, biotin-labelled cRNA was incubated with a GeneChip Mouse Genome 430 2.0 Array Probe at 45^{o}C in a rotating oven for 16 hours. After hybridisation, the probe arrays were washed and stained with the biotin-binding fluorescent streptavidin solution (SAPE Solution). This streptavidin solution was then washed off and a second stain was performed using a biotinylated anti-streptavidin antibody. A third stain was performed using streptavidin solution once again, in order to further amplify the fluorescent signal. After two washes, the array probes were scanned on an Affymetrix GeneChip Scanner 3000.

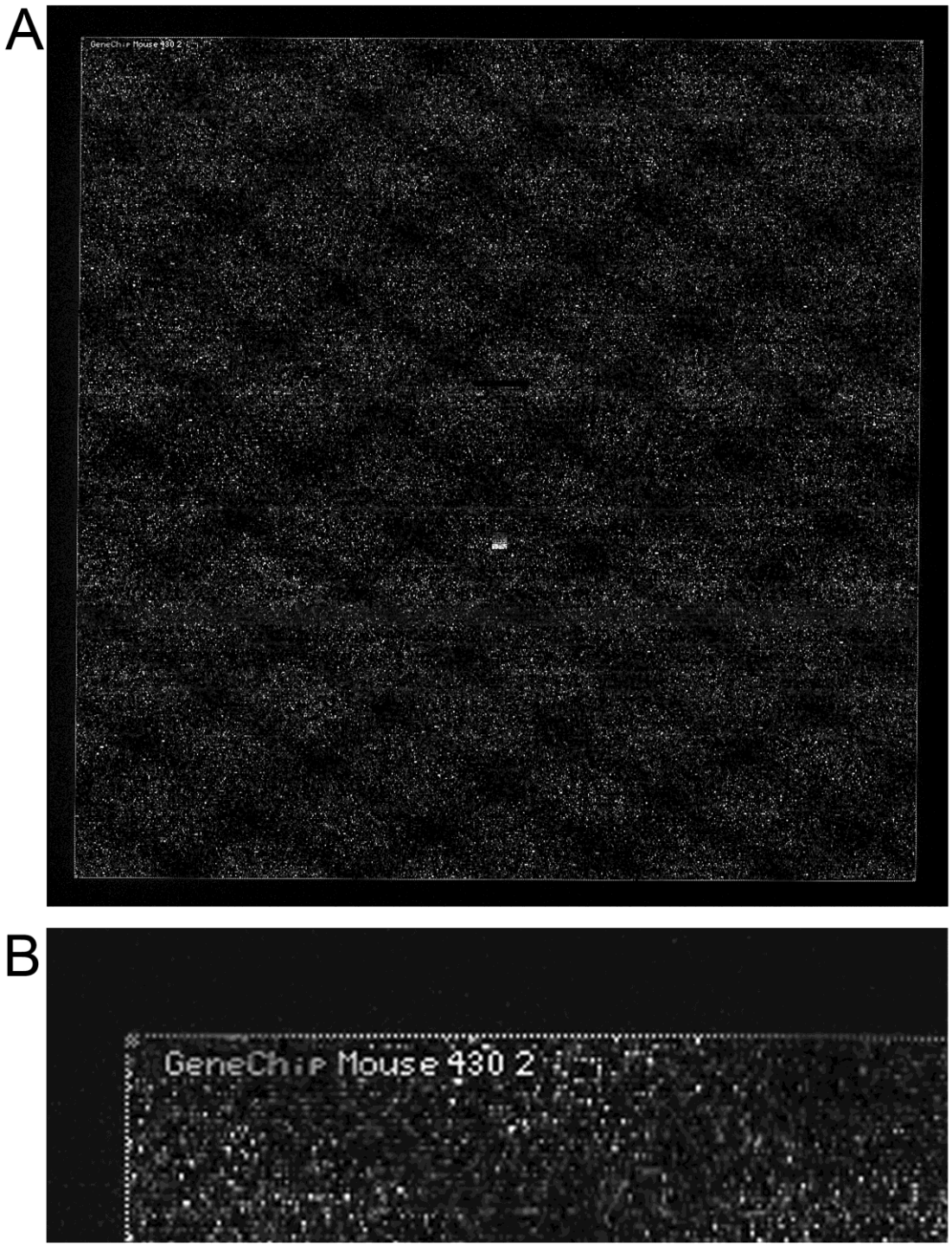

Figure 9 – Scan of an array chip (M1). (A) A low magnification scan of an array probe after being hybridised with biotin-labelled fragmented RNA, stained and washed. (B) High magnification image of the array probe showing quality control

data. Probes are designed to encode the details of the array when control RNA correctly hybridises. This also serves as a way of aligning the probes when scanning, to ensure that fluorescence intensities for the correct probes are being recorded. Other quality control probes are present on the array, such as the dotted line visible around the edge of the probe field, a cross in the centre of the probe field, and a square of increasing fluorescent intensities in the centre of the probe field. When these quality control probes are visible, it serves as further assurance that RNA has correctly hybridised to the array probe.

3.3.5.1 - Microarray Quality Control

In order to assess and compare the quality of the microarrays, Expression Console software from Affymetrix was used to analyse the signal and noise levels of each microarray chip. .CEL files were uploaded to Expression Console software and normalised using the MAS5 algorithm. The log signal for each array was generated using Expression Console software and plotted as a box plot for comparison (Figure 10A). The box plots represent the distribution of signal values for each probe set in the microarray, relative to the other arrays (Figure 10A). As Figure 10 shows, no array appears to show a divergent signal distribution. The arrays' signal is also represented by a histogram (Figure 10B).

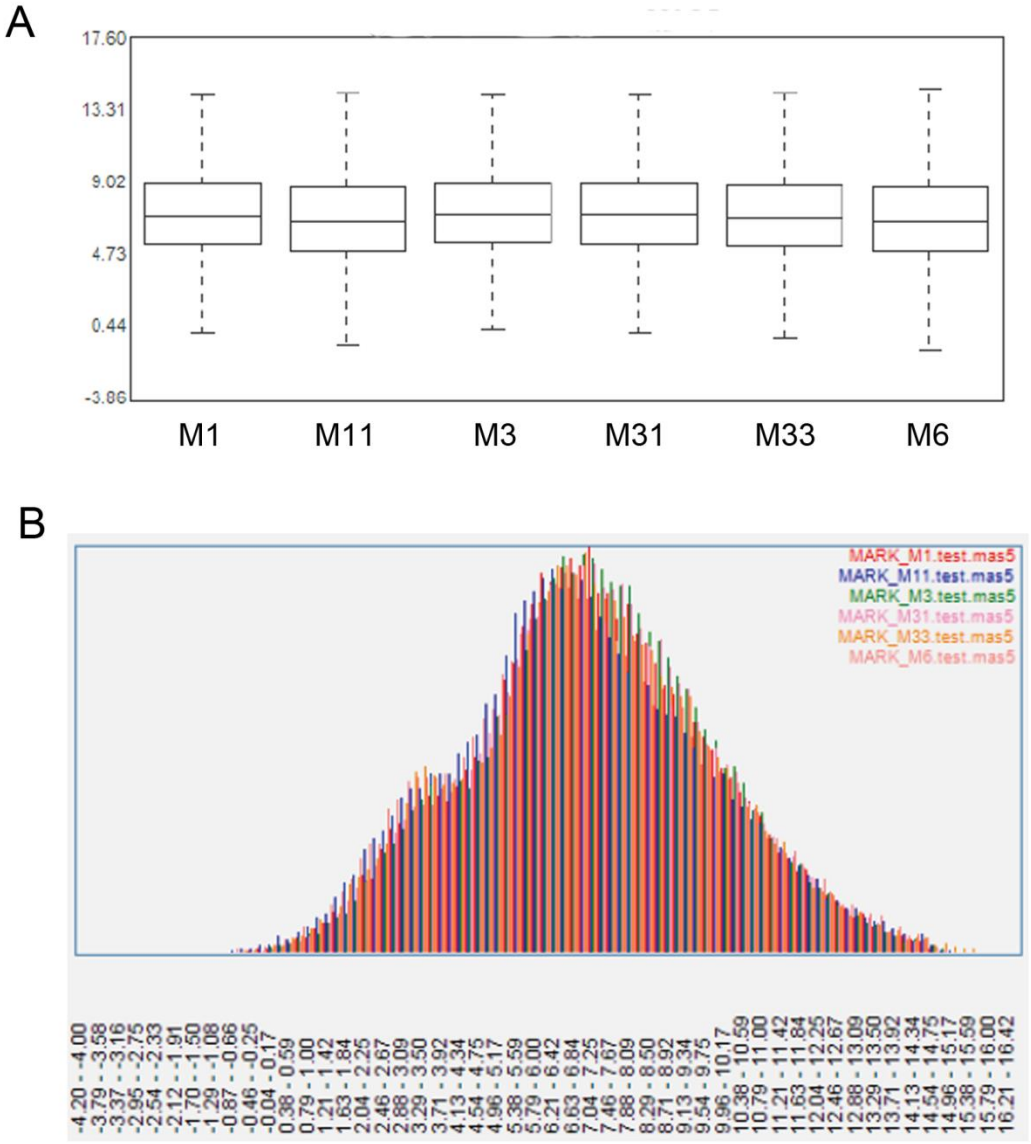

Figure 10 – Box plots and histogram of log signal of probes. (A) Box plots of signal were generated using Expression Console software from Affymetrix. The box plots show the log signal of probe arrays after normalisation. All box plots are comparable, and no box plot appears to be different to any other. (B) A histogram of signal values generated from normalised data. All histograms are comparable, with no probe array skewing from the bell-shaped curve.

The signal values for housekeeping gene probe sets of each array were compared using Expression Console software (Figure 11). The signal values for probe sets representing GAPDH and β-actin were compared across arrays (Figure 11). Figure 11 shows that similar signal values for both β-actin and GAPDH were detected across all arrays, with β-actin signal values being higher and slightly more variable (Figure 11).

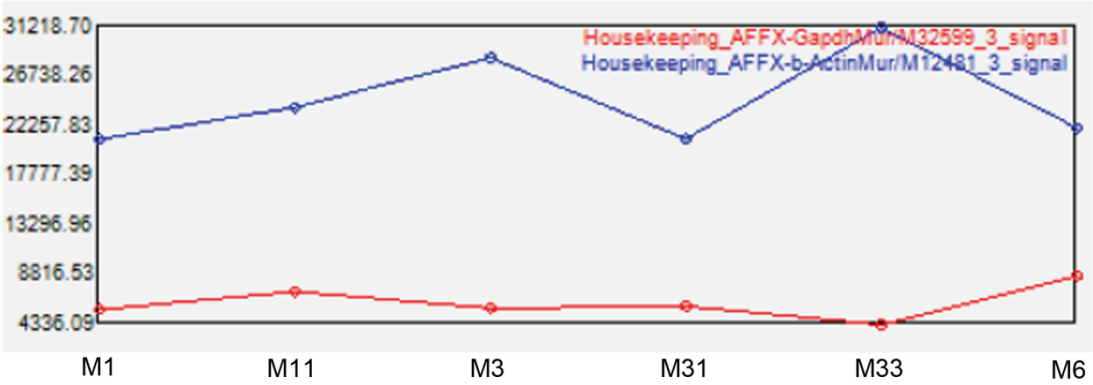

Figure 11 – GAPDH (red) and β-actin (blue) 3' signal intensity across probes after normalisation. Although there is slight variation in the intensity of both GAPDH and β-actin across the probe arrays, no probe array appears to be particularly divergent. GAPDH and β-actin signal intensities are fairly stable across all array probes.

Next, the percentage of probe sets defined as present (a probe set in which a signal was detected) was calculated by the Expression Console software (Figure 12A). Figure 12A shows that on average, approximately 50% of probe sets were defined as present across the arrays. Array M33 shows a slightly reduced percentage of probe

sets present, at 46.58% (Figure 12A). Figure 12B shows the average signal (relative intensity units) of the present probe sets in each array. Despite having a marginally lower percentage of present probes (Figure 12A) array M33 has a higher average intensity of present probes (Figure 12B).

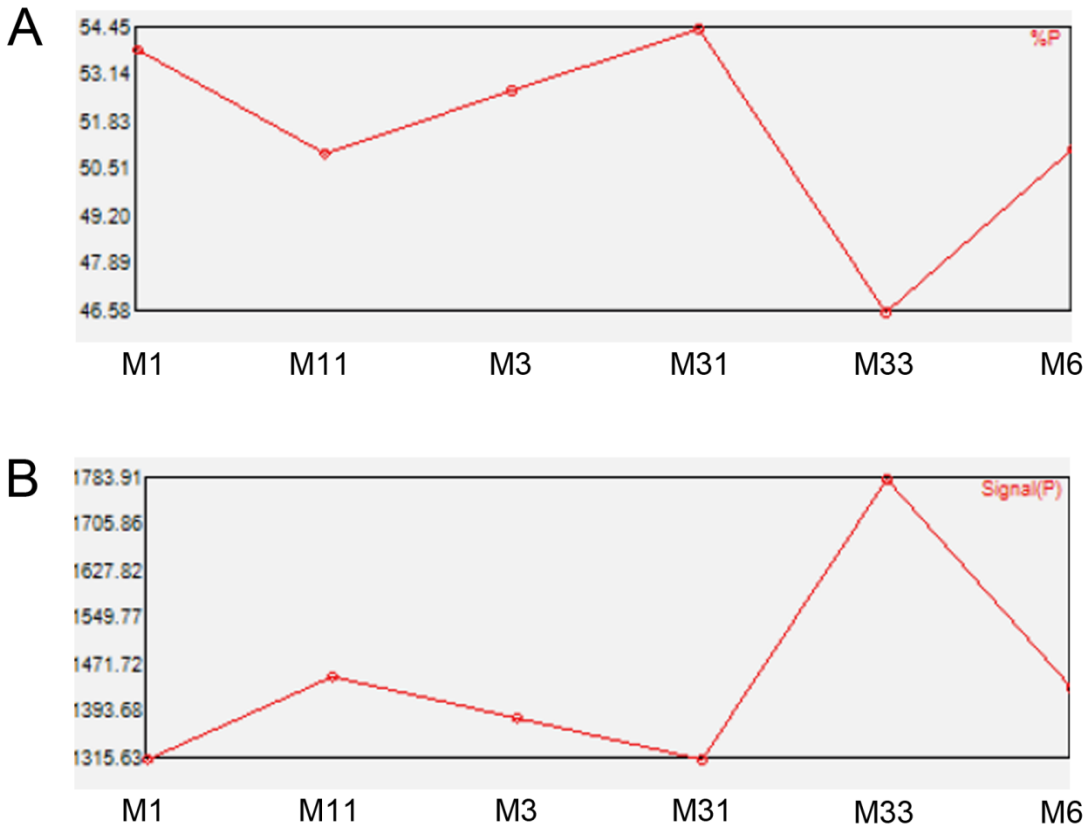

Figure 12 – Percentage of probe sets present. (A) The percentage of probe sets in which a signal was detected for each array, after normalisation. Approximately 50% of probe sets on the array probe were identified by the Expression Console software as being present. This percentage was slightly reduced for M33, with approximately 47% of probe sets being present. (B) The average intensity of probe sets defined as

present. The signal intensity of the present probe sets was comparable across all probe arrays, with M33 showing a slightly more intense signal.

The degree of noise present in each array was calculated by the Expression Console software (Figure 13). The noise values were calculated based on the degree of pixel-to-pixel signal variation among probe cells used to calculate background (Figure 13A). Figure 13A shows that array M33 had the lowest levels of noise, which perhaps explains why M33 had the lowest percentage of present genes (Figure 12A), but the highest average intensity values (Figure 12B). The average background intensity (relative intensity units) followed a similar trend as the noise values (Figure 13B).

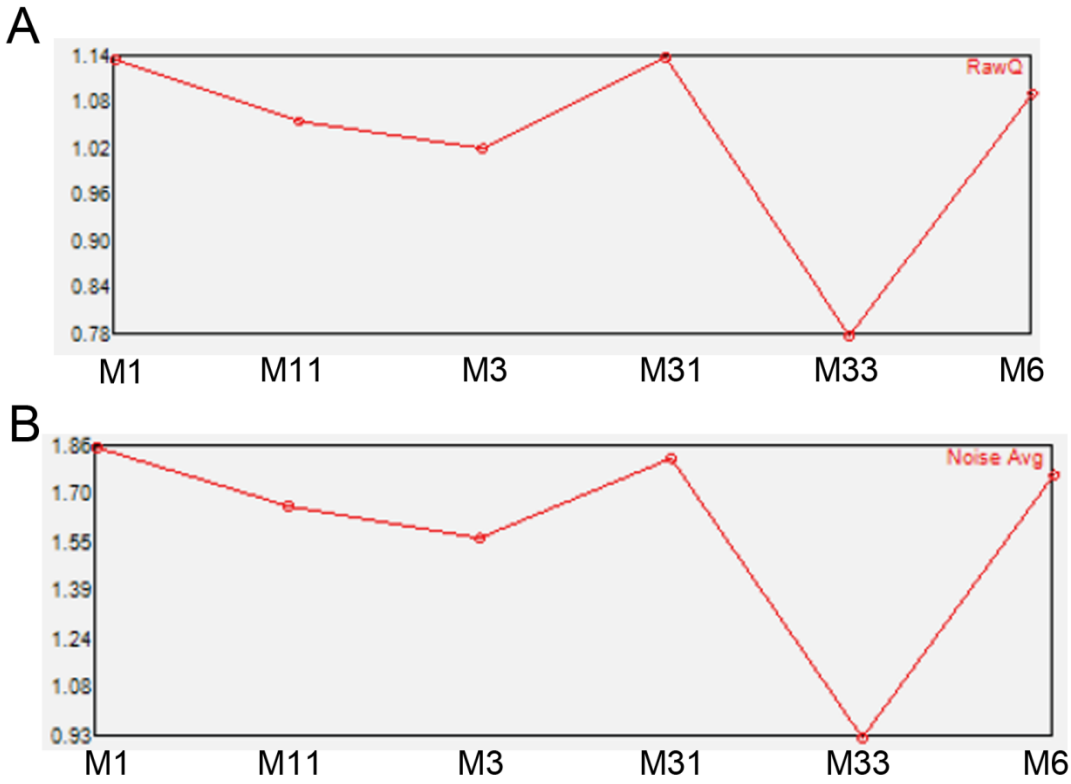

Figure 13 – Noise present in each array. (A) RawQ data is generated by Expression Console software from the degree of pixel-to-pixel variation among probe sets used to calculate noise, or background levels of signal. Noise levels are comparable across arrays, with M33 showing a reduced level of noise compared to the other arrays. (B) The average noise signal intensity for each probe array.

During the RNA amplification process, the 3':5' ratios for each mRNA strand become skewed. This is due to the less than 100% efficiency of the enzymes during replication, resulting in slightly shortened mRNA strands. Figure 14 shows the 3':5' skewing in housekeeping genes, GAPDH (Figure 14A) and β-actin (Figure 14B). In both GAPDH and β-actin, there is a higher signal intensity (relative intensity units) in probes that detect the 3' end of the mRNA strand (Figure 14). However, this does

not represent a significant issue in terms of probe detection, as the array chips used are Mouse Genome 430 2.0 arrays, in which the majority of probes are designed to detect the 3' end of the mRNA strand. From these data, the arrays were considered of sufficient quality to continue with gene expression analysis. Additionally, 3':5' skewing of probe set signals appear to be comparable between all probe arrays (Figure 14).

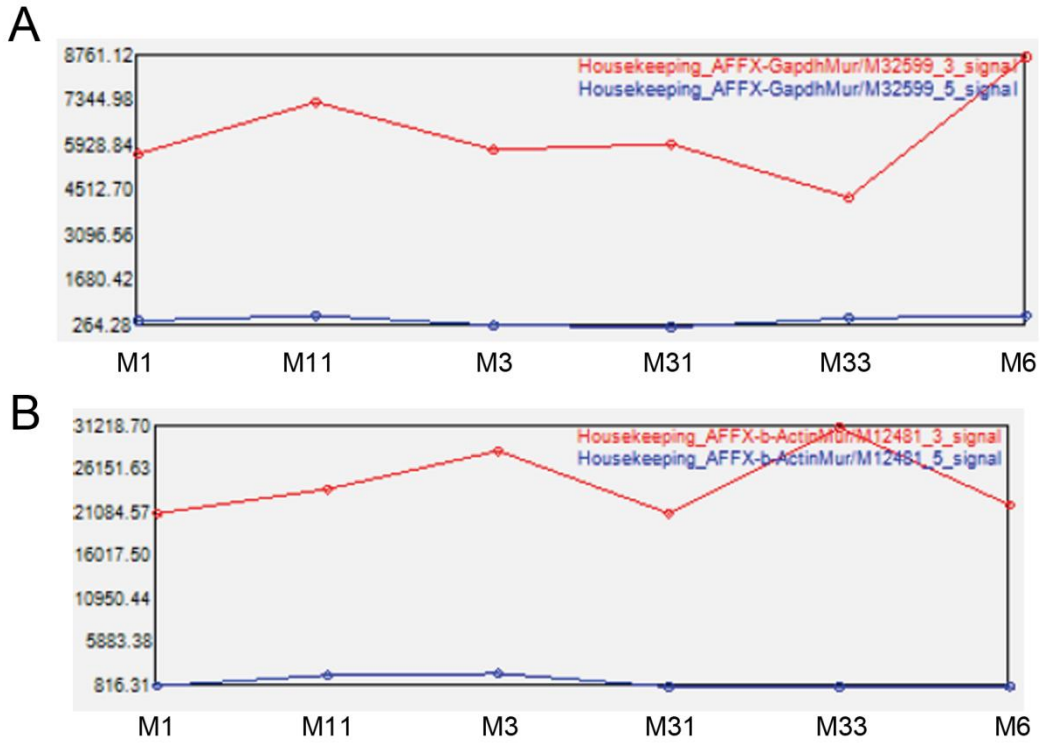

Figure 14 – 5':3' skewing graphs (A) Signal intensities for 3' GAPDH probe sets (red) and 5' GAPDH probe sets (blue). The signal intensity for the 5' GAPDH probe sets is lower than that of the 3' probe sets due to the 3':5' skewing induced by aRNA amplification rounds. (B) Signal intensities for 3' β-actin probe sets (red) and 5' β-actin probe sets (blue). The signal intensity for the 5' β-actin probe sets is lower than that of the 3' probe sets, following the same trend as the GAPDH signal intensities. However, as the vast majority of probe sets on the GeneChip Mouse

Genome 430 2.0 Array Probe are designed against the 3' end of the RNA fragments, this 3':5' skewing will not influence the gene expression ratios produced.

Expression Console data shown here demonstrates that the probe arrays are all comparable in terms of signal intensity, number of probe sets present, housekeeping gene expression, noise levels and 3':5' skewing of RNA. This confirms that hybridization, staining and scanning of probe arrays did not introduce any significant degree of variation into the signal intensities and any changes in gene expression found from the microarrays is due to a difference in gene expression rather than divergence of an entire probe array.

3.3.6 - Microarray Data Analysis

The .CEL files generated from the microarray were then uploaded onto QIUcore software for PLIER normalisation and analysis of gene expression. After normalisation, principal component analysis (PCA) graphs were generated showing that the gene expression profiles of the three vulnerable motor units, and three resistant motor units clustered together (Figure 15). This shows that the gene expression profiles of motor neurons cell bodies of vulnerable motor units are more similar to each other than to the gene expression profiles of motor neuron cell bodies of resistant motor units, and vice versa (Figure 15).

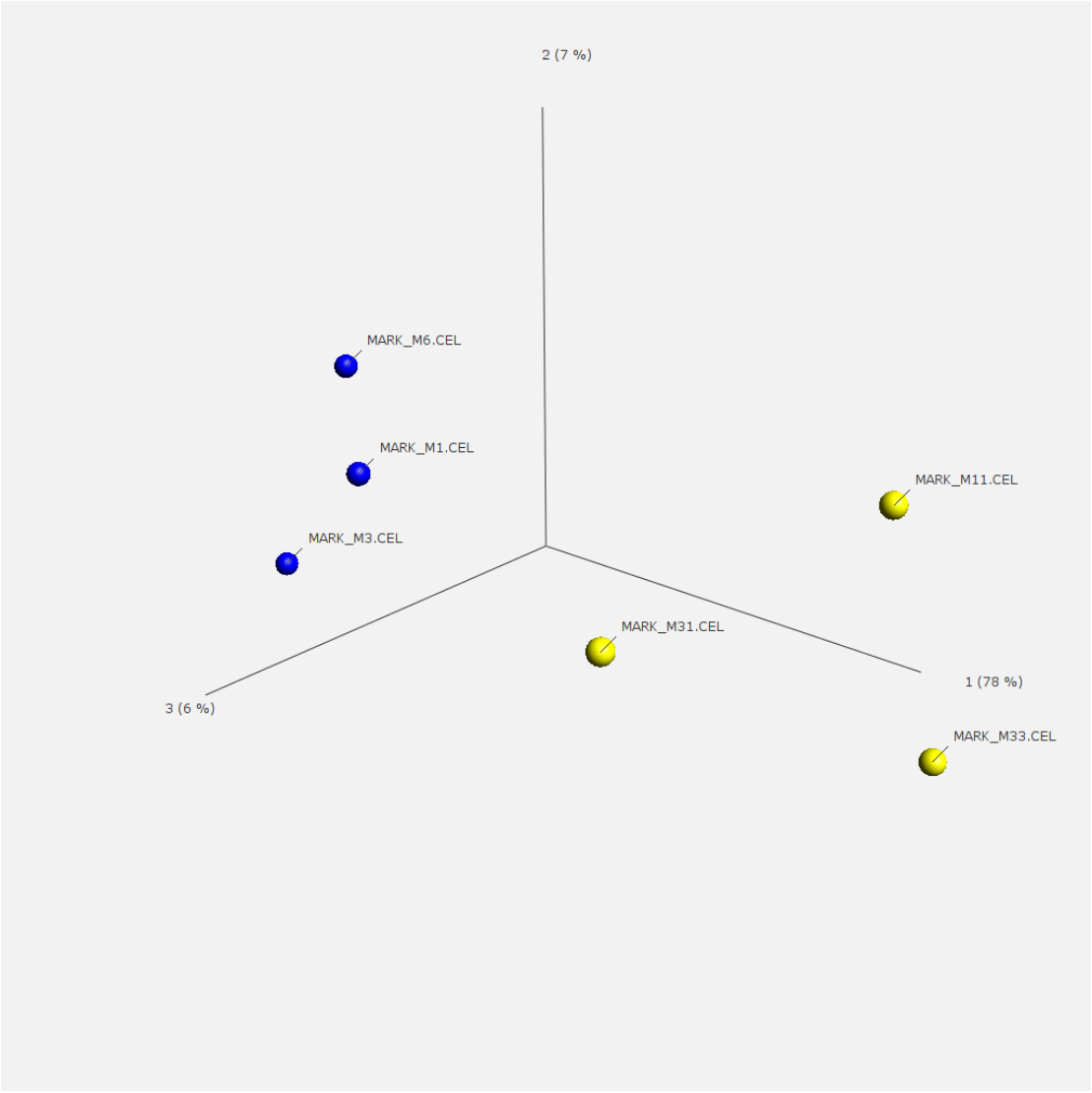

Figure 15 – PCA graph of probe arrays after PLIER normalisation. PCA is a mathematical algorithm that reduces the complexity of data. PCA identifies principle components in which the data varies. By using a few of these components, each sample can be plotted onto a 3D graph, in order to visually assess how similar the samples are. Samples that are similar will appear to group together. Here, gene expression profiles of motor neuron cell bodies that innervate the TA are represented in blue, and appear to cluster closely together. Gene expression profiles of motor neuron cell bodies that innervate the EDL are represented in yellow and also appear

to cluster together, somewhat separately from the motor neurons that innervate the TA.

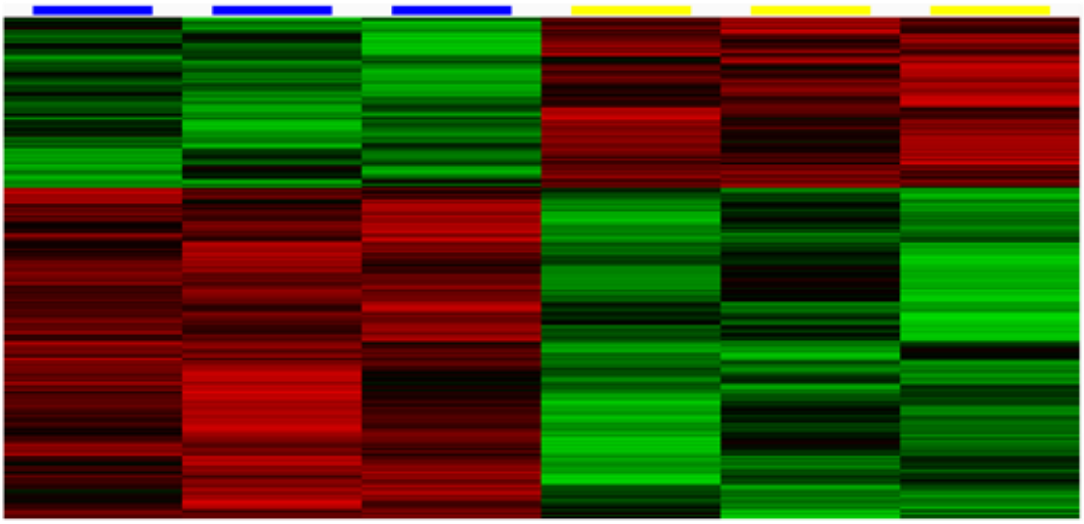

Figure 16 – Heat map of gene expression differences. This heat map shows the relative gene expression of 1029 genes which were found to be significantly altered between vulnerable and resistant motor units. Green represents genes which are down-regulated, while red signals an up-regulation of gene expression. Columns headed in blue represent the relative gene expression profiles of array probes of vulnerable motor units (M1, M3 and M6). Columns headed in yellow represent the relative gene expression profiles of array probes of resistant motor units (M11, M31 and M33).

From the QIUcore software analysis, a list of 1029 genes was identified as being significantly differentially expressed between the two groups of motor units (Figure

16). 343 genes were significantly up-regulated in the resistant motor neurons (motor neurons that innervated the EDL); and 686 genes were significantly up-regulated in vulnerable motor neurons (motor neurons that innervated the TA). A heat map of significantly up- or down-regulated genes ($p \leq 0.05$) was also generated from the QIUcore software (Figure 16).

In order to produce a robust list for pathway analysis and gene searching, a filtered list was created (Figure 17). First, the ratios of gene expression between significantly altered genes were produced, with ratios over 1 representing genes up-regulated in the resistant motor units; and ratios lower than 1 representing genes up-regulated in the vulnerable motor units (Figure 17). Next, genes that had a fold change of 20% or less were removed from the list (Figure 17). The remaining genes represented a robust list of 196 genes which were significantly altered between the two groups of motor neurons.

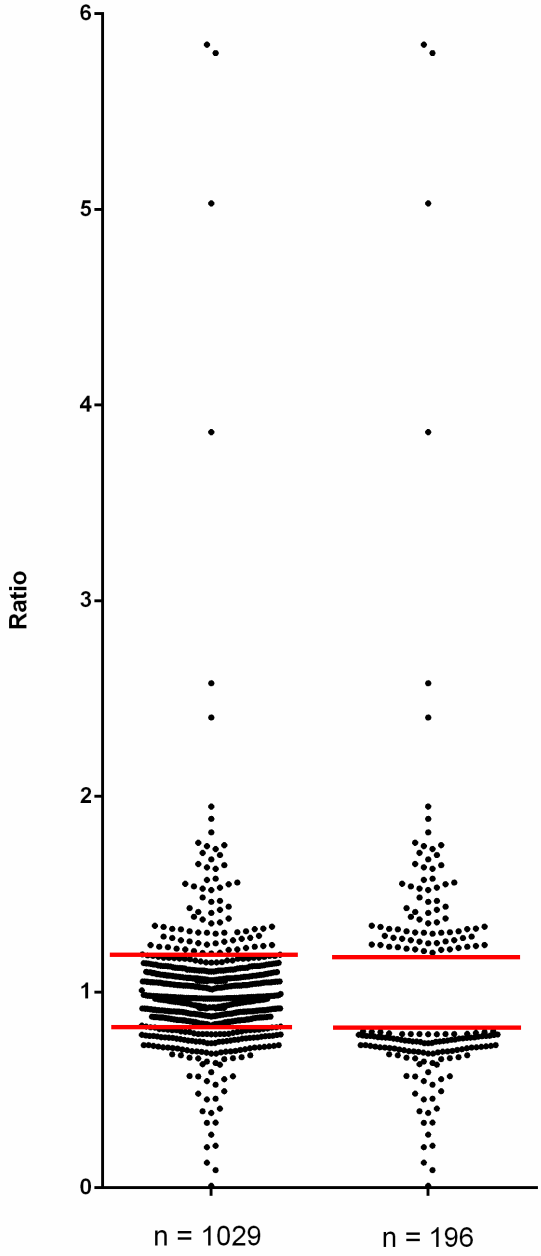

Figure 17 – Scatter plot of ratios of differentially expressed genes. The ratios of differentially expressed genes were plotted with each dot representing a different gene which was found to be significantly up- or down-regulated in vulnerable or resistant motor units. Ratios above 1 represent genes that were up-regulated in resistant motor units, while ratios below 1 represent genes that were up-regulated in

vulnerable motor units. Genes that had a ratio of less than 1.2 and more than 0.8 were removed from analysis. This represents a 20% change cut-off for genes to be included in analysis. Of the 1029 genes that were significantly altered between vulnerable and resistant motor units, 196 genes were also more than 20% up- or down-regulated. This filtered list of 196 genes was used for pathway analysis and in the literature search.

The top 25 genes that were significantly and more than 20% up-regulated in the resistant motor units are listed in Table 8; and the top 25 genes that were significantly and more than 20% up-regulated in the vulnerable motor units are listed in Table 9. A full table of altered genes can be found in Supplementary Tables 1 and 2. The full lists of genes were used for pathway analysis using IPA software and were also subjected to a thorough manual literature search.

Gene Name	Gene Symbol	Ratio	p Value
uncharacterized LOC100861869	LOC100861869	5.84	0.0156
expressed sequence C87122	C87122	5.79	0.0316
keratin 14	Krt14	5.03	0.0088
cDNA sequence BC021785	BC021785	3.86	0.0134
listerin E3 ubiquitin protein ligase 1	Ltn1	2.57	0.0478
RIKEN cDNA 2810429I04 gene	2810429I04Rik	2.40	0.0003
schlafen 10, pseudogene	Slfn10-ps	1.94	0.0255
cyclin B1	Ccnb1	1.88	0.0360
RIKEN cDNA 4932429P19 gene	4932429P19Rik	1.81	0.0110
aldo-keto reductase family 1, member C20	Akr1c20	1.76	0.0437
---	---	1.75	0.0299
basic helix-loop-helix family, member a9	Bhlha9	1.74	0.0158
RIKEN cDNA 5830490A04 gene	5830490A04Rik	1.73	0.0368
RIKEN cDNA 9430031J08 gene	9430031J08Rik	1.71	0.0021
eosinophil-associated, ribonuclease A family, member 11	Ear11	1.70	0.0253
protease, serine, 37	Prss37	1.67	0.0417
---	---	1.65	0.0360
nuclear factor, erythroid derived 2, like 2	Nfe2l2	1.64	0.0009
---	---	1.63	0.0338
ankyrin repeat domain 55	Ankrd55	1.63	0.0312
tumor necrosis factor (ligand) superfamily, member 13b	Tnfsf13b	1.57	0.0497
---	---	1.57	0.0169
toll-like receptor 7	Tlr7	1.55	0.0498
zinc finger and AT hook domain containing	Zfat	1.55	0.0472
platelet-activating factor receptor	Ptafr	1.55	0.0240

Table 8 – The top 25 most up-regulated genes in resistant motor units.

Gene Name	Gene Symbol	Ratio	p Value
---	---	100.70	0.0009
epidermal growth factor receptor	Egfr	10.99	0.0030
---	---	7.77	0.0097
multiple endocrine neoplasia 1	Men1	4.80	0.0268
angiopoietin-like 3	Angptl3	4.65	0.0389
RIKEN cDNA 1700108M19 gene	1700108M19Rik	3.67	0.0014
ryanodine receptor 1, skeletal muscle	Ryr1	3.00	0.0215
purinergic receptor P2Y, G-protein coupled 2	P2ry2	2.99	0.0273
angiogenin, ribonuclease A family, member 2	Ang2	2.60	0.0307
interferon activated gene 202B	Ifi202b	2.55	0.0063
DENN/MADD domain containing 2D	Dennd2d	2.46	0.0094
tubulin, beta 4B class IVB	Tubb4b	2.21	0.0047
elongation factor RNA polymerase II 2	Ell2	2.19	0.0246
piwi-like homolog 1 (Drosophila)	Piwil1	2.07	0.0140
erythrocyte protein band 4.1-like 4b	Epb4.1l4b	2.02	0.0433
G protein-regulated inducer of neurite outgrowth 1	Gprin1	1.89	0.0316
RIKEN cDNA 1700120E14 gene	1700120E14Rik	1.83	0.0327
RIKEN cDNA 4633402D09 gene	4633402D09Rik	1.80	0.0406
Casitas B-lineage lymphoma	Cbl	1.75	0.0099
nidogen 1	Nid1	1.75	0.0232
DNA segment, Chr 2, Brigham & Women's Genetics 1423 expressed	D2Bwg1423e	1.75	0.0377
ubiquitously transcribed tetratricopeptide repeat gene, Y chromosome	Uty	1.69	0.0475
bone marrow stromal cell antigen 1	Bst1	1.58	0.0324
piwi-like homolog 4 (Drosophila)	Piwil4	1.58	0.0330
ATP-binding cassette, sub-family G (WHITE), member 5	Abcg5	1.56	0.0157

Table 9 – The top 25 most up-regulated genes in vulnerable motor units.

3.3.7 - Pathway Analysis

The list of significantly altered genes was subjected to pathway analysis in order to identify specific networks which contained significant numbers of differentially expressed genes. This analysis may help identify particular pathways that, while still functional in both motor pools, may be altered in such a way that they react differently when SMN protein is reduced. This may help explain why some motor pools are better able to cope with the stresses placed upon motor neurons when faced with a reduction in SMN protein.

IPA Pathway Analysis software was used to identify altered networks of genes between the two sets of motor neurons, based on interactions of the proteins that they code. A list of genes that were significantly different between the two groups of motor neurons ($p \leq 0.05$) and were more than 20% up- or down-regulated was submitted to the IPA software for analysis. The ratio denoted the magnitude of change for each gene, with ratios above 1 denoting genes up-regulated in the resistant motor units; and ratios less than 1 denoting genes that were up-regulated in the vulnerable motor units. From this initial list of 196 genes, 149 could be mapped into protein networks by the IPA software. Protein networks were identified that contained either direct or indirect interactions between proteins, and had been confirmed by experimental observation. The IPA software identified five Molecular and Cellular Functions pathways that contained significant numbers of altered genes (Table 10). Of these five pathways identified, all have been shown to be perturbed in SMA (Young et al., 2002; Oprea et al., 2008; Wishart et al., 2010; Nölle et al., 2011; Rathod et al., 2012).

Pathway	P Value	Number of Molecules	Percentage of Gene List	Reference
Cell-to-cell signalling and interaction	4.33E-06 – 1.26E-02	27/149	18.12%	Rathod et al., 2012
Cellular Assembly and Organisation	4.33E-06 – 1.26E-02	9/149	6.04%	Oprea et al., 2008
Cellular Movement	3.86E-05 – 1.26E-02	27/149	18.12%	Nölle et al., 2011
Cell Death and Survival	2.11E-04 – 1.26E-02	19/149	12.75%	Young et al., 2002
Cellular Development	2.49E-04 – 1.26E-02	46/149	30.87%	Wishart et al., 2010

Table 10 – Molecular and Cellular Functions pathways that were identified as containing differentially expressed genes, according to IPA software.

IPA software analysis also identified Physiological System Development and Function pathways that contained significant numbers of altered genes between the two groups of motor neurons (Table 11). Each of the pathways identified were related to SMA. 16.77% of genes in the list uploaded to IPA software related to the pathway Skeletal and Muscular System Development and Function (Shanmugarajan et al., 2007). Additionally, 23.48% of the gene list was involved in pathways relating to Organ Development. This finding was particularly interesting, as SMA is known

to have effects on internal organs such as the heart and spleen (Menke et al., 2008; Hamilton & Gillingwater, 2013; Shababi et al., 2013).

Pathway	P Value	Number of Molecules	Percentage of Gene List	Reference
Skeletal and Muscular System Development and Function	1.25E-05 – 1.26E-02	25/149	16.77%	Shanmugarajan et al., 2007
Connective Tissue Development and Function	1.25E-05 – 1.26E-02	22/149	14.76%	Rathod et al., 2012
Organ Development	1.25E-05 – 1.26E-02	35/149	23.48%	Shababi et al., 2013

Table 11 - Physiological System Development and Function pathways that contained differentially expressed genes, according to IPA software.

Figure 19 shows an example of a protein pathway that was identified as containing a large proportion of altered genes, in a Skeletal and Muscular System Development and Function pathway. This pathway was particularly interesting, as an obvious central protein could be identified, ubiquitin C, which directly interacts with several of the genes that were altered between resistant and vulnerable motor units (Figure 18). Ubiquitin-related proteins are of interest with relation to SMA because recently

an interaction between ubiquitin-related proteins and SMN protein has been reported (Hsu et al., 2010; Han et al., 2012; Kwon et al., 2013).

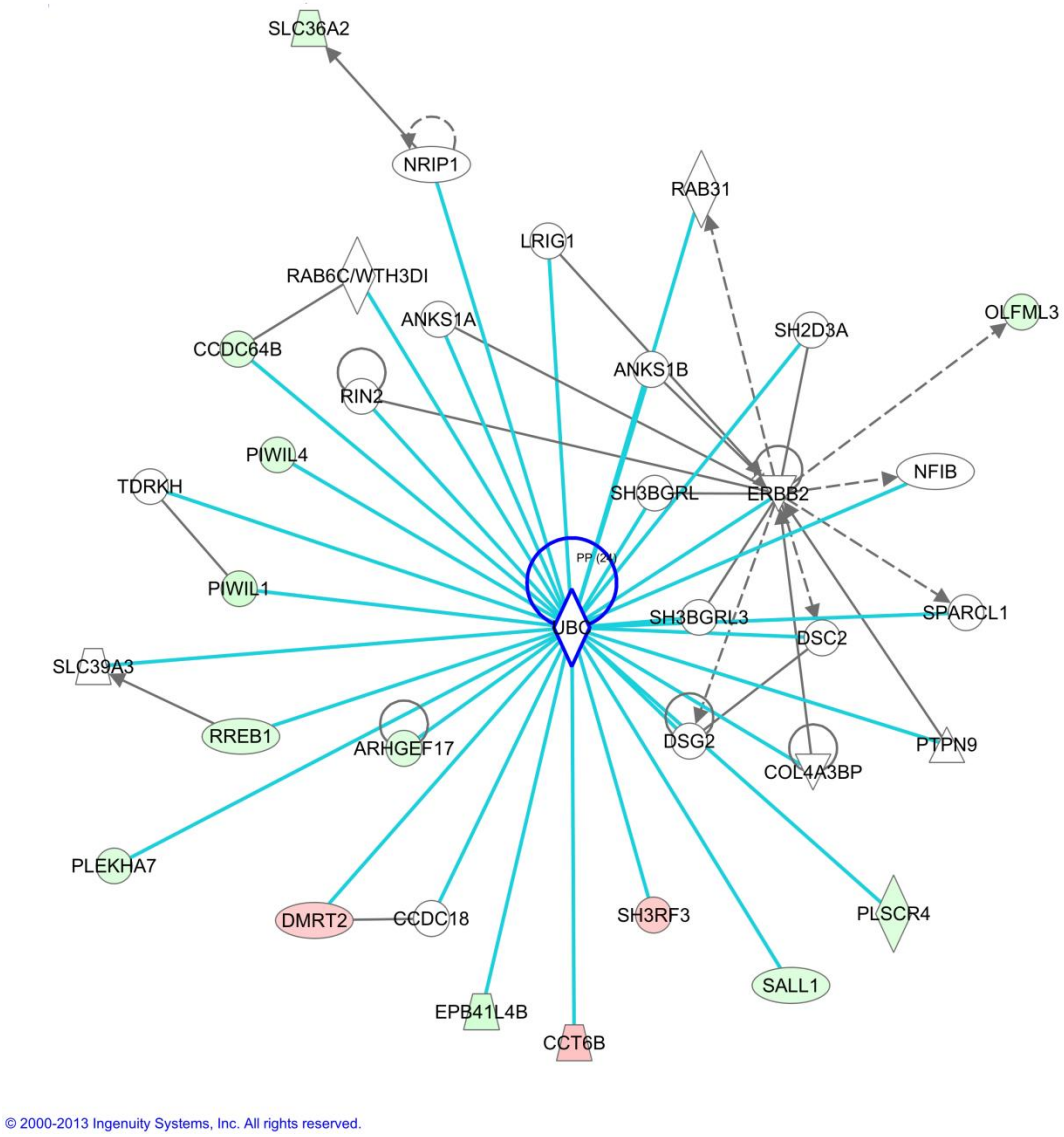

Figure 18 – Protein pathway identified by IPA software analysis. IPA software analysis mapped a pathway in which several genes which were significantly and by more than 20% altered between vulnerable and resistant motor units were involved. This pathway shows that several of the proteins produced by genes named in the robust filtered list directly interact with ubiquitin C. Proteins denoted in red represent genes found to be significantly up-regulated in resistant motor units,

whereas proteins denoted in green represent genes found to be significantly up-regulated in vulnerable motor units. Proteins in white represent genes which are part of this pathway but were not identified as being significantly changed in the microarray.

3.3.8 – Neuro-Protective and Neuro-Detrimental Genes

The list of significantly altered genes was subjected to detailed literature search analysis in order to identify individual genes which may have previously been implicated in neuro-degeneration or neuro-protection; have an involvement in cell death pathways; or an association with the synapse. Each gene was investigated individually, by conducting a manual literature search using the NCBI PubMed database. The findings of this literature search generated a list of genes up-regulated in resistant or vulnerable motor units which were considered to be of interest. These genes were then rated out of five stars, to denote which genes were of most interest for further studies.

A five star rating was awarded to genes that had previously been shown to have a direct influence on neuro-degeneration or neuro-protection, or were known to directly interact with SMN protein. A four star rating was awarded to genes that had previously been shown to been involved in cell death or apoptosis pathways, or had been implicated to interact with SMN protein. A three to one star rating was awarded to genes that had weaker links to the cell death pathway, had an influence on neuro-degeneration, or had an involvement at the synapse. Genes which had a larger number of publications linking them to neuronal or cell death were given a higher star rating.

Gene Name	Gene Symbol	Ratio	p Value	Rating
listerin E3 ubiquitin protein ligase 1	Ltn1	2.57	0.04789	*****
nuclear factor, erythroid derived 2, like 2	Nfe2l2	1.64	0.00095	*****
chaperonin containing Tcp1, subunit 6b (zeta)	Cct6b	1.46	0.01739	*****
N-ethylmaleimide sensitive fusion protein attachment protein beta	Napb	1.53	0.02820	*****
BCL2-like 11	Bcl2l11	1.26	0.02869	*****
cyclin B1	Ccnb1	1.88	0.03609	****
protease, serine, 37	Prss37	1.67	0.04170	****
chemokine (C-X-C motif) receptor 5	Cxcr5	1.30	0.02004	****
toll-like receptor 7	Tlr7	1.55	0.04988	***
zinc finger and AT hook domain containing	Zfat	1.55	0.04726	***
STE20-related kinase adaptor alpha	Strada	1.32	0.03990	***
cytochrome P450, family 17, subfamily a, polypeptide 1	Cyp17a1	1.29	0.00871	***
calcium/calmodulin-dependent protein kinase IV	Camk4	1.22	0.03863	***
nebulin	Neb	1.52	0.01180	**
MORN repeat containing 1	Morn1	1.33	0.02228	*
tumor necrosis factor receptor superfamily, member 11a	Tnfrsf11a	1.22	0.03777	*
linker for activation of T cells family, member 2	Lat2	1.21	0.02914	*

Table 12 - Genes that were identified as genes of interest, generated from a literature search of genes that are more than 20% up-regulated in motor units resistant to SMA.

Gene Name	Gene Symbol	Ratio	p Value	Rating
epidermal growth factor receptor	Egfr	10.996748	0.003065	*****
angiogenin, ribonuclease A family, member 2	Ang2	2.6098124	0.030703	****
purinergic receptor P2Y, G-protein coupled 2	P2ry2	2.9968904	0.027308	****
DENN/MADD domain containing 2D	Dennd2d	2.4693437	0.009495	****
solute carrier family 38, member 5	Slc38a5	1.456894	0.027874	****
signal transducer and activator of transcription 1	Stat1	1.4444052	0.043592	****
ADP-ribosyltransferase 3	Art3	1.3701618	0.036438	****
carnosine dipeptidase 1 (metallopeptidase M20 family)	Cndp1	1.302297	0.046738	****
caspase 4, apoptosis-related cysteine peptidase	Casp4	1.2396865	0.046496	****
integrin alpha 4	Itga4	1.2373559	0.03353	****
ryanodine receptor 1, skeletal muscle	Ryr1	3.0068712	0.02152	***
nidogen 1	Nid1	1.753184	0.023204	***
golgin, RAB6-interacting	Gorab	1.4388443	0.030606	***
nuclear receptor subfamily 2, group F, member 2	Nr2f2	1.3407696	0.047936	***
dual specificity phosphatase 23	Dusp23	1.5099871	0.023197	**
follistatin	Fst	1.3958034	0.030996	**
interleukin 7 receptor	Il7r	1.2936924	0.049496	**
ArfGAP with GTPase domain, ankyrin repeat and PH domain 1	Agap1	1.2835385	0.028188	**
AHNAK nucleoprotein (desmoyokin)	Ahnak	1.2714255	0.034136	**
G protein-coupled receptor 126	Gpr126	1.2063884	0.040024	**
ceruloplasmin	Cp	1.4014308	0.034951	*
bone marrow stromal cell antigen 1	Bst1	1.5892216	0.032415	*
sema domain, immunoglobulin domain (Ig), transmembrane domain (TM) and short cytoplasmic domain, (semaphorin) 4D	Sema4d	1.3914891	0.027624	*

Table 13 - Genes that were identified as genes of interest, generated from a literature search of genes that are more than 20% up-regulated in motor units vulnerable to SMA.

Of the genes which were significantly and more than 20% up-regulated in resistant motor units, 17 genes were identified which had previously been implicated in neuro-degeneration or neuro-protection, had an involvement in cell death pathways, or had an association with synapses (Table 12). Five of these 17 genes were noted as being of particular interest, denoted by their five stars ranking in Table 12. In vulnerable motor units, 23 genes of interest were identified in a literature search (Table 13). Only one of these genes, *Egfr*, was noted as being of particular interest, with a five star rating (Table 13). However, nine genes were considered to be worthy of further investigation, and awarded four star ratings (Table 13).

3.4 - Discussion

The findings of this chapter show that vulnerable and resistant motor units have distinct molecular properties, which may cause their differing vulnerabilities to SMA pathology. In this chapter, motor neuron cell bodies that had previously been identified as belonging to vulnerable or resistant motor units were successfully labelled with a retrograde tracer. Next, these labelled motor neuron cell bodies were identified in the spinal cord and isolated using laser capture micro-dissection. RNA was then successfully extracted from the cells and amplified for use in microarray analysis. Microarrays were performed and the results analysed using QIUcore software. The list of significantly altered genes between the two groups of motor

neurons was refined according to the magnitude of the fold change in order to produce a robust list for in depth analysis. This refined list was then subjected to IPA Pathway Analysis where several pathways of interest were identified such as Cellular Development, Cell-to-Cell Signalling, Organ Development and Connective Tissue. In particular, a specific pathway was identified from Skeletal and Muscular System Development and Function, where several altered genes directly interacted with ubiquitin C. Ubiquitin has previously been identified as being involved in SMA through an interaction between ubiquitin-related proteins and SMN protein (Hsu et al., 2010; Han et al., 2012; Kwon et al., 2013). Also, a list of individual genes of interest was generated from the refined list by performing a literature search. Several genes were identified that have been previously implicated in neuro-degeneration or neuro-protection that may represent new therapeutic drug targets for SMA.

Importantly, *Smn* mRNA transcripts were not found to be significantly altered between vulnerable and resistant motor units. This is an important finding, as the vulnerability spectrum observed in motor units could potentially be explained by different levels of SMN protein expression. However, no significant difference in *Smn* expression was found, providing evidence that differential motor unit vulnerability in SMA is not driven by varying levels of full length SMN protein.

3.4.1 - Functional Pathway Analysis in Vulnerable and Resistant Motor Units

IPA software analysis identified several functional pathways that were altered between vulnerable and resistant motor units. These pathways can be linked to SMA pathologies, and several of the pathways and their relevance to SMA are discussed

below. While the pathways identified by the IPA software undoubtedly link with SMA pathologies, the precise molecular mechanisms underlying motor unit vulnerability or resistance cannot be elucidated from this type of analysis. However, pathway analysis does serve as an important guide to mechanisms and pathways that may underlie motor unit vulnerability.

3.4.1.1 - Cellular Development

Of the 149 genes which could be mapped to functional networks by the IPA software, 30.87% of these genes were found in pathways involved in Cellular Development. There are many examples of alterations in cellular development pathways in SMA, particularly in pathways controlling axon guidance and maturation. Reduced axon outgrowth and growth cone size has been reported in primary motor neuron cultures from mouse models of SMA (Rossoll et al., 2003). In SMA Drosophila models, axons display guidance defects and abnormal arborisation (Rajendra et al., 2007) and the motor axons of SMA zebrafish are characterised as being abnormally short with excessive branching (Gassman et al., 2013; Hao et al., 2013; Sleigh et al., 2013). Also in zebrafish, Hao et al. (2013) demonstrated that SMN protein is required for normal motor neuron development. By conditionally inducing SMN expression in *smn* mutant fish, Hao et al. (2013) were able to rescue the developmental motor neuron defects, but only when SMN protein was induced soon after motor neurons were born. SMN complex activity has also shown to be developmentally regulated in healthy mice, with the complex being most active during embryonic development, and declining after P10 (Gabanella et al., 2005). A

study by Liu et al. (2009) revealed neurodevelopmental alterations in a severe mouse model of SMA, with apoptosis being increased in the telencephalon of developing embryos and truncation of the lumbar and facial nerves being observed. Additionally, perinatal brain development has been shown to be altered in an SMA mouse model, with decreased cell density in the hippocampus and a decrease in neurogenesis (Wishart et al., 2010). Also, a delay in maturation of the motor endplate of the neuromuscular junction has been observed in several mouse models of SMA, which could be due to altered signalling from the nerve terminals (Kariya et al., 2008; Kong et al., 2009; Lee et al., 2011). Based on the high percentage of genes altered between vulnerable and resistant motor neurons belonging to pathways involving cellular development, and the evidence that SMN protein is involved in developmental processes, it seems likely that differences in developmental pathways in different groups of motor neurons could contribute to variations in motor neuron vulnerability in SMA.

3.4.1.2 - Cellular Assembly and Organisation

IPA software analysis identified 9 genes which are altered between vulnerable and resistant motor units as being involved in Cellular Assembly and Organisation pathways. Perturbation in cell organisation has been linked to SMA by filamentous actin. SMN protein has been shown to form complexes with proteins and transport mRNA for β-actin (the monomer of filamentous actin) along the axon (Rossoll et al., 2003). Filamentous actin is an important component of the cytoskeleton in nerve terminals, where it is involved in synaptic vesicle recycling (Shupliakov et al., 2002),

caging synaptic vesicles to the reserve pool and transporting them to the active zone (Bleckert et al., 2012). Studies in SMA mouse models have shown a reduction in synaptic vesicle density throughout the nerve terminal and specifically at the active zone (Kong et al., 2009). Importantly for this study, examples of alterations to Cellular Assembly and Organisation pathways being protective in SMA already exist. The filamentous actin bundling protein, plastin 3, has been identified as a protective factor for SMA in humans (Oprea et al., 2008). High levels of plastin 3 appeared to confer protection on individuals, who despite having a homozygous deletion of *SMN1*, did not develop SMA (Oprea et al., 2008). Plastin 3 has also shown to rescue axon growth defects in primary cultured cells with reduced SMN levels (Oprea et al., 2008) and in zebrafish models of SMA (Hao et al., 2012). However, the protective effects of Plastin 3 alone are likely to be limited, as a mouse model of SMA which also ubiquitously over-expressed Plastin 3 showed an increase in muscle fibre diameter, endplate size, and the number of fully occupied endplates, but no increase in lifespan, motor activity or weight gain (Ackermann et al., 2013). While Plastin 3 was not identified as being altered between resistant and vulnerable motor units in this study, it may be possible that another gene belonging to this functional category may also convey protection on motor neurons via the cytoskeleton.

3.4.1.3 - Cell Death and Survival

IPA software analysis of the microarray results showed that 19 genes were involved in Cell Death and Survival pathways. Interactions between SMN protein and

apoptotic-regulators have been reported previously, such as a direct interaction between SMN protein and the pro-apoptotic gene *p53* (Young et al., 2002). Young et al. (2002) showed that SMN protein interacts with P53 and when P53 is activated they co-localised in Cajal bodies. In the fibroblasts of SMA patients where SMN protein expression was significantly reduced, P53 was found to localise in the nucleus leading Young et al. (2002) to hypothesise that aberrant P53 signalling in SMA could lead to inappropriate activation of cell death pathways. To test this theory Tsai et al. (2006) crossed a *p53* knockout mouse with a severe SMA mouse line and disappointingly found no increase in life span or reduction in disease severity. However in the same year Tsai et al. also crossed their severe SMA mouse model with a different pro-apoptotic gene knockout mouse, *Bax*. Here, they found that there was a modest increase in lifespan and an increase in the number of motor neurons in the spinal cords of $Smn^{-/-};Bax^{-/-};SMN2^{+/-}$ mice, with almost double the number of motor neuron cell bodies being present in $Smn^{-/-};Bax^{-/-};SMN2^{+/-}$ compared to SMA mice with endogenous BAX expression (Tsai et al., 2006). Also, in human foetal spinal cords, Soler-Botija et al. (2003) found that there was a decrease in the anti-apoptotic BCL-2 protein expression in 15 week spinal cords, and a delay in the expression of another anti-apoptotic protein, BCL-X. It may therefore be possible, that aberrant apoptosis induction occurring through distinct pathways may contribute to motor neuron degeneration in SMA. Alterations in the levels of individual apoptotic pathway components between groups of motor neurons may underlie differences in motor unit vulnerability.

3.4.1.4 - Ubiquitin C Pathway

A specific pathway of interest was found in the IPA software analysis that involved several differentially expressed genes directly interacting with *UbC*, a gene that codes for ubiquitin C, a poly-ubiquitin protein. Ubiquitin is a protein that is conjugated onto other proteins to tag them for degradation. Under stressful conditions, ubiquitin protein monomers are released from poly-ubiquitin proteins and used to tag proteins for degradation (Ryu et al., 2007). The genes, *UbB* and *UbC* code for the ubiquitin monomers that form the poly-ubiquitin proteins that are broken down under stressful conditions (Ryu et al., 2007).

Recently, an ubiquitin pathway was identified as being perturbed in a mouse model of SMA (Wishart et al., in press). Ubiquitin-like modifier activating enzyme (UBA1) protein was found to be down-regulated in a severe mouse model of SMA, compared to wild type mice (Wishart et al., In Press). Suppressing *uba1* expression in zebrafish embryos was sufficient to cause an SMA-like phenotype, with truncated motor axons and excessive axonal branching (Wishart et al., In Press). Additionally, both monomeric and multimeric ubiquitin protein levels were down-regulated in SMA mice compared to controls (Wishart et al., In Press).

The pathway identified by the IPA software shows that many of the differentially expressed genes directly interact with ubiquitin C, but the nature of these interactions is not documented. However, based on these results, and those of Wishart et al. (In Press) it may be possible that differences in the efficiency of poly-ubiquitin C protein degradation to monomeric ubiquitin under stressful conditions is different between

vulnerable and resistant motor units, allowing resistant motor units to better cope with cellular stresses induced by a reduction in SMN protein.

3.4.2 - Individual Genes of Interest

The analysis of individual genes which were found to be altered between vulnerable and resistant motor units may provide a greater insight into specific molecular mechanisms underlying motor unit vulnerability in SMA than pathway analysis. For this reason, a literature search of significantly altered genes was conducted. Several of the genes identified as being of particular interest are discussed below.

3.4.2.1 - Ltn1

Ltn1 was first identified as a gene of interest due to its involvement in neuro-degeneration (Chu et al., 2009). A genome-wide mutagenesis screen carried out by Chu et al. (2009) produced a model mouse which developed age-dependent weakness of the hind limbs, loss of motor axons and had a shortened life span, with the mice living to only 2-3 months. Gene mapping identified a gene on chromosome 13, of previously unknown function, with an A-T transversion (Chu et al., 2009). This mutated gene, named *listerin1* (*Ltn1*), produced a protein missing 14 amino acids, and miss-spliced mRNA transcripts could be detected in the brain and spinal cord (Chu et al., 2009). LISTERIN protein was further characterised in the study, and was found to contain a RING finger domain at its C-terminus (Chu et al., 2009). RING finger containing proteins commonly function as E3 ubiquitin ligases

(Deshaies & Joazeiro, 2009), which suggests that LISTERIN protein is involved in the ubiquitination pathway (Chu et al., 2009). The microarray analysis showed that *Ltn1* gene expression was increased 2.57 fold in resistant motor units compared to vulnerable motor units in healthy mice. Based on this, and the fact that a reduction in full length *Ltn1* transcripts in mice leads to neuro-degeneration (Chu et al., 2009), it may be possible that LISTERIN protein has a neuro-protective effect in neurons. Interestingly, LISTERIN protein may also be involved in ubiquitination pathways which have also been identified as being perturbed in SMA mice (Chu et al., 2009; Hsu et al., 2010; Han et al., 2012; Kwon et al., 2013).

3.4.2.2 - Nfe2l2

Nfe2l2 (aka Nrf2) is an antioxidant response element that regulates expression of phase II detoxification enzymes (Joshi & Johnson, 2012). Under unstressed conditions, Nrf2 is associated with Keap1, ubiquitinated, and rapidly degraded (Joshi & Johnson, 2012). Under conditions of oxidative stress, this association with Keap1 is disrupted and Nrf2 is translocated to the nucleus where it can increase expression of detoxification enzymes, such as superoxide dismutase 1 (SOD1), among others (Joshi & Johnson, 2012). There is a growing body of evidence suggesting that oxidative stress plays a major role in many different neurodegenerative disorders, such as Alzheimer's disease (Ramsey et al., 2007; Kanninen et al., 2008; Nouhi et al., 2011), Parkinson's disease (Chen et al., 2009), and ALS (Sarlette et al., 2008; Neymotin et al., 2011). In Parkinson's disease mouse models, knocking out Nrf2 resulted in a greater loss of dopamine transporters in the striatum (Burton et al.,

2006). In Alzheimer's disease Nrf2 expression is reduced in the nucleus of hippocampal neurons (Ramsey et al., 2007). *In vitro* studies of Alzheimer's disease have shown that over-expression of Nrf2 protected against $A\beta_{1-42}$ neuronal death in cultured hippocampal cells (Kanninen et al., 2008). Animal models of Alzheimer's disease have also demonstrated the neuro-protective effects of Nrf2, with β-amyloid-injected rats showing a reduction in both β-amyloid accumulation and β-amyloid-induced apoptosis (Nouhi et al., 2011). In ALS, Nrf2 neuro-protective properties have also been reported (Sarlette et al., 2008; Neymotin et al., 2011). Post-mortem studies of human motor cortex and spinal cord revealed a down-regulation of both Nrf2 mRNA and protein (Sarlette et al., 2008). Also, in $SOD1^{G93A}$ mutant mice, administration of Nrf2 activators to the spinal cord significantly delayed the progression of symptoms and extended the lifespan of $SOD1^{G93A}$ mice (Neymotin et al., 2011).

Oxidative stress involvement in SMA pathology is less well characterised, with some evidence of oxidative damage to DNA being reported in post-mortem brain tissue of type I SMA patients (Hayashi et al., 2002). However, a study by Wan et al. (2008) demonstrates that there may be a link between oxidative stress and SMN protein. Wan et al. (2008) showed in HeLa cells, that SMN complex activity is reduced by reactive oxygen species (ROS) in a dose dependent manner.

Based on these studies and the up-regulation of *Nfe2l2* mRNA in resistant motor units, it may be possible that higher baseline levels the neuro-protective *Nfe2l2* transcripts could underlie the resistance of some motor units to SMA pathology. It is possible that higher levels of Nrf2 in some motor units could result in lower levels of

ROS, thereby allowing SMN complex activity to function at levels necessary for normal motor neuron physiology.

3.4.2.3 - Egfr

Epidermal growth factor receptor (*Egfr*) mRNA was found to be up-regulated 10.99 fold in vulnerable motor units, compared to resistant motor units. Egfr belongs to a family of transmembrane receptors with intrinsic tyrosine kinase activity (Liu et al., 2006). Under normal conditions, Egfr is not present in mature astrocytes but Egfr and its ligands become rapidly up-regulated in astrocytes following damage to neurons, through ischemia, traumatic injury or in brains of Alzheimer's disease patients (Liu et al., 2006). It is the activation of the Egfr pathway that causes quiescent astrocytes to become activated (Liu et al., 2006). Importantly, *Egfr* mRNA transcripts have been found to be up-regulated 10-fold in the spinal cord of both ALS patients and $SOD1^{G93A}$ mouse models (Offen et al., 2009). Additionally, studies have shown that neuro-degeneration can be delayed using Egfr inhibitors (Le Pichon et al., 2013). In SMA, GFAP-positive astrocytes have been detected in both mouse models of SMA (Caraballo-Miralles et al., 2013) and human post-mortem tissue (Simic et al., 2008). It may be possible, therefore, that this higher base-line level of *Egfr* transcripts in some groups of motor neurons makes them more vulnerable, either to the toxic effects of reactive astrocytes in SMA or via the Egfr pathway being activated within the motor neurons themselves.

3.4.2.4 - Dennd2d

DENN/MADD domain contained 2D (*Dennd2d*) mRNA expression was found to be 2.47 times up-regulated in vulnerable motor units compared to resistant motor units in the microarray study. *Dennd2d* encodes a protein reported to induce apoptosis in non-small cell lung cancer (Ling et al., 2012). Ling et al. (2012) found that expression of *Dennd2d* mRNA and protein was reduced in non-small cell lung cancer cell lines and patient tumour tissue. By over-expressing *Dennd2d* via plasmid transfection, Ling et al. (2012) were able to inhibit the proliferation of non-small cell lung cancer cells *in vitro*, and suppress tumorigenicity in a xenograft assay in mice. They propose that DENND2D induces apoptosis by blocking MADD protein binding to the death domain of tumour necrosis factor receptor 1 (TNFR1), which leaves the death domain of TNFR1 free to activate cell apoptosis (Ling et al., 2012). Based on this study, it is possible that higher levels of the apoptosis-inducing factor DENND2D in some motor units may leave the cells more vulnerable to the stresses induced by a reduction in SMN protein.

3.4.2.5 - Slc38a5

The *Slc38a5* gene codes for the protein SNAT5 (aka SN2) which is an amino acid bidirectional transporter which binds to both glutamine and glycine and is found in glial cells in the brain, and other tissues (Cubelos et al., 2005). SNAT5 has recently been implicated in synaptic plasticity via regulation of NMDA receptors by a proposed mechanism of releasing glycine into the synaptic cleft to stimulate NMDA receptors under appropriate conditions (Hamdani et al., 2012).

Slc38a5 mRNA splicing is known to be altered in SMA (Zhang et al., 2008; Liu et al., 2010). A study by Zhang et al. (2008) revealed that SMN protein depletion results in alterations to ratios and miss-splicing of mRNAs in many different tissues. Zhang et al. (2008) show that *Slc38a5* is down-regulated almost three-fold in the spinal cord of *Smn$^{-/-}$;SMN2;Δ7* mice with alterations to 9 out of 16 of its exons, and two-fold in *Smn$^{-/-}$;SMN2;Δ7* brains with 5 out of 16 exons affected. Miss-splicing of *Slc38a5* transcripts was also found in embryos of a severe mouse model of SMA (Liu et al., 2010). In this study, higher levels of *Slc38a5* mRNA were found in vulnerable motor units compared to resistant motor units in healthy mice. This opens up the possibility that miss-spliced *Slc38a5* mRNA products are somehow detrimental to motor neurons.

3.4.3 - Further Work

In order to both validate the microarray and assess the neuro-protective effects of over- or under-expressing the identified genes, genes will be screened in a zebrafish model of SMA by an expert zebrafish laboratory in the near future. Briefly, genes found to be up-regulated in resistant motor units will be over-expressed using over-expression constructs which are introduced into the developing zebrafish embryos. Genes found to be up-regulated in vulnerable motor units will be knocked-down by injecting zebrafish embryos with oligonucleotide morpholinos. Morpholinos are anti-sense oligonucleotides that reduce gene expression by blocking transcription or modification of target mRNAs.

The efficacy of up- or down-regulating genes of interest will be measured using confocal analysis to analyse motor neuron branching patterns, from which the health of the motor neurons can be assessed. It is our hope that by up-regulating genes found in resistant motor units, or down-regulating genes found in vulnerable motor units in zebrafish motor neurons, the neuro-protective effects of these genes can be assessed. After screening in zebrafish, any genes that have been found to have a neuro-protective effect would then be tested in mouse models of SMA, most likely using drugs to inhibit or enhance target gene expression.

Zebrafish were chosen to screen genes for neuro-protective activity due to the relative ease with which zebrafish genomes can be manipulated. SMA models of zebrafish can be screened simply by the injection of morpholinos into the embryos, which are readily accessible, or by the addition of drugs into the water. Additionally, defects in zebrafish motor neurons are easily characterised and quantified, with characteristic truncated, excessively branched motor neurons being a hallmark of SMA pathology in zebrafish (Gassman et al., 2013; Hao et al., 2013; Sleigh et al., 2013).

3.4.4 - Study Weaknesses

One weakness of this study is that for vulnerable and resistant motor units, only one motor pool was analysed. In order to produce a more robust reliable list of candidate genes that could be implicated in motor unit vulnerability, a larger cohort of motor pools should be labelled and analysed. By analysing the gene expression of a larger number of motor pools on different ends of the vulnerability spectrum in SMA, we

could begin to identify genes or pathways that are common to all vulnerable, or all resistant, motor units. However, this was not possible in this study as almost all other muscles examined in Chapter 2 were extremely flat thin muscles which would have proved impossible to confidently inject with WGA tracer. The motor unit vulnerability of other large bellied accessible muscles would need to be determined before the gene expression of other motor pools could be analysed.

A major assumption in the IPA pathway analysis is that all the genes which are up- or down-regulated at the mRNA level, as identified by the microarray, are also up- or down-regulated at the protein level. Similarly, another assumption is that mRNAs that were not found to be changed between vulnerable and resistant motor units are not altered at the protein level. Ratios between mRNAs and proteins are determined by mRNA translation and protein degradation, with many factors influencing the rate at which these often independent processes occur (de Sousa Abreu et al., 2009). A meta-analytical study by de Sousa Abreu et al. (2009) revealed that there is a correlation, albeit a weak correlation, between mRNA and protein levels in bacteria, yeast, and human tissue. Based on this, we can assume that most of the genes identified as being up- or down-regulated in the microarray are also similarly altered at the protein level.

A lack of microarray validation, for example by real time quantitative PCR, is a weakness of this study. In preparation for RT-qPCR validation, primers were generated to assess the relative gene expression between RNA extracted from vulnerable and resistant motor units. However, after the microarray had been performed there was simply not enough RNA left over to perform PCRs. Instead, the microarray will be validated in a later study by screening these genes in

zebrafish. Plans to validate changes in protein levels of altered genes were also in place, but during the course of the experiment, it became evident that extracting appropriate quantities of protein from the labelled motor neuron cell bodies would not be possible.

3.4.5 – Conclusion

Based on the results obtained here, it seems likely that distinct molecular properties of motor units drive selective motor unit vulnerability in SMA. Whether this is due to differential expression of a single neuro-protective or neuro-detrimental gene; or due to the altered state of many protein pathways is yet to be determined. Further work examining the effects of over- or under-expressing individual genes in a zebrafish model of SMA will hopefully shed more light onto the molecular mechanisms of motor unit vulnerability in SMA. It is hoped that by altering expression of these individual genes, a protected status can be conveyed onto all motor units and potentially become a new therapeutic target for SMA.

Chapter 4: Identification of a peptide with potential synapse binding abilities using phage display.

4.1 - Introduction

Pathological changes that take place at the neuromuscular junction in SMA are well-characterised in mice, but comparatively little is known about these changes in human patients. A study by Martínez-Hernández et al. (2013) in aborted foetal tissue showed that there were changes in acetylcholine receptor clustering at the motor endplate; an abnormal distribution of vesicles in the nerve terminal; and an aberrant ultrastructure of the nerve terminal in pre-natal type I spinal muscular atrophy, compared to control tissue. Similarly, Karyia et al., 2008 found that approximately 70% of neuromuscular junctions in type I SMA patient biopsy tissue showed signs of pre-synaptic abnormalities.

Visualising synapses in humans is extremely difficult for a number of reasons. Synapses of the CNS are only ever available to study in post-mortem tissue, and in the case of SMA, this is mostly from elective termination of pregnancies (Martínez-Hernández et al., 2013). In other post-mortem tissues, synapses are at the end stage of disease which gives little insight into disease progression. Neuromuscular junctions are by far the most accessible synapse in humans but can only be accessed via invasive muscle biopsy procedures.

Importantly, the neuromuscular junction is not the only synapse to be affected in SMA: central nervous system synapses are also known to be affected (Ling et al., 2010; Park et al., 2010; Mentis et al., 2011; Gogliotti et al., 2012; Martinez et al., 2012). Mentis et al. (2011) demonstrated that vGlut1-positive synapses onto lower

motor neurons in the spinal cord were significantly reduced between wild type and *Smn*$^{-/-}$*;SMN2;Δ7* mice, implying a perturbation of proprioceptive feedback.

Observing synaptic breakdown *in vivo*, both in human patients and animal models of SMA, using a non-invasive technique would be hugely beneficial to our understanding of the degeneration process. Not only this, but it would allow us to view this dynamic process in real time and correlate synaptic changes with physical symptoms – a read-out likely to be extremely valuable in drug testing. Also, *in vivo* imaging of synapses would allow for a faster and more accurate diagnosis of not only SMA, but other motor neuron diseases as well. Based on this need, we sought a molecule that could transiently bind to synapses to label them. To create this molecule, we screened synaptic preparations with phage display libraries in the hope of identifying peptides that specifically bound to synaptic membranes.

Phage display libraries have been used in the past to screen for peptides that display a binding affinity to a protein of interest (Whitney et al., 2011; Wu et al., 2011). Bacteriophage (phage) are viruses that specifically infect and replicate inside bacterial cells. The M13 filamentous phage consists of a single stranded circular genome core that is surrounded by thousands of coat proteins (pVIII) (Rodi & Makowski, 1999). Clustered at one end of the phage are five copies of coat proteins pIII and pVI, which are involved in infecting the host cell by binding to the F-pilus (Rodi & Makowski, 1999). In 1985, Smith reported that phage particles could be manipulated to express a foreign peptide on the N-terminal of minor coat protein pIII by inserting a foreign DNA sequence into gene III of the phage genome (Smith, 1985). This technique was adapted to create phage display libraries, in which millions of random DNA sequences could be inserted into phage particles, resulting

in millions of phage particles each of which express a different random peptide on their surface (Cwirla et al., 1990).

Phage display libraries are "panned" using a protein of interest that is immobilised on a plastic surface or bead (Figure 1A). The library is incubated with the target protein to allow any fusion peptides with an affinity to the target protein to bind (Figure 1B). The unbound phage are washed away, the bound phage is then eluted and amplified in bacteria (Figure 1C). This creates a new phage display library that is enriched in phage particles that display fusion peptides with a binding affinity to the target protein. Panning is usually carried out three times to sufficiently enrich the library.

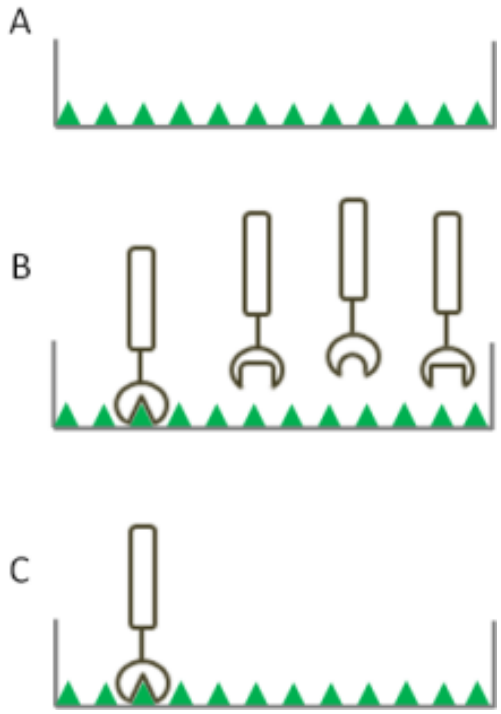

Figure 1 - Schematic of phage display panning principle. (A) A target protein is immobilised onto a surface, usually a cell culture plate or plastic bead. (B) The phage display library containing millions of phage particles is washed on to the

immobilised target. The phage particles each express a random fusion peptide of which there are millions of combinations. Some of these random fusion peptides may show a binding affinity with the target. (C) The unbound phage particles are washed away, leaving only the bound phage due to its binding affinity with the target. The bound phage can now be eluted from the target and amplified in bacteria to produce a new phage library. This new phage library will be enriched in phage particles that display a fusion peptide that has a binding affinity with the target protein.

Next, the DNA of individual phage clones is sequenced. Sequencing of phage clones reveals whether the library has indeed been enriched in phage particles that bind to the target protein, and also the DNA sequence of those peptides. Phage clones are isolated by infecting bacteria with the bound phage elute and culturing this bacteria on an agar plate. The bacteria form a homogeneous lawn that is interrupted by phage plaques. These plaques represent areas of diminished bacterial cell growth due to phage infectivity. These plaques are isolated from the agar plate and amplified individually in bacteria. The phage particles are then isolated and DNA is extracted from the phage and sequenced. An identical peptide can then be manufactured using the DNA sequence information.

Phage display libraries have previously been used to screen for peptides that could be used for transient *in vivo* imaging of the nervous system, specifically those that have a weak binding affinity to myelin protein (Whitney et al., 2011; Wu et al., 2011). The DNA sequence obtained from successive rounds of panning with myelin protein was used to manufacture a peptide with a conjugated fluorescent dye (Whitney et al., 2011; Wu et al., 2011). When this peptide was washed on to peripheral nerves of mice during surgery the nerve could be visualised in finer detail than with the naked

eye, allowing surgeons to avoid cutting fine nervous processes (Whitney et al., 2011; Wu et al., 2011). Importantly, the labelled peptide produced by Whitney et al. (2011) did not bind permanently to the myelin, with no fluorescent signal being observable 24 hours after application.

Using a similar approach, we sought to identify a peptide that displayed a weak binding affinity to the outer membrane of synapses. To be used for *in vivo* imaging, any candidate peptides would need to display a low affinity binding so that they could be easily washed away after imaging. The candidate peptide would also have to bind to a target present on the outer membrane of synapses so that it would not interfere with synapse function.

To do this, we used synaptosome preparations to pan phage display libraries. Synaptosomes are membranous sacs composed of pre-synaptic membranes (Dunkley et al., 2008). They contain nerve terminal cytoskeleton, mitochondria, and synaptic vesicles along with other organelles and cytoplasm present in the pre-synaptic bouton. Synaptosomes are prepared from the homogenisation of fresh brain tissue in an iso-tonic sucrose buffer. The sheer force of homogenisation causes the pre-synaptic boutons to tear away from the axons, post-synaptic cell, and surrounding glial cells; while the iso-tonic sucrose solution forces the pre-synaptic membrane to reseal, maintaining the pre-synaptic intracellular environment (Dunkley et al., 2008). Synaptosomes are then separated from the remaining cellular debris by centrifugation. Synaptosome preparations remain physiologically active for several hours and are routinely used to study synaptic vesicle recycling (Whittaker et al., 1964; Ashton & Ushkaryov, 2005), along with many other physiological properties

of pre-synaptic terminals (De Robertis et al., 1962; Dunkley et al., 1988; Polosa & Attardi, 1991).

We hoped that by panning a phage display library with synaptosomes we could enrich for phage particles that specifically bound to the outer membrane of synapses. By using whole brain homogenate to produce the synaptosomes, we hoped to avoid selecting for phage that would only bind to synapses from a specific brain region. Instead, we hoped that we would identify phage that had a binding affinity for all pre-synaptic membranes: a pan-synaptic marker. This pan-synaptic marker could potentially be used to label synapses not only in the central nervous system, but possibly also synapses of the peripheral nervous system such as the neuromuscular junction.

In this chapter, a phage display library was panned using synaptosome preparations from whole wild type mouse brains. Initially, we demonstrate phage particles can successfully bind to a substrate in the synaptosome preparation. Next, enriched phage libraries were produced by panning with synaptosome preparations and amplifying the bound phage. Individual phage clones were then successfully amplified, their DNA extracted and sequenced to determine the sequence of the random DNA insert that codes for the fusion peptide on the surface of the phage particle. Sequencing of 16 phage clones showed two enriched peptide sequences, and the two most common sequences were taken forward for peptide synthesis. A plasmid was produced that incorporated one of the peptide sequences fused to an mCherry protein and a His-tag, under the control of a T7 promoter. This plasmid was then inserted into (DE3)pLysS cells, which were induced to express genes under the control of a T7 promoter and the resulting protein was collected and purified.

The fluorescently tagged peptide was tested to find if it would bind to synapses using primary cortical neuron cultures and skeletal muscle. By washing the tagged peptide onto unfixed primary neuron cultures we found mCherry positive punctate staining on the surface of the cell bodies of neurons. However, no staining was noted in skeletal muscle preparations.

4.2 – Methods

4.2.1 - Ethics Statement

All animal experiments were approved by a University of Edinburgh internal ethics committee and were performed under license by the UK Home Office (Project License number 60/3891).

4.2.2 - Animal Husbandry

FVB mice were maintained under standard SPF conditions in animal care facilities in Edinburgh. All animal procedures and breeding were performed in accordance with Home Office and institutional guidelines.

4.2.3 - Phage Display Library

The Ph.D.-12 Phage Display Peptide Library Kit (E8110S) was purchased from New England Biolabs. The Ph.D-12 system consisted of a M13 phage vector that had been modified to express a peptide that was twelve residues long and present on all

five minor coat pIII proteins. The library contained 10^9 individual clones and had a starting concentration of 1 x 10^{13} plaque forming units (pfu)/ml. The kit contained sequencing primers, -28 gIII sequencing primer (100pM/µl) and -96 gIII sequencing primer (100pM/µl). These primers bind to phage DNA 28 and 96 base pairs downstream of the random DNA insert on the non-coding strand, respectively. Also supplied was the host strain *E.coli* ER2738 which was used to titre and amplify phage particles.

4.2.4 - E.coli ER2738 Characterisation

The number of ER2738 cells was quantified using spectrophotometric analysis. 10ml of LB broth supplemented with 20µg/ml tetracycline was inoculated with ER2738 and grown in a shaking incubator at 37ºC for 24 hours. 0.1ml of overnight culture was diluted in 9.9ml of sterile 0.1M PBS to make a 10^{-2} dilution. This dilution was repeated to obtain 10^{-4}, 10^{-6} and 10^{-8} dilutions. 0.1ml and 1ml samples were taken from dilutions 10^{-4} to 10^{-8} and mixed with 3ml top agar which was held at 45ºC in a water bath. The top agar was then poured onto agar dishes containing 20µg/ml tetracycline and incubated at 37ºC for 24 hours. The number of colonies was then counted from plates that had between 30-300 colonies. The following formula was used to calculate the number of bacteria per ml.

$$\frac{Number\ of\ Colonies}{Dilution\ x\ Volume\ plated} = number\ of\ bacteria\ per\ ml$$

5ml of the same 24 hour culture was then diluted in 5ml LB broth. 5ml of this dilution was then further diluted in 5ml LB broth. This was repeated to obtain

dilutions 1, ½, ¼, 1/8th and 1/16th. The optical density (OD) of these dilutions was then measured on a spectrophotometer at 600nm (OD_{600}).

Using the data obtained from the colony counts, a graph of bacterial number against OD_{600} was made and a linear line of best fit added in Microsoft Excel. The line equation from this graph was used to determine the number of bacteria at different optical densities throughout the phage panning and amplification experiments.

4.2.5.1 - Synaptosome Preparation

Synaptosomes were prepared from young adult FVB mouse brains. Mice were sacrificed with an overdose of iso-fluorane anaesthetic via inhalation until no plantar reflex could be detected and no breath was taken for at least one minute. To remove the brain, the mouse was decapitated and the skull was cut from foramen magnum along the midline. Perpendicular cuts were then made from the centre of the midline cut and the skull was opened using strong tweezers. The brain was removed and homogenised immediately in 2ml ice cold sucrose solution (0.32M sucrose, 1.3mM EDTA, 5mM Tris-HCl, pH7.4). Homogenisation took place in a Dounce homogeniser with a 0.1-0.15mm clearance. A total of 12-15 strokes were used to fully homogenise the mouse brain. The homogenised brain was then centrifuged at 900rcf for 10 minutes to pellet the P1 fraction. The supernatant (S1 fraction) was removed and added to a new eppendorf and kept on ice. The P1 fraction was then re-suspended in 250µl sucrose solution and centrifuged again at 900rcf for 10 minutes. The supernatant was then added to the original S1 supernatant and this was centrifuged at 15000rcf for 15 minutes to pellet the P2 fraction. The supernatant was

removed and discarded and the P2 pellet gently re-suspended in 1ml sucrose solution, then centrifuged again at 15000rcf for 15 minutes. The supernatant was removed again and discarded and P2 pellets from both eppendorfs were gently re-suspended in 1ml sucrose solution.

4.2.5.2 - Western Blot

Protein from the P1 and P2 fraction of synaptosome preparations was extracted by homogenising the pellets with RIPA buffer (Pierce, 89900) supplemented with 5µl/ml Halt Proteinase Inhibitor (Thermo Scientific, 1861278) – 600µl of RIPA buffer was used for P1 and 200µl for P2. The samples were then centrifuged at 14000rpm for 20 minutes. A BCA assay was then carried out using a Micro BCA Protein Assay Kit (Pierce, 23235). A master mix was made up containing 40µl reagent A, 0.38µl reagent B and 0.02µl reagent C per reaction. 80µl of this master mix was added to 1.5ml eppendorfs. A protein standard curve was produced by adding increasing volumes of 2mg/µl BSA Albumin Protein Standard (Pierce, 23209). 1µl of each sample was added to the 80µl reaction and was measured in triplicate. The samples were vortexed and then incubated at 60^{o}C for one hour. The absorbance of the samples was then measured on the Nanodrop at 562nm. The absorbance readings for the standard curve samples were used to generate a standard curve and the equation of this line was used to calculate the concentration of the P1 and P2 protein extraction samples.

40mg of protein per lane was used for western blots. Samples were made up by diluting with the appropriate volume of water to make a 10µl volume for each lane.

To this, 5µl of NuPage LDS Sample Buffer (Novex, NP0007) was added and vortexed to mix. The samples were then incubated at 98^{o}C for 2 minutes before being vortexed. 15µl of samples were loaded into a NuPage 4-12% Bis-Tris Gel (Novex, NP0323BOX) along with 5µl Sharp Pre-Stained Protein Standard (Novex, LC5800) and run at 80v for 5 minutes, followed by 180v for 45 minutes. The gel was then removed from the cassette, trimmed, and placed onto an iBlot Transfer Stack (Invitrogen, IB3010-01) and transferred onto a membrane using the iBlot Fast Transfer System. The membrane was then removed and washed in Odyssey Blocking Buffer (Licor, 402-467-0700) for 30 minutes on a rolling platform. Primary antibody against H2B (LP Bio, AR-0139-200) was added to blocking solution at a concentration of 1:1000 and this was incubated with the membrane on a rolling platform overnight at 4^{o}C. The following day, the primary antibody was washed with 6 x 5 minute washes in 0.1M PBS. The membrane was then incubated in Odyssey Blocking Buffer + 1:1000 Tween 20 and a 1:5000 dilution of IRDye 680RD Goat Anti-Rabbit IgG (H+L) (Licor, 926-68071) for 1 hour at room temperature on a rolling platform. The membrane was then washed in 6 x 5 minute washes with 0.1M PBS. The membrane was then dried and scanned on the Licor Odyssey at 700nm.

4.2.6 - Phage panning

Serial dilutions were made of synaptosomes (200µl of synaptosomes added to 800µl sucrose solution). These dilutions were arbitrarily labelled 1, 2, 3, 4 and 5; with 1 being the most concentrated synaptosome sample. Dilutions 2, 3, 4 and 5 were used

to pan phage libraries. 5µl/ml Proteinase Inhibitor Cocktail was added to each dilution.

Following the Ph.D.-12 Phage Display Peptide Library Kit manual, a 1:100 dilution of the phage library was added to each synaptosome dilution and incubated for one hour at 4^{o}C on a rocking platform.

800µl of the synaptosome dilutions were then transferred to new 1.5ml eppendorfs and centrifuged at 15000rcf for 15 minutes to pellet the synaptosomes. The supernatant was removed and discarded and the pellets were re-suspended in 1ml ice-cold sucrose solution. This was repeated twice and the pellets were then re-suspended in 1ml ice cold pH 7.5 tris buffered saline (TBS) (50mM Tris-HCl, 10mM Tris Base, 150mM NaCl, pH7.3).

To ensure that phage had bound to synaptosomes the samples were titered. 1µl of each synaptosome dilution was further diluted in 9µl LB broth to obtain a dilution series ranging from 10^{-1} to 10^{-4}. 200µl of OD_{600}0.5 ER2738 grown in LB broth supplemented with 20µg/ml tetracycline was then added to each sample and left at room temperature for 5 minutes. Each sample was then added to 3ml top agar supplemented with 20µg/ml tetracycline that was held at 45^{o}C and transferred to an agar plate containing 20µg/ml tetracycline. Samples were incubated overnight at 37^{o}C (for no more than 18 hours) and the number of plaques was counted.

4.2.7 - Phage Library Amplification

Synaptosome bound phage particles were amplified the following day to create a new enriched phage display library. An overnight culture of ER2738 grown in 10ml LB broth supplemented with 20µg/ml tetracycline was diluted 1:100 in 20ml LB broth supplemented with 20µg/ml tetracycline, and 5µl of synaptosome dilution 2 was added. This was incubated in a shaking incubator for 4.5 hours at 37^{o}C. This was then centrifuged at 12000rcf for 10 minutes to pellet the bacteria. The supernatant was transferred to a clean tube and centrifuged again at 12000rcf for 10 minutes. The supernatant was then transferred to a 50ml falcon tube and 1/6th of the volume of 20% PEG: 2.5M NaCl was added. This was left overnight at 4^{o}C to precipitate the phage. The following day the sample was centrifuged at 10000rcf for 15 minutes to pellet the phage. The supernatant was removed and the samples centrifuged briefly and the remaining supernatant was removed using a P1000. The phage pellet was re-suspended in 1ml pH7.5 TBS and 1/6th of the volume 20% PEG: 2.5M NaCl was added and incubated on ice for 45 minutes. The phage was then centrifuged at 14000rpm for 10 minutes to pellet the phage. The supernatant was removed, the sample centrifuged again briefly and the remaining supernatant removed with a P200 pipette. The pellet was then re-suspended in 200µl pH7.5 TBS and centrifuged at 14000rpm for 1 minute. The supernatant was then transferred to a new eppendorf and mixed with 200µl sterile glycerol and stored at -20^{o}C. This was the new amplified phage library. This process, including panning the libraries with synaptosomes, was repeated three times.

4.2.8 - Phage Clone Amplification

Individual phage clones were amplified by picking phage plaques from titre plates. Plates that had between 30 and 100 plaques present were chosen for picking. Well separated plaques were picked by pushing a sterile glass Pasteur pipette into the centre of the phage plaque and removing this core along with the underlying agar. Plaques were then blown into 1.5ml eppendorfs and suspended in 100µl pH7.5 TBS and kept on ice. These individual phage clones were titered in order to estimate the number of plaque forming units per plaque. 1µl of the re-suspended phage plaques were diluted in 9µl LB broth. This was then mixed with 3ml top agar held at 45ºC and plated onto agar supplemented with 20µg/ml tetracycline plates. They were incubated overnight at 37ºC and the number of plaques was counted the following day.

10µl of re-suspended phage plaque was added to 1ml OD_{600}0.1 and incubated in a shaking incubator for 4.5 hours at 37ºC. Samples were then transferred to 1.5ml eppendorfs and centrifuged at 14000rpm for 30 seconds. The supernatant was transferred to a new eppendorf and centrifuged at 14000rpm for 30 seconds again.

4.2.9.1 - DNA Extraction

500µl of the supernatant was then transferred to a new eppendorf. 200µl 20% PEG: 2.5M NaCl was added to each sample, vortexed to mix and left to stand at room temperature for 10 minutes. The samples were then centrifuged at 14000rpm for 15 minutes. The supernatant was removed and the samples briefly centrifuged again. The remaining supernatant was removed. The phage pellet was re-suspended in

200µl pH7.5 TBS. 200µl phenol was added and the samples were vortexed, then centrifuged at 14000rpm for 10 minutes. The aqueous phase of the phenol was added to a new tube, being careful not to disturb the interface. The phenol extraction was repeated. The aqueous phase was removed again and transferred to a new tube. 200µl of chloroform was added to each sample, vortexed and centrifuged at 14000rpm for 10 minutes. The aqueous phase was removed and the chloroform extraction was repeated.

1/10th the volume (10µl) 3M pH6.5 NaOAc was added to each sample followed by 2.5 volumes (250µl) ethanol. Samples were left to precipitate overnight at -20^{o}C.

The following day, samples were centrifuged at 14000rpm for 15 minutes to pellet the DNA. The supernatant was removed and 1ml 95% ethanol was added to each sample. The samples were centrifuged at 14000rpm for 30 seconds. The supernatant was removed and the 95% ethanol wash was repeated. The supernatant was removed and the samples centrifuged briefly. The remaining supernatant was then removed with a P200 and the samples were placed in a heat block at 37^{o}C for approximately 15 minutes to evaporate all traces of ethanol. The samples were then re-suspended in 30µl tris-EDTA (TE) buffer and stored at -20^{o}C.

4.2.9.2 - DNA Sequencing

DNA concentration was measured using a Nanodrop. Approximately 100ng of DNA in 5µl was used per sample with 1µl -96 gIII sequencing primer (100pmol/µl). DNA was sequenced at The GenePool, Ashworth Laboratories, The King's Buildings, The University of Edinburgh, using Sanger Sequencing technique with BigDye reagents

and an ABI 3730 capillary sequencing instrument (http://genepool.bio.ed.ac.uk/sanger/index.html). DNA sequences were then viewed using Sequencher 5.1 Demo.

4.2.10 - Peptide Synthesis

4.2.10.1 - PCR

A pET30a(+) vector was linearised using PCR (Table 1). In a separate PCR, the peptides of interest were cloned into His-tagged bacterial expression vectors for mCherry (Table 1). Additionally, 15bp which were complementary to the linearised pET30a(+) vector were added to the peptide + mCherry vector ends.

PCR	5’ Primer	3’Primer	Product Length (Approximate)
P1 + mCherry	TCT TCT GAG TTT CCT CGG TCT TGG GAT ATG GAG ACT AAT ATG GTG AGC AAG GGC GAG	GCA GCC GGA TCT CAG CTA CTT GTA CAG CTC GTC	700bp
P2 + mCherry	TCT TGG TCT GAG TAT GAT ATT CCG ACT CCG CAG ATT CCG ATG GTG AGC AAG GGC GAG	GCA GCC GGA TCT CAG CTA CTT GTA CAG CTC GTC	700bp
P1 pET30a(+) vector	AGG AAA CTC AGA AGA AGC CAT GGC CTT GTC GTC GTC G	CTG AGA TCC GGC TGC TAA CAA AGC C	5500bp
P2 pET30a(+) vector	ATA CTC AGA CCA AGA AGC CAT GGC CTT GTC GTC G	CTG AGA TCC GGC TGC TAA CAA AGC C	5500bp

Table 1 – Primer sequences.

PCR was performed using Phusion High Fidelity DNA Polymerase (MO530S, New England BioLabs). 5x Phusion HF Buffer was used in the reactions which were made to a 50µl final volume. PCRs for linearisation of pET30a(+) vectors were performed according to Table 2; PCRs for peptide addition to mCherry expression vectors were performed according to Table 3.

100ng of His-tagged bacterial expression vector for mCherry (kindly gifted by Dr Jing Qui) was added to P1+mCherry and P2+mCherry reactions. 100ng pET30a(+) template vector was added to the pET30a(+) vector reactions.

Step	**Temperature (ºC)**	**Time (s)**
1	96	120
2	50	30
3	72	240
4	96	20
	Go to Step 2, repeat 5 times	
5	60	10
6	72	240
7	96	20
	Go to Step 5, repeat 20 times	
8	72	240

Table 2 – PCR settings for pET30a(+) linearised vector.

Step	Temperature (ºC)	Time (s)
1	96	120
2	50	30
3	72	60
4	96	20
	Go to Step 2, repeat 5 times	
5	60	10
6	72	60
7	96	20
	Go to Step 5, repeat 20 times	
8	72	60

Table 3 – PCR settings for peptide addition to His-tagged bacterial expression vector for mCherry.

4.2.10.2 - Ligation

PCR fragments were purified from an agarose gel using a QIAGEN Quick DNA Extraction Kit (QIAGEN, 28104). PCR products were resolved on a 0.8% agarose gel for 45 minutes at 100v. Using an Invitrogen SafeImager, the PCR fragments were visualised and cut from the gel using a clean razor blade. The excised agarose was weighed in 1.5ml eppendorfs before being dissolved in 3 volumes (300µl buffer per 100mg gel) of buffer QG at 50ºC for 10 minutes with vortexing every 2-3 minutes. 1 gel volume of isopropanol was added and mixed. The samples were then transferred to QIAquick columns in 2ml collection tubes and centrifuged at

13000rpm for 1 minute. 0.5ml Buffer QG was added to the columns and centrifuged at 13000rpm for 1 minute. 0.75ml Buffer PE was added to the columns before being allowed to stand for 2 minutes and then centrifuged at 13000rpm for 1 minute. The flow through was discarded and the columns were centrifuged again at 13000rpm for 1 minute to remove all traces of ethanol from Buffer PE. The columns were then moved to clean 1.5ml eppendorfs and 50µl Buffer EB was added to the membrane and allowed to stand for 1 minute before being centrifuged at 13000rpm for 1 minute. This step was repeated with the flow through to ensure maximum DNA concentration.

Gel purified PCR fragments were ligated using In-Fusion HD Cloning Kit (Clontech, PT5162-1). Approximately 50ng of PCR fragments P1+mCherry and P1 pET30a(+), and separately P2+mCherry and P2 pET30a(+) were ligated at 50^{o}C for 15 minutes before being placed on ice.

One Shot TOP10 Chemically Competent *E.coli* (Invitrogen, C4040-03) cells were transformed with the newly ligated plasmid. Two vials of cells were thawed on ice before 4µl of the ligation mixture was added and mixed gently. This was incubated on ice for 30 minutes before being heat shocked at 42^{o}C for 30 seconds. The bacteria were then placed on ice again for 2 minutes. Next, 250µl S.O.C. media was added and the bacteria were incubated at 37^{o}C in a shaking incubator for one hour. Two volumes, 20µl and 200µl were then plated out on agar plates containing 50ng/ml kanamycin and incubated overnight at 37^{o}C.

4.2.10.3 - Sequencing

The following day, three colonies from 20µl plates were selected and amplified up separately in 1ml LB broth containing 50ng/µl kanamycin for 16 hours. A Miniprep Kit (QIAGEN, 27104) was used to extract the DNA from the bacteria. Briefly, bacteria were pelleted at 10000rpm for 3 minutes and the supernatant was removed. Cells were re-suspended in 250µl buffer P1 + RNase + LyseBlue. 250µl lysis buffer P2 was added and the eppendorfs were gently inverted until a uniform blue colour had appeared, indicating complete lysis of the cells. 350µl Buffer N3 was added and mixed immediately by inverting the tubes until the blue colour had completely disappeared and the solution had become cloudy. The samples were then centrifuged at 13000rpm for 10 minutes. The supernatants were then added to QIAprep spin columns and centrifuged at 13000rpm for 1 minute. 0.5ml Buffer PB was then added to the spin columns and centrifuged at 13000rpm for 1 minute. 0.75ml Buffer PE was then added and the spin columns were centrifuge at 13000rpm for 1 minute. The flow through was discarded and the columns were centrifuged again at 13000rpm for 1 minute to ensure all traces of ethanol from Buffer PE were removed. The spin columns were removed from their collection tubes and transferred to clean 1.5ml eppendorfs. 50µl Buffer EB was added to the membrane and allowed to stand for 1 minute before being centrifuged at 13000rpm for 1 minute. This step was repeated with the flow through in order to maximise the concentration of DNA.

DNA extracted from the mini-prep was measured using a Nanodrop. Approximately 200ng of DNA in 5µl was used per sample with 1µl 25ng/ml T7 Promoter Primer (5' – TAATACGACTCACTATAG – 3'). DNA was sequenced at The GenePool, Ashworth Laboratories, The King's Buildings, The University of Edinburgh, using

Sanger Sequencing technique with BigDye reagents and an ABI 3730 capillary sequencing instrument (http://genepool.bio.ed.ac.uk/sanger/index.html). DNA sequences were then viewed using Sequencher 5.1 Demo.

4.2.10.4 - Peptide Synthesis

DNA from colonies that had ligated correctly were used to transform Rosetta (DE3)pLysS cells (EMD Millipore, 70956). (DE3)LysS cells were grown on agar plates supplemented with 34µg/ml chloramphenicol overnight at 37°C, and then a single colony was used to inoculate 10ml LB broth supplemented with 34µg/ml chloramphenicol. The bacteria were incubated in a shaking incubator at 37°C until it reached log phase. The bacteria were then made electro-competent by pelleting the bacteria and washing the bacteria in ice cold water three times. Bacteria were then re-suspended in S.O.C media. DNA from the mini-prep was diluted 1:10 and 3µl was added to 50µl of (DE3)pLysS bacteria and electroporated. 300µl S.O.C. media was used to flush the bacteria out of the electroporation cuvette and this was incubated at 37°C with shaking for 40 minutes. The bacteria were then plated on agar plates containing 50ng/ml kanamycin and 34µg/ml chloramphenicol overnight at 37°C.

The following day, a single colony was used to inoculate 10ml LB broth containing 50ng/ml kanamycin and 34µg/ml chloramphenicol. This was incubated overnight at 37°C with shaking. The following day, this overnight culture was added to 150ml LB broth containing 50ng/ml kanamycin and 34µg/ml chloramphenicol and incubated in and shaking incubator at 37°C until it reached OD_{600} 0.8. 50mM IPTG

was then added and this was incubated at room temperature overnight in a shaking incubator.

The following day, the bacteria were pelleted at 10000 x g for 10 minutes, the supernatant was discarded and the bacterial pellet was re-suspended in 10ml buffer (50mM sodium phosphate, 300mM sodium chloride). This was frozen at -80^{o}C. The suspension was then thawed at room temperature and the bacteria were allowed to lyse for 40 minutes with gentle agitation. The suspension was passaged through a 30G needle until no longer viscous and centrifuged at 10000 x g for 10 minutes.

4.2.10.5 - Peptide Purification

The peptide + mCherry tag was then purified on a TALON 2ml Disposable Gravity Column (ClonTech, 635606). The supernatant was applied to the column and allowed to flow through. The column was then washed with wash buffer (50mM sodium phosphate, 300mM sodium chloride, 5mM imadizole). The P1+mCherry tag was then eluted from the column with elution buffer (50mM sodium phosphate, 300mM sodium chloride, 150mM imadizole).

Imidazole was removed from the elution by inverse filtration. The elution was added to a centrifuge inverse filtration unit and centrifuged at 2000 x g for 30 minutes. The filtrate was removed and centrifugation repeated several times. 0.1M PBS was added to the elution and the centrifugation was repeated. This was repeated several times. The elution was then centrifuged several times without the addition of PBS to concentrate the protein. Finally, elute was mixed 1:1 with sterile glycerol and stored at -20^{o}C.

4.2.11 - Peptide Analysis

4.2.11.1 - Concentration Analysis

A BCA assay was carried out as described above. The protein concentration of the purified peptide was measured in triplicate. Using the slope of the line generated from the standard curve, the concentration of protein (mg/µl) in the P1+mCherry purification was calculated.

4.2.11.2 - Molecular Weight Analysis

5µl samples of non-induced (DE3)pLysS bacteria, induced (DE3)pLysS bacteria, gravity column run through, gravity column wash, and purified peptide were diluted with 5µl water in 1.5ml eppendorfs. 5µl NuPage LDS Sample Buffer 4x (Novex, NP0007) was added and thoroughly mixed before being heated at 98^{o}C for 2 minutes. 15µl of the samples and 5µl Sharp Pre-Stained Protein Standard (Novex, LC5800) were then run on a NuPage 4-12% Bis-Tris Gel (Novex, NP0323BOX) for 5 minutes at 80v followed by 45 minutes at 180v. The gel was then stained in 0.1% Coomassie (0.1% Coomassie, 40% methanol, 10% acetic acid) for one hour on a rocking platform. The gel was then de-stained in three changes of 50% methanol + 10% acetic acid for 1.5 hours.

4.2.12 - Binding Analysis

4.2.12.1 - Primary Cortical Neuron Binding Analysis

15 days *in vitro* (15 DIV) mouse primary cortical neuron cultures were kindly provided by Sean McKay. A 1:50-1:100 dilution of P1+mCherry was added to media in a selection of wells for 30 minutes at 37ºC, the cells were briefly washed with 0.1M PBS prior to fixation with 4% PFA in 0.1M PBS for 10 minutes at room temperature. Cells were then permeabilised with 0.25% triton X-100 in 0.1M PBS for 10 minutes followed by blocking in 1% BSA + 0.25% triton X-100 in 0.1M PBS for 30 minutes. Primary antibody solution was a 1:100 dilution of mouse anti-SV2 (Developmental Studies Hybridoma Bank) in blocking solution. Primary antibody solution was incubated for one hour at room temperature then washed off with 3 x 5 minute 0.1M PBS washes. Secondary antibody solution was a 1:100 dilution of AlexaFluor 488 Donkey Anti-Mouse (H+L) (Jackson Immuno, 715-545-150) in blocking solution. Secondary antibody was incubated for one hour at room temperature in the dark, then washed off with 3 x 5 minute 0.1M PBS washes.

Cells that had not been exposed to the P1+mCherry protein prior to fixation were then incubated with 1:50 -1:100 dilutions for 10-30 minutes before being washed briefly with 0.1M PBS. Cells were then mounted on glass slides with Mowiol and left to dry at room temperature overnight.

Each dilution of P1+mCherry was tested on at least three different coverslips, both before and after fix.

4.2.12.2 - Skeletal Muscle Binding Analysis

Lumbricals were removed from the hind limbs of young adult male FVB mice. The lumbricals were then either fixed in 4% PFA for 10 minutes on a rocking platform; or were incubated with a 1:50-100 dilution of the P1+mCherry protein in PBS for 30 minutes before being fixed with 4% PFA for 10 minutes on a rocking platform. A selection of lumbrical muscles were then stained with FITC-conjugated α-bungarotoxin (5µl/ml) for 10 minutes on a rocking platform before being washed with 0.1M PBS. Lumbricals that were not incubated with P1+mCherry were then washed with 1:50-1:100 dilutions of P1+mCherry in 0.1M PBS for 10-30 minutes before being washed briefly in 0.1M PBS. All lumbricals were mounted onto glass slides with glass coverslips using Mowiol mounting medium.

Each dilution of P1+mCherry was tested on at least three different lumbrical muscles, both before and after fix.

4.2.12.3 - Imaging

Images were taken at IMPACT Imaging Facility at the University of Edinburgh on a Zeiss LSM510 laser scanning confocal (63x Plan Apochromat oil objective/1.4NA). 488nm and 543mn with long pass filter laser lines were used for excitation and confocal Z-series were merged using Zeiss LSM510 AIM v3.2 software.

4.3 - Results

4.3.1 - Bacteria Characterisation

Initially, the number of bacterial cells per ml (cfu/ml) of *E.coli* ER2738 was determined. This information was necessary in order to ensure that an optimal multiplicity of infection (the ratio of bacterial cells to infectious agents) was achieved during phage amplification. Bacterial numbers were estimated using turbidity/spectrophotometry analysis. Briefly, a single colony of ER2738 was used to inoculate 10ml LB broth supplemented with 20µg/ml tetracycline and cultured in a shaking incubator for 24 hours. From this culture, a dilution series was made and plated on agar plates containing 20µg/ml tetracycline which were incubated for 24 hours. The number of colonies on these plates was counted (Figure 2) (from plates containing between 30 and 300 colonies) and the following equation was used to determine the number of bacterial cells present per ml:

$$\frac{Number\ of colonies}{dilution\ x\ volume\ plated} = No.of\ bacteria\ per\ ml$$

Secondly, a standard curve of the 24 hour culture's optical density was generated. A second dilution series of the initial 24 hour culture was made in LB broth. The OD_{600} of each dilution was measured using a spectrophotometer and the results were recorded. The OD_{600} was plotted against the number of bacteria per ml and a linear

line of best fit was added (Figure 3). The equation of this line was used to determine the number of bacterial cells at any given OD_{600}.

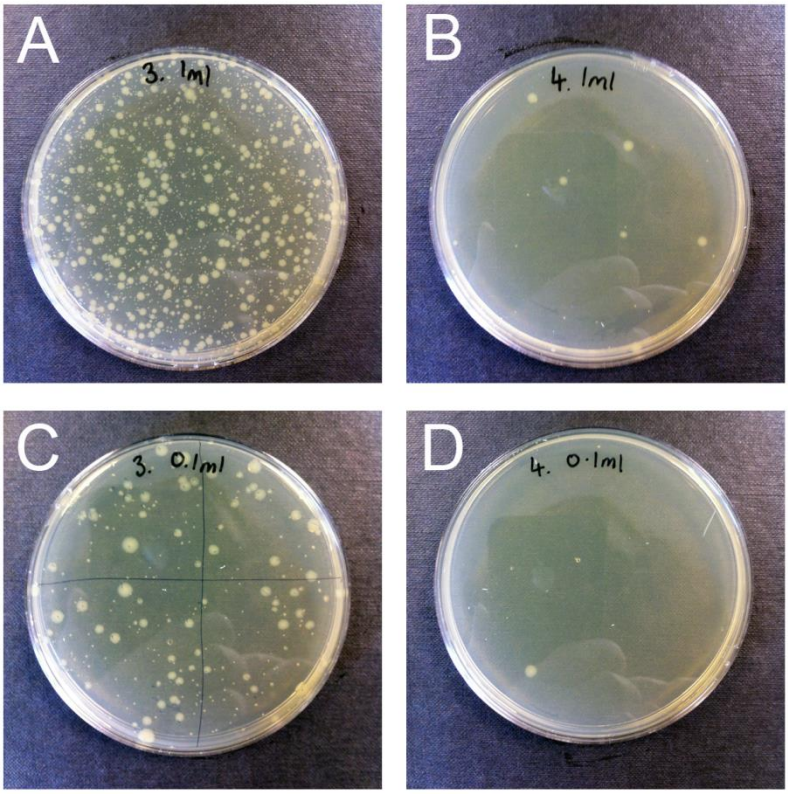

Figure 2 - Agar plates with ER2738 colonies. A dilution series of a 24 hour culture of ER2738 was produced. From dilutions 10^{-4} to 10^{-8}, a 1ml and 0.1ml sample were added to top agar and plated on agar plates. These plates were incubated for 24 hour at 37°C and the number of colonies on plates with fewer than 300 colonies was counted (A/B/C/D). (A) A 1ml sample of 10^{-7} dilution of ER2738. (B) A 0.1ml sample of 10^{-7} dilution of ER2738. (C) A 1ml sample of 10^{-8} dilution of ER2738. In this plate, there are noticeably fewer colonies than in the 1ml sample of 10^{-7} dilution. The number of plaques on this plate was counted to estimate the number of bacteria in the undiluted 24 hour culture. (D) A 0.1ml sample of 10^{-8} dilution of ER2738.

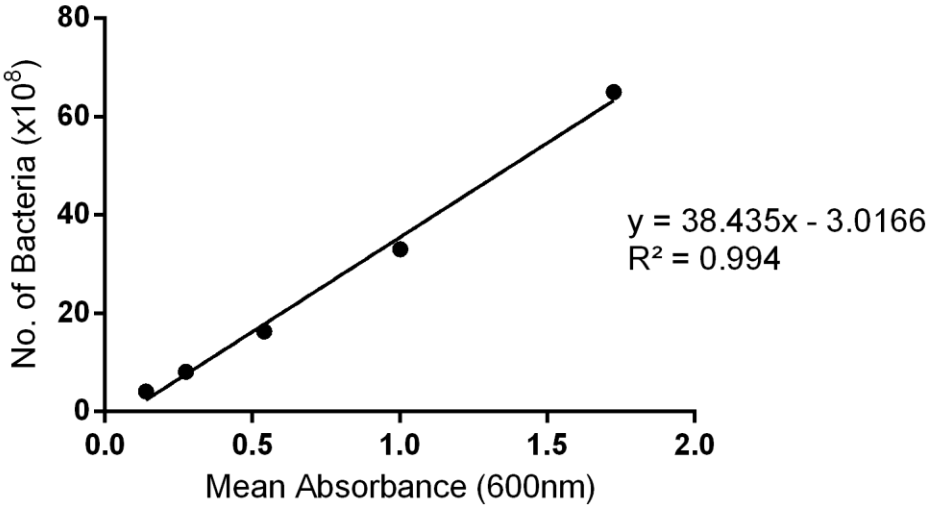

Figure 3 - Scatter plot of number of bacteria per ml and mean absorbance at 600nm. A scatter plot was generated using the number of bacterial per ml plotted against the mean absorbance at 600nm for each dilution. The number of bacteria per sample was halved for each dilution to give an estimate of the number of bacteria per dilution. A linear line of best fit was added and the equation of this line was used to calculate the number of bacteria present at different optical densities in the study.

4.3.2 – Proof of Concept Concentration Dependant Binding Assay

4.3.2.1 – Synaptosome Preparation and Analysis

Phage panning is usually carried out using a target protein or peptide that has been adhered to a surface such as a plastic well or bead, however in this study, synaptosomes were used to pan the phage library. Synaptosomes were produced from fresh brain tissue (Figure 4) and kept in suspension in an iso-tonic sucrose buffer (Figure 5).

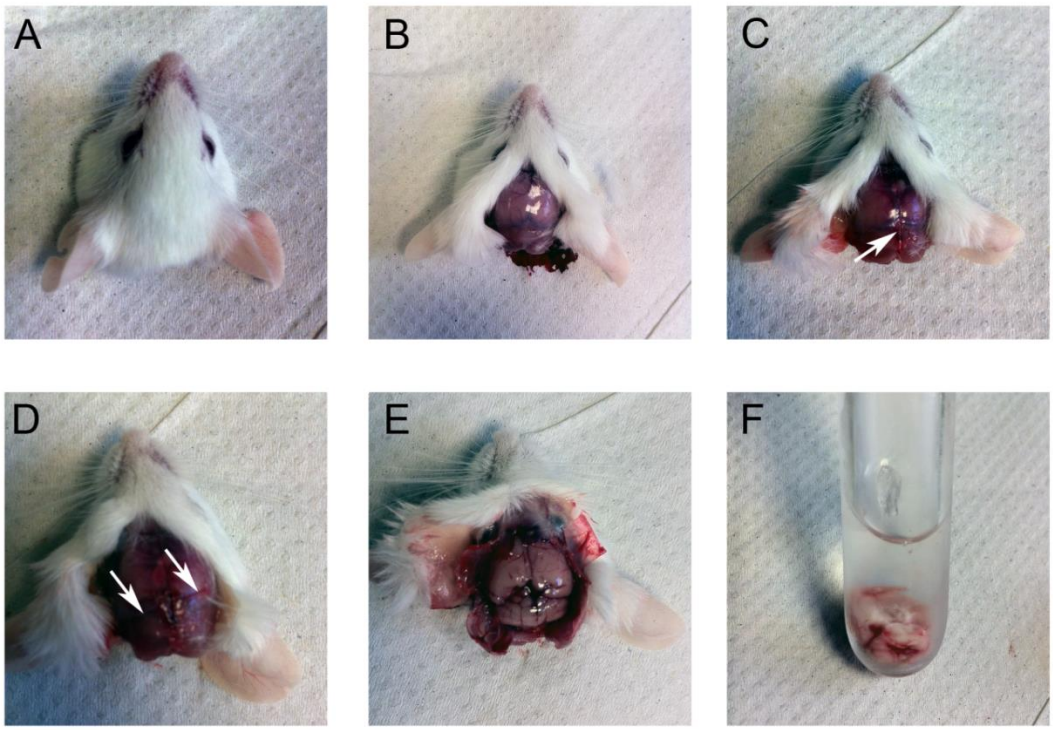

Figure 4 - Mouse brain removal for homogenisation. The mouse was decapitated (A) and an incision was made in the skin which was reflected to reveal the skull (B). An incision was made from the foramen magnum along the midline (white arrow) (C). Perpendicular incisions were made from the midline incision (white arrows) (D). The skull was opened using strong forceps to reflect the skull and expose the brain (E). The brain was removed and placed in ice-cold sucrose solution in a Dounce homogeniser and homogenised immediately (F).

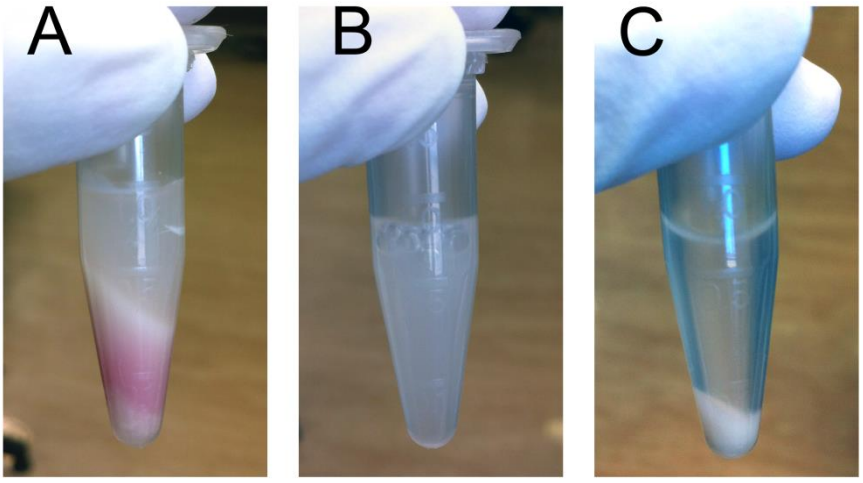

Figure 5 - Synaptosome preparation from homogenised fresh brain tissue. (A) The whole brain homogenate was centrifuged at 900rcf for 10 minutes to pellet cell body debris (P1). (B) The supernatant (fraction S1) was removed and transferred to a clean 1.5ml eppendorf before being centrifuged at 15000rcf to pellet the synaptosomes (P2). (C) The supernatant was removed and the pellet of synaptosomes was re-suspended in sucrose buffer before being centrifuged again at 15000rcf. This pellet was then re-suspended in sucrose buffer again and used for phage panning.

To ensure that synaptosome preparations were relatively pure of cell body contamination, a western blot was performed. Protein was extracted from P1 (cell body and debris) (Figure 5A) and P2 (synaptosome) fractions (Figure 5C) and run on an SDS-PAGE gel. The protein was then transferred to a PVDF membrane using iBlot Fast Transfer System and incubated with an antibody against histone H2B, a

histone protein specific to the nucleus. Figure 6 shows that at approximately the 15kDa band of the Sharp Pre-Stained Protein Standard, a protein band was clearly present in the P1 (or cell body) fraction but was absent from the P2 (or synaptosome) fraction. From this, it was concluded that there was little or no cell body contamination in the P2 fraction and therefore the synaptosomes were sufficiently pure to use in the phage panning experiments.

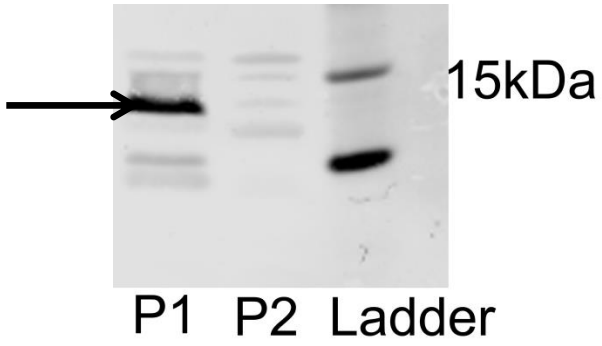

Figure 6 - Western blot of anti-H2B (~14kDa) of P1 and P2 synaptosome fractions. A western blot was carried out to ensure no cell body contamination was present in the P2 fraction of synaptosomes which would be used to pan the phage library. An antibody against the histone protein H2B (approx. 14kDa) was used to detect nuclear contamination. In the P1 fraction, which contains cell bodies, there was a strong band present at approximately 15kDa (black arrow). In the P2 fraction, which contains synaptosomes, there was no protein band present at approximately 15kDa.

4.3.2.2 – Concentration Dependent Binding Assay

In order to determine that M13 phage particles could bind a target in suspension, a concentration dependent binding assay was carried out. A dilution series of

synaptosomes was prepared (Figure 7) and a 1:10 dilution of the original phage library was added and incubated for 1 hour at 4°C.

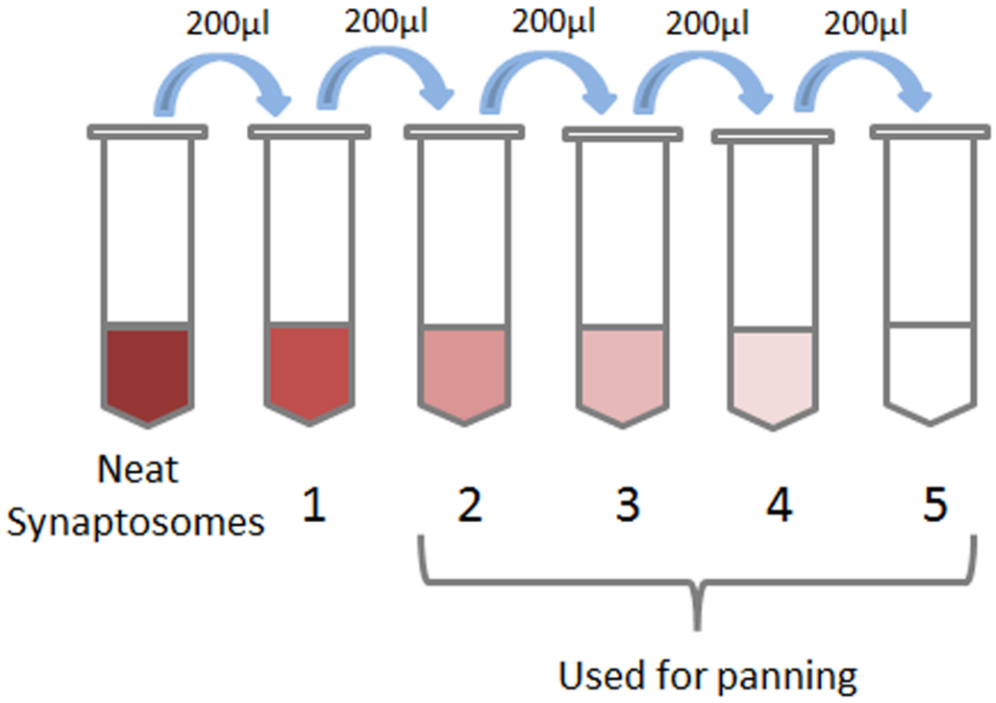

Figure 7: Schematic representation of synaptosome dilution series. After purification, the P2 fraction containing synaptosomes was re-suspended in 1ml sucrose buffer which was used to create a dilution series. 200µl of the neat synaptosome fraction was diluted in 800µl sucrose buffer to create dilution 1. From this, 200µl was diluted in 800µl sucrose buffer to create dilution 2 and so on until dilution 5 was reached. Each dilution was mixed gently by inverting several times to ensure the synaptosomes were fully dispersed. Dilutions 2-5 were used for synaptosome panning. Proteinase inhibitor cocktail (5µl/ml) was added to each dilution and a 1:10 dilution of the original phage library was added to each dilution before being incubated at 4°C on a rocking platform for 1 hour.

The synaptosomes were then pelleted at 15000rcf for 15 minutes and washed in sucrose buffer to remove unbound phage particles. This washing step was repeated twice and the synaptosomes with bound phage were finally re-suspended in TBS buffer.

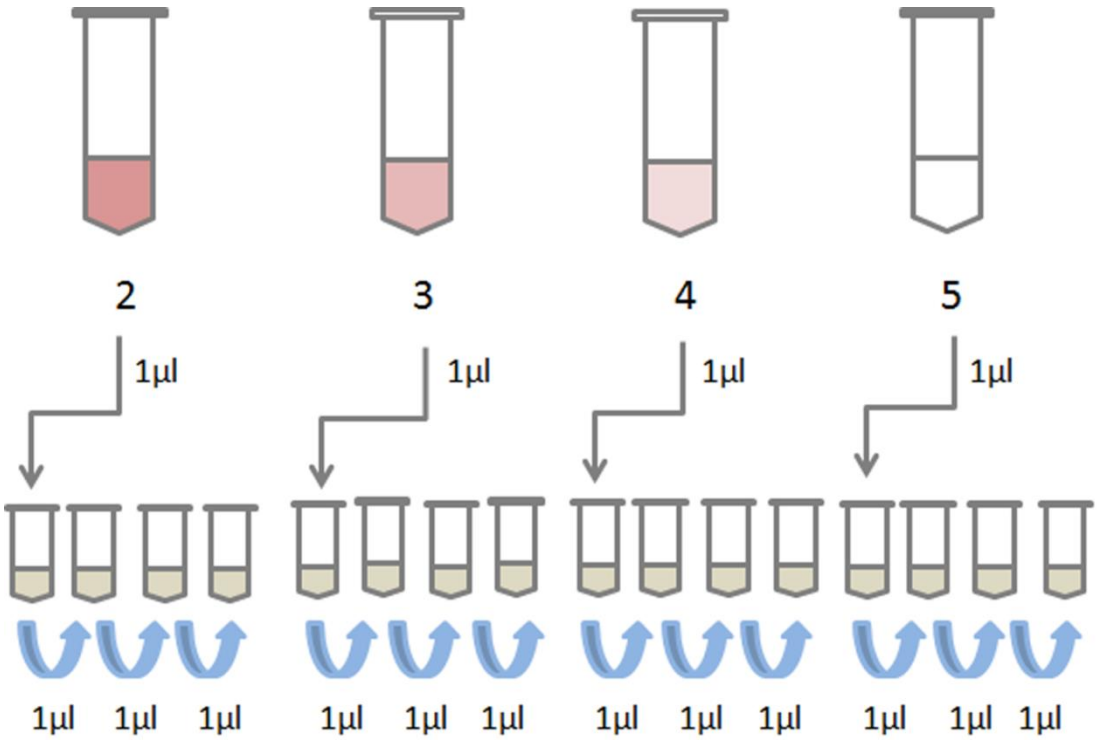

Figure 8: Schematic representation of synaptosome dilution series titering. Each synaptosome dilution series was titered after being washed with sucrose buffer twice and re-suspended in TBS buffer. 1µl was taken from each synaptosome dilution and diluted in 9µ LB broth to make a 10^{-1} dilution. Each of these was then diluted 10 fold until a 10^{-4} dilution was reached. To each of these, 200µl OD_{600}0.6 ER2738 was added and incubated for 5 minutes at room temperature before being added to 3ml top agar that was held at 45°C in a water bath and plated onto LB agar plates supplemented with 20µg/ml tetracycline.

Each sample was diluted ten-fold until the series reached 10^{-4} (Figure 8). To each dilution, 200µl of OD_{600}0.5 ER2738 bacteria was added and incubated at room temperature for 5 minutes. The samples were then transferred to 3ml top agar that was held at 45ºC and plated onto an agar plate containing 20µg/ml tetracycline. Cultures were incubated overnight at 37ºC and the number of plaques was counted the following day.

Following overnight incubation at 37ºC, phage plaques were observed on the bacterial lawn (Figure 9). The phage plaques appeared as dark areas on an otherwise homogeneous bacterial lawn (Figure 9). When held against a light source, or dark background, the phage plaques could be easily distinguished from the bacterial lawn. Qualitatively, the number of plaques appeared to diminish as the dilution series increased (Figure 9).

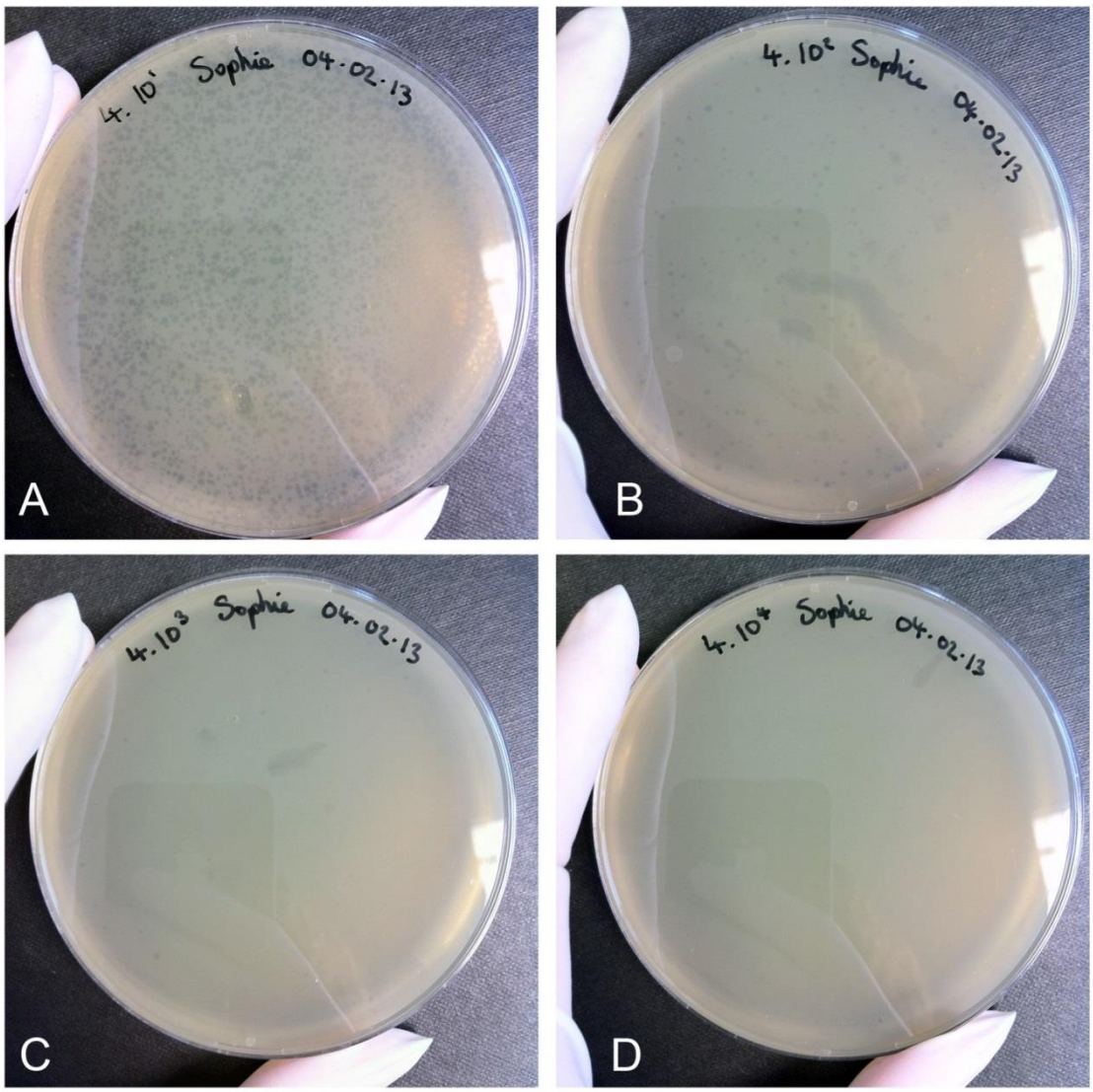

Figure 9 - The number of phage plaques observed on the bacterial lawn decreased with increasing dilutions of bound phage. (A) A 1:10 dilution of bound phage particles from synaptosome dilution 4 is shown. There were a large number of phage plaques interrupting the bacterial lawn. (B) A 1:100 dilution of bound phage particles from synaptosome dilution 4. Fewer phage particles were observed on the bacterial lawn. (C) A 1:1000 dilution of bound phage particles from synaptosome dilution 4. There were only six phage plaques on the bacterial lawn. (D) A 1:10000 dilution of bound phage particles from synaptosome dilution 4. No phage particles were observed on the bacterial lawn.

The number of phage plaques per plate was counted and plotted against dilution (Figure 10). Between each synaptosome dilution series, the number of phage plaques observed decreased with synaptosome concentration (Figure 10). Similarly, in each synaptosome dilution series, the number of phage plaques observed decreased with the concentration of synaptosomes that had been exposed to phage particles (Figure 10). From this relationship, it was concluded that the phage particles did have a binding affinity with an unknown target in the synaptosome preparation. Not only this, but the phage particles were able to bind to this target in solution. This binding affinity was used to create new phage libraries which were enriched with phage particles that specifically bound to synaptosome preparations.

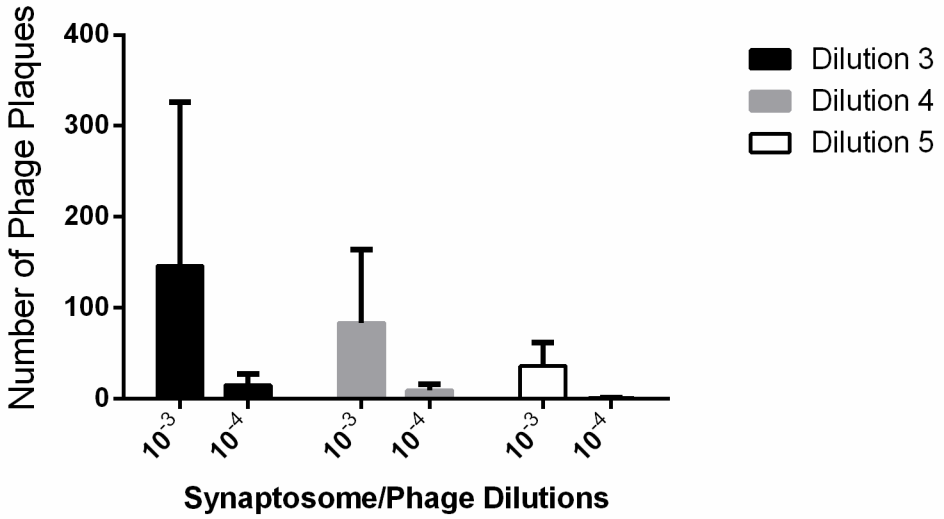

Figure 10 - Concentration dependent binding assay quantification. Bar chart (mean ± SEM, n = 3) showing number of phage plaques present on a bacterial lawn for different dilutions of synaptosomes and phage. Black bars represent the most

concentrated synaptosome sample from which accurate plaque counts could be made, dilution 3. Grey bars represent phage plaque counts from synaptosome dilution 4, and white bars represent phage plaque counts from the most dilute synaptosome dilution, dilution 5. After incubation with the original phage library, synaptosome samples were washed and titered. Phage plaque counts from two titering plates are shown here for each synaptosome dilution: titres 10^{-3} and 10^{-4}. From these results, we can see that as the concentration of synaptosomes decreased, the number of phage plaques also decreased. Similarly, the phage particles also decreased down the titre dilution. Together, these results provide evidence of the concentration dependent binding of phage particles to a substrate present in the synaptosome sample.

4.3.3 - Library Amplification

Once it had been established that phage particles could bind to synaptosomes in suspension, rounds of phage panning were carried out followed by library amplification. The original phage library was panned using the same protocol as for the concentration dependant binding assay. The following day, a 5µl sample of synaptosome dilution 2 was added to an overnight culture of ER2738 which had been diluted 1:20 in 20ml LB broth containing 20µg/ml tetracycline. This was incubated in a shaking incubator at 37°C for 4.5 hours. During this time, phage particles that have bound to synaptosomes infect the bacterial cells and replicate, resulting in an amplification of phage particles with fusion peptides that had a binding affinity with synaptosomes.

After 4.5 hours, bacteria were removed from the suspension by centrifugation and the phage particles were precipitated out overnight at 4^{o}C using 20% PEG: 2.5M NaCl. The following day, the phage particles were removed from suspension by centrifugation and re-suspended in 1ml TBS. The phage particles were then re-precipitated again briefly using 20% PEG: 2.5M NaCl. The re-precipitated phage was then pelleted out by centrifugation and re-suspended in 30µl TBS. This was the newly amplified phage library. This new library was used in the next round of panning and a second new amplified library was produced which was further enriched in phage particles that specifically bound to synaptosomes. Each new library produced was titered to ensure phage particles were present (Table 4).

Library	**Plaque Forming Units (per 10µl)**
Original	$1x10^{13}$
New Library 1	$5.6x10^{10}$
New Library 2	$3.1x10^{10}$
New Library 3	$2.9x10^{10}$

Table 4 – Titration results for each new phage display library produced from panning.

Panning was carried out a third time to produce a third new amplified phage library and it is from this library that phage plaques were picked, amplified individually and the DNA of each clone was sequenced.

4.3.4 - Plaque Amplification

After three successive rounds of panning and library amplification it was assumed that any phage particles which exhibited binding affinity to the target would be sufficiently enriched to show a consensus binding sequence.

Plaques were picked from titering plates from synaptosome panning with the third new amplification library. Plaques were picked by stabbing an individual plaque with a sterile Pasteur pipette and blowing the plaque and agar into a 1.5ml eppendorf (Figure 11). Each plaque should have contained phage particles that had identical DNA sequences. From a titering plate with less than 100 phage plaques, 16 plaques were chosen at random for Sanger sequencing. Typically, between 10 and 20 plaques are needed to reveal a consensus binding sequence.

Before plaque amplification was carried out, the plaque and agar were dissolved in 100µl TBS buffer and titered to determine the average number of pfu/10µl for each plaque. This was carried out to ensure that an optimal multiplicity of infection was used when amplifying the phage clone. Initially, entire phage plaques were used during the amplification process, which resulted in poor amplification and a low yield of DNA being extracted. By titering the plaques, it was determined that the number of pfu/10µl was in the thousands for each plaque.

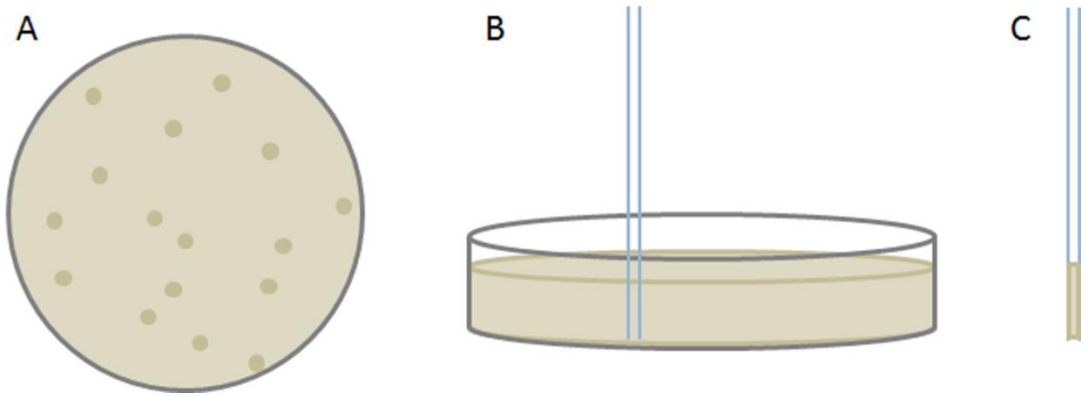

Figure 11: Schematic of plaque extraction from agar plate. (A) Plaques were picked from agar plates that had between 30 and 100 well separated plaques. (B) A sterile Pasteur pipette was used to stab the plaque through the entire depth of the agar. (C) Gentle suction was applied and the pipette tip was removed, bringing with it a plug of agar and the phage plaque. This was then blown into a 1.5ml eppendorf where it was re-constituted in 100µl TBS.

In order for phage particles to efficiently infect bacterial cells, the bacterial cells must be in the early log stages of the growth curve and the number of bacterial cells must be in considerable excess. An optimal multiplicity of infection for M13 phage particles is 10^{-4} (Reddy & McKenney, 1996). Using the turbidity analysis that had been performed on ER2738 earlier, it was determined that the number of bacteria present in the early log stages of the growth curve (OD_{600} 0.1) was approximately $8.269x10^{8}$ cells per ml. Based on these data, adding 10µl of re-constituted phage plaque to 1ml of OD_{600} 0.1 resulted in an optimal multiplicity of infection. Phage clones were amplified for 4.5 hours before the bacteria were removed by centrifugation and phage particles were precipitated out of solution using 20% PEG:

2.5M NaCl. DNA was extracted from the phage pellet using a phenol: chloroform extraction method with an ethanol precipitation step being carried out overnight at -20^{o}C. The DNA concentrations for each plaque were measured on the Nanodrop and a sufficient yield of DNA was obtained for sequencing (Table 5).

Phage Clone	**ssDNA Concentration (ng/µl)**	**260/280**
1	12	2.58
2	18.9	2.18
3	11.7	2.44
4	12.3	2.57
5	4.6	2.88
6	16	2.24
7	17.7	2.19
8	27	2.14
9	22.3	2.11
10	25.5`	2.03
11	19.4	2.21
12	20.6	2.29
13	31.1	2.10
14	6.2	3.31
15	24.9	2.10
16	27.2	2.14

Table 5 – Concentrations (ng/µl) and 260/280 absorbance ratios for DNA extracted from amplified phage clones.

4.3.5 - DNA Sequencing

DNA sequencing was carried out by The GenePool using BigDye reagents and an ABI 3730 capillary sequencing instrument. Approximately 100ng of DNA in 5µl was used per sample with 1µl -96 gIII sequencing primer (100pmol/µl) as per The GenePool's request.

Chromatographs were viewed on Sequencher 5.1 Demo software. The "find" function in Sequencher 5.1 Demo software was used to highlight the reverse complementary sequence of phage DNA that was immediately downstream of the random 36bp DNA insert. From this sequence, the next 36 base pairs were noted. After the 36 base pair sequence, the reverse complementary sequence of phage DNA that was upstream of the DNA insert was always observed, ensuring that the correct region was always read.

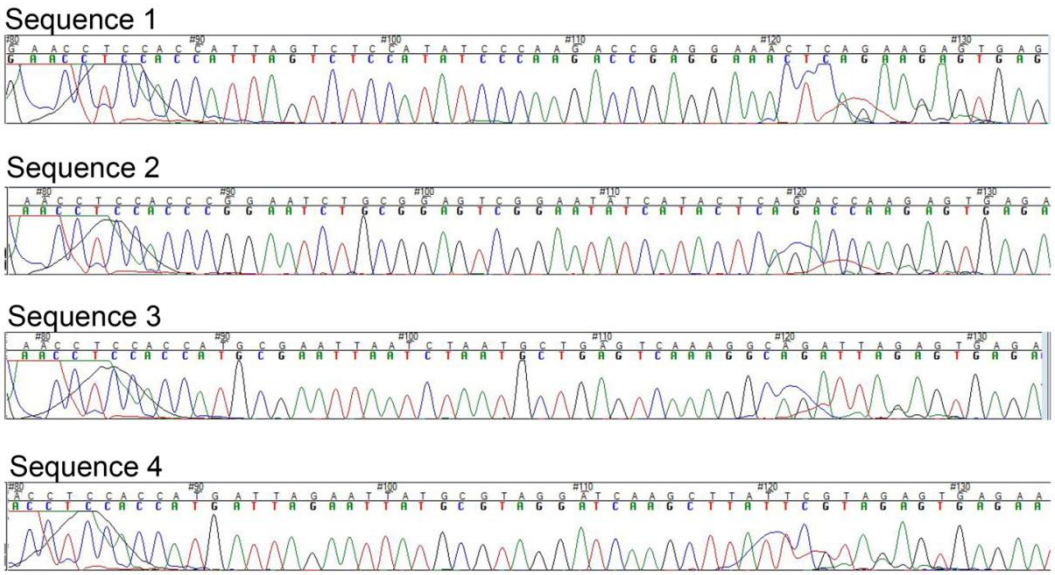

Figure 12 - Raw chromatographs. High quality sequences were obtained from all 16 phage plaques that were sequenced by The GenePool. The correct reading frame was identified in each sequence by using Sequencher 5.1 Demo Software's "Find"

function to highlight the sequence of phage DNA immediately downstream of the random DNA insert: ACC TCC ACC. This sequence was detected in all sequences, approximately 80bp into the DNA sequence.

Chromato-graph	**Sequence**	**Quality**
1	ATT AGT CTC CAT ATC CCA AGA CCG AGG AAA CTC AGA	89.3%
2	ATT AGT CTC CAT ATC CCA AGA CCG AGG AAA CTC AGA	77.9%
3	ATT AGT CTC CAT ATC CCA AGA CCG AGG AAA CTC AGA	78.2%
4	CGG AAT CTG CGG AGT CGG AT ATC ATA CTC AGA CCA	79.7%
5	ATT AGT CTC CAT ATC CCA AGA CCG AGG AAA CTC AGA	76.3%
6	CGG AAT CTG CGG AGT CGG AT ATC ATA CTC AGA CCA	77.8%
7	ATT AGT CTC CAT ATC CCA AGA CCG AGG AAA CTC AGA	87.9%
8	CGG AAT CTG CGG AGT CGG AT ATC ATA CTC AGA CCA	79.1%
9	ATG CGA ATT AAT CTA ATG CTG AGT CAA AGG CAG ATT	83.7%
10	CGG AAT CTG CGG AGT CGG AT ATC ATA CTC AGA CCA	76.7%
11	ATG ATT AGA ATT ATG CGT AGG ATC AAG CTT ATT CGT	84.4%
12	ATT AGT CTC CAT ATC CCA AGA CCG AGG AAA CTC AGA	77.8%
13	ATG CGA ATT AAT CTA ATG CTG AGT CAA AGG CAG ATT	78.9%
14	CGG AAT CTG CGG AGT CGG AT ATC ATA CTC AGA CCA	76.0%
15	ATT AGT CTC CAT ATC CCA AGA CCG AGG AAA CTC AGA	88.6%
16	ATT AGT CTC CAT ATC CCA AGA CCG AGG AAA CTC AGA	84.3%

Table 6 – Sequences obtained from the sequencing of 16 individual phage clones and their quality scores.

From the 16 raw chromatographs (Figure 12; Table 6), four unique peptide sequences were detected in the random DNA insert.

Reference	Sequence	Frequency (%)
P1	ATT AGT CTC CAT ATC CCA AGA CCG AGG AAA CTC AGA	50
P2	CGG AAT CTG CGG AGT CGG AT ATC ATA CTC AGA CCA	31.25
P3	ATG CGA ATT AAT CTA ATG CTG AGT CAA AGG CAG ATT	12.5
P4	ATG ATT AGA ATT ATG CGT AGG ATC AAG CTT ATT CGT	6.25

Table 7 – Sequence references and frequency of observation (%).

Sequences P1 and P2 appeared most frequently; eight and five times, respectively. A third sequence, sequence P3 appeared twice and sequence P4 appeared just once (Table 6; Table 7). From these data, we can conclude that panning with synaptosomes enriched phage particles that specifically bound to a target protein in the synaptosome preparation. Based on their frequency of appearance, sequences 1 and 2 were taken forward for peptide synthesis.

4.3.6 - Peptide Synthesis

4.3.6.1 - Plasmid Synthesis

4.3.6.1.1 – Design

In order to test if the peptides identified from panning the phage library actually bound specifically to synapses, we decided to produce fluorescently tagged peptides. To do this, a plasmid was designed that when induced, would express the peptide of interest fused to mCherry protein (Figure 13).

To produce an mCherry tagged version of the peptides of interest, the peptide sequences were first cloned into DNA vectors for mCherry. Then, the fusion vectors were inserted into a plasmid so that they could be transcribed and translated by bacterial cells. The plasmid that was chosen for this was pET30a(+), as it contains a T7 promoter site. After sequencing to ensure the plasmid contained the correct sequence necessary to produce the mCherry tagged peptide, the plasmids were electroporated into bacterial cells could be induced to produce protein under the control of a T7 promoter. Once the bacterial cells had produced a large quantity of protein, they were lysed and the protein was collected and purified (Figure 13). The tagged peptide was then incubated with preparations that were known to contain synapses to determine if the peptide did indeed bind specifically to synapses.

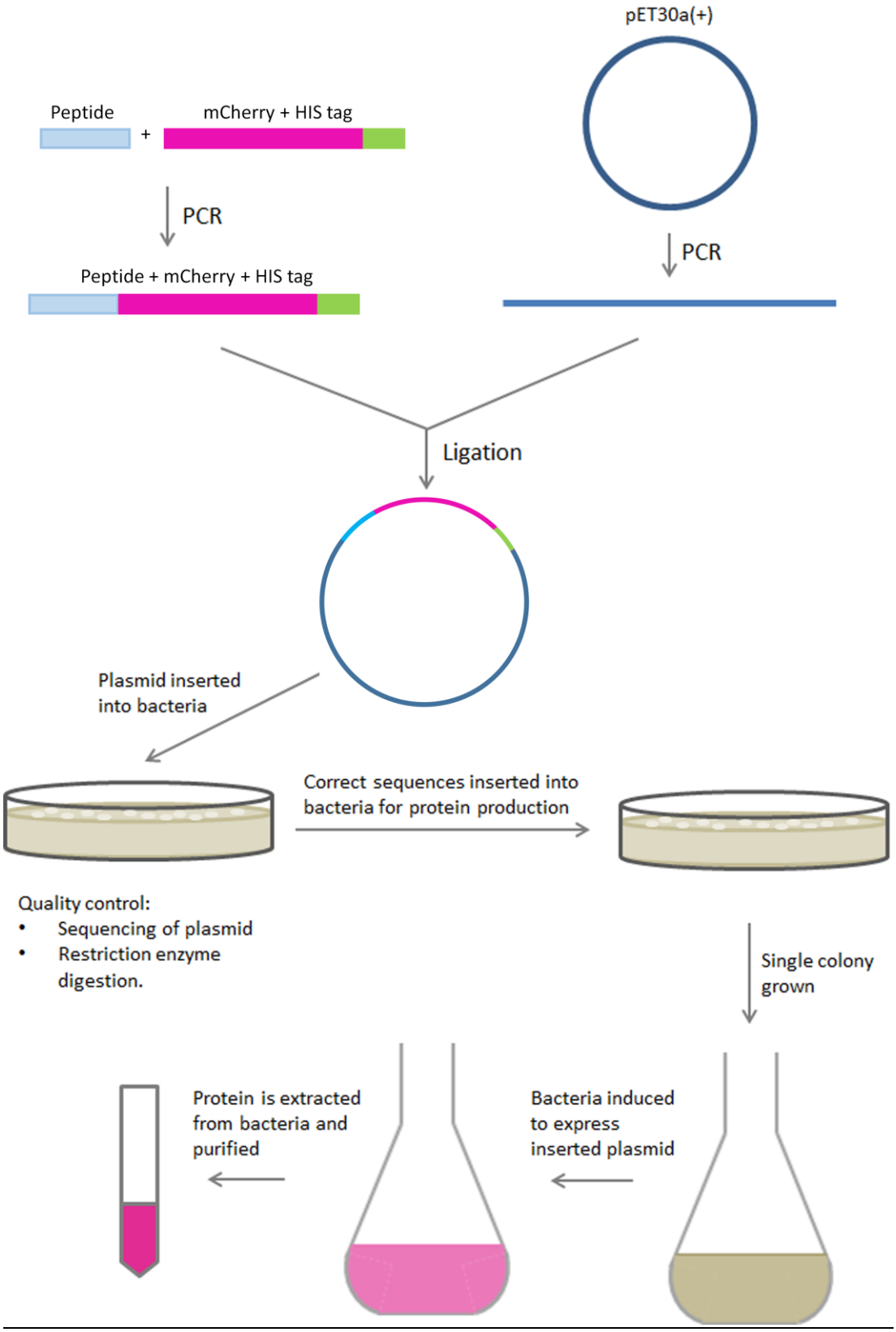
pET30a(+)
Peptide
+
mCherry + HIS tag
PCR
Peptide + mCherry + HIS tag
PCR
Ligation
Plasmid inserted into bacteria
Correct sequences inserted into bacteria for protein production
Quality control:
• Sequencing of plasmid
• Restriction enzyme digestion.
Single colony grown
Protein is extracted from bacteria and purified
Bacteria induced to express inserted plasmid

Figure 13 – Schematic of basic plasmid design. A plasmid was synthesised that, when induced, would produce the peptide sequence of interest fused to an mCherry protein. To do this, the peptide sequence was cloned into an mCherry vector using PCR. In a separate PCR reaction, a pET30a(+) vector was linearised. A ligation reaction was then used to join the peptide + mCherry vector into the linearised pET30a(+) vector to produce a plasmid. This plasmid was then inserted into bacteria, amplified and checked for the correct sequence. Once the correct plasmid sequence had been identified, it was inserted into a different type of bacteria for peptide synthesis. A single colony of transformed bacteria was grown and induced to express protein from the plasmid. The resulting protein was then extracted and purified.

4.3.6.1.2 - Plasmid Synthesis

To construct a plasmid that expressed the peptide of interest fused to mCherry protein, PCRs were carried out in order to amplify expression vectors with complementary ends for ligation.

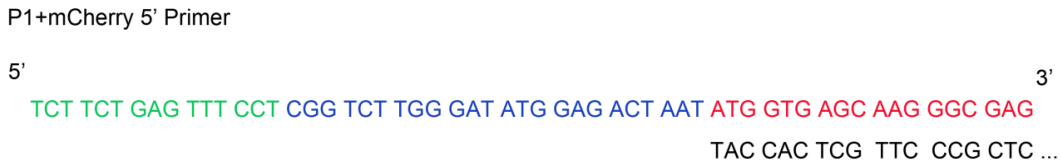

Figure 14 - Schematic of P1+mCherry PCR. This shows the 5' primer of the P1+mCherry PCR and how it incorporated the peptide sequence and the linearised-

pET30a(+) complementary ends. The last 18 base pairs of the primer (red) were complementary to the 5' end of the His-tagged bacterial expression vector for mCherry (black). Upstream of the mCherry complementary region was the peptide coding sequence (blue) and the complementary ends of the linearised vector (green). During the PCR, this extension primer became incorporated into the PCR product. The resulting PCR product contained the peptide-coding sequence, followed by the mCherry-coding sequence. Additionally, the PCR product had complementary ends to the linearised vector, for ligation.

The peptide sequence was added into a His-tagged bacterial expression vector for mCherry (Figure 14). This was achieved by designing 5' primers that contained the peptide sequence followed by the first 18 complementary base pairs of the mCherry vector (Figure 14). This meant that during replication, the peptide coding sequence would be replicated along with the mCherry vector, resulting in a PCR product that contained both the peptide coding sequence and the mCherry coding sequence (Figure 14). The 5' primer also contained 15bp extensions homologous to the vector ends of the pET30a(+) linearised vector (Figure 14). The 3' primer for this PCR reaction also added 15bp extensions homologous to the vector ends of linearised pET30a(+).

In a second PCR, a pET30a(+) vector was linearised by performing PCR with primers that were complementary to 22 base pairs in the vector. These primers also added an additional 15 base pairs to the vector ends that were complementary to the mCherry vector with the P1 peptide sequence.

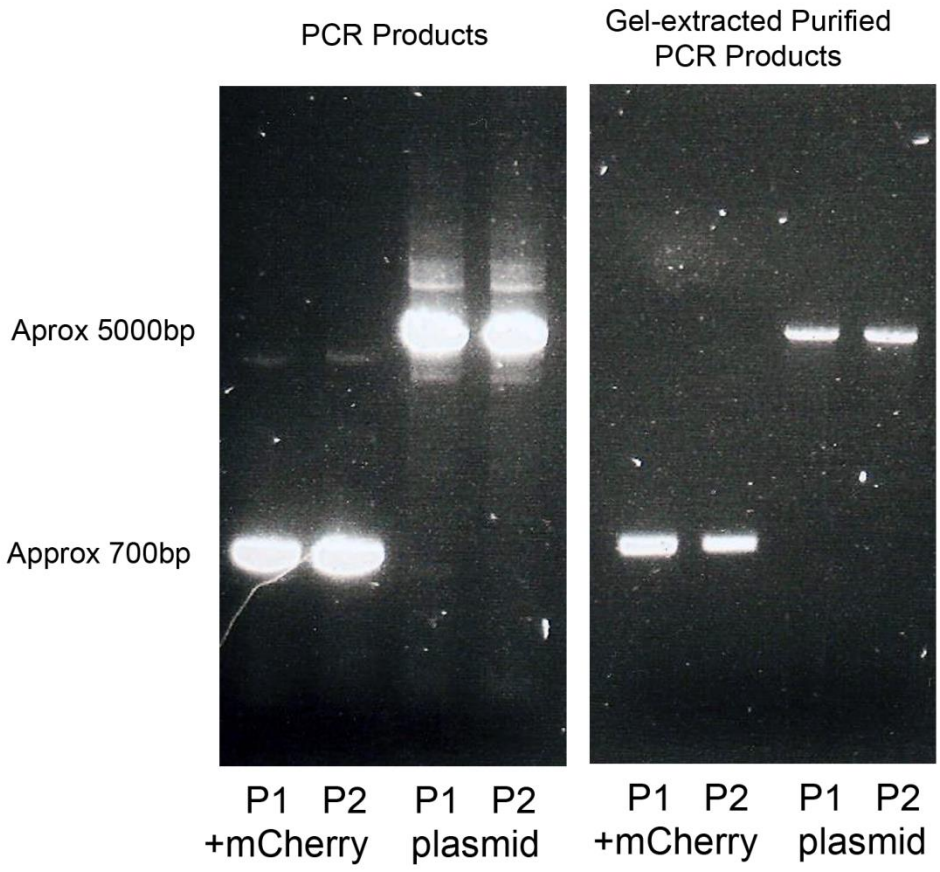

Figure 15 – PCR products on an agarose gel. After the PCR had been performed, samples of the PCR products were resolved on an agarose gel to check that they were the expected sizes. The His-tagged bacterial expression vector with the attached peptide sequence was expected to be around 700bp in size and the linearised pET30a(+) vector was expected to be around 5000bp in size. Both PCR product fragments were observed at the expected sizes. In order to perform a ligation, DNA of the correct size was excised from the agarose gel and purified using QIAGEN Quick DNA Extraction Kit. Samples of the purified DNA were resolved on an agarose gel again to check that the DNA was sufficiently free of contamination and was still of the correct size.

The DNA fragments from each PCR were purified using QIAGEN Quick DNA Extraction Kit (Figure 15). The PCR products were resolved on a 0.8% agarose gel and cut from the gel using a razor blade over an Invitrogen Safe Imager. The excised agarose was weighed and the DNA was extracted from the agarose following the manufacturer's instructions (Figure 15). A Nanodrop was used to measure DNA concentration of each DNA fragment (Table 8).

PCR Product	Concentration (ng/µl)	260/280
P1+mCherry	14.7	1.85
P2+mCherry	8.5	1.72
P1 pET30a(+)	10.2	1.77
P2 pET30a(+)	25.2	1.87

Table 8 – Concentration (ng/µl) of DNA fragment excised and purified from agarose gel.

The linearised pET30a(+) vector and its complementary peptide + mCherry expression vector were ligated using In-Fusion HD Cloning Kit (PT5162-1, Clontech). 4µl of the ligation reaction was then used to transform one aliquot of One Shot TOP10 Chemically Competent E.Coli (C4040-3, Invitrogen) by heat-shocking the cells and forcing them to take up the plasmid. The cells were then plated on agar containing 50ng/ml kanamycin plates and incubated overnight at 37^{o}C. The following day, many colonies were observed, confirming that the transformation was successful (Figure 16).

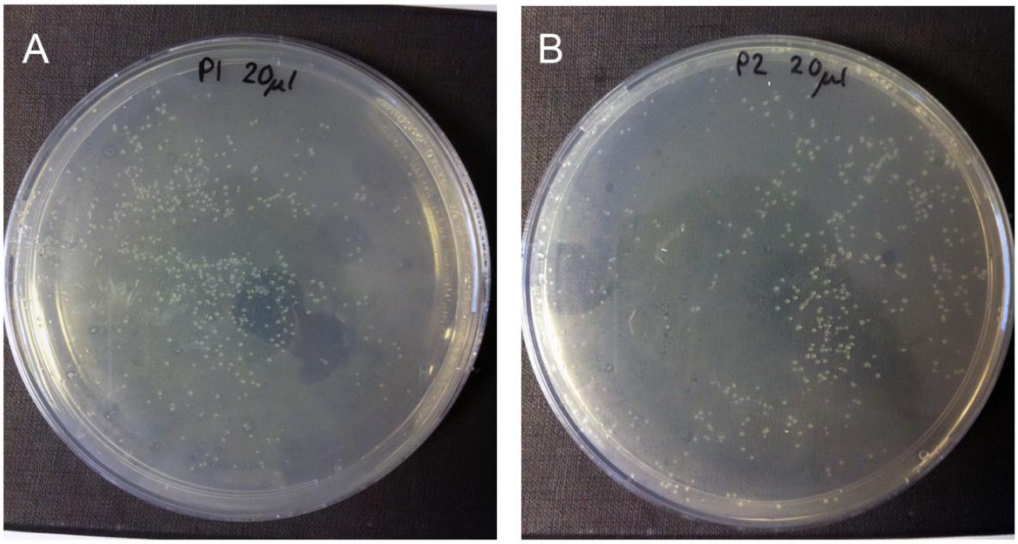

Figure 16 - Colonies of transformed TOP10 E.coli on agar supplemented with 50ng/ml kanamycin plates. Three individual colonies from each plate were amplified and the plasmid DNA sequence was checked to ensure that the plasmid had ligated correctly. (A) Colonies can be seen growing on the agar plate after the P1+mCherry plasmid was inserted into TOP10 cells. (B) Colonies of TOP10 E.coli that contained the P2+mCherry plasmid.

In order to ensure that the ligation had occurred as expected, a Miniprep was performed on three colonies selected at random from P1+mCherry and P2+mCherry plates. The extracted DNA concentration and quality was tested on a Nanodrop (Table 9) and sent to The GenePool for sequencing.

Colony	Concentration (ng/µl)	260/280
P1.1	31.3	1.87
P1.2	31.5	1.84
P1.3	30.5	1.85
P2.1	28.6	1.82
P2.2	29.6	1.87
P2.3	29.4	1.80

Table 9 – Concentration (ng/µl) and 260/280 absorbance ratios of DNA extracted from Minipreps of colonies of transformed TOP10 cells.

Sequencing of the plasmids by The GenePool was successful for two out of six Minipreps, with P1.3, P2.1, P2.2 and P2.3 producing no readable sequence. Chromatographs for P1.1 confirmed that the ligation had occurred correctly (Table 10). However, the chromatographs for P1.2 showed that a codon of the peptide was incorrect and the mCherry coding sequence was disrupted as a result (Table 10). No DNA from Minipreps of any of the P2 colonies was taken forward for peptide synthesis. Peptide synthesis continued with only P1 using the DNA from Miniprep P1.1.

Colony	Sequence
P1.1	ATG GCT TCT **TCT GAG TTT CCT CGG TCT TGG GAT ATG GAG ACT AAT** ATG GTG
P1.2	ATG GCT TCT **TCT GAG TTT CCT CGG TCT TGG GAT ATG GAG ACT** AGG TGA GCA
P1.3	N/A
P2.1	N/A
P2.2	N/A
P2.3	N/A

Table 10 – Sequences obtained from Minipreps. The peptide sequence is highlighted in bold text.

4.3.7 - Peptide Synthesis, Extraction, and Purification

In order to synthesise large quantities of the tagged peptide, (DE3)pLysS cells were used. These cells can express any protein that is under the control of a T7 promoter, which the pET30a(+) vector contained. Isopropyl β-D-1-thiogalactopyranoside (IPTG) un-inhibits the lacUV5 promoter and allows transcription of the T7 RNA polymerase gene, thereby driving expression of genes under the control of a T7 promoter.

(DE3)pLysS cells were made electro-competent and electro-porated with 5µl of a 1:10 dilution of P1.1 mini-prep extracted DNA. The cells were plated on agar plates supplemented with 50ng/ml kanamycin and 34µg/ml chloramphenicol and incubated

overnight at 37°C. The following day, many colonies were observed on the plates, confirming that the electroporation was successful (Figure 17).

Figure 17 - Double selective agar plate (50ng/ml kanamycin supplemented with 34µg/ml chloramphenicol) with successfully transformed (DE3)pLysS cells. Electro-competent (DE3)pLysS cells were electro-porated with the P1+mCherry plasmid that had ligated correctly (P1.1).

In order to force (DE3)pLysS bacterial cells to produce large quantities of protein from the inserted plasmid, cells were induced by addition of 50mM IPTG. The following day, the induction of mCherry was apparent as the bacteria appeared a bright pink colour (Figure 18A). In order to extract the P1+mCherry protein, the (DE3)pLysS bacteria must undergo a freeze/thaw cycle. This disrupts the plasma

membrane of the bacteria, allowing lysosomes to leak out of the cells. These lysosomes then lyse the bacterial cells, releasing the cells contents into the buffer. After the freeze/thaw cycle, the cells were centrifuged at 10000 x g for 10 minutes to pellet cell debris and non-lysed cells (Figure 18B). The supernatant was collected and stored at 4^{o}C.

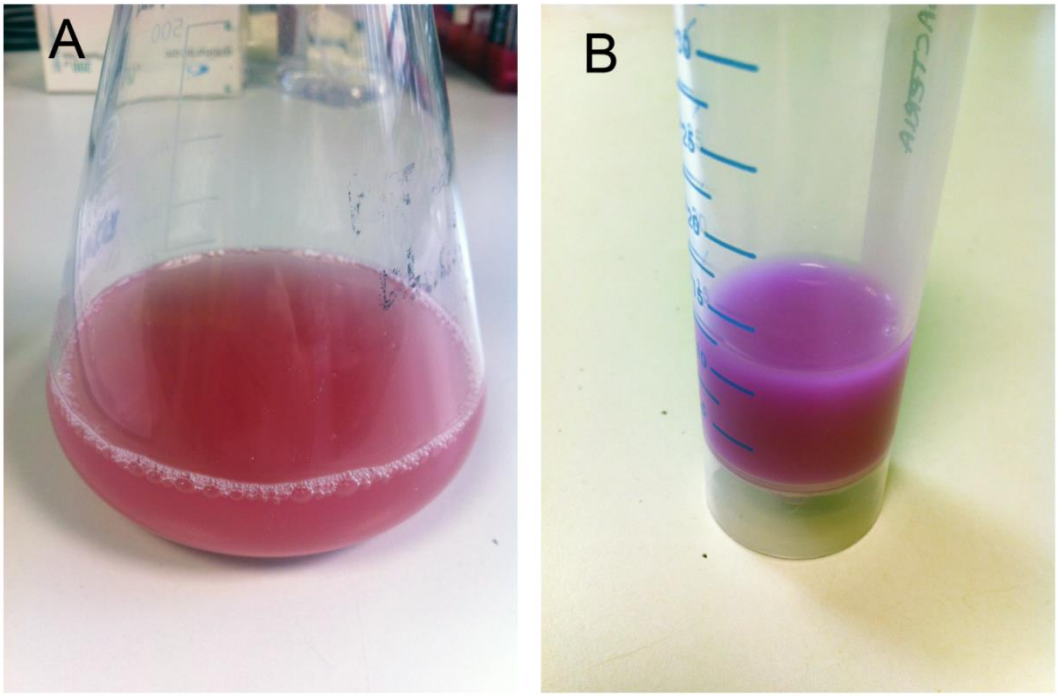

Figure 18 – mCherry expression in induced (DE3)pLysS cells. (A) Bacterial cells were induced overnight at room temperature with 50mM IPTG. Production of mCherry protein was evident in the bright pink colour of the bacteria after induction. (B) The induced cells were pelleted and re-suspended in phosphate buffer where the pink colour of the mCherry protein was even more evident.

The P1+mCherry protein was then purified from the supernatant using a Disposable Gravity Column (Figure 19). The mCherry bacterial vector contained a His-tag which produced a cluster of histidine residues on the N-terminus of the mCherry protein. This cluster of histidines has a binding affinity with ions such as nickel and cobalt, which can be utilised to purify the protein. The supernatant was applied to the Gravity Column containing cobalt ions and allowed to flow through (Figure 19A). The binding of the P1+mCherry protein to the cobalt ions in the column could be observed by a strong pink colour which accumulated in the gel (figure 19B). The Gravity Column was washed to remove any lingering bacterial proteins, and the P1+ mCherry protein was then eluted from the column using a high concentration imidazole buffer (150mM imidazole, 50mM sodium phosphate, 300mM sodium chloride), which competed with the His-tag to bind to the cobalt ions (Figure 19C). The flow through was collected and the imidazole was removed by repeated inverse centrifuge filtration, with the protein being re-suspended in 0.1M PBS. The protein was then mixed 1:1 with sterile glycerol, aliquotted, and stored at -20^{o}C.

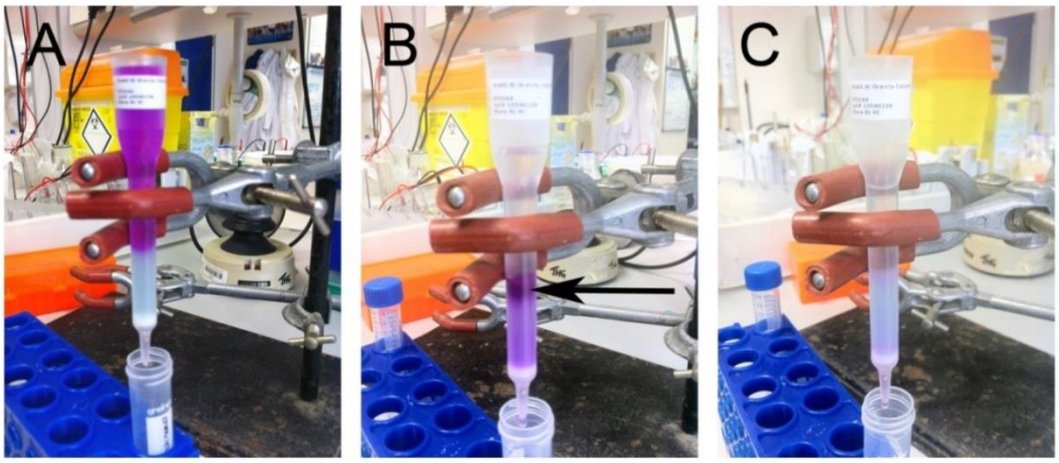

Figure 19 - Purification of P1+mCherry using a Gravity column. (A) The protein in buffer was added to the Gravity column and allowed to flow through. (B) The protein

had bound to the cobalt ions in the gel. The black arrow shows a concentrated section of the gel where the majority of the pink P1+mCherry protein had bound. (C) After washing the gel with a low (5mM) imidazole buffer to remove excess bacteria proteins, the bound P1+mCherry protein was eluted using a high (150mM) imidazole buffer. The cobalt gel had returned to its original green-blue colour as the pink mCherry protein was washed out.

The molecular weight of the purified P1+mCherry (expected to be around 24kDa) was determined using by running the protein, along with samples from various stages of purification, on an SDS-PAGE gel along with a Sharp Pre-Stained Protein Standard (Figure 19). In the non-induced (DE3)pLysS bacteria lysate (Figure 20A), no protein band was detectable at ~24kDa as would be expected. In the induced, but un-purified lysate, a band was detectable at ~24kDa confirming that a protein of the correct molecular weight was produced by the 50mM IPTG induction (Figure 20B). The run-through from the Gravity Column showed that no protein with a molecular weight of ~24kDa was present, confirming that this protein had efficiently bound to the cobalt ions in the column due to the His-tag present on the protein (Figure 20C). The purified and concentrated protein sample showed that a protein of approximately 24kDa was present and appeared to be more concentrated than the 24kDa protein detected in the un-purified lysate (Figure 20D). Additionally, an approximately 50kDa protein was detectable in all lanes but was particularly strongly expressed in the induced bacteria lysate and the purified and concentrated protein (Figure 20). We hypothesised that this 50kDa protein was possibly a dimer of the P1+mCherry protein. An additional approximately 30kDa protein band was detected in all

samples. It was suspected that this was a bacterial protein, due to its presence in the non-induced bacteria lysate sample (Figure 20A), that happened to have a binding affinity with cobalt ions in the Gravity Column.

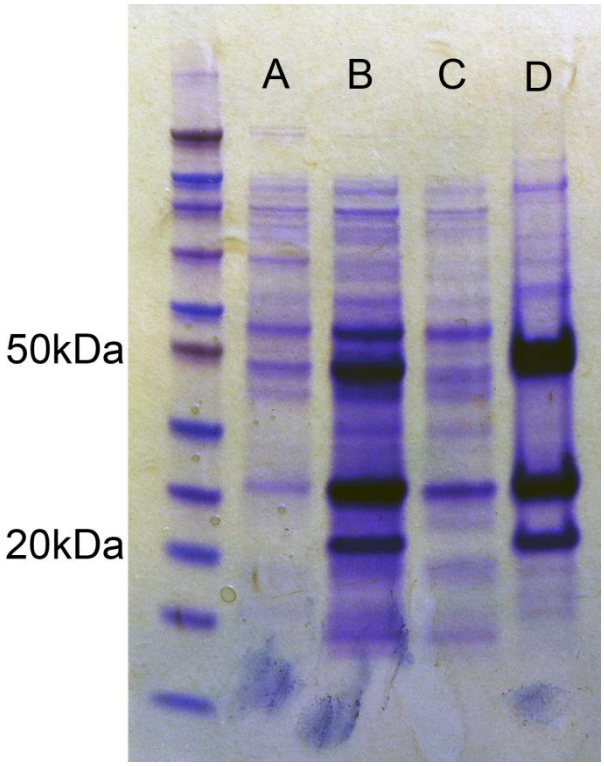

Figure 20 – An SDS-PAGE gel showing weights of proteins present at different stages of P1+mCherry protein induction and purification. (A) Protein extracted from non-induced (DE3)pLysS cells. (B) Protein extracted from induced but un-purified (DE3)pLysS cells. (C) Run-through from the Gravity Column. (D) Purified and concentrated P1+mCherry protein, mixed 1:1 with glycerol.

A BCA assay was carried out in order to determine the concentration of the P1+mCherry protein. From this, it was determined that there was 11.63mg/µl protein in the purified protein sample when mixed 1:1 with glycerol (Figure 21).

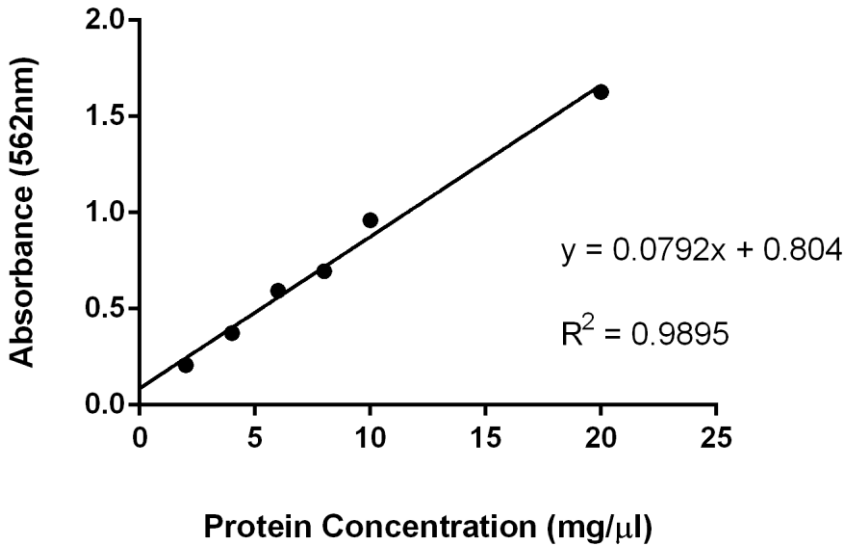

Figure 21 – BCA assay standard curve graph. A BCA assay was carried out to determine the concentration of protein in the purified lysate (mg/µl). The BCA assay for the purified lysate gave a mean 562nm absorbance reading of 1.003 (n = 3). Using the equation of the line from the standard curve graph, this equates to a concentration of 11.63mg/µl of protein, when mixed 1:1 with glycerol.

4.3.8 - Peptide Binding Assays

To test whether the P1+mCherry protein could bind to synapses, varying concentrations were incubated in mouse primary cortical neuron cultures at 15DIV. It was expected that this would be the most likely synaptic preparation in which the protein would bind, as the phage library had been panned with synaptosomes produced from whole brain homogenate.

The P1+mCherry protein was diluted 1:50 and 1:100 in the cells' media and incubated with the live cells at 37^{o}C for 30 minutes. The media was removed, the cells were washed briefly in room temperature 0.1M PBS, and then fixed with room temperature 4% PFA for 10 minutes. From this procedure, mCherry-positive staining was observed in puncta around the cell body, as would be expected from a synaptic marker stain (Figure 22 and 23). Cells were also stained with the vesicle marker, SV2 in order to identify areas of pre-synaptic contact (Figure 24B). In these dual-labelled cells SV2-positive punctate staining was also observed around the cell body; however it did not co-localise with the mCherry-positive puncta (Figure 24C).

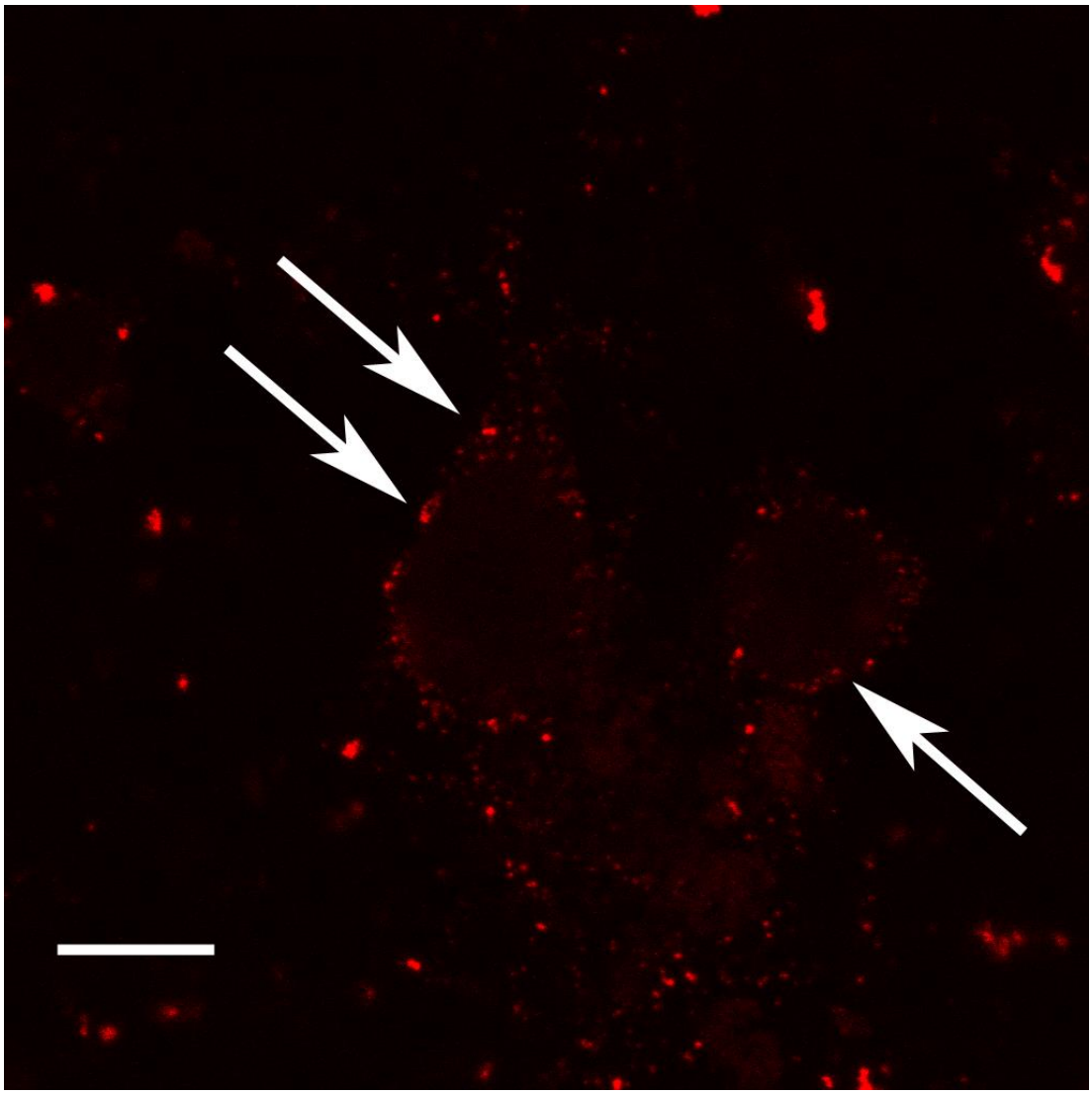

Figure 22 – Z-stack confocal images of mCherry-positive (red) puncta in 15DIV primary cortical neuron cultures. A 1:50 dilution of P1+mCherry was incubated with cells for 30 minutes prior to fixation. Punctate staining was visible on the cell surface of neurons (white arrows), suggesting that the P1+mCherry protein had a binding affinity with a peptide present on the cell surface. Larger aggregates of mCherry-positive staining were also observed on the coverslip where no cells were present. However, these aggregates appeared larger and more angular than the punctate staining observed on the cell surface. The large angular aggregates were also observed less frequently than the punctate staining on the cell surfaces. Scale bar = 10µm.

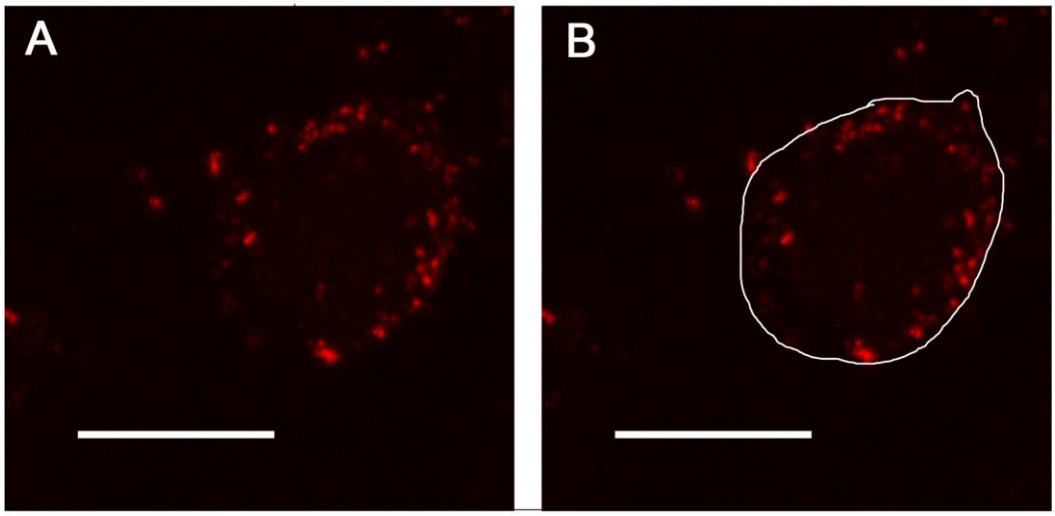

Figure 23 – Z-stack confocal images of P1+mCherry-labelled cells with outline. (A) A cell body of a primary culture neuronal cell with punctate P1+mCherry staining on the surface of the cell. (B) The same cell is shown, but with a white outline added

in Adobe Photoshop to highlight the shape of the cell. The P1+mCherry puncta observed on the cell are concentrated around the cell surface. Scale bar = 10µm

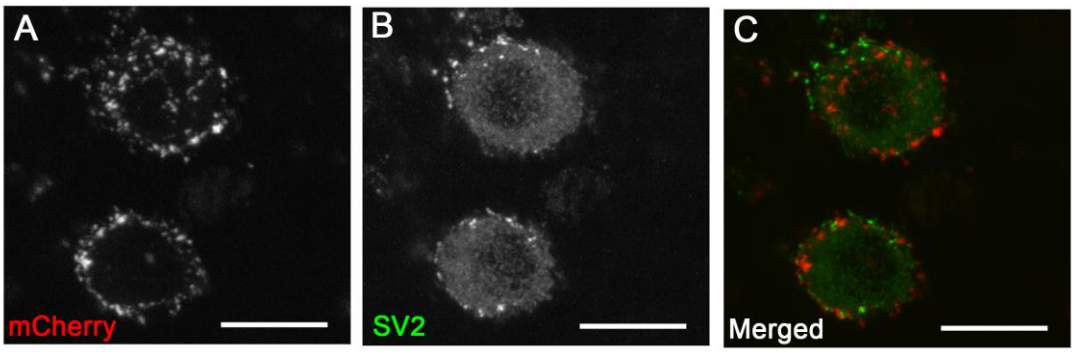

Figure 24 – Z-stack confocal images of dual-labelled cells with SV2 (green) and mCherry (red). A 1:50 dilution of P1+mCherry was incubated with cells for 30 minutes prior to fixation. After fixation, cells were co-stained with anti-SV2 (green). (A) mCherry-positive puncta are again observed on the cell surface. (B) Punctate staining of SV2, a vesicle protein, is also observed on the surface of cells. (C) A merged image of mCherry (red) and SV2 (green) staining shows that there is no co-localisation between the puncta on the surface of the cells. Scale bars = 10µm.

The P1+mCherry protein's binding ability was also tested on cells fixed with 4% PFA (Figure 25). After cells were fixed and stained with SV2, 1:50 and 1:100 dilutions of the P1+mCherry protein in 0.1M PBS was incubated with the cells for 30 minutes, before being washed off briefly with 0.1M PBS. Under these conditions, no mCherry-positive puncta were observed in the cultures (Figure 25B), however SV2-positive puncta were still observed (Figure 25A and 25C). A possible explanation for this lack of mCherry-positive staining after fixation is that the process of fixation

altered the binding site of the peptide in such a way that the peptide no longer had a binding affinity.

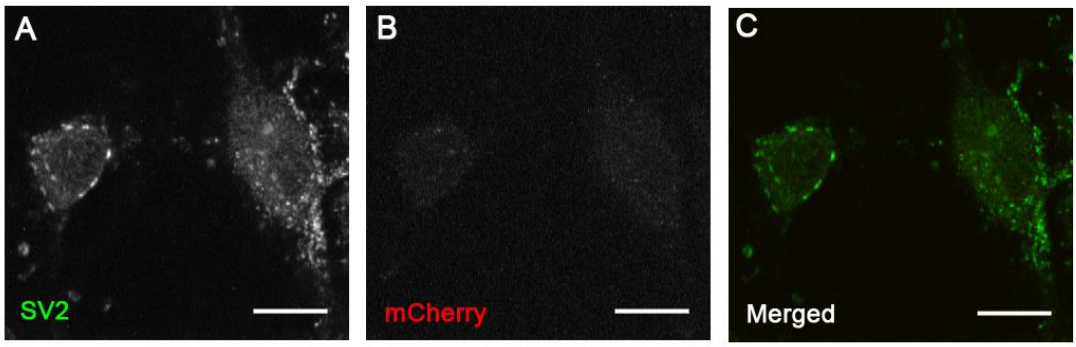

Figure 25 – Z-stack confocal images of 15DIV primary cortical neuron cells stained with a 1:50 dilution of P1+mCherry after fixation and SV2 staining. (A) SV2 punctate staining was visible on the cell surface. (B) No mCherry-positive puncta are visible on the surface of the cells when the P1+mCherry protein is applied to cells after fixation. (C) A merged image of SV2 staining (green) and mCherry staining (red). Scale bars = 10µm.

In order to test whether the P1+mCherry protein would bind to any off-target peptides, 1:50 and 1:100 dilutions of the protein in 0.1M PBS were incubated with skeletal muscle, before and after muscle fixation. Under these conditions, no mCherry-positive staining was noted in any of the muscle fibres, or other cell types present in skeletal muscle such as neurons, glial cells, fibroblasts or endothelial cells (Figure 26B). It was initially hoped that P1+mCherry protein would have the ability to bind to any synapse, including peripheral synapses. However, no mCherry-positive staining was observed at neuromuscular junctions (Figure 26B and 26C).

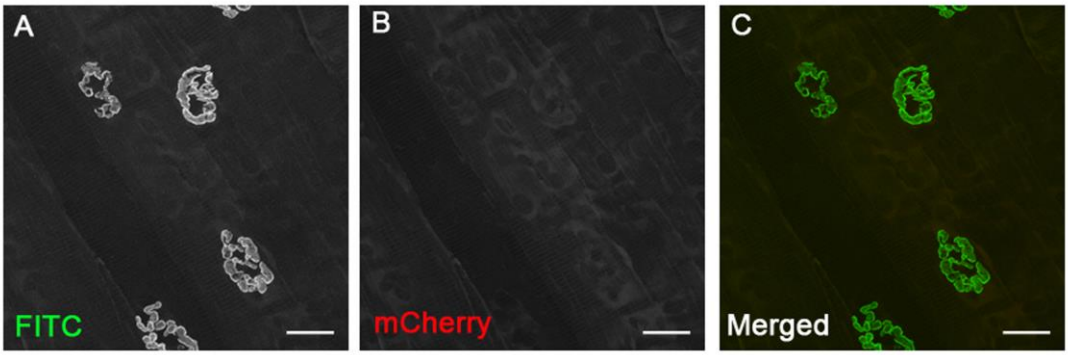

Figure 26 – Z-stack confocal images of wild type adult mouse skeletal muscle stained with a 1:50 dilution of P1+mCherry (red) prior to fixation and FITC-conjugated α-bungarotoxin (green). (A) FITC-conjugated α-bungarotoxin staining the acetylcholine receptor clusters of neuromuscular junctions. (B) mCherry staining of skeletal muscle. No puncta or aggregates were observed in the skeletal muscle. (C) A merged image of FITC-conjugated α-bungarotoxin (green) and mCherry (red) showing no co-localisation in skeletal muscle. Scale bars = 20µm.

4.4 - Discussion

In summary, a peptide with a binding affinity for central synapses was identified via a phage display system and synthesised with a fluorescent label. Initially, it was demonstrated that it was possible to produce repeatable concentration dependent binding of phage particles to synaptosomes in suspension. As far as we are aware, this method of panning a phage display library has not been previously published. Next, we showed that it was possible to enrich specific phage clones by panning a phage display library with synaptosomes in suspension. Out of 16 individual phage

clones sequenced, eight were identical, implying that this fusion peptide was the most likely to show binding affinity for a target in the synaptosome preparation.

Once the sequences of the fusion peptides displayed on the phage particle had been identified, it was possible to synthesise an identical peptide fused to an mCherry protein by producing a plasmid containing the peptide sequence followed by an mCherry sequence and a His-tag, all under the control of a T7 promoter. This plasmid was successfully introduced to (DE3)pLysS bacteria where it was expressed by inducing the bacteria to produce transcripts from a T7 promoter. The P1+mCherry protein was then successfully collected and purified.

Lastly, the results showed that this tagged peptide had the ability to bind to central synapses. By incubating the peptide with primary cortical neuron cultures, we were able to observe punctate staining on the surface of the cell body, similar to that of the vesicle protein, SV2. The P1+mCherry protein was also shown to have specificity for these sites, as the protein did not show a binding affinity to any cell type present in skeletal muscle. However, synaptic binding was not observed in peripheral synapses such as the neuromuscular junction, implying that this peptide has specific affinity for central synapses rather than being a pan-synaptic marker as we had initially hoped.

It will be necessary to further test the P1+mCherry protein's ability to bind to synapses before a definite conclusion can be reached about its specificity. Immunocytochemical staining for more specific synaptic markers, such as the post-synaptic markers PSD-95 and synGAP, and pre-synaptic marker synaptobrevin, would be helpful in addressing whether the protein is binding to synapses.

Quantification of the number of mCherry-positive puncta being formed over time and correlating with the number of synapses being formed in developing primary cortical neuron cultures would also add weight to the theory that P1+mCherry protein is binding to a synaptic target.

4.4.1 - Strategy Rationale

Most phage display panning is carried out using a specific target protein immobilised on a plastic surface. However, we specifically wanted to target extra-cellular domains of synaptic proteins, to ensure that the final produced peptide would be able to bind to the intended target without interfering with synaptic function. By coating a plastic surface with a target protein, we would have no control over which domain, extra-cellular or otherwise, the phage would show affinity for. By using synaptosome preparations, we can ensure that only phage particles with an affinity for an extracellular protein motif present at the surface of the synapse will be selected for. Additionally, we may have selected for phage which bind to a previously unidentified extra-cellular synaptic protein.

An mCherry tag was chosen to label the peptide as mCherry is very bright and photostable. Additionally, an mCherry vector with a His-tag was readily available to use for this projet. However, mCherry has a molecular weight of 25kDa which may have affected the peptide's ability to enter into small areas such as the synaptic cleft. Choosing a fluroscent tag with a smaller molecular weight may have been beneficial.

The peptide sequence was inserted into the mCherry vector so that P1 would be directly conjugated onto the mCherry protein. With hindsight, it would have been

beneficial to also produce a P1+mCherry protein with a linker connecting the P1 sequence and the mCherry protein. This linker region may have allowed the P1 peptide to access small areas of the synapse that the mCherry protein was too large to enter.

4.4.2 - Improvements in Experimental Design

In order to ensure that the mCherry-positive punctate staining observed around cell bodies was not an artefact, it would be necessary to produce an mCherry protein in an identical manner but with no fusion peptide. This would ensure that any signal was not simply due to the mCherry protein, or the His-tag, binding to an unintended target present on the cell body. However, given that no mCherry signal was detected in skeletal muscle preparations, it seems unlikely that the mCherry or His-tag are the cause of the punctate staining observed on the primary cortical neuron cell bodies.

Although no nucleic contamination was detected in the P2 fraction of synaptosomes in these preparations, the synaptosomes produced for panning are known as "crude synaptosomes". This is due to the fact that the P2 fraction may still contain contaminating myelin, plasma membrane and mitochondria (Dunkley et al., 2008). This contamination means that there is a small risk of selecting for phage particles with fusion peptides that have an affinity for contaminates instead of synaptic membranes. It is possible to produce very pure synaptosome preparations using discontinuous gradients of Percoll (Dunkley et al., 2008). Percoll is essentially a suspension of plastic-coated silica particles approximately 17nm in diameter originally developed for subcellular fractionation (Dunkley et al., 2008). To prepare

pure synaptosomes using a Percoll gradient, different concentrations of Percoll are layered on top of one another, from most concentrated to least concentrated (Dunkley et al., 2008). The S1 fraction of homogenised brain tissue is then gently added on top of this gradient and centrifuged at 20000rpm for 5 minutes (Dunkley et al., 2008). During this centrifugation, different components of the S1 fraction are caught at the interfaces down the Percoll gradient, including synaptosomes, mitochondria, membranes and myelin (Dunkley et al., 2008). Synaptosomes are collected at the interface between the 15% and 23% layers (Dunkley et al., 2008). Panning the phage library with these ultra-pure synaptosomes would ensure that only phage particles with fusion peptides capable of binding to a protein on the surface of a synapse would be enriched. However, the gradients must be produced perfectly in order to ensure pure synaptosomes – any blurring of the interfaces could result in contamination. For these reasons, and the lack of detectable nucleic contamination in the P2 fraction, it was decided that crude synaptosome preparations would be adequately pure to pan the phage library. Additionally, the synaptosomes produced for this study were not examined for pre- or post-synaptic markers.

To further ensure that any enriched peptide sequences were specifically binding to a target that was present in only the P2 fraction of the synaptosome preparation, a second amplified phage library could have been produced by panning the phage display library with the P1 fraction. This would enrich for phage particles with fusion peptides which had the ability to bind to unwanted targets such as cell body contaminates, glial cells, or mitochondria. By sequencing phage particles from this second enriched library, it would be possible to eliminate peptide sequences that

appeared in both the P1 and P2 panned libraries and therefore did not bind specifically to a target present in the synaptosome fraction.

4.4.3 – Conclusion

In conclusion, we have shown here that it is possible to pan a phage library with synaptosomes held in suspension. The peptide sequences enriched by the successive rounds of panning may have a synaptic binding ability, as shown by the punctate staining visible on cell bodies of primary culture neurons. However, further testing is required to ascertain whether the peptide has a specific affinity for areas of synaptic contact.

Chapter 5: General Discussion

The work presented in this study has shown that motor unit vulnerability varies across a spectrum in a severe mouse model of SMA. This motor unit vulnerability does not correlate with motor unit morphology, as it does in ALS. Motor unit vulnerability also did not correlate with any other morphological factor investigated. Microarray analysis of vulnerable and resistant motor unit gene expression revealed significant differences in pathways known to be associated with SMA, and significant differences in a number of genes known to be involved in neuro-protection and neuro-degeneration. Based on this, it is likely that the spectrum of vulnerability in SMA is driven by specific molecular properties of motor units. Additionally, a peptide was identified that has shown a potential affinity with areas of synaptic contact. It is hoped that this peptide can be developed further and used to transiently label synapses *in vivo* in both humans and animal models as a research and diagnostic tool.

5.1 - Motor Unit Vulnerability in SMA

The findings of a spectrum of vulnerability in a severe mouse model of SMA are consistent with previous findings (Murray et al., 2008; Ling et al., 2012). Murray et al. (2008) first reported differences in the extent of denervation found in the levator auris longus muscle in two SMA mouse models. This study found the same pattern of denervation as Murray et al. (2008), with the caudal band being severely denervated and the rostral band being almost unaffected. Murray et al. (2008) also noted extensive denervation of the transversus abdominis, a postural muscle found in

the trunk. This study has also observed denervation in the transversus abdominis, and extended the characterisation of trunk muscles to include the triangularis sterni which was also found to be extensively denervated. The triangularis sterni is one of the innermost intercostal muscles, a group of muscles which are known to be denervated in SMA patients, contributing to their characteristic bell-shaped upper torso (Lunn & Wang, 2008). Furthermore, the study by Ling et al. (2012) found a spectrum of vulnerability in a different cohort of muscles, in a different mouse model of SMA. They noted that the postural muscles appeared to be more susceptible to denervation than muscles of other body areas. The findings of extensive denervation in trunk and postural muscles, which are known to be affected in SMA patients, further demonstrates that this selective denervation follows a distinct pattern rather than being caused by random degeneration of motor units.

Additionally, this study has extended the characterisation of NMJ pathology in the *Smn*$^{-/-}$;*SMN2*$^{+/+}$ mouse model by analysing muscles of the hind limbs. Here, vulnerable motor units were found to innervate the tibialis anterior and gastrocnemius muscles, while the extensor digitorum longus muscle was innervated by resistant motor units. These data reported here, and in previous studies, serve as evidence that denervation of motor units in mouse models of spinal muscular atrophy follow a distinct pattern and are not merely a result of natural variation between mice, mouse models, or litters.

5.2 - Underlying Cause of Motor Unit Vulnerability

Prior to this study, there was little evidence of an underlying cause of differential motor unit vulnerability in SMA. Previous studies had suggested muscle fibre type or the synapsing phenotype of motor units could underlie differential vulnerability (Murray et al., 2008; Ling et al., 2012). However, no correlation between muscle fibre type and motor unit vulnerability could be found in this study or the studies by Murray et al. (2008) and Ling et al. (2012). Additionally, pathologies in the post-synaptic compartment of the neuromuscular junction do not correlate with motor unit vulnerability (Murray et al., 2008). Taken together, these data effectively rule out a muscle-based driver of differential motor unit vulnerability in SMA.

In the adult onset motor neuron disease, ALS, a correlation has been extensively reported between large motor units and increased vulnerability, both in mouse models and human patients (Bradley et al., 1983; Fischer et al., 2004; Hegedus et al., 2007; Valdez et al., 2012). In contrast to what has been found in ALS, no correlation could be detected between motor unit size and vulnerability in SMA in this study. This implies that mechanisms underlying motor unit vulnerability differ between ALS and SMA, a result that was quite surprising given the recent evidence suggesting that ALS and SMA are linked at the molecular level (Zou et al., 2007; Turner et al., 2009; Kariya et al., 2012; Yamazaki et al., 2012). This could have important implications on the development of therapeutics in motor neuron disease.

Currently, the only licensed treatment for ALS is the anti-glutamatergic drug riluzole which modestly increases lifespan by providing some protection to neurons against excitotoxicity (Cifra et al., 2013). A number of studies of the effects of riluzole on

SMA have been carried out with disappointing results. In 2003, Haddad et al. administered riluzole to a mouse model of SMA and reported a modest increase in lifespan but no effect on the loss of axons. Also in 2003, Russman et al. conducted a phase I clinical trial of the tolerance of riluzole in type I SMA patients. More than half of the SMA patients prescribed riluzole died within the time period expected for type I SMA, bringing the effectiveness of riluzole as a treatment for SMA into question (Russman et al., 2003). It is possible that riluzole's lack of effectiveness in SMA is due to differences in the mechanisms underlying motor unit vulnerability in ALS and SMA.

5.3 – Gene Expression Profiles in Vulnerable and Resistant Motor Units

This is the first microarray study to be carried out which has compared the gene expression profiles of vulnerable and resistant motor units in healthy mice. A similar study was carried out in 2013 by Brockington et al. in healthy human post-mortem tissue to determine underlying gene expression differences in motor units vulnerable to degeneration in ALS. However, the study by Brockington et al. (2013) was carried out using a less robust design than the microarray performed here. Brockington et al. (2013) examined the gene expression profiles of entire populations of motor units, from areas of the spinal cord that were known to contain vulnerable or resistant motor units in ALS. In this study, specific motor pools which had previously been characterised were labelled and isolated, meaning that the RNA extracted from these motor neurons was much more specific. Brockington et al. (2013) also examined motor neuron populations from two different regions of the

spinal cord, meaning that some of the changes in gene expression observed may simply be due to regional differences, rather than being actual modifiers of motor unit vulnerability. The motor pools examined in this study both innervate hind limb muscles, which are closely related, and groups of labelled cell bodies were always observed in similar areas of the spinal cord.

This microarray has identified individual genes which are known to be involved with neuro-protection or neuro-degeneration as being altered between vulnerable and resistant motor units. If, through further testing in a zebrafish model of SMA, any of these genes are shown to have a protective effect on axonal pathologies, then they could potentially be developed into a new therapeutic target for SMA. However, SMN protein expression is reduced in all body tissues, not only the motor neurons (Lunn & Wang, 2008), and recent studies of pathological changes in other body tissues have established that SMA is a multi-organ disease (Hamilton & Gillingwater, 2013; Shababi et al., 2013). Therefore any therapies for SMA that specifically focus on ameliorating the pathology of the neuromuscular system may be ineffective in treating other pathological components of SMA, unless used in combination with a therapy that increases levels of full length SMN protein such as gene therapy. Mouse models of SMA that have been treated with gene therapy show limited improvements (Lorson & Lorson, 2012). Modest extensions in SMA mouse lifespan have been noted, along with improvements in weight and loco-motor activities (Dominguez et al., 2010; Foust et al., 2010; Valori et al., 2010). One of the main criticisms of gene therapy as a treatment for SMA is the difficulty of ensuring the viral vector can enter the central nervous system and deliver a sufficiently high titre (Lorson & Lorson, 2012). It may be possible that a combination of gene therapy

with a therapeutic targeted specifically to the nervous system could overcome this obstacle. By increasing expression or activity of a neuro-protective factor or pathway, lower titres of viral vector in the central nervous system may no longer be a limiting factor in gene therapy efficiency in treating SMA.

5.4 – In Vivo Synaptic Labelling

Many studies have highlighted the importance of synaptic pathology in SMA. The pathology of the neuromuscular junction has been characterised extensively in mouse models of SMA (Cifuentes-Diaz et al., 2002; Murray et al. 2008; Karyia et al., 2008; Ling et al., 2010; Bowerman et al., 2011; Ling et al., 2012; Murray et al., 2013), but little work has been carried out on human neuromuscular junctions (Kariya et al., 2008; Martinez-Hernandez et al., 2013). Additionally, recent evidence has suggested that central synaptic connections are also vulnerable in SMA, with vGlut1-positive synapses onto lower motor neurons in the spinal cord also showing evidence of denervation in mouse models (Ling et al., 2010; Park et al., 2010; Mentis et al., 2011; Gogliotti et al., 2012; Martinez et al., 2012). However, to date, no work on denervation of central synapses has been carried out in human tissue. Additionally, studies carried out on central synaptic connectivity in humans would be limited to post-mortem tissue, which only provides insights into end stage pathology.

The peptide identified in this study, which has shown a potential synaptic binding affinity, has the potential to be developed into an *in vivo* synaptic label that may allow us to study these central synaptic connections in SMA in living patients. Previous studies using phage display technology have developed fluorescently

labelled peptides to assist surgeons during operations by highlighting small peripheral nerves (Whitney et al., 2010; Wu et al., 2011). In these studies, the peptide was able to specifically and transiently bind to the myelin sheath of the peripheral nerves, with no fluorescence being observed 24 hours after application (Whitney et al., 2010). It was using a similar approach that a peptide with potential synaptic binding abilities was identified in this study, but with some important differences. Phage panning was carried out by Whitney et al. (2010) using a purified protein, in this case myelin, which was immobilised on a plastic surface. In this study, a phage display library was panned using synaptosomes in suspension. It was not known if phage particles had the ability to bind to target peptides in suspension, however a concentration-binding assay revealed that phage particles did have this ability. Secondly, unlike the panning carried out by Whitney et al. (2011), the target peptide in this instance was against an unknown surface protein or peptide present at the pre-terminal of the synapse. While the identity of the protein that the peptide is targeted against is still unknown, the punctate staining observed around the cell body of the primary culture neuronal cells suggests that this protein is indeed concentrated at synapses.

It is hoped that with further testing and development, this peptide will be proved to bind specifically and reversibly to synapses *in vivo*. If this were the case, then it could potentially be developed into an *in vivo* synaptic labelling tool for examining synaptic connections in SMA patients, and indeed other patients with neuro-degenerative conditions.

5.5 – Model of Motor Unit Vulnerability in SMA

Based on the results of these studies, it is probable that differences in motor unit vulnerability are caused by the different gene expression profiles of the motor units themselves. From the results of Chapter 2, it was determined that SMA motor unit vulnerability was not based on motor unit morphology, as is the case in ALS (Bradley et al., 1983; Fischer et al., 2004; Hegedus et al., 2007; Valdez et al., 2012). It was also determined that motor unit vulnerability was not linked to other cell types, such as muscle and terminal Schwann cells. Additionally, it was determined that developmental dynamics did not influence motor unit vulnerability. The results of the microarray performed in Chapter 3 suggests that individual motor units have different gene expression profiles. Genes known to be directly involved in neurodegeneration and neuro-protection were altered between resistant and vulnerable motor units. Based on this, it is likely that the ubiquitous reduction in SMN protein that occurs in SMA affects these motor units differently. Motor units which are high-expressors of neuro-protective genes, or low-expressors of neuro-degenerative genes, are better placed to cope with the cellular stresses that are caused by a reduction in SMN protein. For example, SMN protein is known to bind to and the pro-apoptotic protein Bcl-2 (Sato et al., 2000). It may be possible that some motor units have higher levels of anti-apoptotic proteins which can suppress the excess Bcl-2 activity, whereas others cannot. Motor units that cannot cope with the cellular stresses would begin to undergo degeneration, with the NMJ being the first compartment of the neuron to break down.

The purpose of having different gene expression profiles in different motor units has not been elucidated in this study, but is likely to correlate with a motor unit function or morphology which was not analysed, such as an electrophysiological property.

5.6 - Conclusion

In conclusion, motor unit vulnerability varies in SMA and this variation is not due to morphological differences between motor units, as it is in ALS. Microarray analysis of groups of motor units with differing vulnerabilities revealed differences in gene expression profiles, providing evidence that intrinsic molecular properties of motor units underlie differences in vulnerability in SMA. Many of the genes which were differentially expressed between the two groups of motor units have previously been implicated in neuro-degeneration or neuro-protection and may represent new therapeutic targets in SMA. Separately, a fusion peptide was developed to transiently label synapses *in vivo*. When tested, the peptide produced punctate staining of the cell bodies of primary neuron cultures which may represent areas of synaptic contact. With further development, this peptide could be used to study synapses in neuro-degenerative conditions *in vivo* in living human patients and animal models.

References

Ackermann, B., Kröber, S., Torres-Benito, L., Borgmann, A., Peters, M, Hosseini Barkooie, S.M., et al., 2013. Plastin 3 ameliorates spinal muscular atrophy via delayed axon pruning and improves neuromuscular junction functionality. *Hum Mol Genet*. 22(7): 1328-1347.

Al-Chalabi, A., Jones, A., Troakes, C., King, A., Al-Sarraj, S., van den Berg, L.H., 2012. The genetics and neuropathology of amyotrophic lateral sclerosis. *Acta Neuropathol*. 124(3): 339-352.

Ashton, A.C. & Ushkaryov, Y.A., 2005. Properties of synaptic vesicle pools in mature central nerve terminals. *J Biol Chem*. 280(44): 37278-37288.

Atkin, J.D., Scott, R.L., West, J.M., Lopes, E., Quah, A.K., Cheema, S.S., 2005. Properties of slow- and fast-twitch muscle fibres in a mouse model of amyotrophic lateral sclerosis. *Neuromuscul Disord*. 15(5): 377-388.

Baba, H., Maezawa, Y., Uchida, K., Imura, S., Kawahara, N., Tomita, K., et al., 1997. Three-dimensional topographic analysis of spinal accessory motoneurons under chronic mechanical compression: an experimental study in the mouse. *J Neurol*. 244(4): 222-229.

Bach, J.R., Baird, J.S., Plosky, D., Navado, J., Weaver, B., 2002. Spinal muscular atrophy type 1: management and outcomes. *Pediatr Pulmonol*, 34(1): 16-22.

Battaglia, G., Princivalle, A., Forti, F., Lizier, C., Zeviani, M., 1997. Expression of the SMN gene, the spinal muscular atrophy determining gene, in the mammalian central nervous system. *Hum Mol Genet.* 6(11): 1961-1971.

Bleckert, A., Photowala, H., Alford, S., 2012. Dual pools of actin at presynaptic terminals. *J Neurophysiol*. 107(12): 3479-3492.

Bogaert, E., d'Ydewalle, C., Van Den Bosch, L., 2010. Amyotrophic lateral sclerosis and excitotoxicity: from pathological mechanism to therapeutic target. *CNS Neurol Disord Drug Targets.* 9(3): 297-304.

Bowerman, M., Murray, L.M., Boyer, J.G., Anderson, C.L., Kothary, R., 2012. Fasudil improves survival and promotes skeletal muscle development in a mouse model of spinal muscular atrophy. *BMC Med*. 7: 10-24.

Bowerman, M., Murray, L.M., Beauvais, A., Pinheiro, B., Kothary, R., 2012. A critical Smn threshold in mice dictates onset on an intermediate spinal muscular atrophy phenotype associated with a distinct neuromuscular junction pathology. *Neuromuscul Disord*. 22(3): 263-276.

Bradley, W.G., Good, P., Rasool, C.G., Adelman, L.S., 1983. Morphometric and biochemical studies of peripheral nerves in amyotrophic lateral sclerosis. *Ann Neuro*l. 14(3): 267-277.

Bradley, W.G., 1987. Recent views on amyotrophic lateral sclerosis with emphasis on eletrophysiological studies. *Muscle & Nerve*. 10: 490-502.

Broadwell, R.D. & Balin, B.J, 1985. Endocytic and exocytic pathways of the neuronal secretory process and trans-synaptic transfer of wheat germ agglutinin-horseradish peroxidase in vivo. *J Comp Neuro*. 242(4): 632-650.

Brockington, A., Ning, K., Heath, P.R., Wood, E., Kirby, J., Fusi, N., et al., 2013. Unravelling the enigma of selective vulnerability in neurodegeneration: motor neurons resistant to degeneration in ALS show distinct gene expression characteristics and decreased susceptibility to excitotoxicity. *Acta Neuropathol*. 125(5): 95-109.

Brzustowicz, L.M., Lehner, T., Castilla, L.H., Penchaszadeh, G.K., Wilhelmsen, K.C., Daniels, R., et al.., 1990. Genetic mapping of chronic childhood-onset spinal muscular atrophy to chromosome 5q11.2-13.3. *Nature*. 344(6266): 540-541.

Buchthal, F. & Schmalbruch, H., 1980. Motor unit of mammalian muscle. *Physiol Rev*. 60(1): 90-142.

Burghes, A.H. & Beattie, C.E., 2009. Spinal muscular atrophy: why do low levels of survival motor neuron protein make motor neurons sick? *Nat Rev Neurosci*. 10(8): 597-609.

Burton, N.C., Kensler, T.W., Guilarte, T.R., 2006. In vivo modulation of the Parkinsonian phenotype by Nrf2. *Neurotoxicology*. 27(6): 1094-1100.

Caraballo-Miralles, V., Cardona-Rossinyol, A., Garcera, A., Torres-Benito, L., Soler, R.M., Tabares, L., et al., 2013. Notch signalling pathway is activated in motoneurons of spinal muscular atrophy. *Int J Mol Sci*. 14(6): 11424-11437.

Chan, Y.B., Miguel-Aliaga, I., Franks, C., Thomas, N., Trülzsch, B., Sattelle, D.B., et al., 2003. Neuromuscular defects in a Drosophila survival motor neuron gene mutant. *Hum Mol Genet*. 12(12): 1367-1376.

Chen, B. & May, P.J., 2007. Premotor circuits controlling eyelid movements in conjuction with vertical saccades in the cat: II. Interstitial nucleus of Cajal. *J Comp Neurol.* 500(4): 676-692.

Chen, C.M., Liu, J.L., Wu, Y.R., Chen, Y.C., Cheng, H.S., Cheng, M.L., et al., 2009. Increased oxidative damage in peripheral blood correlates with severity of Parkinson's disease. *Neurobiol Dis*. 33(3): 429-435.

Chu, J., Hong, N.A., Masuda, C.A., Jenkins, B.V., Nelms, K.A., Goodnow, C.C., et al., 2009. A mouse forward genetics screen identifies LISTERIN as an E3 ubiquitin ligase involved in neurodegeneration. *Proc Natl Acad Sci USA.* 106(7): 2097-2103.

Cifra, A., Mazzone, G.L., Nistri, A., 2013. Riluzole: what it does to spinal and brainstem neurons and how it does it. *Neuroscientist.* 19(2): 137-144.

Cifuentes-Diaz, C., Nicole, S., Velasco, M.E., Borra-Cebrian, C., Panozzo, C., Frugier, T., et al.., 2002. Neurofilament accumulation at the motor endplate and lack

of axonal sprouting in a spinal muscular atrophy mouse model. *Hum Mol Genet*. 11(12): 1439-1447.

Coady, T.H. & Lorson, C.L., 2011. SMN in spinal muscular atrophy and snRNP biogenesis. *Wiley Interdiscip Rev RNA*. 2(4): 546-564.

Comley, L.H., Wishart, T.M., Baxter, B., Murray, L.M., Nimmo, A., Thomson, D., et al., 2011. Induction of cell stress in neurons from transgenic mice expressing yellow fluorescent protein: implications for neurodegeneration research. PLoS One. 6(3):e17639.

Coovert, D.D., Le, T.T., McAndrew, P.E., Strasswimmer, J., Crawford, T.O., Mendell, J.R., et al.., 1997. The survival motor neuron protein in spinal muscular atrophy. *Hum Mol Genet.* 6(8): 1205-1214.

Corcia, P., Camu, W., Halimi, J.M., Vourc'h, P., Antar, C., Vedrine, S., et al., 2006. SMN1 gene, but not SMN2, is a risk factor for sporadic ALS. *Neurology*. 67(6): 1147-1150.

Court, F.A., Gillingwater, T.H., Melrose, S., Sherman, D.L., Greenshields, K.N., Morton, A.J., et al.., 2008. Identity, developmental restriction and reactivity of extralaminar cells capping mammalian neuromuscular junctions. *J Cell Sci*. 121(23): 3901-3911.

Cubelos, B., González-González, I.M., Giménez, C., Zafra, F., 2005. Amino acid transporter SNAT5 localizes to glial cells in the rat brain. *Glia*. 49(2): 230-244.

Cwirla, S.E., Peters, E.A., Barrett, R.W., Dower, W.J., 1990. Peptides on phage: a vast library of peptides for identifying ligands. *Proc Natl Acad Sci USA*. 87(16): 6378-6382.

Dadon-Nachum, M., Melamed, E., Offen, D., 2011. The "dying-back" phenomenon of motor neurons in ALS. *J Mol Neurosci.* 43(3): 470-477.

D'Amico, A., Mercuri, E., Tiziano, F.D., Bertini, E., 2011. Spinal muscular atrophy. *Orphanet J Rare Dis*. 6: 71.

De Robertis, E., Rodriguez de Lores Arnaiz, G., Pellegrino de Iraldi, A., 1962. Isolation of synaptic vesicles from nerve endings of the rat brain. *Nature*. 194: 794-795.

Deshaies, R.J. & Joazeiro, C.A., 2009. RING domain E3 ubiquitin ligases. *Annu Rev Biochem.* 78: 399-434.

de Sousa Abreu, R., Penalva, L.O., Marcotte, E.M., Vogel, C., 2009. Global signatures of protein and mRNA expression levels. *Mol Biosyst*. 5(12): 1512-1526.

De Winter, F., Vo, T., Stam, F.J., Wisman, L.A., Bär, P.R., Niclou, S.P., et al., 2006. The expression of the chemorepellent Semaphorin 3A is selectively induced in terminal Schwann cells of a subset of neuromuscular synapses that display limited anatomical plasticity and enhanced vulnerability in motor neuron disease. *Mol Cell Neurosci*. 32(1-2): 102-117.

Dimos, J.T., Rodolfa, K.T., Niakan, K.K., Weisenthal, L.M., Mitsumoto, H., Chung, W., et al., 2008. Induced pluripotent stem cells generated from patients with ALS can be differentiated into motor neurons. *Science*. 321(5893): 1218-1221.

Dominguez, E., Marais, T., Chatauret, N., Benkhelifa-Ziwat, S., Dugue, S., Ravassard, P., et al., 2011. Intravenous scAAV9 delivery of a codon-optimized SMN1 sequence rescues SMA mice. *Hum Mol Genet*. 20(4): 681-693.

Dunkley, P.R., Heath, J.W., Harrison, S.M., Jarvie, P.E., Glenfield, P.J., Rostas, J.A., 1988. A rapid Percoll gradient procedure for isolation of synaptosomes directly from an S1 fraction: homogeneity and morphology of subcellular fractions. *Brain Res*. 441(1-2): 59-71.

Dunkley, P.R., Jarvie, P.E., Robinson, P.J., 2008. A rapid Percoll gradient procedure for preparation of synaptosomes. *Nat Protoc*. 3(11): 1718-1728.

Ebert, A.D., Yu, J., Rose, F.F. Jr., Mattis, V.B., Lorson, C.L., Thomson, J.A., et al., 2009. Inducd pluripotent stem cells from a spinal muscular atrophy patient. *Nature*. 457(7227): 277-280.

Fan, L. & Simard, L.R., 2002. Survival motor neuron (SMN) protein: role in neurite outgrowth and neuromuscular maturation during neuronal differentiation and development. *Hum Mol Genet*. 11(14): 1605-1614.

Feldkötter, M., Schwarzer, V., Wirth, R., Wienker, T.F., Wirth, B., 2002. Quantitative analyses of SMN1 and SMN2 based on real-time lightCycler PCR: fast and highly

reliable carrier testing and prediction of severity of spinal muscular atrophy. *Am J Hum Genet.* 70(2): 358-368.

Feng, G., Mellor, R.H., Bernstein, M., Keller-Peck, C., Nguyen, Q.T., Wallace, M., et al., 2000. Imaging neuronal subsets in transgenic mice expressing multiple spectral variants of GFP. *Neuron.* 28(1): 41-51.

Fischer, L.R., Culver, D.G., Tennant, P., Davis, A.A., Wang, M., Castellano-Sanchez, A., et al.., 2004. Amyotrophic lateral sclerosis is a distal axonopathy: evidence in mice and man. *Exp Neurol*. 185(2): 232-240.

Foust, K.D., Wang, X., McGovern, V.L., Braun, L., Bevan, A.K., Haidet, A.M., et al., 2010. Rescue of the spinal muscular atrophy phenotype in a mouse model by early postnatal delivery of SMN. *Nat Biotechnol*. 28(3): 271-274.

Frey, D., Schneider, C., Xu, L., Borg, J., Spooren, W., Caroni, P., 2000. Early and selective loss of neuromuscular synapse subtypes with low sprouting competence in motoneuron diseases. *J Neurosci*. 20(7): 2534-2542.

Gabanella, F., Carissimi, C., Usiello, A., Pellizzoni, L., 2005. The activity of the spinal muscular atrophy protein is regulated during development and cellular differentiation. *Hum Mol Genet*. 14(23): 3629-3642.

Gamez, J., Barceló, M.J., Muñoz, X., Carmona, F., Cuscó, I., Baiget, M., et al., 2002. Survival and respiratory decline are not related to homozygous SMN2 deletions in ALS patients. *Neurology*. 59(9): 1456-1460.

Gassman, A., Hao Ie, T., Bhoite, L., Bradford, C.L., Chien, C.B., Beattie, C.E., et al., 2013. Small molecule suppressors of Drosophila kinesin deficiency rescue motor axon development in a zebrafish model of spinal muscular atrophy. *PLoS One*. 8(9): e74325.

Gillingwater, T.H. & Ribchester, R.R., 2003. The relationship of neuromuscular synapse elimination to synaptic degeneration and pathology: insights from WldS and other mutant mice. *J Neurocytol*. 32(5-8): 863-881.

Gogliotti, R.G., Quinlan, K.A., Barlow, C.B., Heier, C.R., Heckman, C.J., Didonato, C.J., 2012. Motor neuron rescue in spinal muscular atrophy mice demonstrates that sensory-motor defects are a consequence, not a cause, of motor neuron dysfunction. *J Neurosci*. 32(11): 3818-3829.

Griffin, J.W., & Thompson, W.J., 2008. Biology and pathology of nonmyelinating Schwann cells. *Glia*. 56(14): 1518-1531.

Guo, X., Das, M., Rumsey, J., Gonzalez, M., Stancescu, M., Hickman, J., 2010. Neuromuscular junction formation between human stem-cell-derived motoneurons and rat skeletal muscle in a defined system. *Tissue Eng Part C Methods*. 16(6): 1347-1355.

Haddad, H., Cifuentes-Diaz, C., Miroglio, A., Roblot, N., Joshi, V., Melki, J., 2003. Riluzole attenuates spinal muscular atrophy disease progression in a mouse model. *Muscle Nerve*. 28(4): 432-437.

Hahnen, E., Forkert, R., Marke, C., Rudnik-Schöneborn, S., Schönling, J., Zerres, K., Wirth, B., 1995. Molecular analysis of candidate genes on chromosome 5q13 in autosomal recessive spinal muscular atrophy: evidence of homozygous deletions of the SMN gene in unaffected individuals. *Hum Mol Genet.* 4(10):1927-1933.

Hamdani el, H., Gudbrandsen, M., Bjørkmo, M., Chaudhry, F.A., 2012. The system N transporter SN2 doubles as a transmitter precursor furnisher and a potential regulator of NMDA receptors. *Glia*. 60(11): 1671-1683.

Hamilton, G. & Gillingwater, T.H., 2013. Spinal muscular atrophy: going beyond the motor neuron. *Trends Mol Med.* 19(1): 40-50.

Han, K.J., Foster, D.G., Zhang, N.Y., Kanisha, K., Dzieciatkowska, M., Sclafani, R.A., et al., 2012. Ubiquitin-specific protease 9x deubiquitinates and stabilizes the spinal muscular atrophy protein-survival motor neuron. *J Biol Chem*. 287(52): 43741-43752.

Hao Ie, T., Wolman, M., Granato, M., Beattie, C.E., 2012. Survival motor neuron affects plastin 3 protein levels leading to motor defects. *J Neurosci*. 32(15): 5074-5084.

Hao Ie, T., Duy, P.Q., Jontes, J.D., Wolman, M., Granato, M., Beattie, C.E., 2013. Temporal requirement for SMN in motoneuron development. *Hum Mol Genet*. 22(13): 2612-2625.

Hayashi, M., Araki, S., Arai, N., Kumada, S., Itoh, M., Tamagawa, K., et al.. 2002. Oxidative stress and disturbed glutamate transport in spinal muscular atrophy. *Brain Dev*. 24(8): 770-775.

Hegedus, J., Putman, C.T., Gordon, T., 2007. Time course of preferential motor unit loss in the SOD1 G93A mouse model of amyotrophic lateral sclerosis. *Neurobiol Dis*. 28(2): 154-164.

Hsu, S.H., Lai, M.C., Er, T.K., Yang, S.N., Hung, C.H., Tsai, H.H., et al., 2010. Uniquitin carboxyl-terminal hydrolase L1 (UCHL1) regulates the level of SMN expression through ubiquitination in primary spinal muscular atrophy fibroblasts. *Clin Chim Acta.* 411(23-24): 1920-1928.

Ito, Y., Shibata, N., Saito, K., Kobayashi, M, Osawa, M., 2011. New insights into the pathogenesis of spinal muscular atrophy. *Brain Dev*. 33(4): 321-331.

Jessell, T.M., 2000. Neuronal specification in the spinal cord: inductive signals and transcriptional codes. *Nat Rev Genet.* 1(1): 20-29.

Joshi, G. & Johnson, J.A., 2012. The Nrf2-ARE pathway: a valuable therapeutic target for the treatment of neurodegenerative diseases. *Recent Pat CNS Drug Discov*. 7(3): 218-229.

Kanninen, K., Malm, T.M., Jyrkkänen, H.K., Goldsteins, G., Keksa-Goldsteine, V., Tanila, H., et al., 2008. Nuclear factor erythroid 2-related factor 2 protects against beta amyloid. *Mol Cell Neurosci.* 39(3): 302-313.

Kanning, K.C., Kaplan, A., Henderson, C.E., 2010. Motor neuron diversity in development and disease. *Annu Rev Neurosci*. 33:409-440.

Kariya, S., Park, G.H., Maeno-Hikichi, Y., Leykekhman, O., Lutz, C., Arkovitz, M.S., et al.., 2008. Reduced SMN protein impairs maturation of the neuromuscular junctions in mouse models of spinal muscular atrophy. *Hum Mol Genet.* 17(16): 2552-2569.

Kariya, S., Re, D.B., Jacquier, A., Nelson, K., Przedborski, S., Monani, U.R., 2012. Mutant superoxide dismutase 1 (SOD1), a cause of amyotrophic lateral sclerosis, disrupts the recruitment of SMN, the spinal muscular atrophy protein to nuclear Cajal bodies. *Hum Mol Genet*. 21(15): 3421-3434.

Kong, L., Wang, X., Choe, D.W., Polley, M., Burnett, B.G., Bosch-Marcé, M., et al.., 2009. Impaired synaptic vesicle release and immaturity of neuromuscular junctions in spinal muscular atrophy mice. *J Neurosci*. 29(3): 842-851.

Koyanagi, Y., Sawada, K., Sakata-Haga, H., Jeong, Y.G., Kukui, Y., 2006. Increased serotonergic innervation of lumbosacral motoneurons of rolling mouse Nagoya in correlation with abnormal hindlimb extension. *Anat Histol Embryol*. 35(6): 387-392.

Kwon, D.Y., Motlet, W.W., Fischbeck, K.H., Burnett, B.G., 2011. Increasing expression and decreasing degradation of SMN ameliorate the spinal muscular atrophy phenotype in mice. *Hum Mol Genet*. 20(18): 3667-3677.

Kwon, D.Y., Dimitriadi, M., Terzic, B., Cable, C., Hart, A.C., Chitnis, A., et al., 2013. The E3 ubiquitin ligase mind bomb 1 ubiquitinates and promotes the degradation of survival of motor neuron protein. *Mol Biol Cell*. 24(12): 1863-1871.

Lee, Y.I., Mikesh, M., Smith, I., Rimmer, M., Thompson, W., 2011. Muscles in a mouse model of spinal muscular atrophy show profound defects in neuromuscular development even in the absence of failure in neuromuscular transmission or loss of motor neurons. *Dev Biol*. 356(2): 432-444.

Lefebvre, S., Bürglen, L., Reboullet, S., Clermont, O., Burlet, P., Viollet, L., et al.., 1995. Identification and characterization of a spinal muscular atrophy-determining gene. *Cell*. 80(1): 155-165.

Le Pichon, C.E., Dominguez, S.L., Solanoy, H., Ngu, H., Lewin-Koh, N., Chen, M., Eastham-Anderson, J., et al., 2013. EGFR inhibitor erlotinib delays disease progression but does not extend the survival in the SOD1 mouse model of ALS. *PLoS One*. 8(4): e62342.

Li, X.J., Du, Z.W., Zarnowska, E.D., Pankratz, M., Hansen, L.O., Pearce, R.A., et al., 2005. Specification of motoneurons from human embryonic stem cells. *Nat Biotechnol*. 23(2): 215-221.

Ling, K.K., Lin, M.Y., Zingg, B., Feng, Z., Ko, C.P., 2010. Synaptic defects in the spinal and neuromuscular circuitry in a mouse model of spinal muscular atrophy. *PloS One*. 5(11):e15457.

Ling, K.K., Gibbs, R.M., Feng, Z., Ko, C.P., 2012. Severe neuromuscular denervation of clinically relevant muscles in a mouse model of spinal muscular atrophy. *Hum Mol Genet*. 21(1): 185-195.

Ling, B., Zheng, H., Fu, G., Yuan, J, Shi, T., Chen, S., et al., 2013. Supression of non-small cell lung cancer proliferation and tumorigenicity by DENND2D. *Lung Cancer*. 79(2): 104-110.

Lionikas, A., Blizard, D.A., Gerhard, G.S., Vandenbergh, D.J., Stout, J.T., Vogler, G.P., et al., 2005. Genetic determinants of weight of fast- and slow-twitch skeletal muscle in 500-day-old-mice of the C57BL/6J and DBA/2J lineage. *Physiol Genomics*. 21(2): 184-192.

Liu, Q. & Dreyfuss, G., 1996. A novel nuclear structure containing the survival of motor neurons protein. *EMBO J*. 15(14): 3555-3565.

Liu, B., Chen, H., Johns, T.G., Neufeld, A.H., 2006. Epidermal growth factor receptor activation: an upstream signal for transition of quiescent astrocytes into reactive astrocytes after neural injury. *J Neurosci*. 26(28): 7532-7540.

Liu, H., Shafey, D., Moores, J.N., Kothary, R., 2010. Neurodevelopmental consequences of Smn depletion in a mouse model of spinal muscular atrophy. *J Neurosci Res*. 88(1): 111-122.

Liu, K., Guo, Y., Liu, H., Bian, C., Lam, R., Liu, Y., et al. 2012. Crystal structures of TDRD3 and methyl-arginine binding characterization of TDRD3, SMN and SPF30. *PLoS One*. 7(2): e30375.

Lorenzo, L.E., Barbe, A., Portalier, P., Fritschy, J.M., Bras, H., 2006. Differential expression of GABAA and glycine receptors in ALS-resistant vs. vulnerable-motoneurons: possible implications for selective vulnerability of motoneurons. *Eur J Neurosci.* 23(12): 3161-3170.

Lorson, C.L. & Androphy, E.J., 1998. The domain encoded by exon 2 of the survival motor neuron protein mediates nucleic acid binding. *Hum Mol Genet*. 7(8): 1269-1275.

Lorson, C.L., Hahnen, E., Androphy, E.J., Wirth, B., 1999. A single nucleotide in the SMN gene regulates splicing and is responsible for spinal muscular atrophy. *Proc Natl Acad Sci USA*. 96(11): 6307-6311.

Lorson, M.A. & Lorson, C.L., 2012. SMN-inducing compounds for the treatment of spinal muscular atrophy. *Future Med Chem*. 4(16): 2067-2084.

Lunn, M.R. & Wang, C.H., 2008. Spinal muscular atrophy. *Lancet*. 371(9630): 2120-2133.

Markowitz, J.A., Tinkle, M.B., Fischbeck, K.H., 2004. Spinal muscular atrophy in the neonate. *J Obstet Gynecol Neonatal Nurs*. 33(1): 12-20.

Mailman, M.D., Heinz, J.W., Papp, A.C., Snyder, P.J., Sedra, M.S., et al., 2002. Molecular analysis of spinal muscular atrophy and modification of the phenotype by SMN2. *Genet Med*. 4(1): 20-26.

Marteyn, A., Maury, Y., Gauthier, M.M., Lecuver, C., Vernet, R., Denis, J.A., et al., 2011. Mutant human embryonic stem cells reveal neurite and synapse formation defects in type 1 myotonic dystrophy. *Cell Stem Cell*. 8(4): 434-444.

Martinez, T.L., Kong, L., Wang, X., Osbourne, M.A., Crowder, M.E., Van Meerbeke, J.P., et al.., 2012. Survival motor neuron protein in motor neurons determines synaptic integrity in spinal muscular atrophy. *J Neurosci.* 32(25): 8703-8715.

Martinez-Hernández, R., Bernal, S., Also-Rallo, E., Alías, L., Barceló, M.J., Hereu, M., et al.., 2013. Synaptic defects in type I spinal muscular atrophy in human development. *J Pathol.* 229(1): 49-61.

McAndrew. P.E., Parsons, D.W., Simard, L.R., Rochette, C., Ray, P.N., Mendell, J.R., et al.., 1997. Identification of proximal spinal muscular atrophy carriers and patients by analysis of SMNT and SMNC gene copy number. *Am J Hum Genet*. 60(6): 1411-1422.

Melki, J., Abdelhak, S., Sheth, P., Bachelot, M.F., Burlet, P., Marcadet, A., et al.., 1990. Gene for chronic proximal spinal muscular atrophies maps to chromosome 5q. *Nature.* 344(6268): 767-768.

Menke, L.A., Poll-The, B.T., Clur, S.A., Bilardo, C.M., van der Wal, A.C., Lemmink, H.H., et al., 2008. Congenital heart defects in spinal muscular atrophy type I: a clinical report of two siblings and a review of the literature. *Am J Med Genet A*. 146A(6): 740-744.

Mentis, G.Z., Blivis, D., Liu, W., Drabac, E., Crowder, M.E., Kong, L., et al.., 2011. Early functional impairment of sensory-motor connectivity in a mouse model of spinal muscular atrophy. *Neuron*. 69(3): 453-467.

Murray, L.M., Comley. L.H., Thomson, D., Parkinson, N., Talbot, K., Gillingwater, T.H., 2008. Selective vulnerability of motor neurons and dissociation of pre- and post-synaptic pathology at the neuromuscular junction in mouse models of spinal muscular atrophy. *Hum Mol Genet*. 17(7): 949-962.

Murray, L.M., Gillingwater, T.H., Parson, S.H., 2010. Using mouse cranial muscles to investigate neuromuscular pathology in vivo. *Neuromuscul Disord.* 20(11): 740-743.

Murray, L.M., Beauvais, A., Bhanot, K., Kothary, R., 2013. Defects in neuromuscular junction remodelling in the Smn2B/- mouse model of spinal muscular atrophy. *Neurobiology of Disease*. 49: 57-67.

Neymotin, A., Calingasan, N.Y., Wille, E., Naseri, N., Petri, S., Damiano, M, et al., 2011. Neuroprotective effect of Nrf2/ARE activators, CDDO ethylamide and CDDO trifluoroethylamide in a mouse model of amytrophic lateral sclerosis. *Free Radic Biol Med*. 51(1): 88-96.

Nimchinsky, E.A., Young, W.G., Yeung, G., Shah, R.A., Gordon, J.W., Bloom, F.E., et al., 2000. Differential vulnerability of oculomotor, facial, and hypoglossal nuclei in G86R superoxide dismutase transgenic mice. *J Comp Neurol.* 416(1): 112-125.

Nölle, A., Zeug, A., van Bergeijk, J., Tönges, L., Gerhard, R., Brinkmann, H., et al., 2011. The spinal muscular atrophy disease protein SMN is linked to the Rho-kinase pathway via profilin. *Hum Mol Genet*. 20(24): 4865-4878.

Nouhi, F., Tusi, S.K., Abdi, A., Khodagholi, F., 2011. Dietary supplementation with tBHQ, an Nr2 stabilizer molecule confers neuroprotection against apoptosis in amyloid β-injected rat. *Neurochem Res.* 36(5): 870-878.

Offen, D., Barhum, Y., Melamed, E., Embacher, N., Schindler, C., Ransmayr, G., 2009. Spinal cord mRNA profile in patients with ALS: comparison with transgenic mice expressing the human SOD-1 mutant. *J Mol Neurosci*. 38(2): 85-93.

Ogino, S., Leonard, D.G., Rennert, H., Ewens, W.J., Wilson, R.B., 2002. Genetic risk assessment in carrier testing for spinal muscular atrophy. *Am J Med Genet.* 110(4): 301-307.

Oliveira, A.L., Hydling, F., Olsson, E., Shi, T., Edwards, R.H., Fujiyama, F., et al.., 2003. Cellular localization of three vesicular glutamate transporter mRNAs and proteins in rat spinal cord and dorsal root ganglia. *Synapse*. 50(2): 117-129.

Oprea, G.E., Kröber, S., McWhorter, M.L., Rossoll, W., Müller, S., Krawczak, M, et al., 2008. Plastin 3 is a protective modifier of autosomal recessive spinal muscular atrophy. *Science*. 320(5875): 524-527.

Osborne, M., Gomez, D., Feng, Z., McEwen, C., Beltran, J., Cirillo, K., et al.., 2012. Characterization of behavioural and neuromuscular junction phenotypes in a novel allelic series of SMA mouse models. *Hum Mol Genet.* 21(20): 4431-4447.

Park, G.H, Maeno-Hikichi, Y., Awano, T., Landmesser, L.T., Monani, U.R., 2010. Reduced survival of motor neuron (SMN) protein in motor neuronal progenitors functions cell autonomously to cause spinal muscular atrophy in model mice expressing the human centromeric (SMN2) gene. *J Neurosci*. 30(36): 12005-12019.

Patani, R., Hollins, A.J., Wishart, T.M., Puddifoot, C.A., Alvarez, S., de Lera, A.R., et al., 2011. Retinoid-independent motor neurogenesis from human embryonic stem cells reveals a medial columnar ground state. *Nat Commun*. 2: 1-10.

Pearn, J., 1978. Incidence, prevalence, and gene frequency studies of chronic childhood spinal muscular atrophy. *J Med Genet.* 15(6): 409-413.

Pellizzoni, L., Yong, J., Dreyfuss, G., 2002. Essential role for the SMN complex in the specificity of snRNP assembly. *Science*. 298(5599): 1775-1779.

Polosa, P.L. & Attardi, G., 1991. Distinctive pattern and translational control of mitochondrial protein synthesis in rat brain synaptic endings. *J Biol Chem*. 266(15): 10011-10017.

Pun, S., Santos, A.F., Saxena, S., Xu, L., Caroni, P., 2006. Selective vulnerability and pruning of phasic motoneuron axons in motoneuron disease alleviated by CNTF. *Nat Neurosci*. 9(3): 408-419.

Quarles, R.H., Macklin, W.B., Morell, P., 2006. *Basic Neurochemistry: Molecular, Cellular and Medical Aspects.* American Society for Neurochemistry: Elsevier.

Rajendra, T.K., Gonsalvez, G.B., Walker, M.P., Shpargel, K.B., Salz, H.K., Matera, A.G., 2007. A Drosophila melanogaster model of spinal muscular atrophy reveals a function for SMN in striated muscle. *J Cell Biol*. 176(6): 831-841.

Ramsey, C.P., Glass, C.A., Montgomery, M.B., Lindl, K.A., Ritson, G.P., Chia, L.A., et al., 2007. Expression of Nrf2 in neurodegenerative diseases. *J Neuropathol Exp Neurol*. 66(1): 75-85.

Rathod, R., Havlicek, S., Frank, N., Blum, R., Sendtner, M., 2012. Laminin induced local axonal translation of β-actin mRNA is impaired in SMN-deficient motoneurons. *Histochem Cell Biol*. 138(5): 737-748.

Reddy, P. & McKenney, K., 1996. Improved method for the production of M13 phage and single-stranded DNA for DNA sequencing. *Biotechniques*. 20(5): 858-860.

Riessland, M., Ackerman, B., Förster, A., Jakubik, M., Hauke, J., et al.., 2010. SAHA ameliorates the SMA phenotype in two mouse models for spinal muscular atrophy. *Hum Mol Genet.* 19(8): 1492-1506.

Ringer, C., Weihe, E., Schütz, B., 2012. Calcitonin gene-related peptide expression levels predict motor neuron vulnerability in the superoxide dismutase 1-G93A mouse model of amyotrophic lateral sclerosis. *Neurobiol Dis*. 45(1): 547-554.

Rodi, D.J. & Makowski, L., 1999. Phage-display technology – finding a needle in a vast molecular haystack. *Curr Opin Biotechnol*. 10(1): 87-93.

Rossoll, W., Jablonka, S., Andreassi, C., Kröning, A.K., Karle, K., Monani, U.R., et al., 2003. Smn, the spinal muscular atrophy-determining gene product, modulates axon growth and localization of beta-actin mRNA in growth cones of motoneurons. *J Cell Biol*. 163(4): 801-812.

Ruggui, M., McGovern, V.L., Lotti, F., Saieva, L., Li, D.K., Kariya, S., et al., 2012. A role for SMN exon 7 splicing in the selective vulnerability of motor neuron in spinal muscular atrophy. *Mol Cell Biol*. 32(1): 126-138.

Russman, B.S., Iannaccone, S.T., Samaha, F.J., 2003. A phase 1 trial of riluzole in spinal muscular atrophy. *Arch Neurol*. 60(11): 1601-1603.

Russman, B.S., 2007. Spinal muscular atrophy: clinical classification and disease heterogeneity. *J Child Neurol*. 22(8): 946-951.

Ryu, K.Y., Maehr, R., Gilchrist, C.A., Long, M.A., Bouley, D.M., Mueller, B, et al., 2007. The mouse polyubiquitin gene UbC is essential for fetal liver development, cell cycle progression and stress tolerance. *EMBO*. 26(11): 2693-2706.

Sagade, L.A., 1990. Location of the motoneurons innervating the transverse mandibular muscle in the guinea pig. *Neurosci Lett.* 116(1-2): 64-69.

Sanes, J.R. & Lichtman, J.W., 1999. Development of the vertebrate neuromuscular junction. *Annu Rev Neurosci.* 22: 389-442.

Sarlette, A., Krampfl, K., Grothe, C., Neuhoff, Nv, Dengler, R., Petri, S., 2008. Nuclear erythroid 2-related 2-antioxidative reponse element signaling pathway in motor cortex and spinal cord in amyotrophic lateral sclerosis. *J Neuropatho Exp Neurol*. 67(11): 1055-1062.

Sato, K., Eguchi, Y., Kodama, T.S. and Tsujimoto, Y. 2000. Regions essential for the interaction between Bcl-2 and SMN, the spinal muscular atrophy disease gene product. *Cell Death Differ*. 7(4): 374-383.

Saxena, S., Cabuy, E., Caroni, P., 2009. A role for motoneuron subtype-selective ER stress in disease manifestations of FALS mice. *Nat Neurosci*. 12(5): 627-636.

Shababi, M., Lorson, C.L., Rudnik-Schöneborn, S.S., 2013. Spinal muscular atrophy: a motor neuron disorder or a multi-organ disease? *J Anat*. DOI: 10.1111/joa.12083.

Shanmugarajan, S., Swoboda, K.J., Iannaccone, S.T., Ries, W.L., Maria, B.L, Reddy, S.V., 2007. Congenital bone fractures in spinal muscular atrophy: functional role for SMN protein in bone remodelling. *J Child Neurol*. 22(8): 967-973.

Shupliakov, O., Bloom, O., Gustafsson, J.S., Kjaerulff, O., Low, P., Tomilin, N., et al., 2002. Impaired recycling of synaptic vesicles after acute perturbation of the presynaptic actin cytoskeleton. *Proc Natl Acad Sci USA.* 99(22): 14476-14481.

Simic, G., Mladinov, M., Seso Simic, D., Jovanov Milosevic, N., Islam, A., Pajtak, A., et al., 2008. Abnormal motoneuron migration, differentiation, and axon outgrowth in spinal muscular atrophy. *Acta Neuropathol*. 115(3): 313-326.

Singh Roy, N., Nakano, T., Xuing, L., Kang, J., Nedergaard, M., Goldman, S.A., 2005. Enhancer-specified GFP-based FACS purification of human spinal motor neurons from embryonic stem cells. *Exp Neurol*. 196(2): 224-234.

Sleigh, J.N., Barreiro-Iglesias, A., Oliver, P.L., Biba, A., Becker, T, Davies, K.E., et al., 2013. Chondrolectin affects cell survival and neuronal outgrowth in in vitro models of spinal muscular atrophy. *Hum Mol Genet*. Epub ahead of print.

Smith, G.P., 1985. Filamentous fusion phage: novel expression vectors that display cloned antigens on the virion surface. *Science*. 228(4705): 1315-1317.

Soler-Botija, C., Ferrer, I., Alvarex, J.L., Baiget, M, Tizzano, E.F., 2003. Downregulation of Bcl-2 proteins in type I spinal muscular atrophy motor neurons during fetal development. *J Neuropathol Exp Neurol*. 62(4): 420-426.

Sugiura, Y. & Lin, W., 2011. Neuron-glia interactions: the role of Schwann cells in neuromuscular synapse formation and function. *Biosci Rep.* 31(5): 295-302.

Swoboda, K.J., Prior, T.W., Scott, C.B., McNaught, T.P., Wride, M.C., Reyna, S.P., et al. 2005. Natural history of denervation in SMA: relation to age, SMN2 copy number, and function. *Ann Neurol*. 57(5): 704-712.

Takahashi, K., Okita, K., Nakagawa, M., Yamanaka, S., 2007. Induction of pluripotent stem cells from fibroblast cultures. *Nat Protoc*. 2(12): 3081-3089.

Tsai, M.S., Chiu, Y.T., Wang, S.H., Hsieh-Li, H.M., Li H., 2006. Abolishing Trp53-dependent apoptosis does not benefit spinal muscular atrophy model mice. *Eur J Hum Genet*. 14(3): 372-375.

Tsai, L.K., Tsai, M.S., Ting, C.H., Li, H., 2008. Multiple therapeutic effects of valproic acid in spinal muscular atrophy model mice. *J Mol Med (Berl)*. 86(11): 1243-1254.

Turner, B.J., Parkinson, N.J., Davies, K.E., Talbot, K., 2009. Survival motor neuron deficiency enhances progression in an amyotrophic lateral sclerosis mouse model. *Neurobiol Dis*. 34(3): 511-517.

Valdez, G., Tapia, J.C., Lichtman, J.W., Fox, M.A., Sanes, J.R., 2012. Shard resistance to aging and ALS in neuromuscular junctions of specific muscles. *PLoS One*. 7(4): e34640.

Valori, C.F., Ning, K., Wyles, M., Mead, R.J., Grierson, A.J., Shaw, P.J., et al., 2010. Systemic delivery of scAAV9 expressing SMN prolongs survival in a model of spinal muscular atrophy. *Sci Transl Med*. 2(35): 35ra42.

Van Meerbeke, J.P., Gibbs, R.M., Plasterer, H.L., Miao, W., Feng, Z., Lin, M.Y., et al.., 2013. The DcpS inhibitor RG3039 improves motor function in SMA mice. *Hum Mol Genet*. 22(20): 4074-4083.

Veldink, J.H., van den Berg, L.H., Cobben, J.M., Stulp, R.P., De Jong, J.M., Vogels, O.J., et al., 2001. Homozygous deletion of the survival motor neuron 2 gene is a prognostic factor in sporadic ALS. *Neurology*. 56(6): 749-752.

Voigt, T., Neve, A., Schümperli, D., 2013. The cranio-sacral progression of muscle development influences the emergence of neuromuscular junction alterations in a severe murine model for Spinal Muscular Atrophy. *Neuropathol Appl Neurobiol*. DOI: 10.1111/nan.12064.

Wan, L., Ottinger, E., Cho, S., Dreyfus, G., 2008. Inactivation of the SMN complex by oxidative stress. *Mol Cell.* 31(2): 244-254.

Wang, C.H., Finkel, R.S., Bertini, E.S., Schroth, M., Simonds, A., Wong, B., et al.., 2007. Consensus statement for standard of care in spinal muscular atrophy. *J Child Neurol.* 22(8): 1027-1049.

Whitney, M.A., Crisp, J.L., Nguyen, L.T., Friedman, B., Gross, L.A., Steinbach, P., et al., 2011. Fluorescent peptides highlight peripheral nerves during surgery in mice. *Nat Biotechnol*. 29(4): 352-356.

Whittaker, V.P., Michaelson, I.A., Kirkland, R.J., 1964. The separation of synaptic vesicles from nerve-ending particles (“synaptosomes”). *Biochem J*. 90(2): 293-303.

Wichterle, D., Lieberam, I., Porter, J.A., Jessell, T.M., 2002. Directed differentiation of embryonic stem cells into motor neurons. *Cell.* 110(3): 385-387.

Wirth, B., Brichta, L., Schrank, B., Lochmüller, H., Blick, S., Baasner, A., et al., 2006. Mildly affected patients with spinal muscular atrophy are partially protected by an increased SMN2 copy number. *Hum Genet.* 119(4): 422-428.

Wishart, T.M., Huang, J.P., Murray, L.M., Lamont, D.J., Mutsaers, C.A., Ross, J., et al., 2010. SMN deficiency disrupts brain development in a mouse model of severe spinal muscular atrophy. *Hum Mol Genet*. 19(21): 4216-4228.

Wishart, T.M., Mutsaers, C.A., Riessland, M., Riemer, M.M., Hamilton, G., Hannam, M.L., et al., In Press. Disrupted ubiquitin homeostasis and β-catenin signalling in spinal muscular atrophy.

Workman, E., Kolb, S.J., Battle, D.J., 2012. Spliceosomal small nuclear ribonucleoprotein biogenesis defects and motor neuron selectivity in spinal muscular atrophy. *Brain Res.* 1462: 93-99.

Wu, A.P., Whitney, M.A., Crisp, J.L., Friedman, B., Tsien, R.Y., Nguyen, Q.T., 2011. Improved facial nerve identification with novel fluorescently labeled probe. *Laryngoscopy*. 212(4): 805-810.

Yamazaki, T., Chen, S., Yu, Y., Yan, B., Haertlein, T.C., Carrasco, M.A., et al., 2012. FUS-SMN protein interactions link the motor neuron diseases ALS and SMA. *Cell Rep*. 2(4): 799-806.

Young, P.J., Day, P.M., Zhou, J., Androphy, E.J., Morris, G.E., Lorson, C.L., 2002. A direct interaction between the survival motor neuron protein and p53 and its relationship to spinal muscular atrophy. *J Biol Chem*. 277(4): 2852-2859.

Zhang, Z., Lotti, F., Dittmar, K., Younis, I, Wan, L., Kasim, M., et al., 2008. SMN deficiency causes tissue-specific perturbations in the repertoire of snRNAs and widespread defects in splicing. *Cell*. 133(4): 585-600.

Zou, T., Ilangovan, R., Yu, F., Xu, Z., Zhou, J., 2007. SMN protects cells against mutant SOD1 toxicity by increasing chaperone activity. *Biochem Biophys Res Commun.* 364(4): 850-855.

Supplementary Table 1 – A list of genes significantly ($p \leq 0.05$) up-regulated in resistant motor units, by more than 20%.

Gene Symbol	Gene Title	p-value	Fold Change
LOC100861869	uncharacterized LOC100861869	0.01563	5.843
C87122	expressed sequence C87122	0.03165	5.800
Krt14	keratin 14	0.00882	5.031
BC021785	cDNA sequence BC021785	0.01343	3.862
Ltn1	listerin E3 ubiquitin protein ligase 1	0.04789	2.579
2810429I04Rik	RIKEN cDNA 2810429I04 gene	0.00030	2.404
Slfn10-ps	schlafen 10, pseudogene	0.02556	1.949
Ccnb1 /// Gm5593	cyclin B1 /// predicted gene 5593	0.03609	1.886
4932429P19Rik	RIKEN cDNA 4932429P19 gene	0.01110	1.817
Akr1c20	aldo-keto reductase family 1, member C20	0.04378	1.764
---	---	0.02994	1.751
Bhlha9	basic helix-loop-helix family, member a9	0.01581	1.747
5830490A04Rik	RIKEN cDNA 5830490A04 gene	0.03689	1.732
9430031J08Rik	RIKEN cDNA 9430031J08 gene	0.00213	1.712
Ear11	eosinophil-associated, ribonuclease A family, member 11	0.02538	1.701
Prss37	protease, serine, 37	0.04170	1.678
---	---	0.03608	1.656
Nfe2l2	nuclear factor, erythroid derived 2, like 2	0.00095	1.649
---	---	0.03390	1.639
Ankrd55	ankyrin repeat domain 55	0.03123	1.630
Tnfsf13b	tumor necrosis factor (ligand) superfamily, member 13b	0.04975	1.580
---	---	0.01696	1.574
Tlr7	toll-like receptor 7	0.04988	1.560
Zfat	zinc finger and AT hook domain containing	0.04726	1.554
Ptafr	platelet-activating factor receptor	0.02402	1.552
Gm4850	THO complex 4 pseudogene	0.01326	1.541

	N-ethylmaleimide sensitive fusion protein		
Napb	attachment protein beta	0.02820	1.535
---	---	0.01157	1.530
Neb	nebulin	0.01180	1.522
4930408K08Rik	RIKEN cDNA 4930408K08 gene	0.04270	1.484
	chaperonin containing Tcp1, subunit 6b		
Cct6b	(zeta)	0.01739	1.467
	serine (or cysteine) peptidase inhibitor,		
Serpina3m	clade A, member 3M	0.04746	1.462
	DNA segment, Chr 4, ERATO Doi 199,		
D4Ertd199e	expressed	0.00873	1.437
1700066C05Rik	RIKEN cDNA 1700066C05 gene	0.03740	1.430
Ptgr2	prostaglandin reductase 2	0.04453	1.421
Arhgap26	Rho GTPase activating protein 26	0.00628	1.410
	tumor necrosis factor receptor superfamily,		
Tnfrsf22 ///	member 22 /// tumor necrosis factor receptor		
Tnfrsf23	superfamily, member 23	0.00385	1.405
---	---	0.00992	1.385
Six3os1	Six3 opposite strand transcript 1	0.02441	1.377
Msr1	macrophage scavenger receptor 1	0.04248	1.372
Anxa10	annexin A10	0.04011	1.357
4921501E09Rik	RIKEN cDNA 4921501E09 gene	0.03546	1.352
---	---	0.03753	1.340
4933406F09Rik	RIKEN cDNA 4933406F09 gene	0.00660	1.335
Morn1	MORN repeat containing 1	0.02228	1.334
Strada	STE20-related kinase adaptor alpha	0.03990	1.325
---	---	0.00075	1.324
9430019H13Rik	RIKEN cDNA 9430019H13 gene	0.03736	1.322
Eda	ectodysplasin-A	0.00894	1.321
Dspp	dentin sialophosphoprotein	0.02996	1.312
2700078F05Rik	RIKEN cDNA 2700078F05 gene	0.03092	1.312
Krtap16-5	keratin associated protein 16-5	0.04236	1.306
LOC639905 ///	SAP30-binding protein-like /// SAP30		
Sap30bp	binding protein	0.02249	1.305
8430419K02Rik	RIKEN cDNA 8430419K02 gene	0.01742	1.304

Cxcr5	chemokine (C-X-C motif) receptor 5	0.02004	1.304
Cyp17a1	cytochrome P450, family 17, subfamily a, polypeptide 1	0.00871	1.299
4930503B20Rik	RIKEN cDNA 4930503B20 gene	0.02121	1.287
---	---	0.02486	1.284
C77137	expressed sequence C77137	0.03107	1.278
Sh3rf3	SH3 domain containing ring finger 3	0.04177	1.277
Slurp1	secreted Ly6/Plaur domain containing 1	0.02586	1.273
Bcl2l11	BCL2-like 11 (apoptosis facilitator)	0.02869	1.266
Rap1gds1	RAP1, GTP-GDP dissociation stimulator 1	0.04117	1.265
B4galt4	UDP-Gal:betaGlcNAc beta 1,4-galactosyltransferase, polypeptide 4	0.00238	1.259
---	---	0.00633	1.258
Esrrg	estrogen-related receptor gamma	0.03180	1.251
2010002M12Rik	RIKEN cDNA 2010002M12 gene	0.04500	1.250
---	---	0.04832	1.243
4930526D03Rik	RIKEN cDNA 4930526D03 gene	0.02244	1.242
---	---	0.00539	1.241
4930449I04Rik	RIKEN cDNA 4930449I04 gene	0.01528	1.236
9630013A20Rik	RIKEN cDNA 9630013A20 gene	0.03464	1.233
---	---	0.03909	1.232
Fry	furry homolog (Drosophila)	0.04022	1.230
Tnfrsf11a	tumor necrosis factor receptor superfamily, member 11a	0.03777	1.227
Camk4	calcium/calmodulin-dependent protein kinase IV	0.03863	1.222
Lat2	Linker for activation of T cells family, member 2	0.02914	1.219
---	---	0.01404	1.219
Dzip1	DAZ interacting protein 1	0.03359	1.216
Dmrt2	doublesex and mab-3 related transcription factor 2	0.03149	1.210
Gm7969	predicted gene 7969	0.04736	1.202

Supplementary Table 2 – A list of genes significantly ($p \leq 0.05$) up-regulated in resistant motor units, by more than 20%.

Gene Symbol	Gene Title	p-value	Fold Change
---	---	0.0010	100.703
Egfr	epidermal growth factor receptor	0.0031	10.997
---	---	0.0097	7.772
Men1	multiple endocrine neoplasia 1	0.0268	4.802
Angptl3	angiopoietin-like 3	0.0389	4.652
1700108M19Rik	RIKEN cDNA 1700108M19 gene	0.0015	3.678
Ryr1	ryanodine receptor 1, skeletal muscle	0.0215	3.007
P2ry2	purinergic receptor P2Y, G-protein coupled 2	0.0273	2.997
Ang2	angiogenin, ribonuclease A family, member 2	0.0307	2.610
Ifi202b /// LOC100044068	interferon activated gene 202B /// interferon-activable protein 202-like	0.0064	2.551
Dennd2d	DENN/MADD domain containing 2D	0.0095	2.469
Tubb4b	tubulin, beta 4B class IVB	0.0047	2.216
Ell2	elongation factor RNA polymerase II 2	0.0247	2.192
Piwil1	piwi-like homolog 1 (Drosophila)	0.0141	2.075
Epb4.1l4b	erythrocyte protein band 4.1-like 4b	0.0434	2.024
Gprin1	G protein-regulated inducer of neurite outgrowth 1	0.0316	1.895
1700120E14Rik	RIKEN cDNA 1700120E14 gene	0.0327	1.833
4633402D09Rik	RIKEN cDNA 4633402D09 gene	0.0406	1.801
Cbl	Casitas B-lineage lymphoma	0.0100	1.757
Nid1	nidogen 1	0.0232	1.753
D2Bwg1423e	DNA segment, Chr 2, Brigham & Women's Genetics 1423 expressed	0.0378	1.751
Uty	ubiquitously transcribed tetratricopeptide	0.0476	1.691

	repeat gene, Y chromosome		
Bst1	bone marrow stromal cell antigen 1	0.0324	1.589
Piwil4	piwi-like homolog 4 (Drosophila)	0.0331	1.584
Abcg5	ATP-binding cassette, sub-family G (WHITE), member 5	0.0157	1.568
---	---	0.0386	1.550
Cep55	centrosomal protein 55	0.0448	1.520
---	---	0.0142	1.512
Dusp23	dual specificity phosphatase 23	0.0232	1.510
AI451250	expressed sequence AI451250	0.0406	1.504
---	---	0.0062	1.499
Abca8a	ATP-binding cassette, sub-family A (ABC1), member 8a	0.0303	1.476
Ccr9	chemokine (C-C motif) receptor 9	0.0260	1.475
Vgll3	vestigial like 3 (Drosophila)	0.0487	1.465
Ceacam10	carcinoembryonic antigen-related cell adhesion molecule 10	0.0363	1.457
Slc38a5	solute carrier family 38, member 5	0.0279	1.457
Scn7a	sodium channel, voltage-gated, type VII, alpha	0.0162	1.446
Stat1	signal transducer and activator of transcription 1	0.0436	1.444
Gorab	golgin, RAB6-interacting	0.0306	1.439
Limd2 /// LOC632329	LIM domain containing 2 /// LIM domain-containing protein 2-like	0.0373	1.436
---	---	0.0239	1.434
4933416I08Rik	RIKEN cDNA 4933416I08 gene	0.0238	1.433
Plekha4	pleckstrin homology domain containing, family A (phosphoinositide binding specific) member 4	0.0323	1.432
Fam122c	family with sequence similarity 122, member C	0.0060	1.429

Gngt1	guanine nucleotide binding protein (G protein), gamma transducing activity polypeptide 1	0.0343	1.421
2810403D21Rik	RIKEN cDNA 2810403D21 gene	0.0152	1.419
Slc36a2	solute carrier family 36 (proton/amino acid symporter), member 2	0.0427	1.415
---	---	0.0373	1.412
Dlgap5	discs, large (Drosophila) homolog-associated protein 5	0.0120	1.405
Cp	ceruloplasmin	0.0350	1.401
Frem1	Fras1 related extracellular matrix protein 1	0.0335	1.400
Fst	follistatin	0.0310	1.396
Rreb1	ras responsive element binding protein 1	0.0149	1.394
---	---	0.0225	1.393
Sema4d	sema domain, immunoglobulin domain (Ig), transmembrane domain (TM) and short cytoplasmic domain, (semaphorin) 4D	0.0276	1.391
Car3	carbonic anhydrase 3	0.0100	1.388
Tfpi	tissue factor pathway inhibitor	0.0498	1.385
Myo1b	myosin IB	0.0168	1.383
Gtf2e1	general transcription factor II E, polypeptide 1 (alpha subunit)	0.0118	1.379
Sostdc1	sclerostin domain containing 1	0.0089	1.378
Plekha7	pleckstrin homology domain containing, family A member 7	0.0210	1.372
Gabrg3	gamma-aminobutyric acid (GABA) A receptor, subunit gamma 3	0.0453	1.371
Art3	ADP-ribosyltransferase 3	0.0364	1.370
Lect1	leukocyte cell derived chemotaxin 1	0.0184	1.352
Nr4a2	nuclear receptor subfamily 4, group A,	0.0081	1.352

	member 2		
2900002K06Rik	RIKEN cDNA 2900002K06 gene	0.0301	1.351
Nr2f2	nuclear receptor subfamily 2, group F, member 2	0.0479	1.341
---	---	0.0349	1.340
3830422I06Rik	RIKEN cDNA 3830422I06 gene	0.0410	1.337
D16Ertd472e	DNA segment, Chr 16, ERATO Doi 472, expressed	0.0354	1.337
Twist1	twist homolog 1 (Drosophila)	0.0211	1.336
Cd37	CD37 antigen	0.0162	1.333
4930544N03Rik	RIKEN cDNA 4930544N03 gene	0.0038	1.332
---	---	0.0160	1.329
Rimklb	ribosomal modification protein rimK-like family member B	0.0488	1.327
1700030C10Rik /// 3110053B16Rik /// Gm9158	RIKEN cDNA 1700030C10 gene /// RIKEN cDNA 3110053B16 gene /// predicted gene 9158	0.0095	1.322
---	---	0.0375	1.322
1110059G02Rik	RIKEN cDNA 1110059G02 gene	0.0317	1.320
1810028F09Rik	RIKEN cDNA 1810028F09 gene	0.0083	1.314
Itgav	integrin alpha V	0.0150	1.312
D13Ertd150e	DNA segment, Chr 13, ERATO Doi 150, expressed	0.0412	1.311
Fam101a	family with sequence similarity 101, member A	0.0390	1.310
Arhgef17	Rho guanine nucleotide exchange factor (GEF) 17	0.0154	1.305
Slc25a35	solute carrier family 25, member 35	0.0350	1.305
Ceacam1	carcinoembryonic antigen-related cell adhesion molecule 1	0.0485	1.304
Cndp1	carnosine dipeptidase 1	0.0467	1.302

	(metallopeptidase M20 family)		
Tssk4	testis-specific serine kinase 4	0.0291	1.300
Smr2	submaxillary gland androgen regulated protein 2	0.0070	1.300
---	---	0.0326	1.299
Il7r	interleukin 7 receptor	0.0495	1.294
Ttc23	tetratricopeptide repeat domain 23	0.0349	1.293
Moxd1	monooxygenase, DBH-like 1	0.0273	1.290
Sall1	sal-like 1 (Drosophila)	0.0214	1.289
Galc	galactosylceramidase	0.0309	1.289
Il1rap	interleukin 1 receptor accessory protein	0.0374	1.289
Olfr17	olfactory receptor 17	0.0379	1.287
Agap1	ArfGAP with GTPase domain, ankyrin repeat and PH domain 1	0.0282	1.284
Prrx1	paired related homeobox 1	0.0152	1.281
---	---	0.0066	1.279
Clec4n	C-type lectin domain family 4, member n	0.0427	1.276
C030030A07Rik	RIKEN cDNA C030030A07 gene	0.0260	1.275
---	---	0.0083	1.274
Gxylt2	glucoside xylosyltransferase 2	0.0435	1.273
Cphx /// **Gm2104 ///** **Gm2135**	cytoplasmic polyadenylated homeobox /// predicted gene 2104 /// predicted gene 2135	0.0402	1.273
---	---	0.0039	1.272
Ahnak	AHNAK nucleoprotein (desmoyokin)	0.0341	1.271
Olfml3	olfactomedin-like 3	0.0004	1.271
Gm13111	predicted gene 13111	0.0110	1.270
Plscr4	phospholipid scramblase 4	0.0064	1.266
1700026J04Rik	RIKEN cDNA 1700026J04 gene	0.0119	1.263
---	---	0.0337	1.257
Ccdc64b	coiled-coil domain containing 64B	0.0466	1.257

Xlr3a /// Xlr3b /// Xlr3c	X-linked lymphocyte-regulated 3A /// X-linked lymphocyte-regulated 3B /// X-linked lymphocyte-regulated 3C	0.0362	1.254
1700010N08Rik	RIKEN cDNA 1700010N08 gene	0.0193	1.251
Chrdl1	chordin-like 1	0.0190	1.250
---	---	0.0274	1.243
Ch25h	cholesterol 25-hydroxylase	0.0418	1.242
Slc22a27	solute carrier family 22, member 27	0.0109	1.241
---	---	0.0162	1.241
Casp4	caspase 4, apoptosis-related cysteine peptidase	0.0465	1.240
Itga4	integrin alpha 4	0.0335	1.237
Epsti1	epithelial stromal interaction 1 (breast)	0.0248	1.237
---	---	0.0493	1.233
A430107P09Rik	RIKEN cDNA A430107P09 gene	0.0067	1.232
4930512B01Rik	RIKEN cDNA 4930512B01 gene	0.0489	1.232
Pou3f1	POU domain, class 3, transcription factor 1	0.0424	1.228
Scn7a	sodium channel, voltage-gated, type VII, alpha	0.0335	1.221
Naaladl2	N-acetylated alpha-linked acidic dipeptidase-like 2	0.0459	1.221
Fmo1	flavin containing monooxygenase 1	0.0087	1.218
AU021884	expressed sequence AU021884	0.0191	1.218
4833413E03Rik	RIKEN cDNA 4833413E03 gene	0.0229	1.214
Tmigd1	transmembrane and immunoglobulin domain containing 1	0.0357	1.213
Gpr126	G protein-coupled receptor 126	0.0400	1.206
Taf7l	TAF7-like RNA polymerase II, TATA box binding protein (TBP)-associated factor	0.0448	1.205
4930434J08Rik	RIKEN cDNA 4930434J08 gene	0.0178	1.203

Cphx	Cytoplasmic polyadenylated homeobox	0.0468	1.203

Appendix 3: List of Publications, Posters and Presentations.

List of Publications

Thomson, S.R., Wishart, T.M., Patani, R., Chandran, S., Gillingwater, T.H., 2012. Using induced pluripotent stem cells (iPSC) to model human neuromuscular connectivity: promise or reality? *J Anat*. 220(2): 122-130.

Thomson, S.R., Nahon, J.E., Mutsaers, C.A., Thomson, D., Hamilton, G., Parson, S.H., et al., 2012. Morphological characteristics of motor neurons do not determine their relative susceptibility to degeneration in a mouse model of severe spinal muscular atrophy. *PLoS One*. 7(12): e52605.

Anatomical Society Summer Meeting 2012 - Poster

"NMJ vulnerability in a mouse model of SMA: Characterisation of pathology and correlation with motor unit morphology."

Anatomical Society Summer Meeting 2013 - Talk

"Establishing the basis for selective motor neuron vulnerability in Spinal Muscular Atrophy."

Euan MacDonald Centre Post-Graduate Seminar 2013 – Talk

"Establishing the basis for selective motor neuron vulnerability in Spinal Muscular Atrophy."